

**Synthesis, Characterization, and Phase
Relations of Zinc-Rich Phases in the Binary
Systems Platinum-Zinc and Nickel-Zinc**

Dissertation

zur

Erlangung des Doktorgrades

der Naturwissenschaften

(Dr. rer. nat.)

dem

Fachbereich Chemie

der Philipps-Universität Marburg

vorgelegt von

Srinivasa Thimmaiah

aus Jagalur, India

Marburg/Lahn 2005

This work was carried out from July 2001 to September 2005 at the Department of Chemistry, Philipps University, Marburg under the supervision of Prof. Dr. B. Harbrecht.

Vom Fachbereich Chemie
der Philipps-Universität Marburg als Dissertation am 08.12.2005 angenommen.

Erstgutachter	Prof. Dr. B. Harbrecht
Zweitgutachter	Prof. Dr. W. Massa

Tag der mündlichen Prüfung am 21.12.2005

To my beloved parents

Table of Contents

	Page
1 Introduction	1
2 Experiment	5
2.1 Starting materials for syntheses	5
2.2 Syntheses	6
2.2.1 Solid state syntheses	6
2.2.2 Flux method	6
2.2.3 Pseudo-isopiestic technique	8
2.3 Phase analyses and data processing	10
2.3.1 Powder X-ray diffraction	10
2.3.2 Single crystal X-ray diffraction	10
2.3.3 Energy dispersive X-ray analyses and scanning electron microscopy	12
2.4 Physical properties	12
2.4.1 Density measurement	12
2.4.2 Thermal analyses	12
2.4.3 Magnetic susceptibility	13
2.4.4 Electrical conductivity	14
3 A general introduction to the binary system Pt-Zn	16
4 $\text{Pt}_{1-\delta_1}\text{Zn}_{7+\delta_2}$ - A zinc-rich monoclinic AlB_2-derivative structure	18
4.1 Introduction	18
4.2 Syntheses and characterization	19
4.2.1 Syntheses	19
4.2.2 Phase analyses	19
4.3 Physical properties	23
4.3.1 DTA analyses	23
4.3.2 Magnetic susceptibility	23
4.4 Results and discussion	24
4.4.1 Metrical relation between the commensurate and incommensurate structural models	25
4.4.2 Structural description and phase analyses	27

4.5	Summary	31
5	Pt₂Zn_{11-δ} (0.2 < δ < 0.3) - A γ-brass type phase	34
5.1	Introduction	34
5.2	Syntheses and characterization	34
5.2.1	Single crystal structure analysis	36
5.3	Physical Properties	39
5.3.1	Thermochemical analyses	39
5.3.2	Magnetic susceptibility	39
5.3.3	Electrical resistivity	41
5.4	Discussion	41
5.5	Summary	47
6	γ-Pt₅Zn₂₁ - A reappraisal of a γ-brass type complex alloy phase	48
6.1	Introduction	48
6.2	Syntheses and characterization	49
6.2.1	Solid state syntheses	49
6.2.2	Pseudo-isopiestic method	49
6.3	Single crystal structural determination	50
6.4	Phase analyses and physical properties	53
6.5	Results and discussion	56
6.6	Summary	62
7	Pt₁₁Zn₃₂ - A γ-brass related composite structure	64
7.1	Introduction	64
7.2	Syntheses	65
7.3	Structure determination	65
7.4	Physical properties of Pt ₁₁ Zn ₃₂	69
7.4.1	Thermochemical analyses	69
7.4.2	Magnetic susceptibility	70
7.5	Results and discussion	71
7.6	Summary	79
8	General characteristics of γ-brass related phases	80
9	Pt₁₈Zn₅₁ - A γ-brass related composite structure	83
9.1	Structure determination	83
9.2	Results and discussion	86
9.2.1	Phase relations	86
9.2.2	Structural description	87
9.3	Summary	90

10	Pt₂₉Zn₄₉ - A complex defective AlB₂-type derivative structure	91
10.1	Introduction	91
10.2	Syntheses and structure determination	92
10.2.1	Syntheses	92
10.2.2	Phase analyses	92
10.3	Results and discussion	96
10.4	Summary	103
11	A general introduction to the binary system Ni-Zn	105
12	Ni₇Zn_{57-δ} ($\delta = 0.54(6)$) - A reappraisal of a zinc-rich monoclinic phase	108
12.1	Introduction	108
12.2	Syntheses	108
12.3	Structure determination	109
12.4	Physical properties of NiZn ₈	113
12.4.1	Thermochemical analyses	113
12.5	Results and discussion	114
12.5.1	Metrical relation between commensurate and incommensurate structural models	115
12.6	Summary	120
13	Ni₁₈Zn₅₁ - A γ-brass related composite structure	121
13.1	Introduction	121
13.2	Syntheses	121
13.3	Structure determination	122
13.4	Results and discussion	125
13.4.1	Structural description and phase relation	125
13.5	Summary	129
14	Phase analyses	130
14.1	X-ray powder diffraction	130
14.2	Isopiestic measurements	133
14.3	Thermochemical analyses	134
15	Summary	136
16	Zusammenfassung	141
	Appendix	147
	References	166

Chapter 1

Introduction

Intermetallic compounds offer a rich source of various structure types [1] and special physical properties, such as superconductivity [2, 3], thermoelectric properties [4–6] or shape memory effects [7], *etc.* In recent decades, plenty of new intermetallic compounds have been synthesized and their properties and structure-composition relations were studied, mainly composed of transition metals and main group elements [8, 9].

The transition metal zinc is known to form complex structures with other metals [10–13]. Zinc-rich alloys have been topic of considerable interest over the last few decades because of their structural complexity. Intricate phase relations and structural complexity are prominent features of zinc-rich phases containing a second transition metal as a minor component.

In the year 1926 Hume-Rothery put forward a theory to rationalize the stability and formation of different brass-type alloys based on the valence electron concept [14, 15]. According to the Hume-Rothery concept the crystal structures of brass-like alloys are invariant with respect to a specific valence electron concentration (*vec*). The term *vec* can be defined as an average number of valence electrons per atom ($\frac{e}{a}$). Such alloys are known as Hume-Rothery alloys or so-called electron compounds. This particular types of intermetallic compounds are formed by noble metals and group 2, 12–15 elements. The sequence of the elemental structure types like face centered cubic, body centered cubic and hexagonal close packed being often found in Hume-Rothery systems occurs at a particular $\frac{e}{a}$ ratio. A prominent example is the β -brass type structure as realized by CuZn, AlCu₃, and Cu₅Sn: all three phases have $\frac{3}{2}$ chemically active electrons per atom for bonding.

These three phases adopt the *bcc* W-type structure irrespective of the structural distinctions of the constituents. In addition, this $\frac{e}{a}$ ratio is also favorable for the stabilization of the β -Mn-type structure [16]. β -Mn [17] has a rather complex cubic structure consisting of 20 atoms in the cubic unit cell. This allotropic form is stable at higher temperature. The compounds of CoZn [18] and Ag₃Al [19] adopt the β -Mn structure type.

The γ -brass phases emerging at about $\frac{21}{13}$ ($\frac{e}{a}$) are commonly considered to be the most complex Hume-Rothery phase in brass-like systems. The γ -brass, Cu₅Zn₈ [20] structure has been known since the early days of X-ray crystallography. It can be seen as a defective variant of the W-type or β -brass-like structure. A cluster concept was introduced by Bradley and Thewlis to describe the complex γ -Cu₅Zn₈ structure [20].

The Hume-Rothery rules were further extended by Westgren and Phragmen [21, 22]. They showed that a large number of different binary systems such as Cu-Zn, Ag-Zn and Au-Zn accommodates α -, β -, γ - and η - phases forming at *vec* of $\frac{3}{2}$, $\frac{21}{13}$, and $\frac{7}{4}$, respectively. Among the different structure types in brass-like systems the γ -phases presently attract most attention due to their complexity and challenge the understanding of the underlying stabilization mechanism [23, 24].

Electron counting rules, in particularly for the Hume-Rothery alloys, have played an important role in solid state chemistry and material science although they have not been well understood theoretically. From a theoretical point of view, the first quantum mechanical interpretation of the effect of e/a ratio on phase stability of brass type structures was given by Mott and Jones [25, 26]. Jones' theory successfully explained the extent of formation of primary solid solution and the formation of certain crystal structures in copper-based systems in a quantitative way. The structural stability is due to a stabilization of the energetically least bound electrons near the Fermi level by a partial condensation of these electrons when the Fermi sphere touches those Brillouin zone surfaces which correspond to the planes of the strongest Bragg reflections. As a consequence, a pseudo-gap opens at the Fermi level by a drastic reduction of the density of states (DOS) at the Fermi level [24, 27–31].

Furthermore, electron microscopy studies and constitutional analyses of the γ -regions of selected noble metal alloy systems like Ni-Zn [32], Cu-Zn [33] and Pd-Zn [34] revealed that subtle variations

of *vec* can result in additional structural differentiations. Morton pointed out that the γ -brass fields of Ni-Zn, Cu-Zn and Pd-Zn not only accommodate the γ -phase but a bundle of structurally related, complex phases with lower symmetry than the γ -phase. He uncovered two types of long-periodic regular domain structures in γ -brass and other related alloys with same structure by electron microscopy as shown in Fig. 1.1 and identified them as due to inversion antiphase domain (IAPD) structure. Among these two IAPD structures the striped structure has a periodicity of 70 Å. On the other hand, the triangular structure has a periodicity of about 2000 Å. Note, that the domain ordering changes continuously with composition, see Fig. 1.1a. The symmetry lowering is associated with striped dark and light contrast variations occurring along one of the face diagonal direction (e.g. [110]) of the cubic γ -brass type structure. These kinds of superstructure are known to be stabilized between 1.56 to 1.60 of *vec* with respect to the Ni-Zn system. A similar kind of super-structures were also observed in the Cu-Al [35, 36], Al-Cr [37] and Al-Cr-Fe [38] systems.

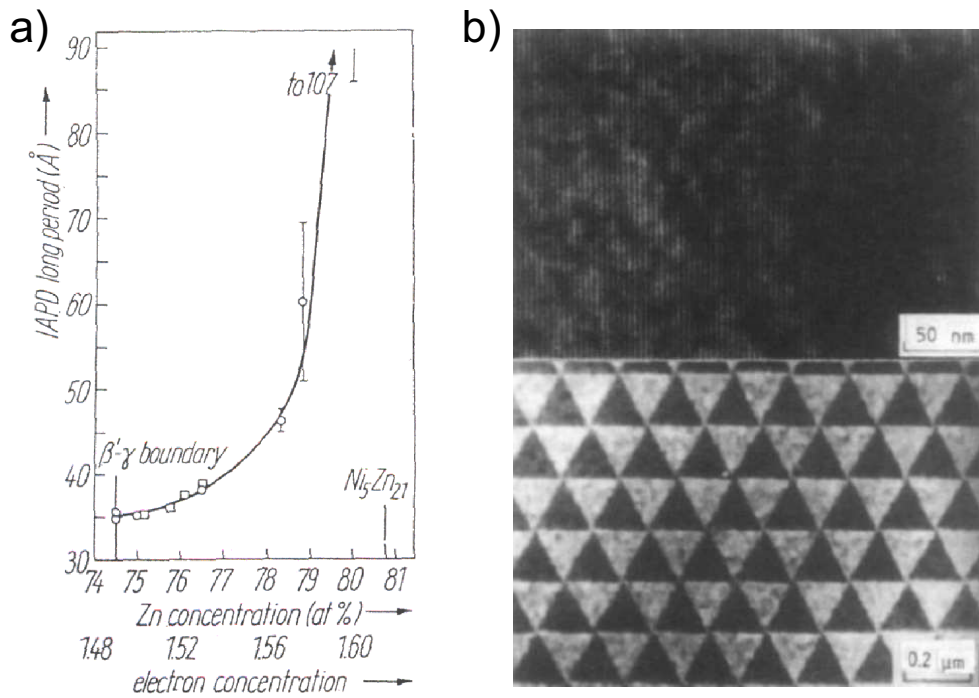


Figure 1.1: **a)** A graph showing the variation of the planar IAPD with composition and with valence electron concentration. **b)** Top: bright-field image of the planer anti-phase domain structure. Bottom: dark field image of the triangular IADP structure along the beam direction [111] (taken from Morton [32, 34]).

Further studies by Schubert *et al.* in the Ni-Zn system demonstrated the existence of the complex γ -brass related phase NiZn_3 [12]. It accommodates 276 atoms in the orthorhombic unit cell with 12 ordered vacancies. The NiZn_3 structure emerges next to the $\gamma\text{-Ni}_5\text{Zn}_{21}$ phase [11]. This structural finding is an additional support for the presence of such complex structures in the so-called γ -region as proposed by Morton. However, the weak X-ray scattering contrast between Ni and Zn hampers an unambiguous assessment of how the structure evolves at varying composition. In addition, a report on the $\text{Pd}_{15}\text{Zn}_{54}$ [39] phase which is structurally closely related to NiZn_3 in the congeneric Pd-Zn system renders support to the assumption that similar phases might yet be hidden near the γ -brass regions of other noble metal-zinc system. Discovery of these γ -brass related phases next to the γ -field in the Ni-Zn and Pd-Zn system dragged more attention to verify the existence of such structurally differentiated γ -phases in the Pt-Zn system.

The Pt-Zn binary system had previously been studied by Nowotny [40], Ekman [41] and Westman [13] and Schubert [42]. The first constitutional phase diagram of Pt-Zn was reported by Nowotny *et al.* [40]. They identified five phases by means of X-ray powder diffraction: Pt_3Zn [40], PtZn [43], $\text{PtZn}_{1.7}$ [40], $\gamma\text{-PtZn}_5$ [40] and PtZn_8 [40]. Structural features derived from single crystal X-ray diffraction studies were known only for the phases $\gamma\text{-Pt}_3\text{Zn}_{10}$ [13] and $\text{Pt}_7\text{Zn}_{12}$ [42]. Hence, the phases and phase relations of the Pt-Zn system are still poorly defined and deserve a closer inspection.

The research performed in the course of this dissertation was strongly motivated and guided by the justified prospect that the Pt-Zn system accommodates a series of structurally complex, yet hidden phases whose structures might provide new insight into expression, mechanisms and causes of structural complexity in chemically simple binary systems. The Pt-Zn system was chosen since the X-ray scattering contrast between Pt and Zn is large enough to allow a precise determination of the chemical composition by X-ray single crystal diffraction means, even for phases which might differ by less than 1 mol % in zinc. Accurate knowledge of the crystal structures will provide a solid basis to analyse how small changes in the valence electron concentration affect structural differentiation beyond the complexity of γ -brass type phases.

A reassessment of structures of related Zn-rich phases in the Ni-Zn system was second goal of this work.

Chapter 2

Experiment

2.1 Starting materials for syntheses

The starting materials were obtained from commercial sources. The materials with their sources which were used for syntheses are summarized together in Table 2.1

Table 2.1: Starting material for the syntheses

Elements	Form	Purity [%]	Source
Platinum	Powder	99.99	Chempur
Platinum	Foil	99.99	Chempur
Platinum	Wire	99.99	Johnson Matthey
Nickel	Rod	99.99	Alpha
Zinc	Powder	99.99	Chempur
Zinc	Granules (1–5 mm)	99.999	Chempur
Zinc chloride	Powder	99.99	Alpha

2.2 Syntheses

2.2.1 Solid state syntheses

All the syntheses were carried out in evacuated quartz glass ampoules with an external diameter of 10 mm. The metals were sealed in previously out-gassed, quartz glass ampoules under a reduced argon pressure (3×10^{-3} m bar). The molar fraction x_{Pt} of the mixtures was varied systematically between 0.05 and 0.50. The ampoules were continuously heated up to 1373 K at a rate of 120 K h^{-1} , kept at this temperature for 12 h, and subsequently cooled down to 973 K at a rate of 5 K h^{-1} . After a further annealing for 12 h the silica ampoules were brought to ambient temperature in the course of 12 h or by turning off the furnace. To avoid eventual loss of zinc due to evaporation, the reactants were kept at a lower temperature than the rest of the ampoule.

2.2.2 Flux method

Molten metals [44, 45] and metal halides [10, 46] have successfully been used as solvents for the growth of a variety of compounds and exploratory syntheses of new intermetallic materials. Flux method [47, 48] is a comparatively simple technique for growing crystal. This method offers more flexibility for opting suitable reaction temperatures for crystal growth. The advantages of the flux method are as following:

- The crystals are grown out of a solvent that reduces the melting temperature of the desired compound.
- Excess flux could be easily removed by dissolving or by applying an external force, such as centrifugation.
- It does not require an elaborate apparatus.
- Crystal growth is relatively fast.

This method was successfully applied for the syntheses of compounds at the zinc-rich side. Here, excess Zn was used as a “self flux”. The reacting mixture was placed into a silica ampoule with a plug of quartz glass wool which acts as a filter for an easy removal of excess flux after the reaction. This quartz glass wool was supported by broken quartz glass pieces. The ampoule consisting of

the reactant mixture and a plug of quartz glass wool was sealed under reduced pressure. The mixture was treated for 12 h at 985 K. Thereafter, the temperature was first decreased by 50 K h^{-1} to 735 K and then by 1 K h^{-1} down to 700 K, where the melt was removed by high-temperature centrifugation aided filtration [44]. More details description about the syntheses procedure can be found elsewhere [47, 49].

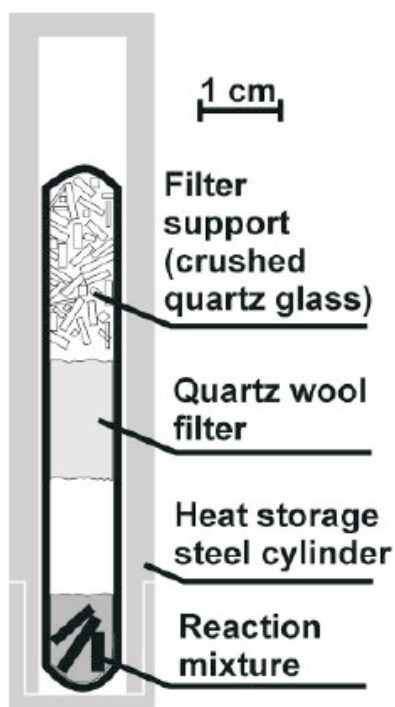


Figure 2.1: **Melt-centrifugation method:** Reaction ampoule containing crushed silica pieces and a plug of silica wool. The quartz glass ampoule was placed inside a steel cylinder filled with quartz glass wool as insulation in order to keep the sample at nearly constant temperature during centrifugation. After the reaction, the crystals were separated from the flux by turning the ampoule up-side down and centrifuging the liquid through the filter (taken from Boström *et al.* [50]).

An attempt was also made to make use of ZnCl_2 as a flux. The reactants Pt and Zn were taken in the ratio 1:15 and then transferred in to a silica ampoule containing dry ZnCl_2 . The ZnCl_2 was taken three times in excess compared to the reactants (wt.%). The silica ampoules were sealed under reduced pressure. The ampoules were heated continuously at a rate of 50 K h^{-1} to 700 K at which the reactants were kept for 7 days. Hereafter, the samples were brought to ambient temperature with a cooling rate 5 K h^{-1} . After the reaction excess ZnCl_2 was removed by washing the product with warm water. The crystals thus obtained were small in size with

regular shape, see Fig. 2.2. Noteworthy, a trace amount of ZnCl_2 remained on the surface of the crystals, though the product was washed several times with warm water. The size of the crystals ranged from ≈ 50 to $80 \mu\text{m}$.

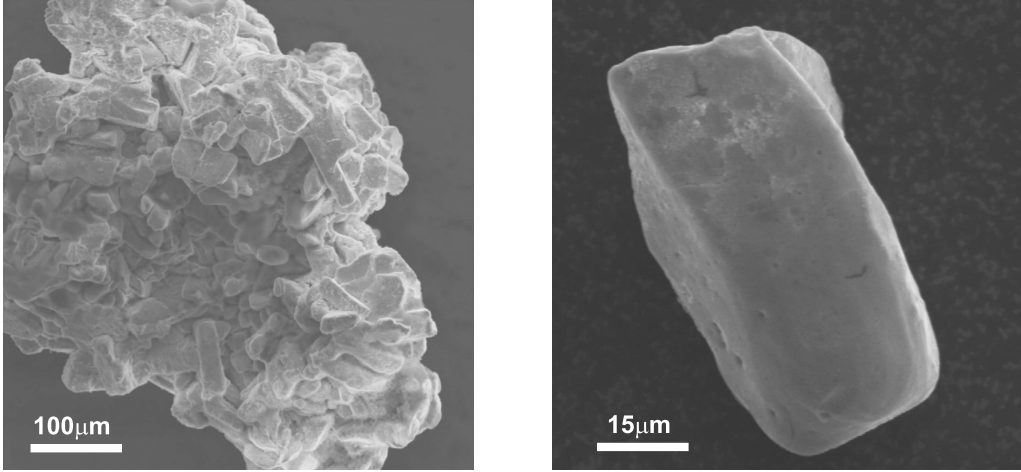


Figure 2.2: SEM micrographs of the phase PtZn_7 produced in a ZnCl_2 flux.

2.2.3 Pseudo-isopiestic technique

The isopiestic vapor pressure method is an advantageous technique for the understanding of phase formation, stability and width (homogeneity range) from one single experiment. The binary and ternary compounds had successfully been prepared by using the pseudo-isopiestic method [51–54]. From this method the thermodynamic activity of the volatile element in the alloys was determined at a fixed temperature of the volatile component.

The working principle is as follows: A non-volatile component ‘A’ (platinum) is equilibrated at the sample temperature T_S in a closed system with vapour from the pure volatile component ‘B’ (zinc) of temperature T_R , R stands for reservoir. The vapour pressure of component A and B should differ by at least three orders of magnitude. Assuming that the vapour pressure of the component A is negligibly small compared to that of component B, the total pressure in the system is determined by the only volatile component. The partial pressure of zinc over each sample at the sample temperature T_S , $p_{\text{Zn}}(T_S)$, must be equal to the vapor pressure of pure zinc at the temperature of the reservoir T_R , $p_{\text{Zn}}^0(T_R)$:

$$p_{\text{Zn}}(T_S) = p_{\text{Zn}}^0(T_R)$$

With this condition the zinc activity in each sample, at the sample temperature can be calculated by the following equation:

$$a_{\text{Zn}}(T_S) = \frac{p_{\text{Zn}}(T_S)}{p_{\text{Zn}}^0(T_S)} = \frac{p_{\text{Zn}}^0(T_R)}{p_{\text{Zn}}^0(T_S)}$$

For the calculation of the activity of the Zn in a sample, one needs to know the temperature dependence of the vapor pressure of pure Zn and the composition of the sample after the reaction. It can be determined by gain in weight by the nonvolatile component before and after the reaction.

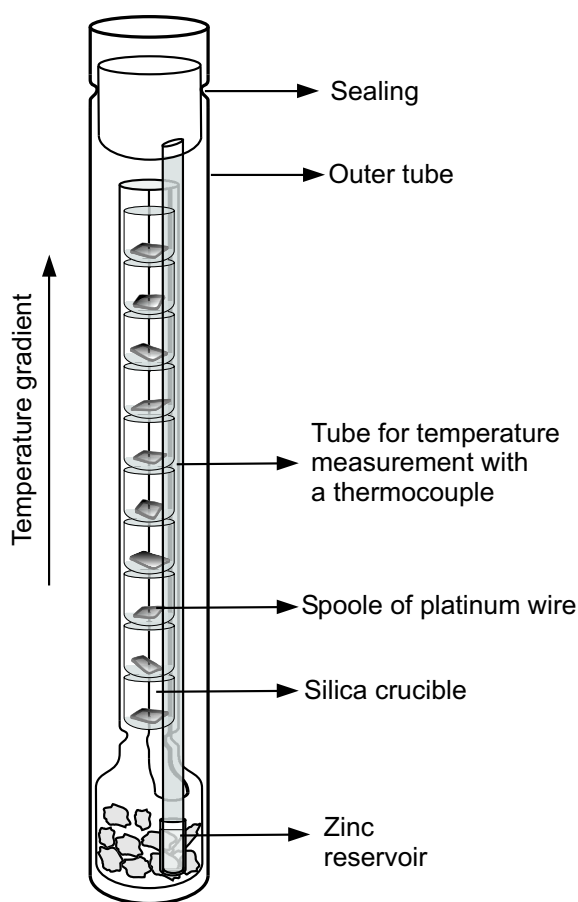


Figure 2.3: Schematic diagram of an isopiestic apparatus.

The experiments were conducted based on the above principle. Approximately 50 mg (± 0.05) of platinum wire was wound into spoolies and then placed into individual silica crucibles after that the crucibles were placed vertically top of one another in a specially designed silica apparatus, as shown in Fig. 2.3. 15 crucibles were arranged in the reaction tube, sealed under vacuum and then placed in the temperature gradient of a two-zone furnace. The platinum spoolies were exposed to

a constant vapor pressure of Zn (determined by the temperature of the Zn-reservoir within the reaction tube) for 14 days at temperatures ranging from 880 K to 1080 K. Pt/PtRh-thermocouple was used for controlling the temperature of the Zn reservoir and the 15 samples. The compositions of the equilibrated samples were determined by measuring the Zn uptake.

2.3 Phase analyses and data processing

2.3.1 Powder X-ray diffraction

X-ray powder diffraction was used as a first step of characterizing the products. The powder patterns were recorded using a X'Pert MPD diffractometer ($\text{CuK}\alpha = 1.5406 \text{ \AA}$, 40kV, 40mA) operating in Bragg-Brentano geometry with a secondary monochromator (Graphite). A single crystal silicon plate was used as a sample holder. All the diffractograms were recorded at room temperature between $10 < 2\theta < 90^\circ$.

High resolution X-ray powder patterns were obtained by synchrotron radiation of wavelength $\lambda = 1.150626 \text{ \AA}$ from the X3B1 beamline at the National Synchrotron Light Source, Brookhaven National Laboratory, New York, USA. The samples were ground in an agate mortar and pestle, passed through a 270 mesh sieve and then placed onto an off-cut quartz sample holder. Powder patterns were recorded with a 0.005° step in the detector. For each step, the sample holder was rotated 3° .

Calculations of theoretical powder patterns and data processing of the obtained powder patterns were carried out with the X'Pert program package supplied by Philips instruments [55]. The diffraction profiles of single or multiphase samples were quantitatively analyzed by a Rietveld method either with the X'Pert Plus [55] or Fullprof program [56].

2.3.2 Single crystal X-ray diffraction

Single crystal X-ray diffraction method was used for the characterization of unknown structures and confirmation of structural aspects for known structures. The crystals were selected from a crushed glittering product and then mounted on glass capillaries of 0.2 mm diameter using silicon

grease. The diffraction intensities of crystals were collected on a Stoe Image Plate Diffraction System, IPDS-I or IPDS-II ($\text{MoK}_\alpha = 0.71073 \text{ \AA}$; Graphite monochromator) at room temperature. More reliable lattice parameters were independently determined from the positions of 25 selected reflections measured on a four-circle diffractometer CAD 4 (Enraf Nonius, $\text{MoK}_\alpha = 0.71073 \text{ \AA}$; Graphite monochromator). The data collection and processing on the IPDS diffractometer was performed using programs supplied by Stoe [57]:

Expose [57]: For data collection
Cell [57]: To obtain the unit cell dimensions
Integrate [57]: For data reduction

For the structural determination the following programs were used.

XPREP: Cell reduction and determination of possible space groups on the basis of systematic extinctions,
SHELX-97 [58]: For structural refinement
JANA2000 [59]: For structural refinement
ADDSYM [60]: For finding missing symmetry

All measured reflections were subjected to Lorentz, polarization and numerical absorption correction using the X-SHAPE and X-RED programs [61, 62].

The definition of the R -values (residuals) are given as follows

$$R_1 = \frac{\sum_{hkl} \left| |F_o| - |F_c| \right|}{\sum_{hkl} |F_o|}$$
$$wR_2 = \sqrt{\frac{\sum_{hkl} w \cdot (F_o^2 - F_c^2)^2}{\sum_{hkl} w \cdot (F_o^2)^2}}$$

Goodness of fit,

$$S = \frac{\sum_{hkl} w \cdot (F_o^2 - F_c^2)^2}{m - n}$$

Where, m = number of reflections, n = number of parameters.

The difference $m - n$ gives the overdetermination of the structure. For a correct structure with a suitable weighting scheme, S will have a value close to one [63].

2.3.3 Energy dispersive X-ray analyses and scanning electron microscopy

The morphology of the samples were acquired from a scanning electron microscope (CS 4DV, CAM Scan, 20 kV). Chemical analyses were performed with an EDX system with a SiLi detector (Noran Instruments, Pt-L, Zn-L) both being attached to the microscope.

2.4 Physical properties

2.4.1 Density measurement

The densities of single phase samples were measured with a He-pycnometer (accupya 1330, Norcross) based on the gas displacement technique. The instrument determines automatically the density and volume of a solid sample by measuring the pressure change of helium in a calibrated volume.

2.4.2 Thermal analyses

Thermochemical analyses were performed employing a differential scanning calorimeter operating in the temperature range 670-1370 K (DSC setsys 16/18 Setaram, Pt/Rh thermocouple). The differential scanning calorimetry is a fingerprint technique that provides information about chemical reactions, phase transitions, and structural changes occurring in a sample during heating and cooling cycles. Usually 25-30 mg samples were pressed to a pellet of 3 mm in diameter, and then placed into a small silica ampoules of external diameter of 5 mm. The silica ampoules were sealed under a reduced pressure. The length of sample container was reduced to ≈ 15 mm to suppress incongruent vaporization of Zn. An empty silica container of similar size was used as a reference. The experiments were carried out under argon atmosphere at constant pressure. To ensure reproducibility of the thermal events the experiments were usually repeated twice at heating and cooling rates of 10 K min^{-1} .

2.4.3 Magnetic susceptibility

The magnetic susceptibility measurements were performed on a SQUID (Superconducting Quantum Interference Device; MPMS, Quantum Design, San Diego) magnetometer from 1.8-330 K with a constant magnetic field. Field dependent measurements were carried out on selected samples between 5 K and room temperature. About 100-130 mg of the substance were used for each measurement. The data were corrected for magnetic contributions from the sample holder manufactured from Teflon.

The molar susceptibilities χ_{mol} of the samples were calculated as follows

$$\chi_{mol} = \frac{M \cdot m_{mol}}{H \cdot m} \quad \text{cm}^3 \text{mol}^{-1}$$

M: magnetic moment [emu]

m: weight of the sample [g]

H: magnetic field [G]

χ_{mol} : molar weight of the sample [g mol⁻¹]

Generally, the susceptibility is the sum of different contributions:

$$\chi_{mol} = \chi_{mol}^{para} + \chi_{mol}^{TIP} + \chi_{mol}^{dia}$$

χ_{mol} = molar susceptibility

χ_{mol}^{para} = T – dependent paramagnetic contribution

χ_{mol}^{TIP} = T – independent paramagnetic contribution (Pauli paramagnetism)

χ_{mol}^{dia} = T – independent diamagnetic contribution

2.4.4 Electrical conductivity

The electrical resistance of microcrystalline samples were measured in the temperature range 12-300 K under vacuum using closed-cycle He cryostat and a temperature controller (Lake Shore). The electrical resistivities were determined by applying a four-point probe method in the d.c. mode. The four Cu wires were attached to a rod-like sample using silver epoxy paste. The sample was prepared in an evacuated sealed quartz glass capillary (0.5 mm diameter) by slowly crystallizing a melt in a 1173-1103 K temperature gradient. Contact distances and the cross sectional area of the rod-like sample were determined using a light microscope. The voltage was measured (Hewlett Packard) at a constant current (Advantest) of 10 mA or 20 mA, respectively.

A constant current I was applied across two electrodes while the potential across the two others was measured. The electrical resistance R can be calculated according to Ohm's law,

$$R = \frac{U}{I}$$

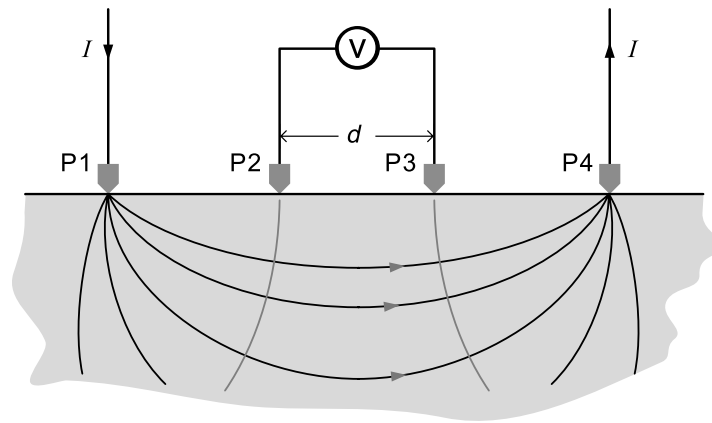


Figure 2.4: Schematic diagram of the four-point method. The constant current (I) is applied between two electrodes (P1 and P4) and the rising difference between the potential (ΔV) is measured between the two inner electrodes (P2 and P3).

According to this method the resistivity ' ρ ' of the sample is a function of the resistance R and the thickness of the sample. The conductivity is the reciprocal of the resistivity,

$$\rho = \frac{U}{I} \cdot \frac{A}{d}$$

EXPERIMENT

where:

U = Potential difference between the inner electrodes [V]

I = constant current applied between the outer electrodes [A]

A = Area of the sample [m]

d = distance between the two inner electrodes [m].

Chapter 3

A general introduction to the binary system Pt-Zn

The phase diagram of the binary system Pt-Zn was first reported by Nowotny *et al.* [40]. They identified five phases by means of X-ray powder diffraction, among them PtZn [43], PtZn_{1.7} [40], Pt₃Zn [40], γ -PtZn₅ [40], and PtZn₈ [40]. The structures of PtZn₅ [40] and PtZn₈ [40] are not known so far. Two compounds were subsequently characterized by means of single crystal X-ray diffraction, namely, Pt₇Zn₁₂ [42] and γ_1 -Pt₃Zn₁₀ [13]. The unit cell volume of γ_1 -Pt₃Zn₁₀ accommodates 392 atoms in a face centered cubic unit cell. Earlier, this phase was discovered by Ekman by means of powder X-ray diffraction, who assigned the composition Pt₅Zn₂₁ to this phase [41]. γ_1 -Pt₃Zn₁₀ is considered to be one of the most complex structure reported in the binary system Pt-Zn.

Furthermore, a comprehensive report on the relation between phases in the intermediate range $0.3 < x_{\text{Pt}} < 0.45$ of the Pt-Zn phase diagram was given by Schubert *et al.* [64]. They provide evidence for the existence of four brass-like phases [64] in this intermediate range. According to Schubert's proposal three of the phases form from a high temperature phase termed PtZn_{1.7} (ht3) with hitherto unknown structure in a cascade of eutectoid reactions upon cooling together with a phase which was considered to be Pt₃Zn₁₀ [13]. The first transition occurs at 1094 K. It leads to PtZn_{1.7} (ht2) for which an AlB₂-type related structure was proposed [40]. According to available data the structure of PtZn_{1.7} possess unreasonably short distances ($d(\text{Zn-Zn}) = 119$ pm). Below 962 K PtZn_{1.7} (ht2) transforms into Pt₇Zn₁₂ (ht1) adopting a superstructure of the

AlB₂-type with ordered defects [42]. The list of known structures in the Pt-Zn binary system are summarized in Table 3.1. The phase diagram of the Pt-Zn binary system is shown in Fig. 3.1.

Table 3.1: The crystallographic data on known structures in the Pt-Zn binary system

Phase	Pearson Symbol	Space group	Structure type
Pt _{1-x} Zn _x	<i>cF4</i>	Fm $\bar{3}$ m	Cu
Pt ₃ Zn [40]	<i>tP4</i>	Pm $\bar{3}$ m	Cu ₃ Au
β -PtZn [43]	<i>cP4</i>	P4/mmm	CuAu
PtZn _{1.7} * [40]	<i>hP6</i>	P321	PtZn _{1.7}
Pt ₇ Zn ₁₂ * [42]	<i>oP38</i>	Pbam	Pt ₇ Zn ₁₂
γ -Pt ₃ Zn ₁₀ [13]	<i>cF392</i>	F $\bar{4}$ 3m	Pt ₃ Zn ₁₀
PtZn ₈ [40]	–	–	–
Zn	<i>hP2</i>	P6 ₃ /mmc	Mg

* High temperature phase.

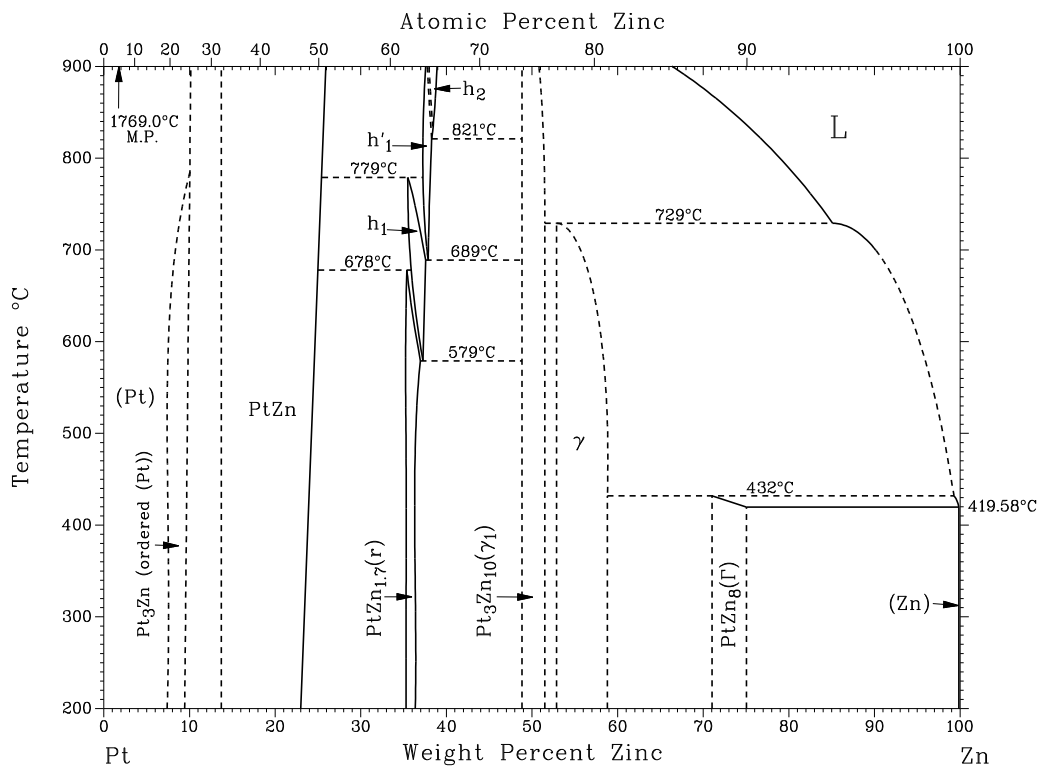


Figure 3.1: Phase diagram of the Pt-Zn binary system from ASM [65].

Chapter 4

$\text{Pt}_{1-\delta_1}\text{Zn}_{7+\delta_2}$ - A zinc-rich monoclinic AlB_2 -derivative structure

4.1 Introduction

The transition metal zinc is known to form structurally complex phases with other metals [10, 66, 67]. Due to its corrosion resistance nature, zinc metal is widely used as a protective coating on steel and in the galvanizing process. A survey of most Zn-rich intermetallic compounds shows a strong tendency for the element to form complex, structurally disordered phases [68–70]. Due to the complexity, however, only few phases have been structurally characterized so far, most recently, e.g., $\text{MoZn}_{20.44}$ [66], FeZn_{10} [10], $\text{Sc}_3\text{Zn}_{18}$ [71], $\text{Ir}_{7+7\delta}\text{Zn}_{97-11\delta}$ [70], and $\text{CoZn}_{7.8}$ [72]. Nevertheless, most commonly observed Zn-rich intermetallic phases are of formula MZn_{13} ($\text{M} = \text{Mn}$ [73], Fe [46, 73], Co [73], and Rh [74]) and they crystallize in the same structure type.

The constitutional phase diagram of Pt-Zn was reported by Nowotny *et al.* [40]. According to them, the most Zn-rich phase has an approximate composition corresponding to the formula PtZn_8 . It has been identified by means of X-ray powder diffraction. According to the available data, the Zn-rich phase undergoes decomposition at 705 K [65]. So far, there is no structural report on this phase. The only known Zn-rich phase in the congeneric Ni-Zn system so far is NiZn_8 . This chapter focuses on the syntheses and characterization of the phase richest in Zn, to which Nowotny assigned the composition PtZn_8 [40].

4.2 Syntheses and characterization

4.2.1 Syntheses

Single crystals of PtZn_7 were prepared in a zinc-rich self flux from 0.008 g Pt (0.5 mm wire) and 1.006 g Zn (granules). The elements (nominal composition Pt_xZn_y) were sealed in an evacuated quartz tube fitted with a quartz wool filter. The mixture was heated at 985 K for 12 h. Thereafter, the temperature was first decreased by 50 K h^{-1} to 735 K and then by 1 K down to 700 K, where the melt was removed by high-temperature centrifugation aided filtration [44].

The polycrystalline samples were prepared from the pure elements Pt and Zn in a ratio $\approx 1:15$ in evacuated silica ampoules. The reactant mixture was heated continuously at a rate of 30 K h^{-1} to 710 K at which reactants were kept for 150 h. Thereafter, samples were quenched in water or brought to ambient temperature within the course of 3 h. Often, the excess Zn was separated from the product, rarely it was observed that the product was embedded in a Zn matrix that was removed by dissolving the regulus in dilute hydrochloric acid.

4.2.2 Phase analyses

The products of single and two phase samples were routinely characterized by means of X-ray powder diffraction.

The powder diffractograms of polycrystalline samples were recorded on a Philips X'Pert MPD diffractometer (CuK_α) operating in Bragg-Brentano geometry equipped with a secondary monochromator. The powder diffractograms showed complex pattern. Occasionally additional peaks of excess Zn or $\text{Pt}_2\text{Zn}_{11}$ could be identified.

X-ray diffraction studies were carried out on a single crystal of $0.10 \times 0.05 \times 0.06$ mm³ in size with an IPDS-I X-ray diffractometer using MoK α radiation ($\lambda = 0.71073$ Å). The diffraction intensities were collected at room temperature in the range of $3.8 \leq 2\theta \leq 56.1$. The collected reflections were subjected to absorption correction using the programs X-RED and X-SHAPE [61, 62]. The atomic parameters for the structure refinement were obtained from direct methods as implemented in the SHELX-97 [58] program package. After few least-squares refinements the residual R1 dropped to $\approx 11\%$ with isotropic thermal displacement parameters for 24 distinct atomic positions. Three positions were assigned to Pt and the remaining to Zn. The thermal displacement parameters of Zn8 and Zn9 were anomalously large compared to the rest of Zn atoms. This tentatively suggested that these Zn sites might be partially occupied so that those positions were refined as partially occupied sites. In addition, the thermal displacement parameter of three atoms showed negative displacement parameters if assigned to be occupied by Zn. Therefore, these positions were treated as mixed occupied positions (M1, M2 and M3). Zn18 also showed a considerably high thermal displacement parameter and some residual electron density close to it. This was the highest peak in the difference Fourier map. It showed physically meaningless short distances to several atoms (Zn18 and Zn8). This feature as well as the large size of some displacement parameters (See Table 4.2) are attributed to the commensurate treatment of this truly incommensurate structure. The final refinement cycles including an extinction correction and anisotropic displacement parameters yield $R1 = 0.0334$, $wR2 = 0.1447$ for 786 reflections with $I_o > 2\sigma(I_o)$ out of 2494 unique reflections. The technical details, atomic coordinates and anisotropic thermal displacement parameters are accumulated in Table 4.1, 4.2 and 4.3, respectively.

The structure of PtZn₇ was confirmed by a refinement of a data set from a second crystal. The lattice constants are: $a = 1353.2(2)$ pm, $b = 762.7(3)$ pm, $c = 1876.9(3)$ pm, and $\beta = 97.41(2)^\circ$.

Table 4.1: Crystallographic and technical data for the single-crystal structure determination

Formula	Pt _{1-δ₁} Zn _{7+δ₂} *
Space group (No.)	C2/m (12)
Z	16
a / pm	1352.1(3)
b / pm	762.10(2)
c / pm	1875.8(4)
β [°]	97.40(3)
V / 10 ⁶ pm ³	1916.8
Molar mass / g mol ⁻¹	652.68
ρ _{cal} / g cm ⁻³	8.917
μ / mm ⁻¹	63.29
<i>Data collection</i>	
Crystal size / mm ³	0.10 × 0.05 × 0.06
Diffractometer	IPDS-I (STOE & Cie)
Temperature / K	293(2)
Radiation / monochromator	MoK _α / Graphite
Distance crystal-IP / mm	60
φ _{min} - φ _{max} ; Δφ	0-211; 1
2θ _{max} / °	56.1
Collected reflections	-17 ≤ h ≤ 17 -10 ≤ k ≤ 10 -24 ≤ l ≤ 24
Total No. of reflections	9846
<i>Data reduction</i>	
Program	IPDS-Software [57] / X-RED [61]
Absorption correction	Numerical, X-SHAPE[62]
max. / min. Transmission	0.3110 / 0.1307
Unique reflections	2494
R _{int}	0.0764
<i>Refinement</i>	
Program	SHELXL-97 [58]
Refined on	F _o ²
Reflections I _o > 2σ(I _o)	786
Variables	173
R ₁ (I _o > 2σ(I _o))	0.0355
R ₁ (all)	0.1244
wR ₂ (all)	0.1530
Goodness of fit	0.664
Δρ _{max} / Δρ _{min} / 10 ⁻⁶ e pm ⁻³	4.742 / -4.305
Extinction coefficient	0.000104(13)
1/w = σ ² (F _o ²) + (0.1(Max(F _o ² , 0) + 2F _c ²)/3) ²	

* In further discussion the phase Pt_{1-δ₁}Zn_{7+δ₂} (δ = δ₂-δ₁) is termed as PtZn₇ for the sake of simplicity.

Table 4.2: Positional and equivalent isotropic displacement parameters $U_{eq}(\text{pm}^2)$ for $PtZn_7$

Atom	Wy.	x	y	z	sof	U_{eq}
Pt1	2a	0	0	0	1	43(4)
Pt2	4i	0.13420(9)	0	0.60932(7)	1	43(4)
Pt3	4i	0.26906(10)	0	0.21742(7)	1	52(4)
Zn1	2c	0	0	$\frac{1}{2}$	1	203(16)
Zn2	4i	0.0619(3)	0	0.7363(2)	1	120(10)
Zn3	4i	0.0702(3)	0	0.8713(2)	1	120(10)
Zn4	4i	0.1984(3)	0	0.4797(2)	1	130(10)
Zn5	4i	0.1969(3)	0	0.3444(2)	1	112(10)
Zn6	4i	0.3258(3)	0	0.0881(2)	1	112(10)
Zn7	4i	0.1309(3)	0	0.1110(2)	1	218(13)
Zn8	4i	0.4484(4)	0	0.6965(3)	1	238(16)
Zn9	4i	0.2618(3)	0	0.7216(2)	0.82(2)	370(30)
Zn10	8j	0.0306(2)	0.1818(5)	0.37496(15)	1	129(7)
Zn11	8j	0.1089(2)	0.1874(5)	0.23593(16)	1	173(7)
Zn12	8j	0.16545(19)	0.1802(5)	0.98402(15)	1	103(7)
Zn13	8j	0.2989(2)	0.1801(4)	0.59245(16)	1	122(7)
Zn14	8j	0.2552(2)	0.3086(5)	0.15089(17)	1	166(7)
Zn15	8j	0.3785(2)	0.1933(5)	0.46335(17)	1	180(8)
Zn16	8j	0.4329(2)	0.1806(3)	0.19715(18)	1	101(5)
Zn17	8j	0.4874(2)	0.1951(4)	0.92703(15)	1	162(7)
Zn18	8j	0.3545(3)	0.1924(5)	0.32005(16)	1	425(11)
M1(Zn)	4i	0.3339(3)	0	0.95499(19)	0.94(1) ^a	73(14)
M2(Zn)	4i	0.40094(11)	0	0.82591(8)	0.19(1) ^a	31(5)
M3(Zn)	4i	0.46831(17)	0	0.56545(12)	0.57(1) ^a	87(9)

^a sof of Pt = 1 - sof Zn

 Table 4.3: Anisotropic displacement parameters U (pm^2) for $PtZn_7$

Atom No.	U11	U22	U33	U12	U13	U23
Pt1	40(9)	66(11)	24(9)	0	0	9(7)
Pt2	39(7)	61(9)	27(7)	0	0	-5(5)
Pt3	51(7)	66(8)	37(7)	0	0	1(5)
Zn1	80(30)	430(50)	90(30)	0	0	-20(20)
Zn2	160(20)	150(30)	60(20)	0	0	56(17)
Zn3	190(20)	130(30)	50(20)	0	0	45(17)
Zn4	170(20)	150(30)	80(20)	0	0	52(17)
Zn5	130(20)	110(30)	110(20)	0	0	41(17)
Zn6	130(20)	180(30)	29(19)	0	0	18(15)
Zn7	160(30)	410(40)	70(20)	0	0	-50(20)
Zn8	450(30)	190(20)	73(17)	0	0	70(18)
Zn9	50(30)	990(60)	60(30)	0	0	-41(18)
Zn10	120(14)	106(18)	170(15)	-51(13)	-35(13)	49(12)
Zn11	177(15)	150(19)	210(16)	92(14)	74(14)	90(12)
Zn12	38(13)	118(18)	155(14)	-13(12)	-25(14)	12(11)
Zn13	93(14)	87(17)	185(16)	-31(13)	-9(13)	13(12)
Zn14	120(14)	129(18)	260(16)	72(13)	98(14)	68(12)
Zn15	159(16)	178(19)	215(16)	89(14)	111(14)	67(13)
Zn16	70(10)	97(11)	139(10)	-2(15)	-8(16)	24(8)
Zn17	214(15)	143(18)	135(15)	-71(13)	-73(13)	51(12)
Zn18	510(20)	630(30)	187(16)	-448(19)	-279(16)	215(14)
M1	130(20)	80(30)	14(19)	0	0	30(14)
M2	36(8)	44(10)	12(7)	0	0	2(5)
M3	121(13)	86(15)	62(12)	0	0	37(8)

4.3 Physical properties

4.3.1 DTA analyses

According to DTA investigations, the zinc-rich monoclinic phase decomposes incongruently at 753(2) K to γ -brass phase Pt₂Zn₁₁ and elemental Zn. This event is indicated by an endothermic peak. The successive endothermic peak at 1130(3) K attributes for the incongruent melting of Pt₂Zn₁₁. During the cooling process, the first exothermic peak at 1125(3) K corresponds to re-crystallization of Pt₂Zn₁₁ and the next peak at 692(1) K refers to the solidification of Zn. There is no evidence of re-crystallization of PtZn₇ upon cooling at a cooling rate of 10 K min⁻¹. However, noticeable amounts of Zn were condensed on the top of silica ampoule. Due to the lack of zinc, the composition seems to be close to Pt₂Zn₁₁. Consecutive cycles of heating showed endothermic peaks at 693(2) K and 1130(3) K assigned to the melting of Zn and Pt₂Zn₁₁, respectively.

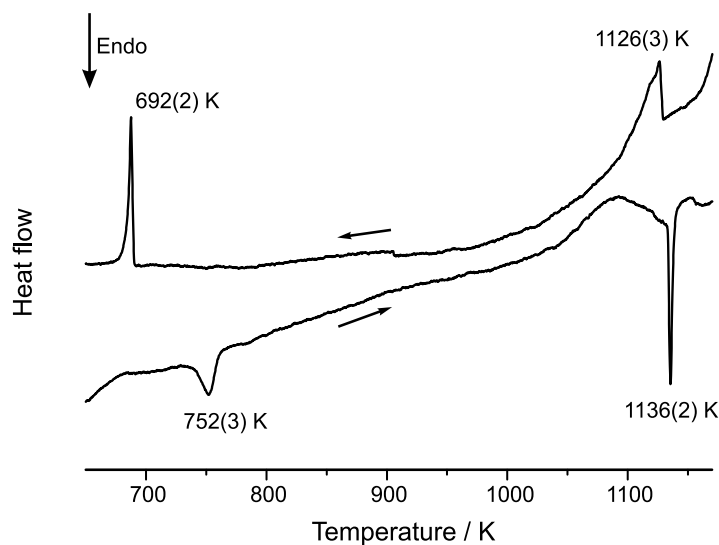


Figure 4.1: A typical thermogram of the phase PtZn₇.

4.3.2 Magnetic susceptibility

The magnetic susceptibility of polycrystalline PtZn₇ samples were measured as a function of temperature between 5 and 330 K with a magnetic flux density of 1 Tesla. The diamagnetic contribution of the sample holder was subtracted from the magnetization data. The Pauli paramagnetism of the metallic conductor was found to be overcompensated by the core diamagnetism of the constituents of the phase. The temperature independent diamagnetic contribution was

obtained from the slope of a χT versus T plot. The value obtained was $-4.5 \times 10^{-10} \text{ m}^3 \text{ mol}^{-1}$ for $\frac{1}{8+\delta}$ PtZn_{7+δ} compared to the value $-5.4 \times 10^{-10} \text{ m}^3 \text{ mol}^{-1}$ for $\frac{1}{13}$ γ -Pt₂Zn₁₁ [75]. A plot of the magnetic susceptibility as a function of temperature is shown in Fig. 4.2.

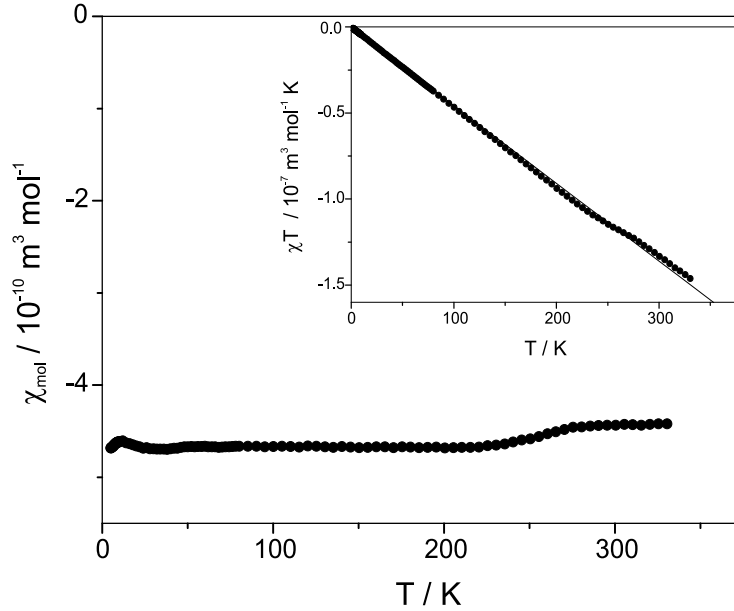


Figure 4.2: Molar magnetic susceptibility of a polycrystalline PtZn₇ sample scaled to $\frac{1}{8.3}$ PtZn₇ as a function of temperature.

4.4 Results and discussion

The zinc-rich PtZn₇ phase crystallizes in a monoclinic cell in the space group C2/m. The obtained lattice parameters are: $a = 1352.1(3)$ pm, $b = 762.1(2)$ pm, $c = 1875.8(4)$ pm, $\beta = 97.40(3)^\circ$ (Pearson symbol, mC128). The reported structure is a spatially averaged structure, since the superstructure reflections along \mathbf{c}^* are not perfectly commensurate. The structural refinement of the averaged structure yielded large correlations between different atoms. Significant charge densities are shown in the difference Fourier map. Moreover, some additional reflections remain unindexed in the averaged cell. This indicates that the structure is presumably incommensurately modulated. Furthermore, analyses of intensities in the reciprocal space section $h0l$ revealed that the modulation is quite strong and can be clearly seen in the section $h0l$ plane, see Fig. 4.3.

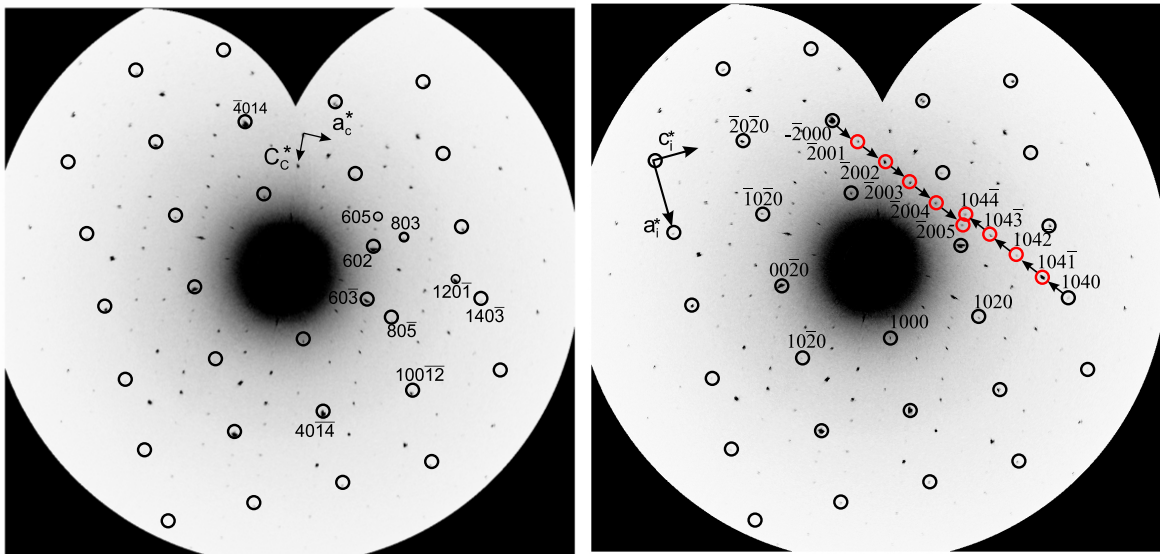


Figure 4.3: The $h0l$ section of the reconstructed reciprocal lattice of the phase PtZn_7 . **Left:** The conventional commensurate supercell with reflections marked by circles are indexed accordingly. **Right:** The incommensurate lattice with $\mathbf{q} \equiv \frac{1}{9}[304]^*$. Note, the subset of strong reflections indicated by large black circles and the satellites are indicated by red.

The PtZn_7 structure can be adequately described in the (3+1)-dimensional superspace. A set of strong reflections could be indexed on the basis of an unconventional A-centered cell with lattice parameters $a = 258.77$, $b = 763.35$, $c = 423.14$ pm and $\beta = 92.05^\circ$. The subset of weak reflections, the so-called satellites, can be indexed with a \mathbf{q} vector of approximately $\frac{1}{9}[304]^*$. Finally, the structure was refined in the (3+1)-dimensional superspace group $A2/m(\alpha 0 \gamma)00$ using the program JANA2000 [59]. Fig. 4.3 shows two indexing schemes of reflections based on the cells of the commensurate and incommensurate structure, respectively.

4.4.1 Metrical relation between the commensurate and incommensurate structural models

The single crystal X-ray diffraction pattern of the compound PtZn_7 displays a subset of strong reflections that leads to a fairly straight-forward indexing on the basis of an A-centred monoclinic unit cell:

$$\begin{aligned} a &= 258.77 \text{ pm} \\ b &= 763.35 \text{ pm} \quad \beta = 92.05^\circ \\ c &= 423.14 \text{ pm} \end{aligned}$$

Note however that several strong reflections remain un-indexed in Fig. 4.3b. The subset of weaker reflections forms a set that may be indexed using an additional vector, $q \approx \frac{1}{9} [3 \ 0 \ 4]^*$. This choice enables it to index all reflections and gives a clear, hierarchical intensity distribution. The q vector refines to (0.345, 0, 0.426).

The commensurate super cell for PtZn_7 is given by the following parameters:

$$\begin{aligned} a &= 1352.1 \text{ pm} \\ b &= 762.1 \text{ pm}, \quad \beta = 97.40^\circ \\ c &= 1875.8 \text{ pm}. \end{aligned}$$

The commensurate q vector indicated in Fig. 4.3a implies a transformation matrix of the form (ignoring the setting)

$$M1 = \begin{pmatrix} -7 & 0 & 2 \\ 0 & -1 & 0 \\ 1 & 0 & 3 \end{pmatrix}$$

or, for the reciprocal cell

$$M1^{-1} = \begin{pmatrix} \frac{-3}{23} & 0 & \frac{2}{23} \\ 0 & -1 & 0 \\ \frac{1}{23} & 0 & \frac{7}{23} \end{pmatrix}$$

Though the structure is modulated, the spatially averaged structure (commensurate or lock-in) is a very close approximation to the real incommensurate structure. Hence, the structural description is given for the commensurate model for aiming to get a better understanding of the distribution of the atoms in the unit cell.

4.4.2 Structural description and phase analyses

At first glance, the structure PtZn₇ appears to be rather complex. The analysis of local coordination configurations, however, reveals that four crystallographic distinct sites out of 24 are enough to describe the whole structure. Even though the phase crystallizes in the monoclinic system, the atomic arrangements of particular atoms are highly regular. As seen in Fig. 4.4, the entire structure can be described by using three different kinds of coordination polyhedrons constructed about four crystallographic distinct atoms, Zn1, Pt1, Pt3 and M2. These polyhedrons include all crystallographic independent atomic sites. The polyhedrons are namely, an icosahedron, two polyhedrons with coordination number CN11 and a Bergman-type cluster. The CN 11 polyhedron is a hybrid polyhedron of an icosahedron and a monocapped distorted cube.

The icosahedron is constructed over Pt1 with Wyckoff position 2a. Its polyhedron is surrounded by six other polyhedrons due to C-centering into a motif of densely close-packed layers. The polyhedrons of the mixed occupied site M2 ($\approx 20\%$ of Zn) and Pt3 have CN11. They are connected by sharing common edges leading to a puckered, garland-type arrangement. The polyhedrons about M2 are the most disordered ones compared to the rest. They incorporate a mixed occupied site M1 ($\approx 93\%$ of Zn) and another partially occupied site Zn9 ($\approx 82\%$ of Zn) in the vicinity of the central atom.

The third polyhedron is 33 atom fragment of a Bergman cluster. Indeed, the Bergman cluster is made up of 105 atoms around a central atom in successive shells of an icosahedron, a dodecahedron, a large icosahedron and a truncated icosidodecahedron (polyhedron with 32 faces). The final shell with 60 atoms has the same appearance as the Bucky ball (Fullerenes). The motif of Bergman cluster is very often used to describe the structure of quasicrystals/crystalline approximants [76, 77]. The Bergman-type cluster consists only of the two inner shells. The first shell is made up of icosahedrons encapsulating central Zn1 atoms. The pentagonal anti-prismatic frame is formed by ten Zn atoms capped with two Pt atoms. The distances between the central Zn1 and the peripheral atoms range from 255.7 – 288.8 pm. The consecutive shell consists of 20 atoms which are located over each triangular face of the icosahedron. It forms a slightly distorted pentagonal dodecahedron. The distances between the central Zn1 and the peripheral atoms are spread from 404.3 – 440.7 pm. This is the dual polyhedron of the icosahedron and vice versa.

The Bergman-type clusters are connected via edges to each other forming a dense close-packed arrangement as seen in Fig. 4.4.

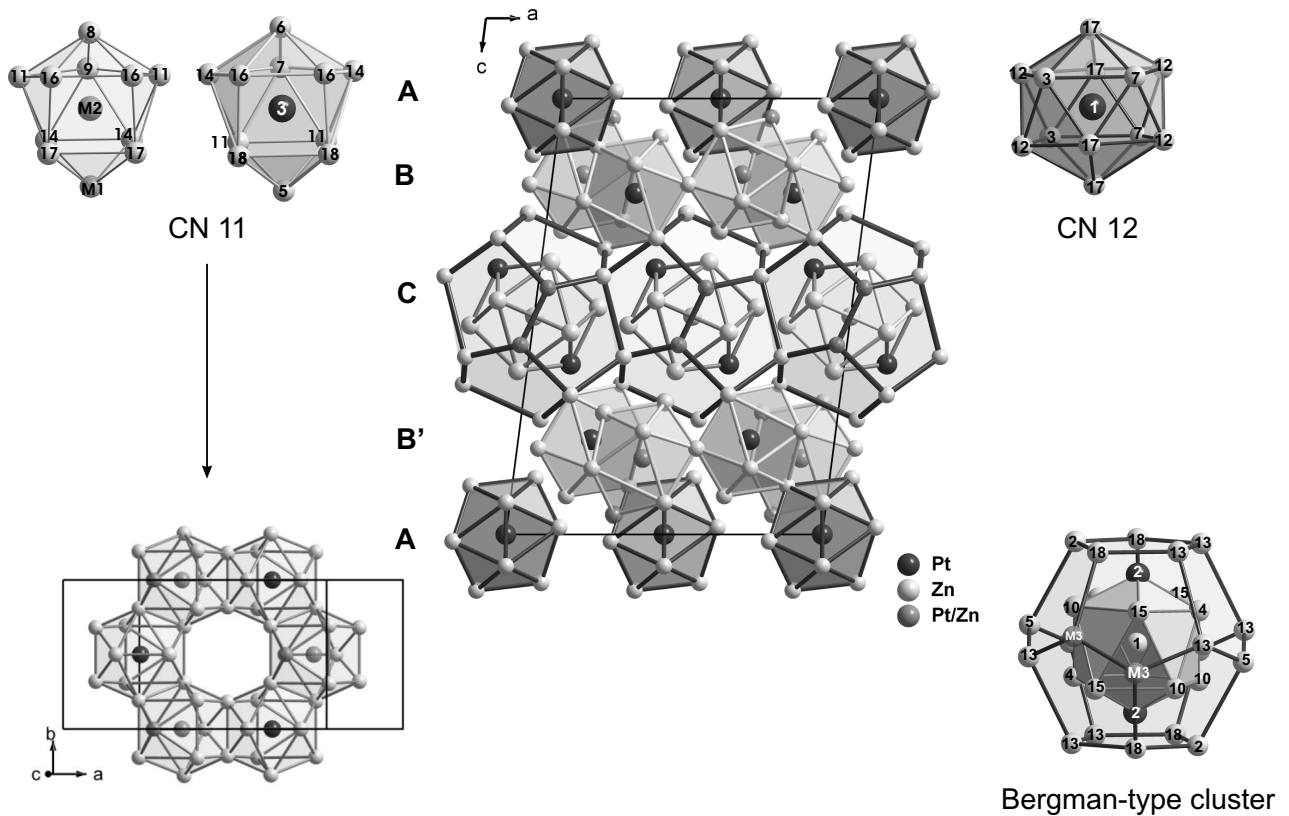


Figure 4.4: Building units of the phase $PtZn_7$. The structure is built up by three different polyhedrons namely, an icosahedron, polyhedron of CN11 and Bergman-type cluster. **Lower left:** condensed polyhedrons of CN11 forming a puckered garland-type arrangement. **Lower right:** Bergman-type cluster composed of 33 atoms.

The structure of $PtZn_7$ can be seen as being built up of condensed layers of polyhedrons stacked along the b axis. The layers are named as A, B, C and B' located at the heights $z = 0, \approx \frac{1}{4}, \frac{1}{2}$ and $\approx \frac{3}{4}$. The polyhedral layer A is composed of icosahedrons which are condensed with the polyhedra layer B via common vertices. The layers designated as B and B' are made up of CN11 polyhedrons which are connected among each other by sharing common edges leading to a garland-type arrangement. The layers B and B' have the same composition because they are related by an inversion center. The polyhedral layer C is formed by densely packed edged sharing Bergman-type clusters.

The structural kinship of the PtZn_7 structure with the AlB_2 -type structure becomes apparent when it is decomposed into atomic layers parallel to $(\bar{2} 0 7)$. The structure of PtZn_7 is composed of alternating 3^6 and defective 6^3 atomic layers. This kind of structural features are observed in several intermetallic compounds [78].

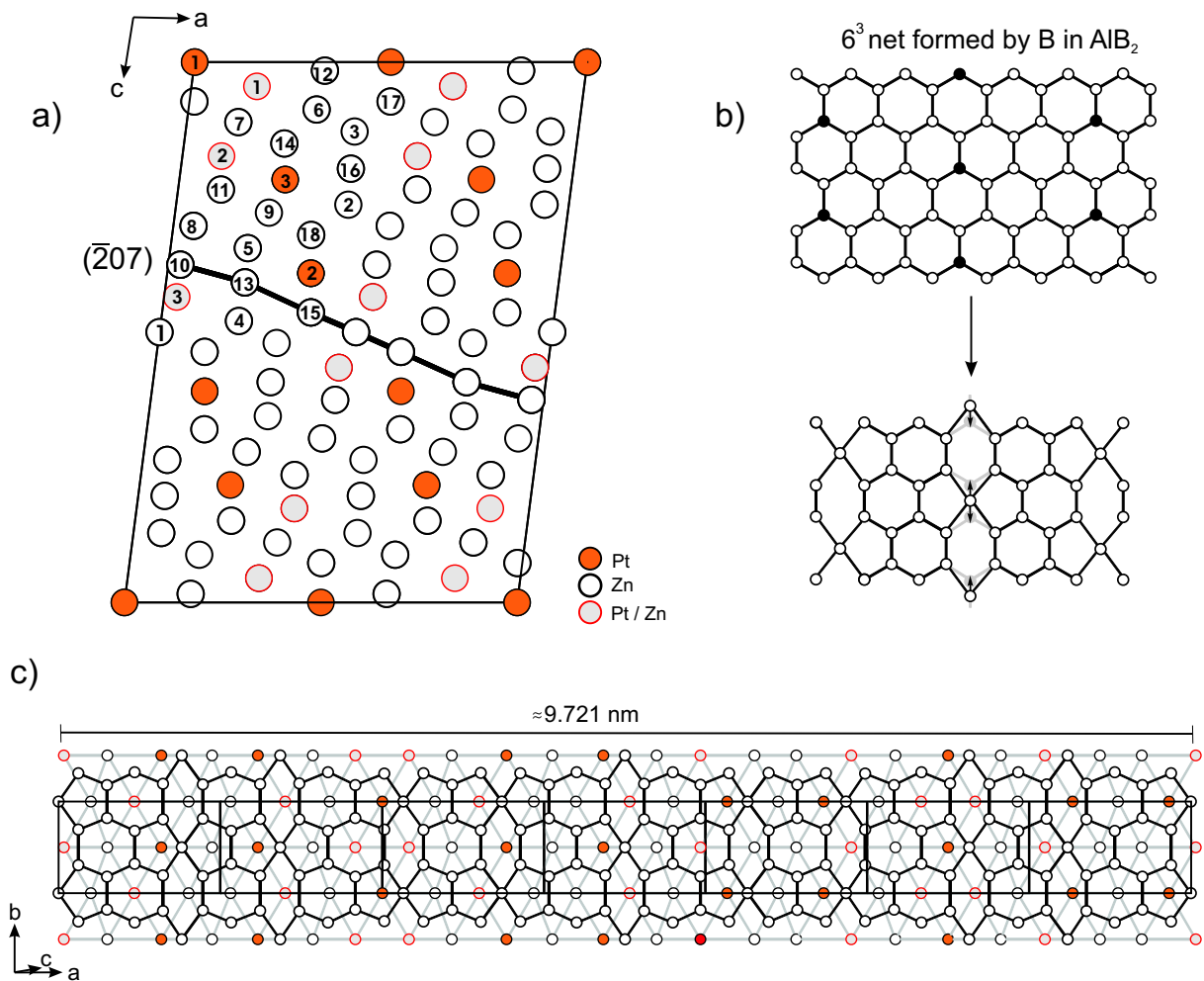


Figure 4.5: a) Unit cell of PtZn_7 and the orientation of the defective AlB_2 -type layers. b) Schematic representation of an undistorted honeycomb net (6^3 net) and the deformed net by introducing vacancies. c) A projection of a defective AlB_2 -type layer in PtZn_7 structure viewed approximately along $[\bar{1}03]$.

The atomic layers of the AlB_2 -type structure can be adequately described in terms of nets. The vertices of the nets correspond to the position of the atoms in the layers. For AlB_2 , the Al atoms are arranged in planar 3^6 nets and the B atoms in honeycomb-type 6^3 nets. In this notation (Schläfli symbol) the number of the basis refers to the polygon of the net and the exponent refers to the vertex configuration *i.e.*, the number of polygons arranged around each vertex. The two

distinct nets are stacked alternately approximately along $[\bar{1}03]$.

Fig. 4.5 shows the architecture of a decomposed atomic layer of the PtZn₇ structure. The length of the repeating unit of the AlB₂-type atomic layer is equivalent to ≈ 9.721 nm. The 3⁶ atomic layers are defined by both Pt and Zn atoms, similar to the arrangement of B atoms in AlB₂. The 6³ atomic layer is exclusively formed by Zn atoms, similar to the arrangement of Al atoms in AlB₂. These two atomic layers are stacked alternately along $[\bar{1}03]$. The irregularity in the net arises from a concerted distortion of a 6³ honeycomb net due to the presence of vacancies. Fig. 4.5b sketches the basic principle of the distortion associated with the defects.

In addition, the thermal displacement parameters of the atoms which are located in the elongated hexagons, Zn₉ and Zn₁₈ show relatively large displacement parameters compared to average. This may be associated with the before mentioned residual electron density close to these atoms. Local structural disorder or a structural modulation may cause these phenomena. A pair of layers topologically similar to those in AlB₂-type structure includes all crystallographic distinct atoms, see Fig. 4.5c. The formula of the phase can be rewritten with respect to that of AlB₂ as (Pt₁₅Zn₃₁)(Zn₄₁□₅)₂ with □ denoting vacancies. For counting the atoms in the AlB₂-type atomic nets, the partially occupied sites are considered to be fully occupied for avoiding confusion.

The interatomic distances of Pt–Zn cover the range from 253.6 – 270.4 pm. The distances less than 260 pm compare well with the sum of the covalent radii of Pt ($r_{\text{Pt}}^{\text{c}} = 128$ pm) and Zn ($r_{\text{Zn}}^{\text{c}} = 131$ pm), while longer distances compare fairly well with the sum of the atomic radii $r_{\text{Pt}}^{\text{a}} = 137.3$ pm and $r_{\text{Zn}}^{\text{a}} = 133.5$ pm. The interatomic distances Zn–Zn ranging from 252.7 – 300.9 pm are prominent. M–M (mixed Pt/Zn positions) distances range from 269.3 – 270.0 pm, and Zn–M distances from 251.3 – 277.4 pm. For more detailed information see the interatomic distances for PtZn₇ listed in Table 4.4.

The Zn-rich monoclinic phase is stable at ambient temperature and undergoes decomposition at 753 K into γ -Pt₂Zn₁₁ and Zn. This was confirmed by X-ray powder diffraction of the sample after DTA experiments. The decomposition temperature reported in the available Pt-Zn phase diagram is nearly 50 K off from the observed temperature.

EDX analyses on selected crystals revealed a composition of the phase of 12 ± 1 at.% of Pt which is in good agreement with the single crystal structure refinement (12.04 at.% of Pt). According to single crystal structural analyses the homogeneity range of PtZn₇ is found to be very narrow. Despite the structural modulation the measured intensities for the phase match well with calculated ones as Fig. 4.6 proves.

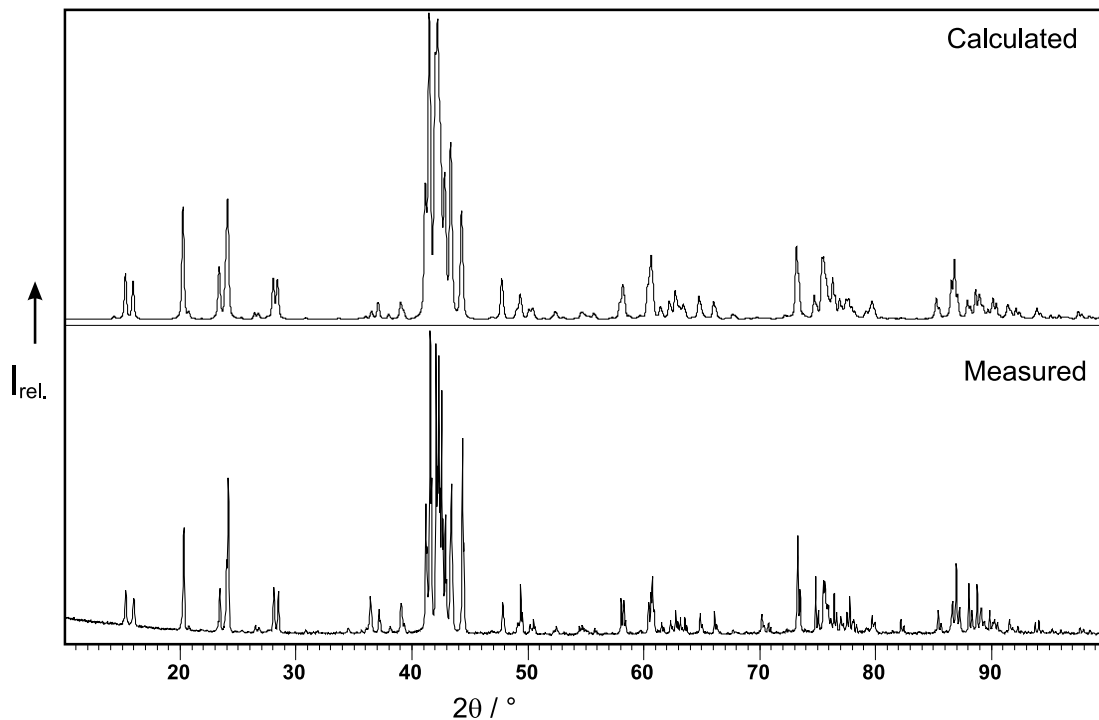


Figure 4.6: Calculated and measured X-ray powder intensities ($\lambda = 1.54187 \text{ \AA}$) for PtZn₇ phase.

4.5 Summary

- Single crystals of PtZn₇ were prepared by the melt centrifugation technique. PtZn₇ forms from a zinc-rich melt above 693 K and decomposes incongruently at 752 K. Good quality crystals are accessible by the melt centrifugation technique.

- The structure is approximated as a commensurate superstructure of a defective AlB₂-structure with the following lattice parameters; a = 1352.1(3) pm, b = 762.1(2) pm, c = 1875.8(4) pm, β = 97.40(3)° in space group C2/m. The structure can be more precisely described as an incommensurate modulated structure with a modulation vector close to $\frac{1}{9}[304]^*$, A2/m(α0γ)00, a = 258.77 pm, b = 763.35 pm, c = 423.14 pm and β = 92.05°.
- The structure is described in terms of a minimal set of non-interpenetration coordination polyhedrons including as the largest polyhedron a 33 atoms fragment of a Bergman cluster. Alternatively, the analysis of the structure in terms of layers reveals a defective AlB₂-type structure with vacancies located in the 6³ honeycomb nets according to Pt₁₅Zn₃₁Zn₈₂□₁₀.

Table 4.4: Interatomic distances for $PtZn_7$ (< 320 pm)

Pt1	Zn7	255.6(6)	2×	Zn6	M1	251.3(5)	1×	Zn12	Zn12	252.7(4)	1×	Zn17	M2	257.1(4)	1×
	Zn12	267.3(3)	4×		Pt3	263.7(5)	1×		Pt1	267.3(3)	1×		M1	266.2(5)	1×
	Zn17	269.2(3)	4×		Zn7	272.0(6)	1×		Zn17	267.5(5)	1×		Zn12	267.5(5)	1×
	Zn3	270.4(5)	2×		Zn16	272.2(5)	2×		M1	269.3(3)	1×		Zn16	269.1(5)	1×
Pt2	Zn9	253.6(7)	1×	Zn7	Zn12	279.8(4)	2×	Zn3	270.1(5)	1×	Pt1	269.2(3)	1×		
	Zn1	255.7(4)	1×		Zn14	285.0(4)	2×	Zn12	274.5(4)	1×	Zn17	271.3(4)	1×		
	Zn13	266.9(3)	2×		Zn17	297.2(5)	2×	M1	277.4(5)	1×	Zn3	283.6(4)	1×		
	Zn10	267.6(3)	2×		Zn12	305.2(6)	2×	Zn6	279.8(4)	1×	Zn7	286.5(4)	1×		
	Zn18	268.5(4)	2×		Pt3	254.9(6)	1×	Zn7	284.0(4)	1×	Zn17	297.1(4)	1×		
	Zn4	268.6(5)	1×		Pt1	255.6(6)	1×	Zn14	287.4(5)	1×	Zn6	297.2(5)	1×		
	Zn2	268.8(5)	1×		Zn6	272.0(6)	1×	Zn17	297.7(5)	1×	Zn12	297.7(5)	1×		
	Zn15	269.8(4)	2×		Zn3	278.6(6)	1×	Zn6	305.2(6)	1×	Zn18	Pt3	257.2(4)	1×	
Pt3	Zn7	254.9(6)	1×	Zn11	279.2(4)	2×	Zn13	Zn10	253.3(4)	1×		Zn10	265.4(5)	1×	
	Zn18	257.2(4)	2×	Zn12	284.0(4)	2×		Pt2	266.9(3)	1×		Zn16	266.1(5)	1×	
	Zn6	263.7(5)	1×	Zn17	286.5(4)	2×		Zn15	267.0(5)	1×		Zn15	266.5(4)	1×	
	Zn11	265.4(3)	2×	Zn14	293.2(4)	2×		Zn5	270.8(3)	1×		Zn5	267.2(5)	1×	
	Zn14	265.9(3)	2×	Zn8	M3	251.3(6)		1×	Zn4	273.3(5)		1×	Pt2	268.5(4)	1×
	Zn16	267.6(3)	2×		M2	258.6(6)		1×	Zn13	274.5(4)		1×	Zn2	286.2(4)	1×
	Zn5	268.8(5)	1×		Zn9	263.9(8)		1×	M3	277.2(4)		1×	Zn9	286.2(5)	1×
	Zn1	Pt2	255.7(4)		2×	Zn9		263.9(8)	1×	Zn15	277.7(5)	1×	Zn18	293.9(5)	1×
Zn4		275.7(4)	2×		Zn16	275.7(6)	2×	Zn4	279.0(4)	1×	Zn13	296.5(5)	1×		
Zn10		280.4(3)	4×		Zn10	280.1(4)	2×	Zn9	288.6(6)	1×	Zn8	309.6(6)	1×		
Zn15		Zn11	285.2(5)		2×	Zn11	285.2(5)	2×	Zn18	296.5(5)	1×	M1	Zn6	251.3(5)	1×
		Zn18	288.8(4)		4×	Zn13	296.6(7)	2×	Zn8	296.6(7)	1×		Zn14	262.9(5)	2×
Zn2	Zn3	252.2(5)	1×	Zn9	Zn18	309.6(6)	2×	Zn14	M1	262.9(5)	1×		Zn17	266.2(5)	2×
	Zn10	267.8(5)	2×		Pt2	253.6(7)	1×		Zn16	263.1(4)	1×		Zn12	269.3(3)	2×
	Pt2	268.8(5)	1×		M2	254.3(7)	1×		M2	264.9(3)	1×		M2	269.3(5)	1×
	Zn16	273.2(3)	2×		Zn8	263.9(8)	1×		Pt3	265.9(3)	1×	Zn12	277.4(5)	2×	
	Zn9	273.9(7)	1×		Zn2	273.9(7)	1×		Zn9	283.5(6)	1×	M2	Zn9	254.3(7)	1×
	Zn11	282.1(5)	2×		Zn14	283.5(6)	2×		Zn3	284.7(5)	1×		Zn17	257.1(4)	2×
	Zn18	286.2(4)	2×		Zn18	286.2(5)	2×		Zn6	285.0(4)	1×		Zn8	258.6(6)	1×
	Zn3	Zn2	252.2(5)		1×	Zn13	288.6(6)		2×	Zn11	285.3(5)		1×	Zn11	264.6(3)
Zn12		270.1(5)	2×	Zn11	300.9(5)	2×	Zn12	287.4(5)	1×	Zn14	264.9(3)		2×		
Pt1		270.4(5)	1×	Zn10	Zn13	253.3(4)	1×	Zn14	291.4(4)	1×	M1		269.3(5)	1×	
Zn16		275.0(3)	2×		Zn18	265.4(5)	1×	Zn7	293.2(4)	1×	Zn16		271.8(3)	2×	
Zn7		278.6(6)	1×		M3	266.9(3)	1×	Zn15	M3	259.2(4)	1×		M3	Zn8	251.3(6)
Zn17	283.6(4)	2×	Pt2		267.6(3)	1×	M3		265.4(4)	1×	Zn15	259.2(4)		2×	
Zn14	284.7(5)	2×	Zn2		267.8(5)	1×	Zn18		266.5(4)	1×	Zn15	265.4(4)		2×	
Zn4	Zn5	253.4(5)	1×	Zn5	276.1(5)	1×	Zn13		267.0(5)	1×	Zn10	266.9(3)		2×	
	Pt2	268.6(5)	1×	Zn10	277.6(4)	1×	Pt2		269.8(4)	1×	M3	270.0(4)		1×	
	Zn13	273.3(5)	2×	Zn8	280.1(4)	1×	Zn13		277.7(5)	1×	Zn13	277.2(4)		2×	
	Zn1	275.7(4)	1×	Zn1	280.4(3)	1×	Zn4		282.3(4)	1×	Zn11	Zn11		260.1(4)	1×
	Zn13	279.0(4)	2×	Zn11	293.5(5)	1×	Zn1		288.8(4)	1×		Zn11		264.0(5)	1×
	Zn15	282.3(4)	2×	Zn15	296.2(5)	1×	Zn4	289.8(5)	1×	M2		264.6(3)	1×		
	Zn15	289.8(5)	2×	Zn4	312.6(6)	1×	Zn15	294.9(5)	1×	Pt3		265.4(3)	1×		
	Zn10	312.6(6)	2×	Zn11	Zn16	260.1(4)	1×	Zn10	296.2(5)	1×		Zn7	279.2(4)	1×	
Zn5	Zn4	253.4(5)	1×		Zn5	264.0(5)	1×	Zn16	Zn11	260.1(4)	1×	Zn2	282.1(5)	1×	
	Zn11	264.0(5)	2×		M2	264.6(3)	1×		Zn14	263.1(4)	1×	Zn8	285.2(5)	1×	
	Zn18	267.2(5)	2×		Pt3	265.4(3)	1×		Zn18	266.1(5)	1×	Zn14	285.3(5)	1×	
	Pt3	268.8(5)	1×		Zn7	279.2(4)	1×		Pt3	267.6(3)	1×	Zn11	285.5(4)	1×	
	Zn13	270.8(3)	2×		Zn2	282.1(5)	1×		Zn17	269.1(5)	1×	Zn10	293.5(5)	1×	
	Zn10	276.1(5)	2×		Zn8	285.2(5)	1×		M2	271.8(3)	1×	Zn9	300.9(5)	1×	
	Zn6	Zn16	272.2(5)		2×	Zn14	285.3(5)		1×	Zn6	272.2(5)	1×	Zn16	Zn6	275.0(3)
		Zn12	279.8(4)	2×	Zn11	285.5(4)	1×		Zn2	273.2(3)	1×	Zn16		275.4(3)	1×
Zn17		297.2(5)	2×	Zn10	293.5(5)	1×	Zn3	275.0(3)	1×	Zn8	275.7(6)	1×			
Zn12		305.2(6)	2×	Zn9	300.9(5)	1×	Zn16	275.4(3)	1×						
							Zn8	275.7(6)	1×						

Chapter 5

Pt₂Zn_{11- δ} (0.2 < δ < 0.3) - A γ -brass type phase

5.1 Introduction

The γ -brass phases are of particular interest among intermetallic compounds because of their structural complexity and underlying stabilization mechanism. According to Hume-Rothery's theory these phases emerges at particular valence electron concentration (*vec*) values close to $\frac{21}{13}$ electron per atom. There are several recent reports on binary γ -brass phases having composition M₂Zn₁₁ (M = Ni [11], Rh [79] and Ir [80]). It is interesting to see whether such a γ -brass phase could exist at the same composition in the binary system Pt-Zn. Moreover, there are some evidence from earlier work by Nowotny *et al.* [40] for the existence of such a γ -brass type phase. This chapter is mainly concerned with the synthesis and characterization of γ -Pt₂Zn_{11- δ} . An account on Pt₂Zn_{11- δ} has already been published [75].

5.2 Syntheses and characterization

Single phase samples of Pt₂Zn_{11- δ} have been synthesized by conventional solid state syntheses and the flux method. The preparations were carried out on a 0.3 gram scale from Pt and Zn in previously out-gassed, evacuated quartz glass ampoules. The metals were heated at a rate of 60 Kh⁻¹ up to 1323 K and were kept at this temperature for 12 h. Hereafter, the temperature was reduced to 973 K over the course of 72 h after which the ampoules were either quenched in water

or cooled to ambient temperature over the course of 24h. The synthesis has also been carried out with zinc and platinum in excess in order to determine the homogeneity range of the phase. The products were characterized by powder diffraction and single crystal diffraction methods.

Synthesis was also carried out by the melt centrifugation method (flux method). The crystals were grown by slow cooling of the reactants from a Zn-rich melt containing 4 wt.% Pt. The reaction mixtures were sealed in silica ampoules under a reduced pressure with a quartz glass wool filter placed below a support of pieces of quartz glass. The silica tube was then placed inside a stainless steel cylinder in such a way that the reactants were placed on the bottom and the filter and broken silica pieces on the top of the cylinder. The steel cylinder preserves hot condition of the silica ampoule until centrifugation. The reactants were heated up to 1000 K and allowed to stay for 12 h and then cooled down to 730 K with a rate 50 K h^{-1} . Hereafter, the temperature was reduced to 700 K at the rate of 1 K h^{-1} . Finally, the steel cylinder containing the silica ampoule was taken out of the furnace, turned upside-down, and centrifuged (during hot condition). The excess molten Zn was forced down through the filter thereby leaving behind the product. The size of the crystals ranged from about $100 - 450 \mu\text{m}$ (c.f. Fig. 5.1). The solid showed equiaxed dendritic growth. The morphology of the phase and its approximate composition was studied by using a scanning electron microscope (SEM) equipped with an energy dispersive X-ray analysis system (EDX).

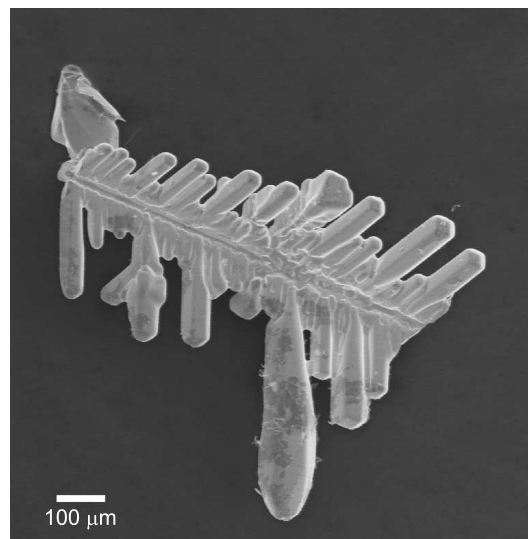


Figure 5.1: SEM micrograph of the phase $\text{Pt}_2\text{Zn}_{11-\delta}$ shows equiaxed dendritic growth of crystals synthesized by the flux method.

5.2.1 Single crystal structure analysis

Suitable crystals for recording X-ray diffraction intensities were selected from the Zn-rich (**C1**) and Pt-rich side (**C2**), a sample containing Pt₅Zn₂₁ as an additional minor phase. X-ray diffraction intensities were collected on an IPDS-I instrument at room temperature. The lattice parameters were independently determined from the Bragg position of 25 selected reflections measured with a four cycle diffractometer CAD 4 (Mo K α). Diffraction intensities were collected up to $2\theta_{\max} \approx 65.5^\circ$. The Laue symmetry was $m\bar{3}m$, the systematic extinction $h+k+l = 2n+1$ pointed to the cubic space group I $\bar{4}3m$ (No. 217). The data was subsequently corrected for Lorentz and polarization effects. A numerical absorption correction based on the shape of the crystal was applied to the data [61, 62]. The initial positional parameters were obtained by direct methods using SHELXS-97 [58]. The structure was refined in the cubic space group I $\bar{4}3m$. All the atomic positions were refined anisotropically with the SHELX-97 [58] program package based on full-matrix least-squares refinements. The final refinement performed on $|F|^2$ with 293 unique reflections (**C1**) yielded residuals $R_1 = 0.0302$ and $wR_2 = 0.0818$. Details of the data collection, atomic coordinates, equivalent isotropic displacement parameters and anisotropic displacement parameters are given in tables 5.1, 5.2 and 5.3, respectively.

Sample of single phase and two phase mixtures were also characterized by powder X-ray diffraction. The lattice parameters of a single phase sample and those prepared in excess of Zn and Pt ranged from 908.2(1) to 908.9(1) pm. The diffraction profiles of homogeneous Pt₂Zn_{11- δ} samples were quantitatively analyzed by the Rietveld method [56]. Positional parameters of the single crystal X-ray structure analysis were used as starting parameters for the refinements of the X-ray powder data. The refinement of the occupancy factors were in accordance with the results of the single crystal structure analysis with about 14% vacancies on the Zn(1) site. The Rietveld fit for a single phase sample of Pt₂Zn_{11- δ} is shown the Fig. 5.2.

Table 5.1: Crystallographic and technical data for the single-crystal structure determination

Sum formula	Pt ₂ Zn _{10.72(1)} ^a (C1)	Pt ₂ Zn _{10.77(1)} ^b (C2)
Space group (No.)		I $\bar{4}3m$ (217)
Z		4
a / pm	908.19(4)	908.82(4)
V / 10 ⁶ pm ³	749.09(6)	750.64(6)
Molar mass / g mol ⁻¹	1091.14	1094.46
ρ_{cal} / g cm ⁻³	9.670	9.679
μ / mm ⁻¹	70.3	70.94
<i>Data collection</i>		
Crystal size / mm ³	0.13 × 0.18 × 0.15	0.12 × 0.08 × 0.10
Diffractometer		IPDS-I (STOE & Cie)
Temperature / K		293(2)
Radiation / monochromator		MoK α / Graphite
Distance crystal-IP / mm	40	40
$\phi_{\text{min}} - \phi_{\text{max}}; \Delta\phi$	0 – 320; 2	0 – 330; 2
2 θ_{max} / °	65.5	65.6
Collected reflections	-12 ≤ h ≤ 12 -13 ≤ k ≤ 13 -13 ≤ l ≤ 13	-12 ≤ h ≤ 12 -13 ≤ k ≤ 13 -13 ≤ l ≤ 13
Total No. of reflections	6556	8924
<i>Data reduction</i>		
Program	IPDS-I Software [57]	X-RED [61]
Absorption correction	Numerical	X-SHAPE [62]
max. / min. Transmission	0.0200 / 0.0706	0.026 / 0.0282
Unique reflections	293	284
R _{int}	0.0719	0.167
<i>Refinement</i>		
Program		SHELXL-97[58]
Refined on		F _o ²
Reflections I _o > 2σ(I _o)	274	284
Variables	19	19
R ₁ (I _o > 2σ(I _o))	0.0302	0.0283
R ₁ (all)	0.0319	0.0296
wR ₂ (all)	0.0818	0.0840
Goodness of fit	1.120	1.484
$\Delta\rho_{\text{max}} / \Delta\rho_{\text{min}} / 10^{-6} \text{e pm}^{-3}$	4.13 / -2.61	4.66 / -1.46
Extinction coefficient	0.0032(3)	0.0037(4)

^a $1/w = \sigma^2(F_o^2) + (0.0283(\text{Max}(F_o^2, 0) + 2F_c^2)/3)^2$

^b $1/w = \sigma^2(F_o^2) + (0.0368(\text{Max}(F_o^2, 0) + 2F_c^2)/3)^2$

Table 5.2: Positional and equivalent isotropic displacement parameters U_{eq} (pm²) for Pt₂Zn_{11- δ}

Atom	Wy.	x	y	z	sof	U_{eq}
Pt1	8c	0.82631(6)	x	x	1	54.5(3)
		0.82626(4)*	x	x	1	150(3)
Zn1	8c	0.1091(3)	x	x	0.86(1)	137(11)
		0.1085(2)	x	x	0.87(1)	214(8))
Zn2	12e	0.3551(3)	0	0	1	116(6)
		0.3565(3)	0	0	1	205(6)
Zn3	24g	0.3107(2)	x	0.0392(2)	1	119(6)
		0.3102(2)	x	0.0400(2)	1	219(5)

* atomic parameters for the crystal **C2**Table 5.3: Anisotropic displacement parameters U (pm²) for Pt₂Zn_{11- δ}

Atom	U_{11}	U_{22}	U_{33}	U_{12}	U_{23}	U_{13}
Pt1	54.5(3)	U_{11}	U_{11}	6.1(2)	U_{12}	U_{12}
	146(3)	U_{11}	U_{11}	4(2)	U_{12}	U_{12}
Zn1	137(11)	U_{11}	U_{11}	68(9)	U_{12}	U_{12}
	212(8)	U_{11}	U_{11}	51(7)	U_{12}	U_{12}
Zn2	151(14)	97.8(7)	U_{22}	0	60(9)	0
	227(10)	187(6)	U_{22}	0	51(7)	0
Zn3	146(8)	U_{11}	65(7)	38(6)	-54(5)	U_{23}
	238(7)	U_{11}	171(6)	25(5)	-48(4)	U_{23}

Single crystal structure refinement revealed that the Zn(1) site is partially occupied with an approximate occupancy of 85%.

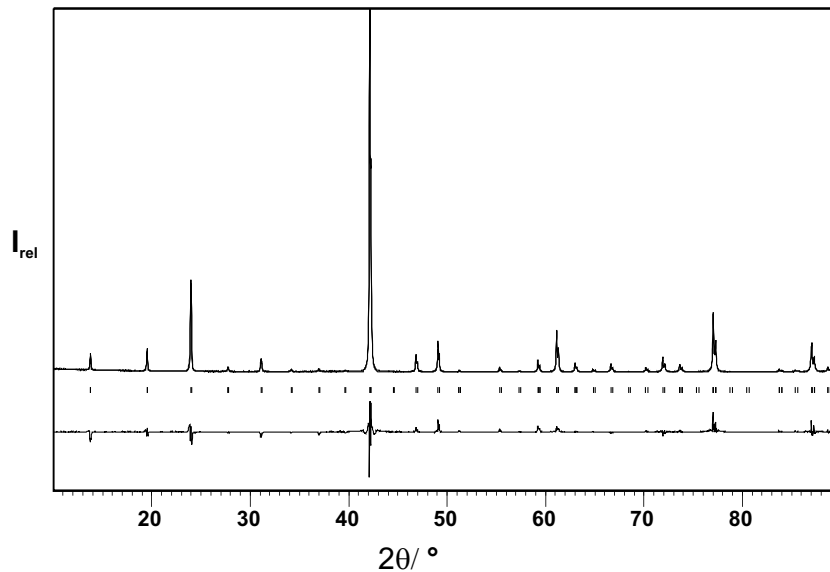


Figure 5.2: X-ray powder diffractogram of Pt₂Zn_{10.73(2)} together with the Rietveld profile fit, the difference plot and Bragg positions; CuK α , $a = 908.89(2)$ pm, $R_B = 0.0578$, $R_P = 0.096$ and $GoF = 2.7$.

5.3 Physical Properties

5.3.1 Thermochemical analyses

According to DTA measurement of single phase sample, Pt₂Zn_{11- δ} begins to melt incongruently at 1132K. The peak maximum is found at 1136 K. For the subsequent heating cycles the peak onset is shifted by 3 K towards higher temperature whereas the onset temperature of the solidification remains 1123 K. The shift of melting is attributed to a slight increase in Pt due to evaporation of Zn. The DTA plot as a function of temperature is shown in Fig. 5.3.

5.3.2 Magnetic susceptibility

The magnetic susceptibilities of polycrystalline Pt₂Zn_{11- δ} were measured for three distinct samples. Magnetic flux densities of 10 and 20 kG were applied to each sample. In all the cases the Pauli paramagnetism of the metallic conductor was found to be overcompensated by the core diamagnetism of the constituents of the phase. The temperature independent diamagnetic contribution was obtained from the slope of a χT versus T plot. The values obtained were found to vary between $-4.6(2)$ and $-5.4(2) \cdot 10^{-10} \text{m}^3 \text{mol}^{-1}$ for $\frac{1}{(13-\delta)}$ Pt₂Zn_{11- δ} ($0.2 < \delta < 0.3$). The molar susceptibility of Pt₂Zn_{11- δ} as a function of temperature is shown in Fig. 5.4.

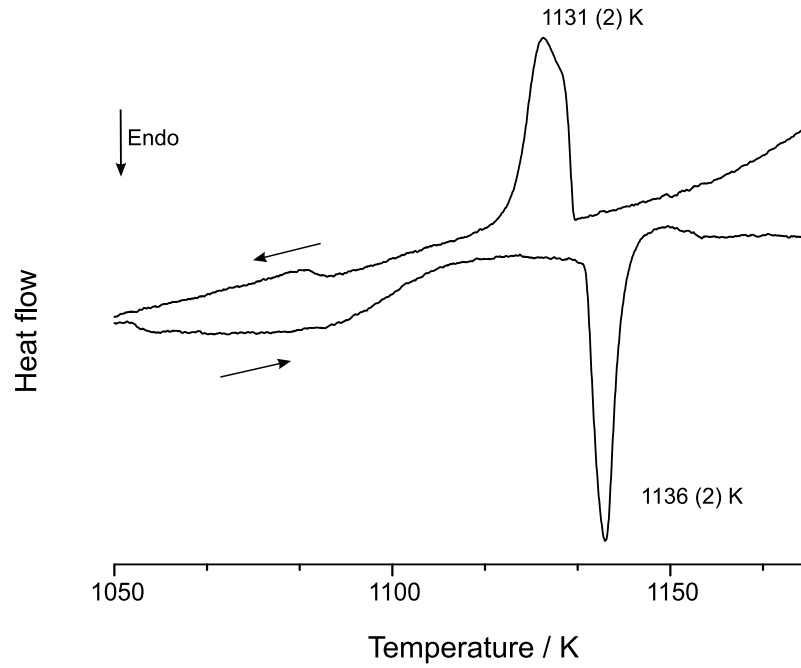


Figure 5.3: A typical thermogram of $\text{Pt}_2\text{Zn}_{11-\delta}$ phase.

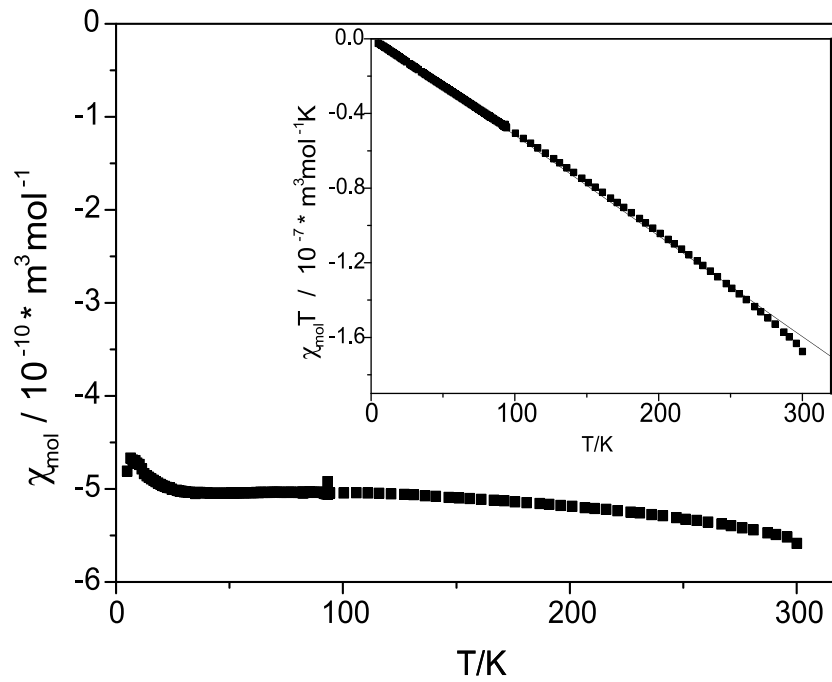


Figure 5.4: Magnetic susceptibility as a function of temperature for $\text{Pt}_2\text{Zn}_{11-\delta}$.

5.3.3 Electrical resistivity

The resistivities of Pt₂Zn_{11- δ} were determined by applying a four-probe method in the d.c. mode in the temperature range 10–315 K. The obtained values found to range from 0.2 to 0.9 m Ω cm for three polycrystalline samples. These values point to a partial localization of the conduction electrons of the two elemental metallic components whose resistivities are about two orders of magnitude smaller at ambient temperature than those of Pt₂Zn_{11- δ} . The electrical resistivity of Pt₂Zn_{11- δ} as a function of temperature is shown in Fig. 5.5

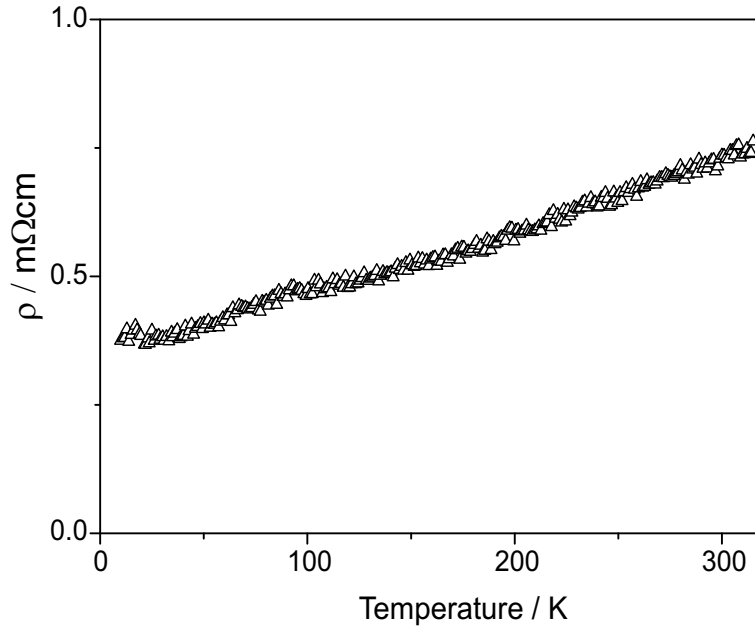


Figure 5.5: Electrical resistivity of Pt₂Zn_{11- δ} as a function of temperature.

5.4 Discussion

Pt₂Zn_{11- δ} crystallizes in the cubic space group $I\bar{4}3m$ with $54-2\delta$ atoms per unit cell (Pearson symbol, cI52). The phase adopts a γ -brass type structure which is isopointal to the structure of M₅Zn₈ [M = Cu, Ag], M₅Cd₈ [M = Cu, Ag], Pd_{2+ δ} Zn_{11- δ} [81], M₂Zn₁₁ [M = Ni [11], Rh [79], Ir [80]] and Fe₃Zn₁₀. These γ -brass type structures are typical Hume-Rothery phases which form at the specific valence electron concentration (*vec*), $\frac{21}{13} \approx 1.615$, and adopt the same structure type. The electron counting rule for these phases is as follows: The transition metals for instance, Ni, Rh, Ir, Pd and Pt are taken to be zero-valent and Zn is taken to contribute two electrons per atom (only the electrons from s sub-shell are considered, even though d sub-shells are not completely

occupied they are not taken into account). According to single crystal structure analyses the $\text{Pt}_2\text{Zn}_{11-\delta}$ phase is not completely ordered. Vacancies on Zn sites reduce the valence electron concentration vec $\frac{22}{13}$ towards $\approx \frac{21}{13}$. This value is generally assumed to be particularly favorable for the formation of γ -phases and is close to the value determined for the congeneric Ni and Pd phases. However, for these phases vec is optimized by partial replacement of Zn by group 10 metal atoms. The presence of defects in the structure $\text{Pt}_2\text{Zn}_{11-\delta}$ gives rise to significant lowering of the density ρ_{cal} from 9.831 g cm^{-3} to 9.670 g cm^{-3} which is confirmed by the pycnometrically determined density of $9.66(3) \text{ g cm}^{-3}$.

The $\gamma\text{-Pt}_2\text{Zn}_{11-\delta}$ in turn can be described as a $3a_\beta \times 3a_\beta \times 3a_\beta$ superstructure of a β -brass type structure with two out of 54 positions being vacant, one at the origin and an other at the center of the triply expanded cubic unit cell. The structural kinship is established by group-subgroup relations [82, 83] existing between the symmetry of a β -brass type structure and that of $\text{Pt}_2\text{Zn}_{11-\delta}$. The symmetry reduction from aristo-type β -brass to $\text{Pt}_2\text{Zn}_{11-\delta}$ is schematically shown in Fig. 5.6. The symmetry relation includes two minimal symmetry reductions. The letter assigned to each pair of group symbols indicates the type of symmetry reduction, ‘i’ for *isomorphic*, ‘t’ for *translationengleich*. The number in brackets refers to the *index* of the symmetry reduction which corresponds to the number by which the number of translation and/or rotational symmetry is reduced in the subsequent subgroup relative to the preceding group. Included in the scheme are also the atomic sites and idealized positional parameters of a β -brass type structure in the setting of the respective space groups. The third member in the genealogical tree corresponding to the symmetry of $\text{Pt}_2\text{Zn}_{11}$. Note that the special position 2a is unambiguously not occupied, see Fig. 5.6.

The γ -brass structure type has been described as consisting of 26 atom clusters which are arranged like atoms in bcc W-type structures [84]. Each cluster is built up by four crystallographic distinct atoms. For $\text{Pt}_2\text{Zn}_{11-\delta}$ one ‘8c’ site is occupied by eight Zn(1) forming two inner tetrahedrons designated as IT, one grouped around the origin and the other around the center of the unit cell. The next shell of four atoms is built by 4 Pt(1) which are situated at a second ‘8c’ site. The Pt(1) atoms define an outer tetrahedron OT which together with the complementary IT forms a distorted, empty cube. The next shell around the distorted empty cube consists of six Zn(2) atoms situated above the faces of the cube, thus forming an octahedron OH. The respective ‘12e’

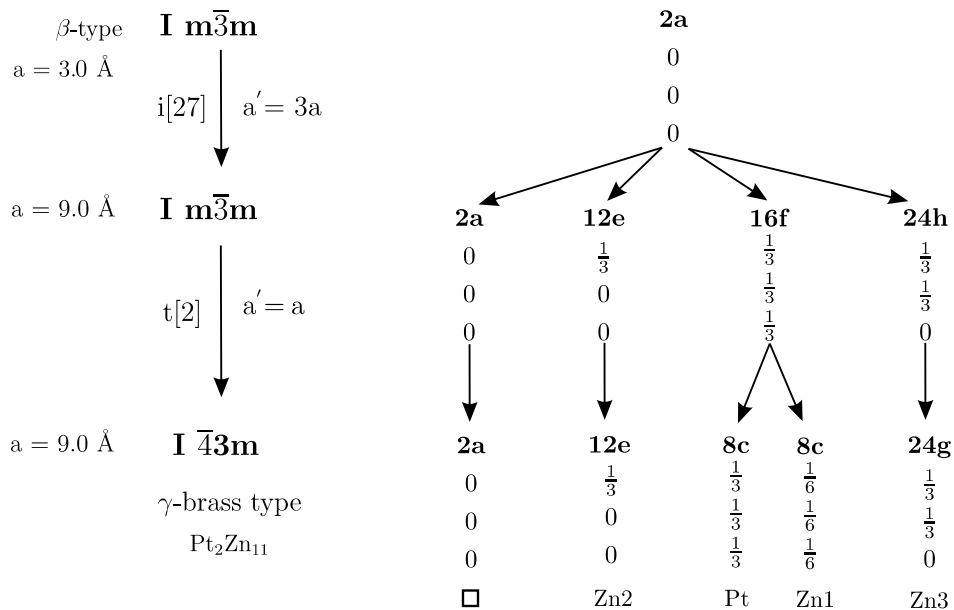


Figure 5.6: Group-subgroup structural relations between $\text{Pt}_2\text{Zn}_{11}$ and aristo-type bcc structure. The Wykoff position 2a is unoccupied. The deviation between the ideal positions and the real ones listed in Table 5.2 are a measure of the degree of distortion of the structure due to the vacancies.

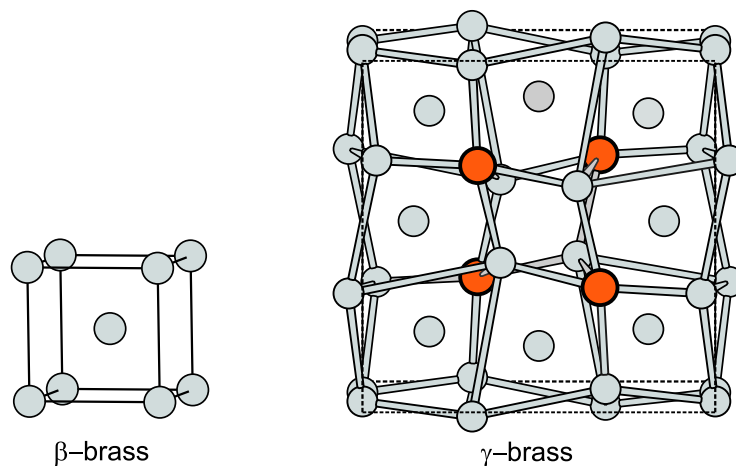


Figure 5.7: Relationship between $\beta\text{-brass}$ and $\gamma\text{-brass}$: the $\gamma\text{-brass}$ can be described as a $3a_\beta \times 3a_\beta \times 3a_\beta$ superstructure of a $\beta\text{-brass}$ type structure with two ordered vacancies, one at the origin and other at the center of the triply expanded cubic unit cell. A representative part of a unit cell ($\frac{1}{3}$) is shown.

site is occupied by Zn(2) atoms. In the third sphere of a bcc type arrangement of atoms there are 12 neighbors forming a distorted cuboctahedron CO at a mean distance of $a_c\sqrt{2}$ apart from the center. Here, a_c refers to the lattice parameter of a bcc W-type unit cell. The respective ‘24g’ site is occupied by Zn(3) complementing the 26 atom unit.

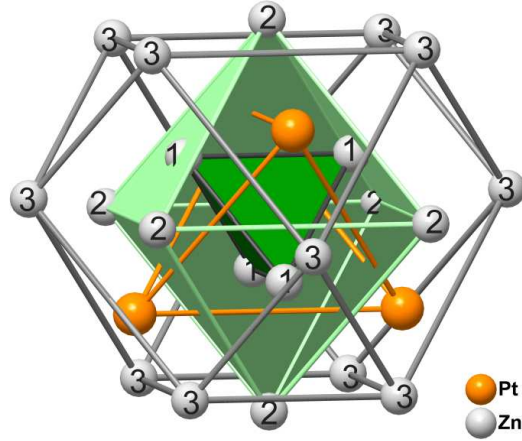


Figure 5.8: The 26 atom cluster of γ -brass type $\text{Pt}_2\text{Zn}_{11-\delta}$: depicted is the four shells structure of the 26 atom cluster. The clusters are arranged around the high symmetry points $0, 0, 0$ and $\frac{1}{2}, \frac{1}{2}, \frac{1}{2}$.

The γ -brass $\text{Pt}_2\text{Zn}_{11-\delta}$ structure can be emphasized as $3a$ supercell of the bcc W-type cell in which two vacancies have been introduced, one at origin and other is at the center of the supercell. Thus, there are 52 instead 54 atoms in the $(3a)^3$ cubic supercell. The ordered vacancies give rise to a cooperative displacement of the atoms, transforming the defected bcc-type dodecahedral coordination of the atoms into three topologically distinct coordination configuration. Formation of vacancies is typical for γ -brass and related phases. The coordination polyhedrons of the four crystallographic distinct atoms of $\text{Pt}_2\text{Zn}_{11-\delta}$ are shown in Fig. 5.9.

As seen from Fig. 5.9, the Pt(1) and Zn(1) have 12 next atoms (CN 12) forming a distorted polyhedrons. For Pt(1), the distances range from 261.4(2) pm to 277.5(2) pm, and for Zn(1), the distances range from 263.9(3) pm to 279.9(8) pm. Zn(2) on the OH site has 13 nearest neighbors, the distances scattered from 261.5(2) to 295.2(3) pm. Zn(3) on the CO site has 11 nearest neighbors the distances are scattered from 261.4(2) to 295.2(3) pm. A list of interatomic distances for $\text{Pt}_2\text{Zn}_{11-\delta}$ are given in Table 5.4. The interatomic distances agree well with the sum of the

atomic radii $r_{\text{Pt}} = 137.3$ pm and $r_{\text{Zn}} = 133.5$ pm.

An alternative view of the structure puts emphasis on the icosahedral coordination of the minority component (Pt content). Face-shared distorted PtZn_{12} icosahedra are fused into tetrahedral-shaped quadruples encapsulating a $\text{Zn}(1)_4$ IT about the center. Again, these units are arranged around the origin and center of the $(3a)^3$ super cell. Each quadruple is surrounded by 14 others in form of a dodecahedron by sharing vertices of PtZn_{12} polyhedrons. The complex arrangement of edge, face and corner-sharing PtZn_{12} polyhedrons resulting from one central quadruple that is tetrahedrally surrounded by four others situated on vertices of the unit cell, is shown in Fig. 5.10.

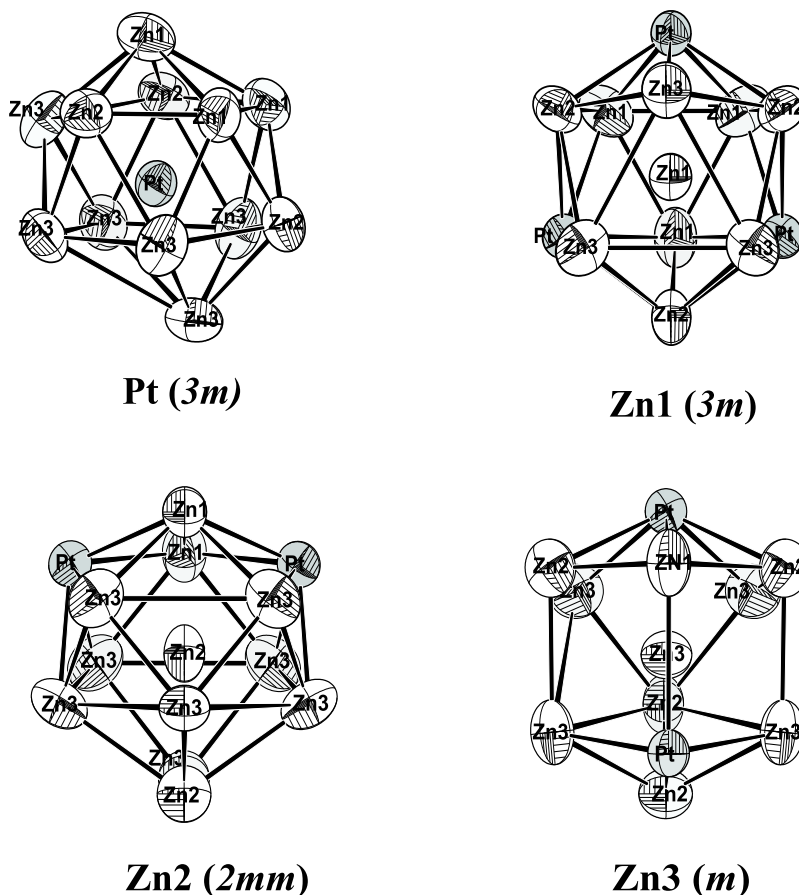


Figure 5.9: The coordination polyhedrons around the four crystallographic distinct atoms.

Table 5.4: Interatomic distance for Pt₂Zn_{11- δ} (< 400 pm)

Pt1-	Zn3	261.4(2)	3×		Zn1-	Zn2	263.8(4)	3×	
	Zn3	261.5(2)	3×			Zn3	266.6(3)	3×	
	Zn1	269.9(3)	3×	< 276.6 >		Pt1	269.9(3)	3×	< 270.1 >
	Zn2	277.4(2)	3×			Zn1	280.3(4)	3×	
	Zn1	341.7(3)	1×			Pt1	341.7(3)	1×	
Zn2-	Zn3	261.5(2)	2×		Zn3-	Pt1	261.4(2)	1×	
	Zn2	263.2(4)	1×			Zn2	261.5(2)	1×	
	Zn1	263.8(4)	2×			Pt1	261.6(2)	1×	
	Pt1	277.4(2)	2×	< 277.5 >		Zn1	266.6(3)	1×	
	Zn3	287.3(2)	4×			Zn3	271.7(2)	4×	< 273.4 >
	Zn3	295.1(2)	2×			Zn2	287.3(2)	2×	
					Zn2	295.1(2)	1×		
					Zn3	348.7(2)	2×		
					Zn3	351.2(2)	2×		

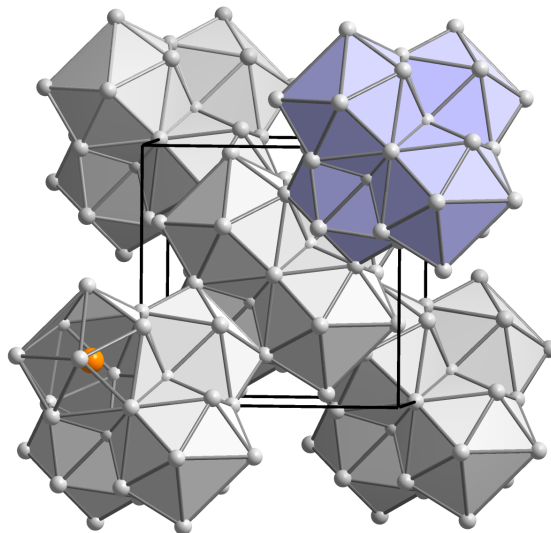


Figure 5.10: A view of the structure of Pt₂Zn_{11- δ} with emphasis of the distorted icosahedral coordination about the minority component Pt(1). The four polyhedrons form a quadruple encapsulating a Zn(1)₄ tetrahedron. The quadruples are arranged around the high symmetry points 0, 0, 0 and $\frac{1}{2}, \frac{1}{2}, \frac{1}{2}$.

5.5 Summary

Single crystals of $\text{Pt}_2\text{Zn}_{11-\delta}$ were obtained from melt centrifugation and solid state syntheses. The structure represents the characteristic $3a \times 3a \times 3a$ superstructure of β -brass type structure. The structure is described in terms of a 26 atom cluster arranged over high symmetric points $0,0,0$ and $\frac{1}{2}, \frac{1}{2}, \frac{1}{2}$. Vacancies on one Zn site reduces the valence electron concentration thereby affording an optimal adjustment of this structure-determining electronic factor towards $\approx \frac{21}{13}$ electrons/atom. The single crystal X-ray diffraction studies prove the γ -brass type phase $\text{Pt}_2\text{Zn}_{11-\delta}$ ($0.2 < \delta < 0.3$) to exhibit a marginally small homogeneity range.

Chapter 6

γ -Pt₅Zn₂₁ - A reappraisal of a γ -brass type complex alloy phase

6.1 Introduction

Hume-Rothery phases [14] are intermetallic alloys or compounds for which the valence electron concentration (*vec*) in terms of the average number of valence electrons per atom is crucial in determining the structural outcome. This particular electronic factor has been shown by various experimental and theoretical means to control the formation, sequence, and structures of brass-like phases as preferentially formed by noble metals and elements of groups 2 and 12–15. The γ -phase evolving at about $\frac{21}{13}$ electrons/atom is commonly considered the structurally most complex Hume-Rothery phase in brass-like systems. Although the structure of the γ -prototype, Cu₅Zn₈, has been known since the early days of X-ray crystallography, such phases have been a continuous challenge for scientists due to their structural complexity and intricate physical properties. The identification of new giant cell structures related to γ -brass are Ir_{7+7 δ} Zn_{97–11 δ} [70], Al₆₉Ta₃₉ [85], Ir₄Mg₂₉ [86] and Li₂₁Si₅ [87].

A comprehensive phase diagram of Pt-Zn system was reported by Nowotny *et al.* [40]. According to them γ -phase in the Pt-Zn system exist between 20 and 22 at.% of Pt. They assign the composition PtZn₅ to this phase. However, this phase was previously known to be Pt₅Zn₂₁ [41]. Furthermore, Westman *et al.* [13] proposed a structural model to the γ -phase by means of single crystal X-ray diffraction. According to the proposed model, γ_1 -Pt₃Zn₁₀ accommodates 392 atoms

in a face centered cubic unit cell [13]. There is some structural ambiguity about the proposed model and the assigned composition to the γ -phase. This chapter is concerned with syntheses and characterization of $\gamma\text{-Pt}_5\text{Zn}_{21}$. An account on $\gamma\text{-Pt}_5\text{Zn}_{21}$ has already been published [68].

6.2 Syntheses and characterization

Single phase samples of $\text{Pt}_5\text{Zn}_{21}$ have been synthesized by conventional solid state and pseudo-isopiestic methods.

6.2.1 Solid state syntheses

About fifty zinc-rich samples were prepared from the elements in previously out-gassed, evacuated silica ampoules. The nominal compositions of the samples ranged from 16 to 23 at.% with respect to the amount of Pt. The metals, about 0.3 g in total, were heated at a rate of 60 K h^{-1} to a temperature of 1320 K at which the ampoule was kept for 12 h. Hereafter, the temperature was reduced to 970 K in the course of 72 h before the sample was either quenched in cold water or over the course of 24 h cooled to ambient temperature. To avoid eventual loss of zinc due to evaporation, the reactants were kept at a lower temperature than the rest of the ampoule.

6.2.2 Pseudo-isopiestic method

The sequence of phases in the Zn-rich part of the Pt-Zn system was determined by means of the non-isothermal isopiestic method [53]. Platinum wire (0.1 mm diameter, 99.9 % Johnson Matthey) was wound into spools of 50 mg each and weighed into individual quartz glass crucibles to an accuracy of ± 0.05 mg. The measurements were performed in a specially designed quartz glass apparatus. 15 crucibles were arranged in the reaction tube, sealed under vacuum and then placed in the temperature gradient of a two-zone furnace. The platinum spools were exposed to a constant vapor pressure of Zn (14 hPa; determined by the temperature of the Zn-reservoir within the reaction tube) for 14 days at temperatures ranging from 880 K to 1080 K. Pt/PtRh-thermocouple was used for controlling the temperature of the Zn reservoir and the 15 samples. The compositions of the equilibrated samples were determined by measuring the Zn uptake. The products were characterized by X-ray powder diffraction means and thermal analyses.

6.3 Single crystal structural determination

Seven single crystals were selected from different compositional range 16-23 at.% of Pt. Since the results of four structure refinements unambiguously confirm those of the rest, the structures of the three most distinct phases are described here. Crystal **c1** was selected from a Pt-rich sample (22.5 at.% Pt) containing the cubic phase as the minor component. Crystal **c2** was selected from a single phase sample (19 at.% Pt). The crystal **c3** was chosen from a sample containing 18 at.% Pt. The diffraction intensities were recorded with an imaging plate diffraction system IPDS-I (Stoe, MoK α). More reliable lattice parameters were obtained from the positions of 25 selected reflections measured on a four circle diffractometer CAD 4 (Enraf Nonius, MoK α). The collected intensities were corrected for absorption effects [61, 62]. The structures were refined in space group F $\bar{4}3m$ (No. 216) using the SHELX-97 [58] program package based on full-matrix least-squares refinements. The structural data reported for Pt₃Zn₁₀ [13] were used as starting parameters for the first refinements. Sites with mixed Zn and Pt occupation were assumed to be fully occupied. Atoms for which the refined occupancy factors deviated by less than twice the standard deviation from unity were reset to unity in the final refinement cycles. Local structural disorder phenomena were adequately recorded by introducing split positions. A few displacement parameters of partly occupied sites were fixed at an unobtrusive value of 200 pm². This was applied to atoms showing a strong correlation between the displacement parameter and the site occupancy factor. Otherwise, anisotropic displacement parameters were refined. In consideration of anomalous dispersion effects each structure was checked for possible twinning by inversion and for its absolute configuration. The final refinements performed on $|F|^2$ with ≈ 1150 unique reflections yielded residual values $R_1 = 0.0427$, 0.0343 , and 0.0543 for the three distinct crystals of different compositions. Further details concerning the crystallographic data and structure determination are given in Table 6.1. The positional and equivalent displacement parameters are given in Tables 6.2 and 6.3, respectively.

Table 6.1: Crystallographic and technical data for the single-crystal structure determination

Sum formula	Pt _{5.12} Zn _{21.47} (C1) ^a	Pt _{4.72} Zn _{20.92} (C2) ^b	Pt _{4.25} Zn _{20.34} (C3) ^c
Space group (No.)	F $\bar{4}3m$ (216)	F $\bar{4}3m$ (216)	F $\bar{4}3m$ (216)
Z	16	16	16
a / pm	1809.1(1)	1812.8(2)	1814.0(1)
V / 10 ⁶ pm ³	5920.9(1)	5957.4(12)	5969.2(5)
Molar mass / g mol ⁻¹	2336.42	2344.79	2158.19
ρ_{cal} / g cm ⁻³	10.484	10.190	9.606
μ / mm ⁻¹	80.538	76.860	71.578
<i>Data collection</i>			
Crystal size / mm ³	0.12 × 0.10 × 0.08	0.16 × 0.10 × 0.08	0.14 × 0.10 × 0.08
Diffractometer		IPDS-I (STOE & Cie)	
Temperature / K		293(2)	
Radiation / monochromator		MoK α / Graphite	
Distance crystal-IP / mm	40	40	40
$\phi_{min} - \phi_{max}; \Delta\phi$	0 – 200; 1	0 – 200; 1	0 – 184; 1
$2\theta_{max}$ / °	66.1	66.0	65.7
Collected Reflections	$-27 \leq h \leq 27$ $-27 \leq k \leq 27$ $-27 \leq l \leq 27$	$-27 \leq h \leq 27$ $-27 \leq k \leq 27$ $-27 \leq l \leq 25$	$-26 \leq h \leq 26$ $-27 \leq h \leq 24$ $-27 \leq h \leq 27$
Total No. of reflections	21972	21822	20484
<i>Data reduction</i>			
Program	IPDS-Software [57]	X-RED [61]	
Absorption correction	Numerical	X-SHAPE [62]	
max. / min. Transmission	0.3523 / 0.2145	0.0833 / 0.0089	0.3587 / 0.0741
Unique reflections	1150	1150	1152
R_{int}	0.2095	0.0943	0.1290
<i>Refinement</i>			
Program		SHELXL-97 [58]	
Refined on		$ F_o ^2$	
Reflections $I_o > 2\sigma(I_o)$	626	948	819
Variables	71	76	73
R ₁ ($I_o > 2\sigma(I_o)$)	0.0427	0.0343	0.0543
R ₁ (all)	0.0981	0.0455	0.1558
wR ₂ (all)	0.0888	0.0848	0.0763
Goodness of fit	0.719	0.902	1.009
$\Delta\rho_{max} / \Delta\rho_{min} / 10^{-6} e pm^{-3}$	3.57 / -3.117	1.817 / -1.90	2.906 / -2.767
Extinction coefficient	0.000008(2)	0.000058(4)	0.000029(7)

$$^a \& ^b \quad 1/w = \sigma^2(F_o^2) + (0.0657(\text{Max}(F_o^2, 0) + 2F_c^2)/3)^2 \quad ^c \quad 1/w = \sigma^2(F_o^2) + (0.0968(\text{Max}(F_o^2, 0) + 2F_c^2)/3)^2$$

Table 6.2: Positional and equivalent isotropic displacement parameters U_{eq} (pm²) for γ_1 -Pt₅Zn₂₁ (C1 and C2)

Cluster	Site	Wy.	Atom	x	y	z	sof	U_{eq}
A (0 0 0)	IT	16e	Zn11	0.9464(1)	x	x	1	98(6)
				0.9460(3) ^a			1	77(12)
	OT	16e	Pt12	0.0895(4)	x	x	1	43(3)
				0.0903(1)			1	40(5)
	OH	24f	Zn13	0.1762(2)	0	0	1	187(10)
				0.1770(4)	0	0	1	73(15)
	CO	48h	Zn14	0.3442(1)	x	0.9808(1)	1	114(4)
				0.3444(2)		0.9809(3)	1	117(11)
B ($\frac{1}{2}$ $\frac{1}{2}$ $\frac{1}{2}$)	IT	16e	Zn21	0.4368(2)	x	x	0.68(6)	187(35)
				0.4245(5)			0.62(3)	200 ^b
	IT'	16e	Zn21'	0.4230(20)	x	x	0.17(5)	200 ^b
				–	–	–	–	–
	OT	16e	Zn22	0.5812(3)	x	x	0.70 ^c	23(9)
				0.5675(4)			1	205(2)
	OT'	16e	Zn22'	0.5658(6)	x	x	0.31(4)	210(45)
				–	–	–	–	–
	OH	24f	Zn23	0.6797(1)	0	0	0.14(2)	74(4)
				–	–	–	–	–
	OH	24f	Pt23	0.6797(1)	0	0	0.86(2)	74(4)
				0.6798(1)	0	0	1	79(6)
	CO	48h	Zn24	0.3419(1)	x	0.4858(2)	0.90(1)	140(8)
				0.3414(3)		0.4895(4)	0.87(2)	277(25)
CO'	48h	Zn24'	–	–	–	–	–	
			0.3909(14)		0.4496(14)	0.12(1)	200 ^b	
C ($\frac{1}{4}$ $\frac{1}{4}$ $\frac{1}{4}$)	IT	16e	Zn31	0.6962(1)	x	x	1	70(6)
				0.6956(2)			1	63(13)
	OT	16e	Zn32	0.8368(1)	x	x	0.86(1)	77(10)
				0.8368(2)			0.88(2)	112(22)
	OT	16e	Pt32	0.8368(1)	x	x	0.14(1)	77(10)
				0.8368(2)	x	x	0.12(2)	112(22)
	OH	24g	Zn33	0.56934(6)	$\frac{1}{4}$	$\frac{1}{4}$	0.15(1)	72(4)
				–	–	–	–	–
	OH	24g	Pt33	0.56934(6)	$\frac{1}{4}$	$\frac{1}{4}$	0.85(1)	72(4)
				0.5701(1)			1	79(6)
CO	48h	Zn34	0.40365(8)	x	0.7279(1)	1	142(5)	
			0.4040(2)		0.7262(2)	1	235(14)	
D ($\frac{3}{4}$ $\frac{3}{4}$ $\frac{3}{4}$)	IT	16e	Zn41	0.1918(2)	x	x	1	203(9)
				0.1898(4)			1	170(18)
	OT	16e	Pt42	0.33550(5)	x	x	1	79(4)
				0.3341(1)			1	60(6)
	OH	24g	Zn43	0.4277(2)	$\frac{1}{4}$	$\frac{1}{4}$	1	84(9)
				0.4285(4)			1	70(13)
	CO	48h	Zn44	0.09115(9)	x	0.2361(1)	1	128(4)
				0.0902(2)		0.2390(3)	1	150(10)

^a Atomic coordinates correspond to crystal C2 ^b Displacement parameter fixed at 200 pm² ^c sof fixed to 0.70

Table 6.3: Positional and equivalent isotropic displacement parameters $U_{\text{eq}}(\text{pm}^2)$ for γ'_1 -Pt₅Zn₂₁ (C3)

Cluster	Site	Wy.	Atom	x	y	z	sof	U_{eq}
A	IT	16e	Zn11	0.9466(2)	x	x	1	182(11)
	OT	16e	Pt12	0.0889(1)	x	x	1	50(5)
	OH	24f	Zn13	0.1731(6)	0	0	0.69(2)	200 ^a
	CO	48h	Zn14	0.3448(1)	x	0.9796(2)	1	124(7)
B	IT	16e	Zn21	0.4429(5)	x	x	0.50(4)	193(40)
	IT'	16h	Zn21'	0.4216(14)	x	x	0.27(4)	36(11)
	OT	16e	Zn22	0.5856(2)	x	x	0.24(2)	72(13)
	OT	16e	Pt22	0.5856(2)	x	x	0.39(2)	72(13)
	OT'	16e	Zn22'	0.5646(8)	x	x	0.34(3)	130(50)
	OH	24f	Zn23	0.6793(1)	0	0	0.53(2)	120(10)
	OH	24f	Pt23	0.6793(1)	0	0	0.47(2)	120(10)
	CO	48h	Zn24	0.3434(3)	x	0.4839(2)	0.91(2)	222(15)
C	IT	16e	Zn31	0.6965(2)	x	x	1	154(11)
	OT	16e	Zn32	0.8368(1)	x	x	0.61(2)	64(9)
	OT	16e	Pt32	0.8368(1)	x	x	0.39(2)	64(9)
	OH	24g	Zn33	0.5698(1)	$\frac{1}{4}$	$\frac{1}{4}$	0.49(2)	116(9)
	OH	24g	Pt33	0.5698(1)	$\frac{1}{4}$	$\frac{1}{4}$	0.51(2)	116(9)
	CO	48h	Zn34	0.4034(1)	x	0.7271(1)	1	180(8)
D	IT	16e	Zn41	0.1928(2)	x	x	1	267(16)
	OT	16e	Pt42	0.3359(1)	x	x	1	62(4)
	OH	24g	Zn43	0.4255(5)	$\frac{1}{4}$	$\frac{1}{4}$	0.71(3)	200 ^a
	CO	48h	Zn44	0.0924(1)	x	0.2341(1)	1	162(8)

^a Displacement parameter fixed at 200 pm²

6.4 Phase analyses and physical properties

The homogeneity ranges and constitutions of the cubic γ -phases in the Pt-Zn systems were examined by means of preparative methods, isopiestic and calorimetric measurements, by and X-ray diffraction. According to X-ray structure analyses, the homogeneity range of the γ_1 -phase was found to range from $0.184 \leq x_{\text{Pt}} \leq 0.20$. A Rietveld refinement was performed on a single phase sample containing 19 at.% of Pt using the X'pert Plus program package [55]. A profile fit is shown in Fig. 6.1. At the Pt-rich border the phase coexists with Pt₂₇Zn₈₅ with orthorhombic symmetry ($a = 1291.64(9)$ pm, $b = 5529.8(3)$ pm, $c = 911.62(7)$ pm). The lattice parameters of the single phase and the phase co-existing with the orthorhombic one scatter between 1809.1(1)

to 1814.0(1) pm.

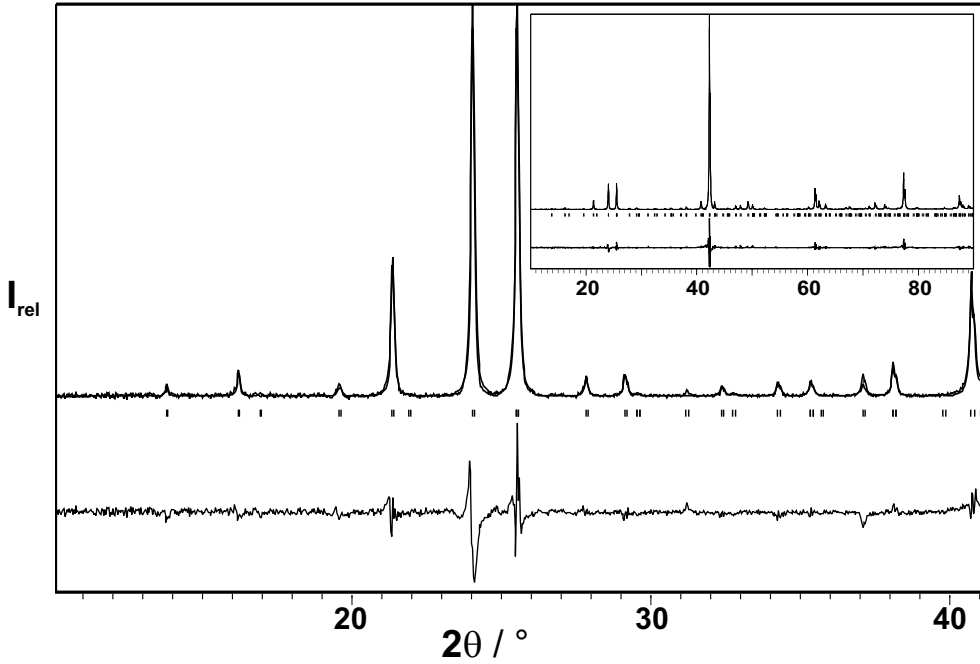


Figure 6.1: Low angle Rietveld profile fit of γ_1 -Pt₅Zn₂₁ ($x_{\text{Pt}} = 0.193$). The insert shows the complete pattern (CuK $_{\alpha}$, $2\theta_{\text{max}} = 90^\circ$, $a = 1811.9(1)$ pm, $R_{\text{B}} = 4.94$, $R_{\text{p}} = 12.0$).

According to DTA measurements of a single phase sample, Zn-rich Pt₅Zn₂₁ (19.2 at.% of Pt) begins to melt nearly congruently at 1237 K. The peak maximum is found at 1251 K. For the Pt-rich sample (Nominal composition of 22 at.% of Pt) the peak maximum is found at 1264 K. The shift of 13 K in the melting temperature of the Pt-rich sample is attributed to the phase width the cubic large γ -phase. The DTA plots of two distinct samples as a function of temperature are shown in Fig. 6.2.

Magnetic susceptibilities of clean polycrystalline samples were recorded with a SQUID magnetometer in the temperature range 1.8–300 K at a magnetic flux density of 1 Tesla. The data were corrected for diamagnetism of the sample holder manufactured from KLF (Polytetrafluoroethen). Fig. 6.3 shows a plots of the magnetic susceptibilities of various homogeneous samples as a function of temperature and composition. The Pauli paramagnetism of these metallic phases is found to be overcompensated by the core diamagnetism of its constituents. The values range from -4.7 to $-3.1 \times 10^{10} \text{ m}^3 \text{ mol}^{-1}$ compared to $-5.4 \times 10^{10} \text{ m}^3 \text{ mol}^{-1}$ for the ordinary γ -phase Pt₂Zn_{11- δ} [75]. In each case the value refers to an average atom of the formula, *i.e.* $\frac{1}{x+y} \text{Pt}_x\text{Zn}_y$.

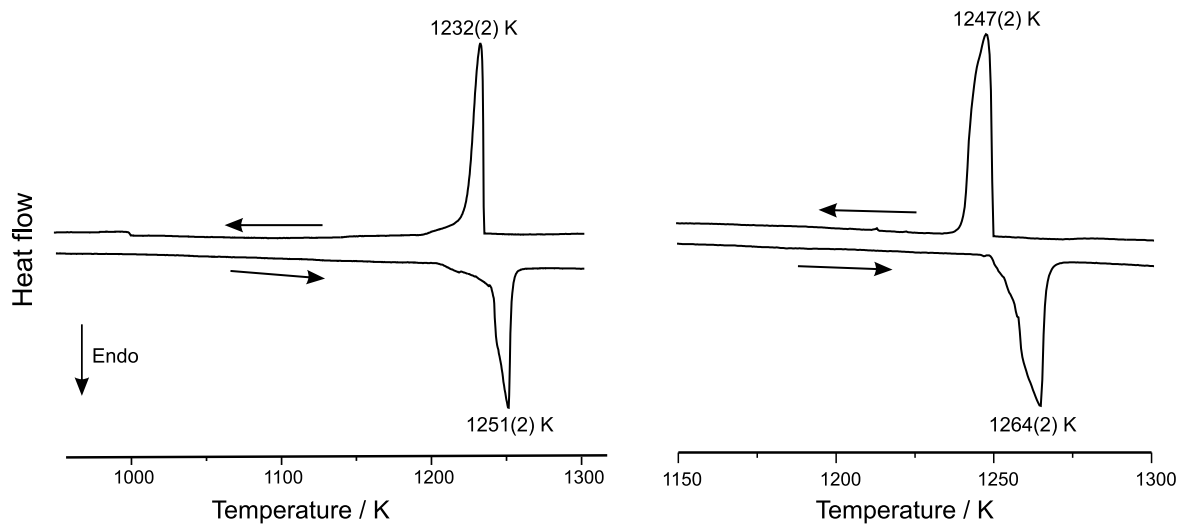


Figure 6.2: DTA plots of two single phase sample of nominal compositions of 0.192 and 0.22 at.% of Pt, respectively.

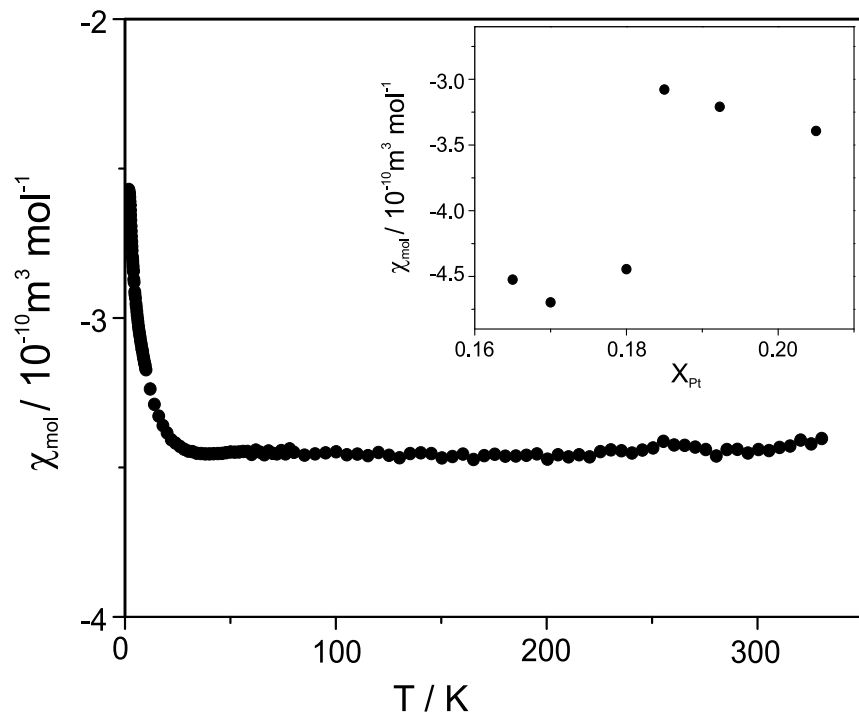


Figure 6.3: Magnetic susceptibilities of γ_1 -Pt₅Zn₂₁ as a function of temperature. Inset shows the change in magnetic susceptibilities with composition.

6.5 Results and discussion

The cubic F-centered structure of Pt₅Zn₂₁ is a complex 6a × 6a × 6a superstructure of a β-brass type structure with ordered vacancies. The ordered vacancies are characteristic for γ-brass type or related structures. In the structure of Pt₅Zn₂₁ the vacancies are located at the centers of M₂₆ clusters around the special positions 4a, 4b, 4c, and 4d. Group-subgroup relations have been used to analyse the structural relation between γ-Pt₅Zn₂₁ and the aristo-type bcc structure. The symmetry reduction from aristo-type β-brass to Pt₅Zn₂₁ includes four minimal symmetry reductions. The corresponding Bärnighausen tree [82] is shown in Fig. 6.4.

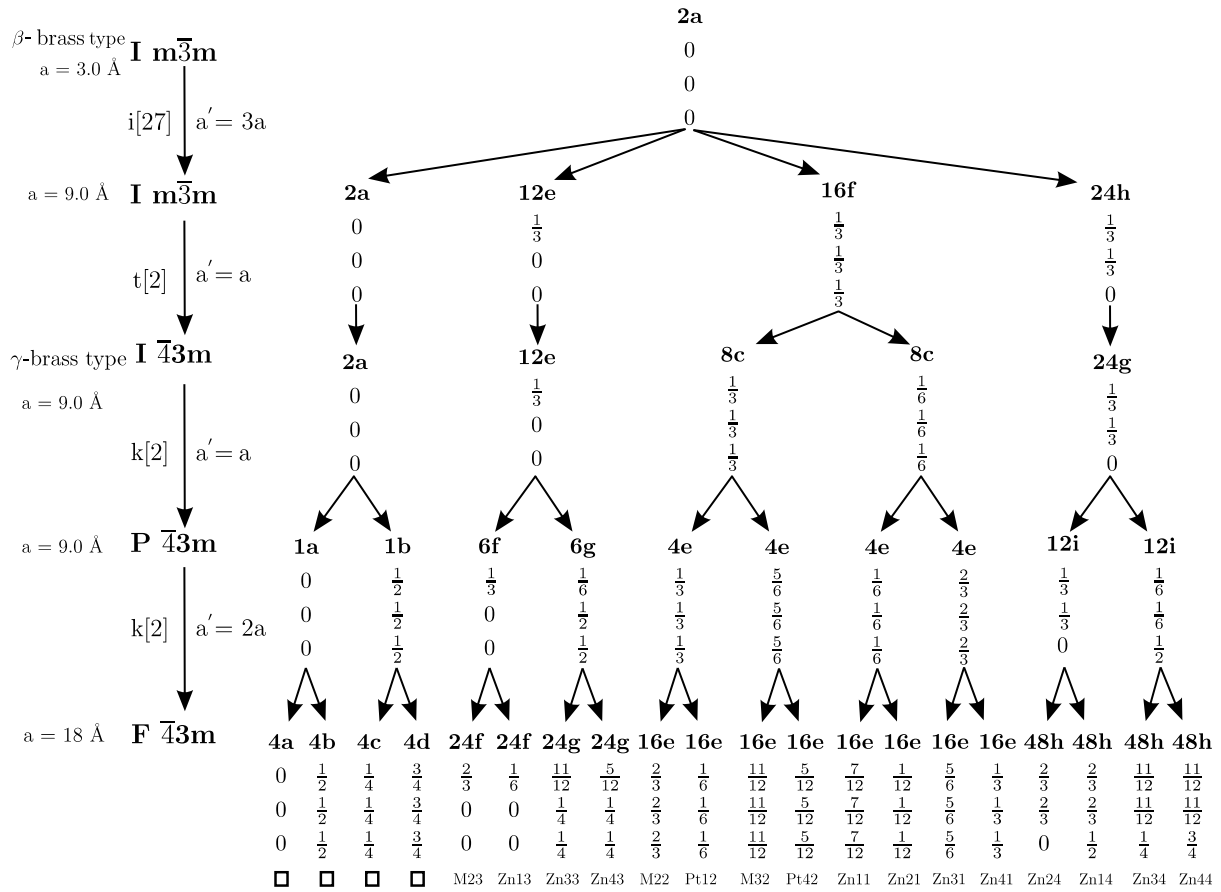


Figure 6.4: Group-subgroup relations between Pt₅Zn₂₁ and aristo-type bcc structure. Deviations between the ideal positions and the real ones (c.f. Table 6.2) are a measure of the degree of distortion of the structure due to the vacancies at $0\ 0\ 0$, $\frac{1}{4}\ \frac{1}{4}\ \frac{1}{4}$, $\frac{1}{2}\ \frac{1}{2}\ \frac{1}{2}$, and $\frac{3}{4}\ \frac{3}{4}\ \frac{3}{4}$.

The crystal structure of Pt₅Zn₂₁ represents a structurally complex γ -phase belonging to a class of cubic giant cell structures. They all are composed of four symmetrically independent atomic units. Each unit, also termed cluster [84], consists of 22 - 29 atoms which are arranged in shells around the high symmetry points $0\ 0\ 0$, $\frac{1}{2}\ \frac{1}{2}\ \frac{1}{2}$, $\frac{1}{4}\ \frac{1}{4}\ \frac{1}{4}$, and $\frac{3}{4}\ \frac{3}{4}\ \frac{3}{4}$ of a face centered cubic lattice. The clusters correspond to distinct fragments either of the body centered cubic (bcc) W-type or the α -Mn type structure[88]. Prototypical examples are Cd₄₁Pt₈ (cI392) [89], Mg₆Pd (cF392) [90, 91], Na₆Tl (cF408) [92], Li₂₁Si₅ (cF416) [87], Cu₄₁Sn₁₁ (cF416) [93], Al₆₉Ta₃₉ (cF432) [85], Li_{4.4}Sn [94], Cd₄₅Sm₁₁ (cF448) [95] and Ir_{7+7 δ} Zn_{97-11 δ} (cF403-406) [70].

A specific feature of Pt₅Zn₂₁ is the occurrence of one type of cluster, the so-called γ -type comprising 26 atoms. Its constitution corresponds to a bcc fragment with a vacancy at the center. Atoms next to the void occupy the corners of an inner tetrahedron (IT). Four atoms somewhat further distant from the center are situated at the corners of an outer tetrahedron (OT). The atoms of the next shell constitute an octahedron (OH). Twelve more atoms completing the 26 atom unit define a distorted cub-octahedron (CO). Fig.6.5 shows two distinctly composed clusters, Pt₄Zn₂₂ having the Pt atoms located at the OT site, and Pt₆Zn₂₀ with the minority component situated at the OH sites.

The voids give rise to a cooperative distortion of the bcc typical dodecahedral coordination towards an icosahedral coordination for the IT and OT atoms. As a result of the cooperative distortion the clusters can alternatively be viewed as a quadruple of condensed icosahedra about the OT atoms encapsulating a tetrahedron formed by IT atoms. In this case adjacent clusters are not connected by metal-metal contacts as there are the γ -type fragments but rather share corners and edges [75].

To avoid confusions with γ -Pt₂Zn₁₁ the phase is further termed as γ_1 -phase. The structure of the γ_1 -phase can be subdivided into two chemically distinct but topologically equivalent partial structures, one with constant, the second with variable composition. The two parts correspond exactly to two sets of γ -clusters. The clusters labeled A and D at $0\ 0\ 0$ and $\frac{3}{4}\ \frac{3}{4}\ \frac{3}{4}$ are both completely ordered. They build up the compositionally invariant part of the structure. The Zn atoms are situated at IT, OH and CO sites, the Pt atoms at the OT site. Thus, the composition Pt₄Zn₂₂ results for cluster of type A and D. They are arranged like carbon atoms in diamond. The other two clusters B and C vary in composition. They also form a diamond-like atomic ar-

arrangement which penetrates its counterpart by being shifted by half of a lattice vector, see Fig. 6.5.

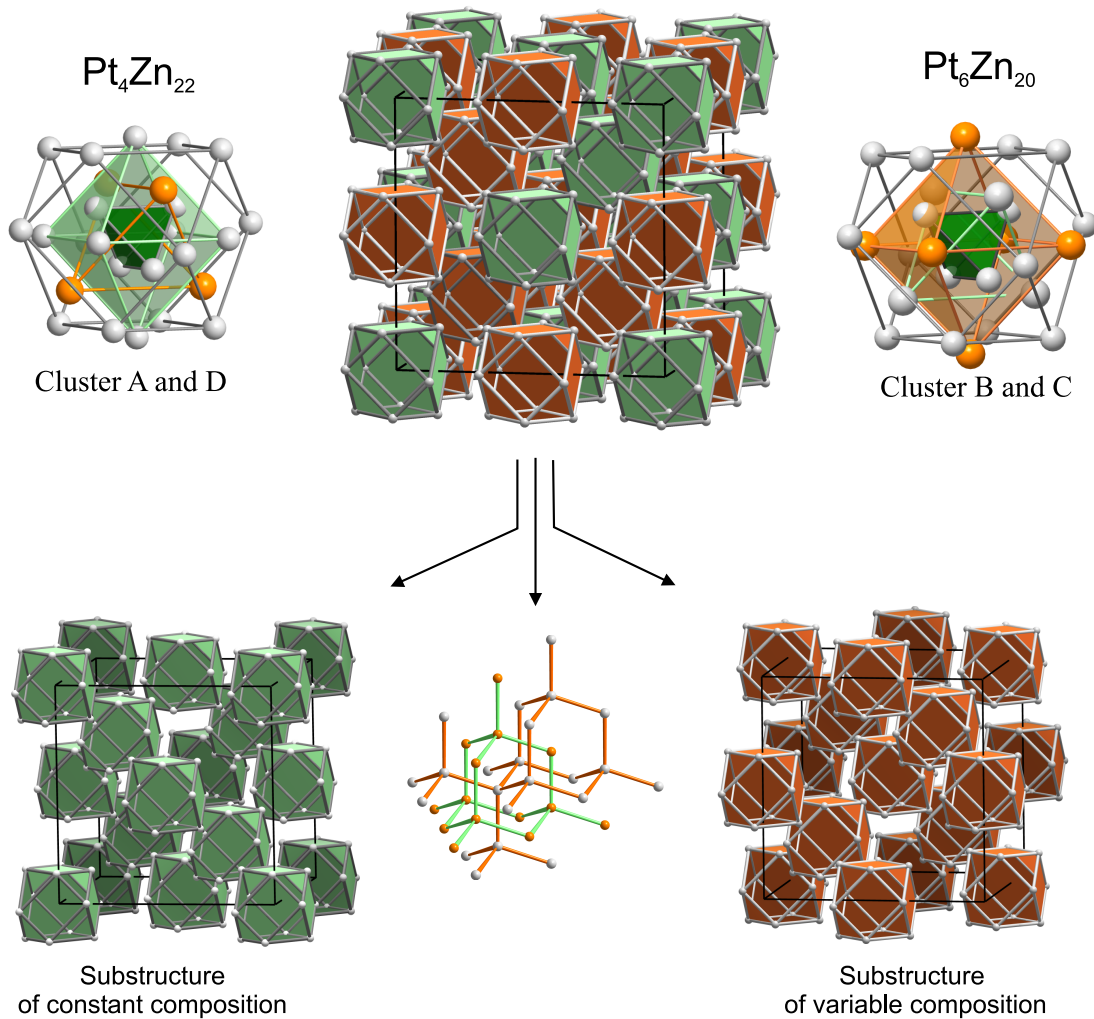


Figure 6.5: The structure $\text{Pt}_5\text{Zn}_{21}$ is comprised by two distinct γ -type clusters. Clusters A and D at $0\ 0\ 0$ and $\frac{3}{4}\ \frac{3}{4}\ \frac{3}{4}$ have constant composition $\text{Pt}_4\text{Zn}_{22}$ over the whole homogeneity range. The centers of these clusters define the diamond-like net shown in green. Clusters B and C at $\frac{1}{4}\ \frac{1}{4}\ \frac{1}{4}$ and $\frac{1}{2}\ \frac{1}{2}\ \frac{1}{2}$ vary in composition due to partial substitutional disorder. Their centres define a second diamond-like net (orange). The two nets interpenetrate mutually.

Clusters B and C show three kinds of disorder as typical for structurally complex alloys:

- i) mutual substitution of Zn and Pt,
- ii) partial depletion of Zn sites, and concomitantly,
- iii) positional disorder ascertained by split positions.

The disorder in cluster C is constrained to mutual substitution. At the Pt-rich boundary of the γ_1 -phase (c1, 20 at.% Pt) the OH site of cluster C is exclusively occupied by Pt atoms. In addition, 12 at.% of the OT site are Pt. For the phase at the Zn-rich stability limit (c2) Pt atoms on the OH site are partly replaced by Zn (15 at.%) and, again, about 14 at.% of the OT site are occupied by Pt. Accordingly, the composition of cluster C varies between $\text{Pt}_{5.7}\text{Zn}_{20.3}$ and $\text{Pt}_{6.5}\text{Zn}_{19.5}$ for $\gamma_1\text{-Pt}_5\text{Zn}_{21}$. By contrast, cluster B shows three types of disorder. The occupation of the OH sites - 86 at.% and 100 at.% Pt, respectively - match well with that of cluster C. The vacancies of the structure are exclusively accumulated on IT and CO sites of cluster B. Furthermore, the IT and OT sites of Zn-rich $\gamma_1\text{-Pt}_5\text{Zn}_{21}$ and a smaller fraction of the CO site of Pt-rich $\gamma_1\text{-Pt}_5\text{Zn}_{21}$ are split. Noticeably, for both crystals the occupation factors of corresponding OH and CO split positions add up to approximately 100% even though the factors were refined independently. The disorder in the clusters B and cluster C is summarized in Table 6.4 and Table 6.5. This has been taken as an additional sign that the electron density is reasonably attributed to the two distinctly scattering species. Thus, the formula for cluster B is $\text{Pt}_{5.2}\text{Zn}_{19.0}$ for 18.4 and $\text{Pt}_6\text{Zn}_{18.4}$ for 20.0 at.% Pt, respectively. The overall compositions and densities of the two boundary phases are $\text{Pt}_{4.7}\text{Zn}_{20.9}$, $\rho = 10.19 \text{ g cm}^{-3}$ and $\text{Pt}_{5.2}\text{Zn}_{20.5}$, $\rho = 10.48 \text{ g cm}^{-3}$. These values compare nicely with the measured density of $10.29(5) \text{ g cm}^{-3}$ that we measured for a homogeneous Pt-rich $\gamma_1\text{-Pt}_5\text{Zn}_{21}$ sample.

Table 6.4: Mutual substitution of Pt/Zn in cluster B and C for $\text{Pt}_5\text{Zn}_{21}$

x_{Pt}	OH(B)	OH(C)	OT(C)
0.184	86/14	85/15	14/86
0.198	100/0	100/0	6/94
0.200	100/0	100/0	12/88

Table 6.5: Vacancies and positional disorder in cluster B for Pt₅Zn₂₁

x_{Pt}	IT/IT (split)	OT/OT (split)	CO/CO (split)
0.184	68/17	70/30	–
0.198	60/0	100/0	89/11
0.200	62/0	100/0	87/13

The structural results call for a critical comment on the previously reported phase Pt₃Zn₁₀: The homogeneity range of the γ_1 -phase in the Pt-Zn system does not extend to Pt₃Zn₁₀ (corresponding to 23.3 at.% Pt) but reaches its stability limit on the Pt-rich side at 20 at.% Pt. Furthermore, the structure of γ_1 -Pt₅Zn₂₁ is less disordered than suggested earlier by Westman *et al.* [13]. In particular, it can be ruled out that one of the cluster sites is completely empty.

During this studies, a third phase has been found with cubic symmetry which occurs on the zinc-rich side intermediate to γ -Pt₂Zn₁₁ and γ_1 -Pt₅Zn₂₁ exhibiting a slightly modified cubic giant cell structure. Since the structure is intimately related to that of γ_1 -Pt₅Zn₂₁ this new structure is termed as γ'_1 -phase. Its homogeneity range extends from about 0.165 to about 0.175 at.% of Pt. The structural resemblance is reflected in the spectral distribution of the interatomic distances for the three phases as listed in Table 6.6. Major differences between the two phases γ_1 and the γ'_1 concern:

- i) A plot of the sample composition versus temperature obtained from isopiestic measurements shows a discontinuity between samples containing γ_1 -Pt₅Zn₂₁ and γ'_1 -Pt₅Zn₂₁, as expected for two phases separated by a miscibility gap, see Fig.6.6.
- ii) The temperature of the endothermic effects attributed to the melting points of the γ -phases increases discontinuously from 1133(2) K for Pt₂Zn_{11- δ} to 1238(5) K for γ'_1 -Pt₅Zn₂₁ to 1251(3) K for γ_1 -Pt₅Zn₂₁.
- iii) The vacancy concentration increases discontinuously from 1.5 % for Pt_{4.72}Zn_{20.92} (18.4 at. % Pt) to 5.4 % for Pt_{4.25}Zn_{20.34} (17.4 at. % Pt).

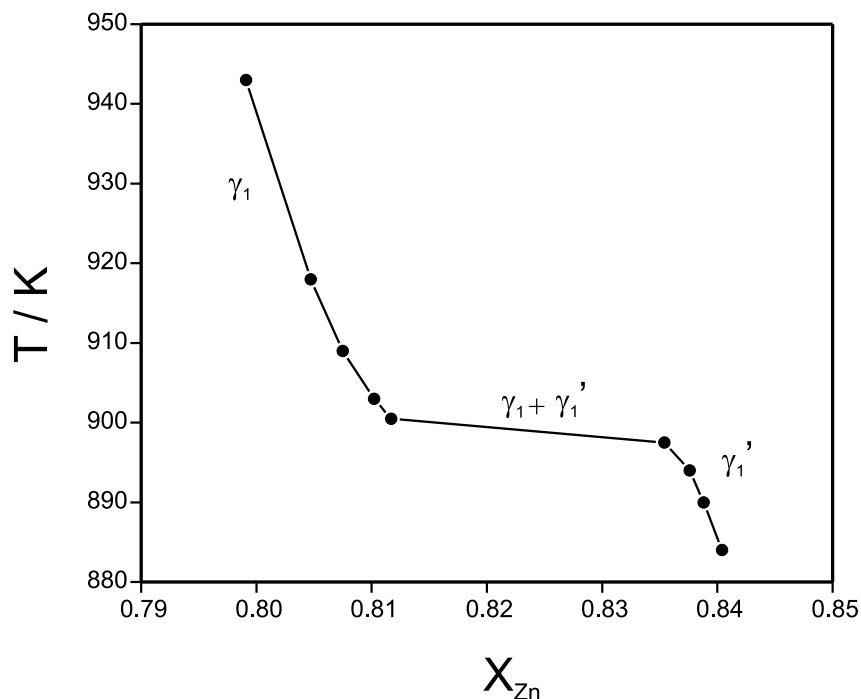


Figure 6.6: Variation of composition with temperature for samples exposed to a Zn pressure of 15 hPa.

- iv) By contrast to $\gamma_1\text{-Pt}_{4.72}\text{Zn}_{20.92}$, about 30 at. % of the OH sites of clusters A and D are empty. The vacancies are associated with an abrupt increase of the Pt content in the otherwise compositionally invariant part of the structure. The Pt content in this part of the structures changes abruptly from 15.4 at. % for $\gamma_1\text{-Pt}_5\text{Zn}_{21}$ to 16.5 at. % for zinc-rich $\gamma_1'\text{-Pt}_{4.25}\text{Zn}_{20.34}$.
- v) The Pt content of the remaining part of the structure is appropriately reduced for $\gamma_1'\text{-Pt}_{4.25}\text{Zn}_{20.34}$. The reduction is mainly achieved by an enrichment of about 50 at. % Zn on the OH sites which in case of γ_1 -phase is (mainly) occupied by Pt atoms. In spite of this striking redistribution of Zn and Pt atoms at OT and OH sites the pattern of the positional disorder in clusters B and C resembles that of the γ_1 -phase.
- vi) The crystal structures of the two phases show discontinuities which are incompatible with structures of phases of a homogenous phase field.

Table 6.6: Minimum (d_{\min}), maximum (d_{\max}) and mean interatomic distances ($\langle d \rangle$) and coordination numbers (C.N.) for various Pt₅Zn₂₁ phases

Cluster	Site	C1		C2		C3	
		$\frac{d_{\min} - d_{\max}}{\langle d \rangle}$ pm	C.N.	$\frac{d_{\min} - d_{\max}}{\langle d \rangle}$ pm	C.N.	$\frac{d_{\min} - d_{\max}}{\langle d \rangle}$ pm	C.N.
A	IT	261.5 – 275.3 < 270.2 >	12	262.0 – 277.1 < 270.7 >	12	256.8 – 274.2 < 268.2 >	12
	OT	260.2 – 278.3 < 269.9 >	12	259.1 – 279.3 < 271.2 >	12	261.1 – 274.6 < 268.4 >	12
	OH	257.6 – 301.9 < 277.2 >	13	256.7 – 301.6 < 277.4 >	13	256.8 – 306.9 < 277.8 >	13
	CO	258.1 – 293.3 < 274.2 >	11	258.5 – 291.9 < 273.8 >	11	259.2 – 298.0 < 274.3 >	11
B	IT	243.0 – 283.3 < 260.0 >	10	252.1 – 310.6 < 273.1 >	12	252.3 – 293.1 < 269.2 >	12
	OT	259.4 – 296.2 < 272.6 >	12	262.1 – 274.3 < 268.1 >	12	258.3 – 279.1 < 268.6 >	12
	OH	259.2 – 285.4 < 272.3 >	13	260.9 – 279.0 < 275.5 >	13	262.6 – 288.5 < 276.0 >	13
	CO	243.0 – 290.0 < 270.1 >	13	258.2 – 290.4 < 270.4 >	11	253.2 – 288.5 < 270.8 >	11
	IT'	–		238.5 – 276.9 < 263.7 >	10	230.2 – 285.4 < 263.2 >	10
	OT'	–		234.7 – 304.8 < 271.0 >	12	235.6 – 306.4 < 271.5 >	12
	CO'	238.0 – 286.0 < 266.1 >	8	–		–	
C	IT	260.9 – 278.2 < 268.5 >	12	262.5 – 275.6 < 268.5 >	12	262.1 – 275.0 < 268.2 >	12
	OT	261.4 – 278.7 < 268.1 >	12	261.8 – 280.06 < 267.9 >	12	260.6 – 278.8 < 267.8 >	12
	OH	256.2 – 285.9 < 273.7 >	13	256.8 – 285.66 < 274.8 >	13	259.1 – 286.0 < 274.6 >	13
	CO	254.7 – 301.6 < 274.3 >	11	261.5 – 301.9 < 273.9 >	11	262.1 – 306.9 < 274.6 >	11
D	IT	263.7 – 308.1 < 277.5 >	12	263.0 – 298.5 < 275.4 >	12	260.8 – 293.4 < 273.1 >	12
	OT	258.9 – 278.6 < 270.1 >	12	260.4 – 275.7 < 269.7 >	12	260.1 – 274.0 < 268.3 >	12
	OH	256.2 – 291.8 < 277.0 >	13	256.8 – 293.0 < 277.0 >	13	260.0 – 298.0 < 277.4 >	13
	CO	256.7 – 291.1 < 272.6 >	11	257.6 – 291.1 < 272.3 >	11	261.0 – 289.1 < 273.0 >	11

6.6 Summary

- Syntheses of Pt₅Zn₂₁ phase were carried out using isopiestic and solid state syntheses methods.
- Systematic studies of the Pt-Zn system in the range $0.165 \leq x_{\text{Pt}} \leq 0.20$ revealed two distinct γ -phases all exhibiting cubic symmetry. They adopt a $2a \times 2a \times 2a$ superstructure of the ordinary γ -Pt₂Zn₁₁ phase.
- The homogeneity range of the γ_1 -phase extends from 18.4 to 20.0 at.% Pt. Hence, the

γ_1 -domain includes $\text{Pt}_5\text{Zn}_{21}$ but not $\text{Pt}_3\text{Zn}_{10}$.

- The structure comprises four symmetrically independent and three compositionally inequivalent 26 atom clusters. They are pair-wise arranged according to the motif of two interpenetrating diamond-like nets, one with constant composition ($\text{Pt}_4\text{Zn}_{22}$) and perfectly ordered, the second richer in Pt and variable in composition ($\text{Pt}_{6\pm\delta}\text{Zn}_{20\pm\delta'}$).
- Experimental evidence has been provided for the existence of a second cubic giant cell structure in the Pt-Zn system. A discontinuous change of the vacancy concentration and the Pt/Zn distribution and isopiestic measurements indicate a miscibility gap between $\gamma_1\text{-Pt}_5\text{Zn}_{21}$ and $\gamma'_1\text{-Pt}_{4.25}\text{Zn}_{20.34}$.

Chapter 7

Pt₁₁Zn₃₂ – A γ -brass related composite structure

7.1 Introduction

The reinvestigation of the Pt-Zn system in the zinc-rich part is motivated by the existence of a structurally complex γ -brass related phase in the congeneric Ni-Zn system situated in the γ -phase field at the valence-electron-poor site next to γ -Ni₅Zn₂₁ [11]. As indicated by electron diffraction (ED) and transmission electron microscopy (TEM) the structural complexity is associated with a modulation along the [110] direction of the parent γ -phase [32, 34]. The structural differentiation is reflected by striations appearing in suitably oriented TEM images. The image contrast is suggested to arise from inversion anti-phase domains whose size sensitively depends on composition. The presumed structural relation with γ -brass-related Ni₅Zn₂₁ is corroborated by an X-ray single crystal structure analysis of NiZn₃, a Ni-rich representative with 276 atoms in the A-centred orthorhombic unit cell [12]. However, the weak X-ray scattering contrast between Ni and Zn hampers an unambiguous assessment of how the structure evolves at varying composition. Hence, in order to resolve the modulation on an atomic scale we searched for similar γ -derivates in other brass-related systems. In the course of a preliminary investigation of the Pd-Zn systems we uncovered a symmetrically closely related phase ($a = 1291.0(3)$ pm, $b = 910.9(2)$ pm, $c = 3404.7(7)$ pm, Cmca, oC276) whose composition turned out to be approximately Pd₁₅Zn₅₄ ($x_{\text{Pd}} = 0.217$) [39]. These findings rendered support to the assumption that a similar phase might exist in the Pt-Zn system, too. In view of the strong X-ray scattering contrast between

Pt and Zn, the structure analyses of related PtZn_x phases would afford optimal resolution of the composition-dependent modulation. Indeed, a detailed study of the zinc-rich portion of the Pt-Zn system brought to light that the phase field which was previously considered to be the domain of the cubic phase Pt₃Zn₁₀ ($x_{\text{Pt}} = 0.23$) [13] actually accommodates a series of intimately related structures exhibiting orthorhombic symmetry. This chapter deals with the synthesis and characterization of γ -brass related composite structure Pt₁₁Zn₃₂. A short communication of this phase has already been published [96].

7.2 Syntheses

The syntheses were carried out in previously out-gassed, evacuated silica ampoules using pure Pt and Zn elements as a starting materials. The mole fraction x_{Pt} was systematically varied between 0.24 and 0.30. The ampoules were heated continuously at a rate of 120 K h⁻¹ to a temperature of 1320 K at which mixtures of the reactants were kept for 12 h. Subsequently, the ampoules were cooled to 970 K in the course of 72 h, and then brought to room temperature in less than 24 h.

7.3 Structure determination

Several crystals of regular shape from two different batches were selected from the crushed samples. X-ray diffraction data of three crystals were recorded within the range $5^\circ < 2\theta < 65.7^\circ$ at ambient temperature with an IPDS-I instrument (MoK α). The data were subsequently corrected for Lorentz and polarisation effects. Numerical absorption corrections were applied in all cases. The numerical absorption corrections were performed by optimizing the crystal shape using X-SHAPE and X-RED program [61, 62]. The reported results refer to a nearly rectangular shaped crystal, approximately $0.18 \times 0.08 \times 0.07$ mm³ in size. The crystal was selected from an as prepared sample. The Laue symmetry *mmm* and the systematic extinctions hkl: $h+k = 2n+1$, h0l: $h = 2n+1$, and hk0: $h,k = 2n+1$ unequivocally pointed to the orthorhombic space group Cmce (No. 64). Direct methods (SHELXS [58]) produced a coherent structural model. The full-matrix least-square refinements including anisotropic displacement parameters converged at residual values $R1 = 0.0464$ for $I_o > 2\sigma(I_o)$ and $wR2 = 0.1052$ at a maximal residual electron density of $3.7 \cdot 10^{-6}$ e pm⁻³. Further details concerning the data collection and the refinement are

summarized in Table 7.1. The atomic positions and anisotropic thermal displacement parameters are listed in Table 7.2 and 7.3, respectively.

The reciprocal space sections were acquired by re-evaluating the crystal with a Lattice Explorer (Stoe) attached to an IPDS-I instrument. The crystal was oriented with \mathbf{c}^* parallel to the rotating axis (goniometer head) and in addition, the \mathbf{a} or \mathbf{b} axis was aligned parallel to the X-ray beam. The diffracted intensities were collected on an image plate using monochromatized MoK $_{\alpha}$ radiation ($\phi = 74.5^{\circ}$ and 164.5°). The data were reduced with the laser of the IPDS-I instrument.

Two further single crystal studies revealed that annealing of the samples at 770 K for 7 days triggers a subtle structural transition. The change shows up in violations of the extinctions $hk0$: $h, k = 2n+1$, reflecting the loss of the e glide operation perpendicular to the c axis, cf. Fig. 7.7. Consequently, $Cmc2_1$ is the most likely space group of the phase. The loss of the centre of symmetry is associated with a splitting of Wyckoff sites including the single statistically occupied site (47 % Pt, 53 % Zn) in the high-symmetrical structure. Thus, a further ordering of the structure could be seen as a driving force of the detected symmetry reduction. Indeed, structure refinements in the $Cmc2_1$ space group resulted in an enrichment of Pt (70%) on one and Zn (86%) on the second site. Without altering the rest of the atomic arrangement significantly, the refinements converged at $R1 = 0.0413$. The atomic positions and anisotropic thermal displacement parameters are listed in Table 7.4.

Table 7.1: Crystallographic and technical data for the single-crystal structure determination

Sum formula	Pt _{10.8} Zn _{32.2(1)} ^a	Pt _{10.7} Zn _{32.3(1)} ^b
Space group (No.)	Cmce (64)	Cmc2 ₁ (36)
Z	4	4
a / pm	1293.8(3)*	1290.1(1)
b / pm	914.4(2)	912.5(1)
c / pm	2126.3(4)	2122.3(2)
V / 10 ⁶ pm ³	2515.5(9)	2498.6(4)
Molar mass / g mol ⁻¹	4215.13	4202.16
ρ_{cal} / g cm ⁻³	11.130	11.171
μ / mm ⁻¹	89.883	90.029
<i>Data collection</i>		
Crystal size / mm ³	0.18 × 0.08 × 0.07	0.16 × 0.10 × 0.06
Diffractometer	IPDS-I (STOE & Cie)	
Temperature / K	293(3)	293(3)
Radiation / monochromator	MoK α / Graphite	
Distance crystal-IP / mm	40	40
$\phi_{min} - \phi_{max}; \Delta\phi$	0–202; 1	0–200; 1
$2\theta_{max}$ / °	65.7	65.7
Collected reflections	–18 ≤ h ≤ 19 –13 ≤ k ≤ 13 –32 ≤ l ≤ 32	–18 ≤ h ≤ 19 –13 ≤ k ≤ 13 –32 ≤ l ≤ 32
Total No. of reflections	17408	21116
<i>Data reduction</i>		
Program	IPDS-Software [57]	X-RED [61]
Absorption correction	Numerical, X-SHAPE [62]	
Max. / Min. transmission	0.1368 / 0.0251	0.1272 / 0.0151
Unique reflections	2372	4758
R _{int}	0.0940	0.0868
<i>Refinement</i>		
Program	SHELXL-97 [58]	
Refined on	F _o ²	
Reflections I _o > 2σ(I _o)	1456	3410
Variables	111	217
R ₁ (I _o > 2σ(I _o))	0.0461	0.0413
R ₁ (all)	0.0800	0.0572
wR ₂ (all)	0.1205	0.1277
Goodness of fit	1.200	0.832
$\Delta\rho_{max} / \Delta\rho_{min} / 10^{-6}$ e pm ⁻³	3.709 / –3.88	5.808 / –6.276
Extinction coefficient	0.000123(10)	0.000058(4)
Absolute structure factor	–	0.52(2)

$$^a 1/w = \sigma^2(F_o^2) + (0.0474(\text{Max}(F_o^2, 0) + 2F_c^2)/3)^2 \quad ^b 1/w = \sigma^2(F_o^2) + (0.1(\text{Max}(F_o^2, 0) + 2F_c^2)/3)^2$$

* Lattice parameters are obtained from CAD 4 X-ray diffractometer.

Table 7.2: Atomic coordinates and equivalent isotropic displacement parameters $U_{\text{eq}}(\text{pm}^2)$ for Pt₁₁Zn₃₂ (Cmce)

Atom No.	Wy.	x	y	z	sof	U_{eq}
Zn1	8f	0	0.3050(2)	0.40363(12)	1	86(4)
Zn2	8f	0	0.2008(3)	0.28547(12)	1	109(5)
Zn3	8f	0	0.2599(3)	0.15650(14)	1	140(5)
Zn4	8f	0	0.2811(3)	0.03053(13)	1	117(5)
Zn5	8d	0.3753(3)	0	0	1	127(6)
Zn6	16g	0.3248(2)	0.3442(2)	0.00996(9)	1	132(4)
Zn7	16g	0.1863(2)	0.1240(2)	0.39356(9)	1	133(3)
Zn8	16g	0.1179(2)	0.0463(2)	0.09938(9)	1	101(3)
Zn9	16g	0.3769(2)	0.4660(2)	0.29812(9)	1	123(4)
Zn10	16g	0.1822(2)	0.3572(2)	0.31312(7)	1	94(3)
M11(Zn)	16g	0.32102(10)	0.16091(9)	0.28916(4)	0.54(1) ^a	88(3)
Pt1	4a	0	0	0	1	37(2)
Pt2	8f	0	0.0280(1)	0.3984(1)	1	72(2)
Pt3	8f	0	0.4827(1)	0.3007(1)	1	89(2)
Pt4	16g	0.18101(5)	0.33102(5)	0.09462(3)	1	64(1)

^a sof of Zn, sof of (Pt) = 1 – sof of (Zn)Table 7.3: Anisotropic displacement parameters $U(\text{pm}^2)$ for Pt₁₁Zn₃₂ (Cmce)

Atom No.	U11	U22	U33	U12	U13	U23
Zn1	105(12)	64(7)	88(7)	0	-4(8)	0
Zn2	123(16)	51(8)	155(10)	0	-42(7)	0
Zn3	69(13)	136(10)	214(10)	0	76(8)	0
Zn4	46(14)	108(10)	196(10)	0	-81(8)	0
Zn5	75(15)	216(12)	92(10)	0	104(8)	0
Zn6	95(12)	190(7)	112(6)	-46(8)	-16(6)	53(7)
Zn7	59(9)	82(6)	259(9)	-36(6)	0(6)	-7(7)
Zn8	115(9)	126(6)	61(5)	-56(5)	15(6)	-12(7)
Zn9	94(11)	209(8)	67(6)	-44(7)	14(6)	-5(6)
Zn10	42(9)	146(7)	93(6)	62(7)	-2(5)	-24(6)
M11	69(6)	97(4)	98(4)	17(3)	-15(2)	8(3)
Pt1	11(6)	47(4)	52(4)	0	8(3)	0
Pt2	34(4)	77(3)	105(3)	0	14(2)	0
Pt3	52(5)	127(3)	87(3)	0	-6(2)	0
Pt4	37(3)	78(2)	76(2)	10(2)	-18(1)	13(2)

Table 7.4: Atomic coordinates and equivalent isotropic displacement parameters $U_{\text{eq}}(\text{pm}^2)$ for Pt₁₁Zn₃₂ (Cmc2₁)

Atom No.	Wy.	x	y	z	sof	U_{eq}
Zn1	4a	0	0.9448(2)	0.5970(4)	1	87(4)
Zn1A	4a	0	0.4461(4)	0.9060(3)	1	71(9)
Zn2	4a	0	0.0433(4)	0.7195(3)	1	108(9)
Zn2A	4a	0	0.5528(5)	0.7894(3)	1	110(11)
Zn3	4a	0	0.9964(7)	0.8484(4)	1	154(5)
Zn3A	4a	0	0.4837(5)	0.6607(3)	1	117(8)
Zn4	4a	0	0.9612(5)	0.9749(3)	1	147(9)
Zn4A	4a	0	0.4742(5)	0.5349(3)	1	117(8)
Zn5	8b	0.3757(3)	0.2370(5)	-0.0015(2)	1	116(5)
Zn6	8b	0.3236(3)	0.5973(4)	0.0110(2)	1	81(7)
Zn6A	8b	0.6759(3)	0.0934(5)	0.4909(2)	1	147(10)
Zn7	8b	0.1873(3)	0.3807(4)	0.3896(2)	1	104(7)
Zn7A	8b	0.814(1)	0.8715(2)	0.1013(3)	1	129(3)
Zn8	8b	0.1172(1)	0.2946(2)	0.0994(2)	1	102(3)
Zn8A	8b	0.8803(4)	0.7988(4)	0.4014(2)	1	112(7)
Zn9	8b	0.3791(4)	0.7088(4)	0.2990(2)	1	114(7)
Zn9A	8b	0.6245(3)	0.2263(4)	0.2020(2)	1	119(6)
Zn10	8b	0.1835(3)	0.6180(4)	0.3127(2)	1	106(7)
Z10A	8b	0.8197(3)	0.0997(4)	0.1872(2)	1	111(8)
M11	8b	0.3202(1)	0.4142(2)	0.2893(1)	0.30(1) ^a	70(4)
M11A	8b	0.6759(2)	0.9092(3)	0.2105(2)	0.84(1) ^a	95(7)
Pt1	4a	0	0.2463(3)	0	1	49(2)
Pt2	4a	0	0.22212(8)	0.5999(2)	1	73(2)
Pt2A	4a	0	0.7216(2)	0.8984(1)	1	68(3)
Pt3	4a	0	0.7607(3)	0.70018(5)	1	56(3)
Pt3A	4a	0	0.2722(3)	0.8026(1)	1	102(3)
Pt4	8b	0.1819(1)	0.5789(1)	0.0983(2)	1	62(1)
Pt4A	8b	0.8199(1)	0.0840(1)	0.4076(1)	1	77(3)

^a sof of Zn, sof of (Pt) = 1 - sof of (Zn)

7.4 Physical properties of Pt₁₁Zn₃₂

7.4.1 Thermochemical analyses

Thermochemical analyses were carried out on the samples of nominal compositions of 24–24.5 at.% of Pt. The samples (30–50 mg) were pressed into small pellet and sealed in self-manufactured, evacuated silica crucibles. The silica crucibles are continuously heated up to 1320 K with a heating rate of 10 K min⁻¹. The Pt₁₁Zn₃₂ phase begins to melt nearly congruently at 1270 K. The peak maximum is found at 1284 K. To ensure reproducibility of the thermal events the experiments were usually repeated at least twice at heating and cooling rates of 10 K min⁻¹. A

typical thermogram of the sample as a function of temperature is shown in Fig. 7.1.

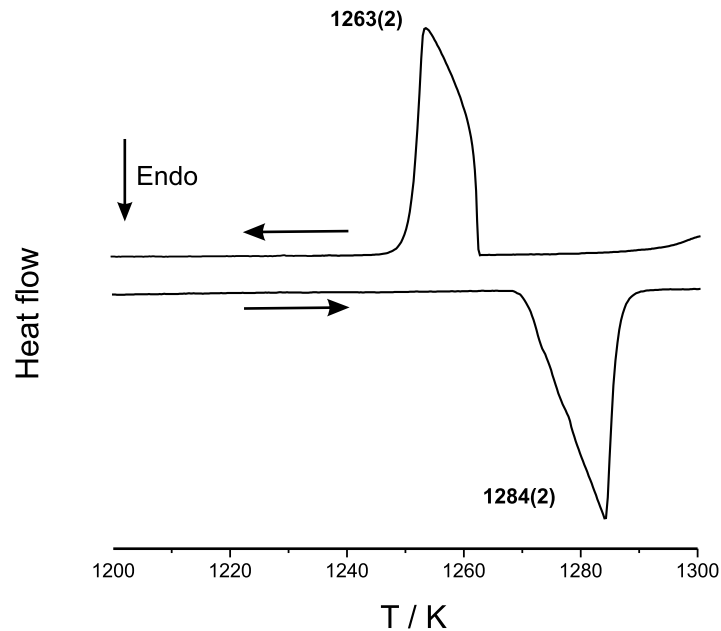


Figure 7.1: A typical thermogram of Pt₁₁Zn₃₂.

7.4.2 Magnetic susceptibility

Magnetic susceptibilities of polycrystalline samples were recorded with a SQUID magnetometer in the temperature range 1.8–300 K at a magnetic flux density of 1 Tesla. The data were corrected for diamagnetic contributions of the sample holder manufactured from KLF (Polytetrafluoroethen). The Pauli paramagnetism of the metallic phase is found to be overcompensated by the core diamagnetism of its constituents. The value obtained was found to be $-1.52 \times 10^{-10} \text{ m}^3 \text{ mol}^{-1}$ for $\frac{1}{11+32} \text{ Pt}_{11}\text{Zn}_{32}$. The molar susceptibility of Pt₁₁Zn₃₂ as a function of temperature is shown in Fig. 7.2.

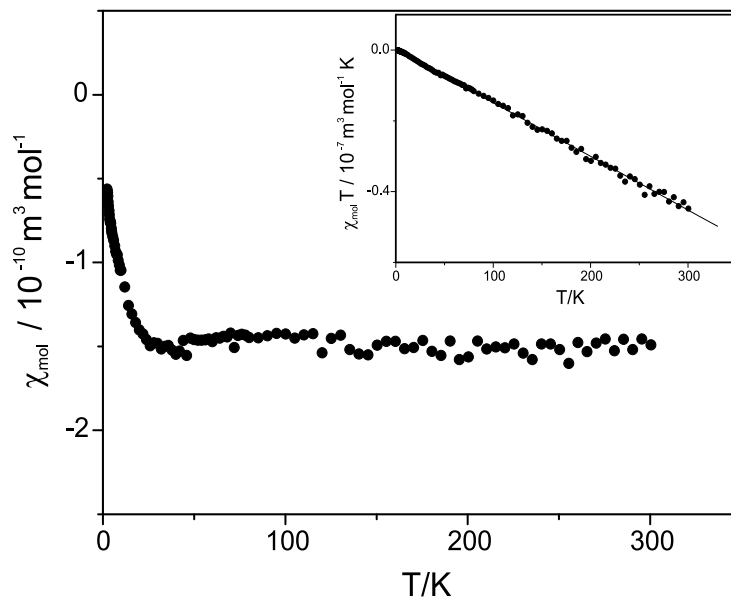


Figure 7.2: Molar magnetic susceptibility as a function of temperature for $\frac{1}{11+32}$ Pt₁₁Zn₃₂.

7.5 Results and discussion

The structure of Pt₁₁Zn₃₂ crystallizes in a C-centered orthorhombic cell, space group Cmce (No. 64). The lattice parameters are: $a = 1290.2(4)$, $b = 910.3(4)$ and $c = 2120.3(6)$ pm. The unit cell accommodates 172 atoms. The Pearson symbol is oC172. The lattice is related to that of γ -brass type Pt₂Zn₁₁ [75] according to $a_o \approx \sqrt{2} a_\gamma$, $b_o \approx a_\gamma$, and $c_o \approx 5 \sqrt{2} \frac{a_\gamma}{3}$.

The volume of the orthorhombic phase Pt₁₁Zn₃₂ offers space for 180 atoms per unit cell, consequently, 8 positions in the unit cell are vacant. Thus, the vacancy concentration is increased to $\frac{2}{45}$ compared to $\frac{1}{27}$ for the γ -phase (cI52). The γ -phase in turn can be seen as a $3 a_\beta \times 3 a_\beta \times 3 a_\beta$ superstructure of a β -brass type structure with two out of 54 positions being vacant, one at the origin and another at the centre of the triply expanded cubic unit cell [75]. The structural kinship is substantiated by group-subgroup relations existing between the symmetry of a β -brass type structure and that of Pt₁₁Zn₃₂.

As seen from Fig. 7.3 the symmetry path between the β -brass aristo-type and the Pt₁₁Zn₃₂ structure includes six minimal symmetry reductions. The letter assigned to each pair of group symbols indicates the type of symmetry reduction, i stands for isomorphic, t for translationengleich, and k for klassengleich [82]. The number in brackets refers to the index of the symmetry reduction

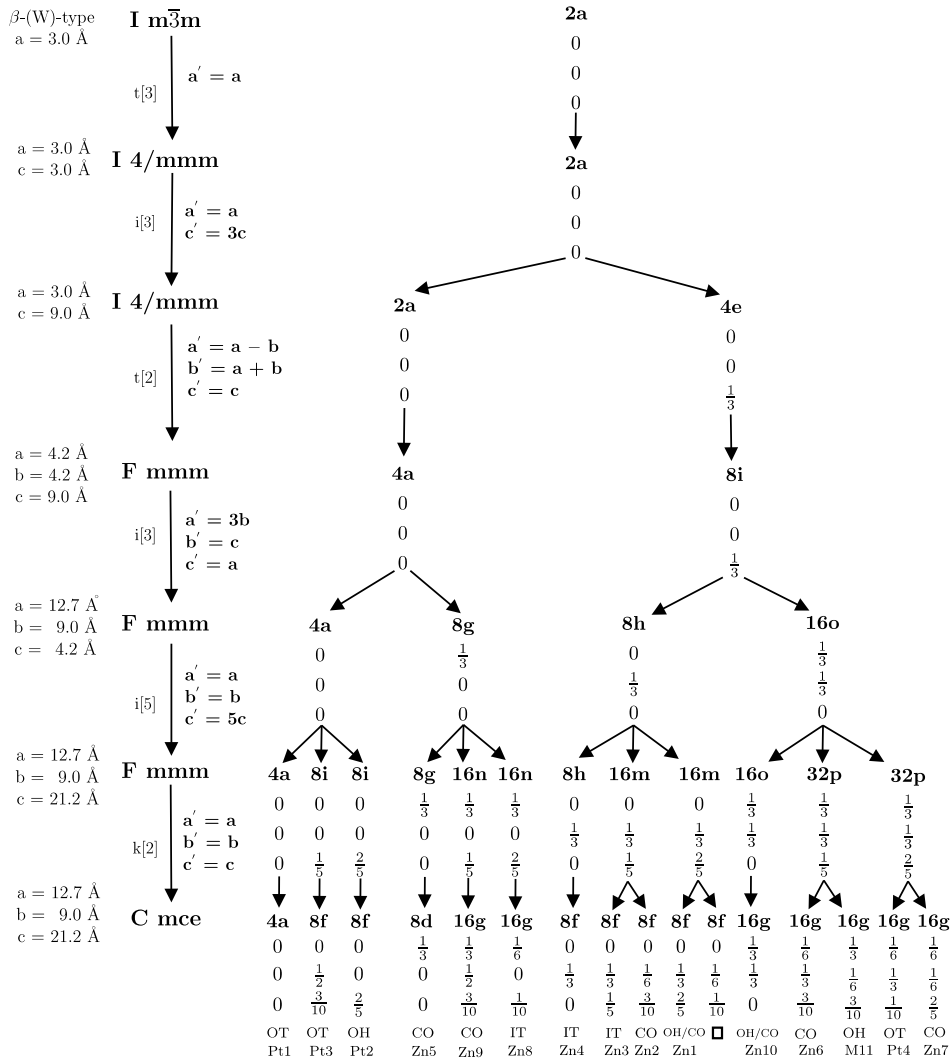


Figure 7.3: Group-subgroup relations between the Pt₁₁Zn₃₂ structure and the aristo-type β -brass type structure.

which corresponds to the factor by which the number of translation and/or rotational symmetry operations are reduced in the subsequent subgroup relative to the preceding group. Included in the scheme are also the atomic sites and idealized positional parameters of the atoms of a β -brass type structure in the setting of the respective space group. The final member in the genealogical symmetry tree [82] corresponds to the symmetry of Pt₁₁Zn₃₂. The derived positional parameters are clearly related with the true parameters of Pt₁₁Zn₃₂ listed in Table 7.2. The difference between corresponding parameters of the two parameter sets provides a measure of the distortion associated with the ordering of the vacancies. Note, that the Wykoff position 8f at $0, \frac{1}{6}, \frac{1}{10}$ is unoccupied. In the cubic γ -phase the arrangement of the vacancies complies with the principle of maximal self-avoidance. There, the voids are separated by the maximal distance of $\frac{3}{2} \sqrt{3} a_\beta$. In

the orthorhombic structure of Pt₁₁Zn₃₂ the vacancies converge pair-wise as close as $\sqrt{3} a_\beta$, 519.1 pm.

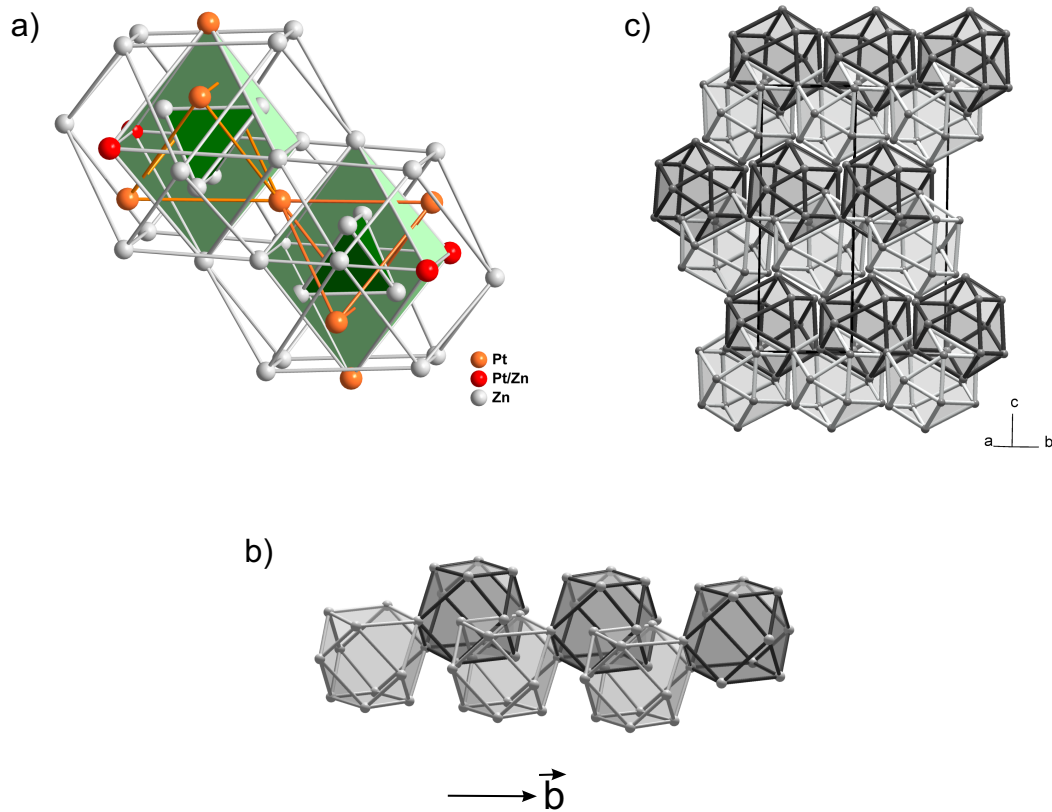


Figure 7.4: (a) A pair of single interpenetrating γ -brass type clusters consisting of 45 atoms. (b) The γ -brass type clusters are condensed into chains along [010] by sharing edges. (c) The chains of condensed clusters piled up along [110] form a dense packed array. Only the cuboctahedral shells of the cluster is shown for the clarity.

Subsequently, the structure is analyzed with respect to the impact of the increased vacancy concentration for Pt₁₁Zn₃₂ on the packing of the salient structural motif common to both structures, an agglomerate of 26 atom encasing a vacancy. This so-called γ -cluster displays an extended concentric fragment of a β -brass type structure for which the vacancy at the centre gives rise to a coherent distortion: Eight atoms which are originally situated at the corner of a cube next to the centre at a distances of $\frac{1}{2} \sqrt{3} a_\beta$ split into two tetrahedral sets. Four atoms situated at the vertices of an inner tetrahedron (IT) are closer to the center than the rest defining an outer tetrahedron (OT). Six further atoms which are about a_β apart from the void are located above the six faces of the distorted cube built up by IT and OT atoms. They form an octahedron (OH). Twelve outer atoms situated at the vertices of a distorted cuboctahedron (CO) complete the cluster. Their

ideal distance from the void is $\sqrt{2} a_\beta$.

In the structure of γ -Pt₂Zn₁₁ the Pt atoms occupy exclusively the OT site resulting in Pt₄Zn₂₂ clusters which are arranged like W atoms in bcc-W. In the Pt₁₁Zn₃₂ structure the atoms of the minority component occupy additionally two out of six OH positions in an ordered way whereas a third OH position is statistically occupied by Pt and Zn in almost equal proportions. Quite characteristically for Pt₁₁Zn₃₂, the resulting Pt_{6.5}Zn_{19.5} clusters interpenetrate pair-wise by sharing a Pt atom of the OH site. As illustrated in Fig. 7.4 the conjoint cluster pairs are fused into chains parallel [010] by sharing edges according to $\frac{1}{\infty}[\text{Pt}_{11}\text{Zn}_{30} \text{Zn}_{4/2}]$. The chains are arranged along c into layers which in turn pile up along [110], see Fig. 7.4b. Thus, contrary to an ordinary γ -phase, the clusters in Pt₁₁Zn₃₂ are not only connected to each other but - concomitant with the increased vacancy concentration - partly interpenetrate or share edges. The three modes of cluster arrangements in Pt₁₁Zn₃₂ give rise to three distinct distances between next vacancies: 519.1(1) pm for two interpenetrating clusters, 746.0(1) pm for condensed clusters, and 792.7(1) pm for adjacent clusters in contiguous chains. This values concur with $\sqrt{3} a_\beta$, $3\frac{\sqrt{3}}{2} a_\beta$ and $2\sqrt{2} a_\beta$ for an idealized defective β -brass type structure, if we replace a_β by 303 pm corresponding to $\frac{1}{3} a_\gamma$ (Pt₂Zn₁₁ [75]).

So far, the γ -brass derivative structure of Pt₁₁Zn₃₂ has been analysed with respect to W-type structure in terms of symmetry, atomic decoration and vacancy ordering. The vacancies trigger a change of the local atomic arrangement from dodecahedral towards icosahedral coordination. Hence, a detailed analysis may provide insight into how a bcc-like structure can rearrange displacively into a complex structure with atomic coordination configurations complicating an integration into a lattice.

All members of the new γ -brass related structure family can be generated by starting from the β -brass (W) structure type. The transformation from the elemental bcc to a pentagonal anti-prismatic columnar structure can be formally be subdivided into the following steps:

- i) The starting point is a suitable extended array of two consecutive atomic layers of a bcc-type structure arranged along a face diagonal of the cubic lattice. To be consistent with the setting of the orthorhombic lattice of the γ -brass related structures we chose a projection

along, e.g., [01 $\bar{1}$] in Fig. 7.5a.

- ii) In a first step the atoms located inside the blue ellipsoids ($\frac{2}{9}$ of all atoms) are cooperatively shifted pair-wise within the plane towards each by $\frac{1}{4} a_{bcc}$ ($= \frac{1}{12} a_\gamma$) along $\pm [010]$ and simultaneously by $\frac{1}{4}\sqrt{2} a_{bcc}$ perpendicular to the plane.
- iii) The described atomic displacements are fostered by additional atomic moments of $\frac{4}{9}$ of the atoms within the plane as indicated by black and light gray arrows resulting in ribbons of edge- and vertex sharing pentagons. Note that pentagons in contiguous rows and layers are in anti-parallel orientation. Moreover, the described co-operative atomic movements imply that the repeat distance of the atoms inside the pentagonal anti-prismatic columns. This particular displacive transformation of a tungsten type structure results in a hitherto unknown pentagonal anti-prismatic columnar structure (depicted as projection in Fig. 7.5b) with the following metrical characteristics: $a = 3 a_{bcc}$, $b = 3\sqrt{2} a_{bcc}$, $c = \sqrt{2} a_{bcc}$, Pearson symbol oF36.

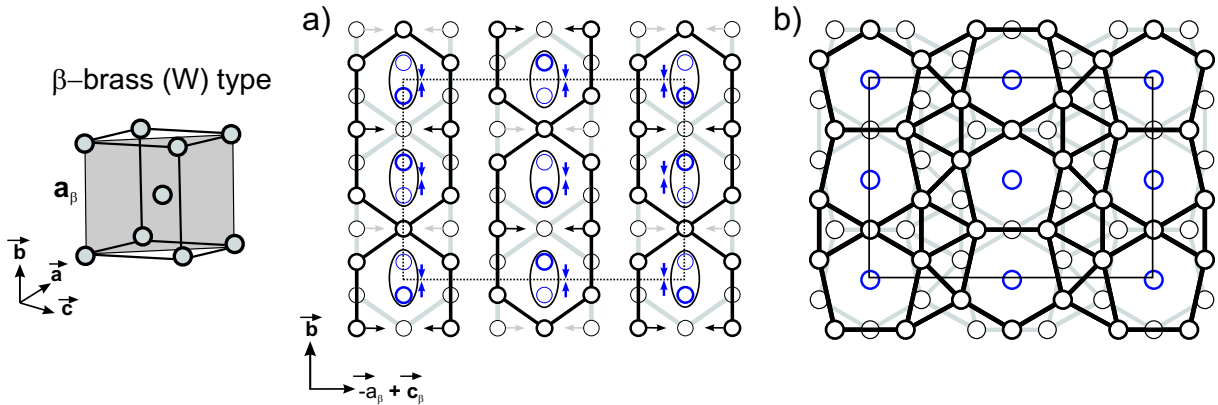


Figure 7.5: A schematic illustration of the construction of the pentagonal antiprismatic columnar structure starting from the β -brass type structure.

- iv) The structures we found lack of a specific fraction ‘f’ of atoms in the interior of the pentagonal anti-prismatic columns. The voids imply that the structures relax in a characteristic manner. The length of the repeat distance along the columns depends upon the missing fraction.

In the case of the Pt₁₁Zn₃₂ structure the fraction $f = \frac{2}{10}$, *i.e.* two out of ten atoms per repeat unit inside the pentagonal columns are missing. An appropriate section of the relaxed structure of Pt₁₁Zn₃₂ is shown in Fig 7.6b. Adjacent atoms are connected by lines in order to emphasize

the distorted octahedral and tetrahedral arrangement of the atoms in the inter-columnar region. These extra atoms convert the columns of face-sharing pentagonal anti-prisms into strands of interpenetrating M13 icosahedrons. Accordingly, the arrangement of the central atoms of the M13 icosahedrons results from merging two rows of atoms of the W-type structure into a single row in the distorted structure. This particular set of atoms is highlighted in the structural sections shown in Fig 7.6c. All other atoms are arranged in rows with $n = 5$ atoms within the repeat unit $c = 5 \sqrt{2} a_\beta = 2126.3(4)$ pm.

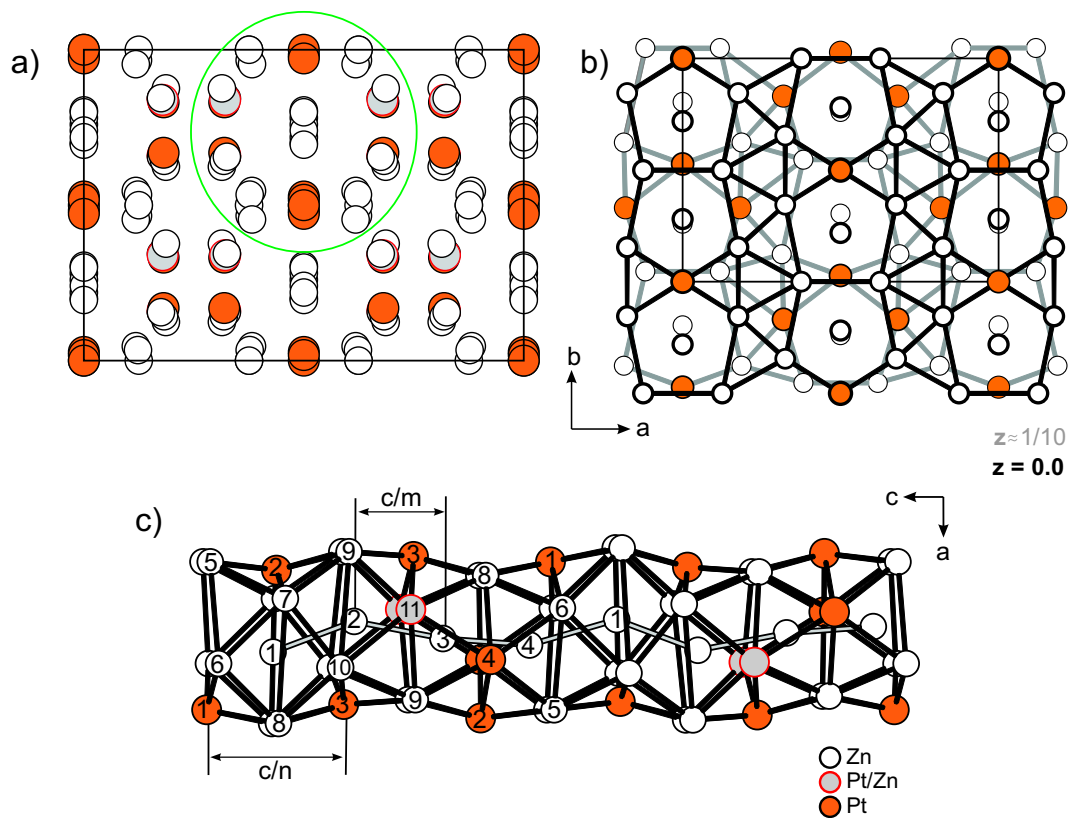


Figure 7.6: a) Unit cell of Pt₁₁Zn₃₂ structure viewed along [001] direction. The encircled atoms represent the pentagonal anti-prismatic column. b) Two pentagonal anti-prismatic frames at the heights $z = 0$ and $\frac{1}{10}$, respectively. c) A structural motif, the pentagonal anti-prismatic column with a zig-zag chain of Zn atoms inside. The labels c/m and c/n refers to the two sublattice which give rise to a mismatch between the chimney and the ladder, where c signifies the long axis of the unit cell.

Up to now the impact of the eight vacancies per unit cell on the structure has been neglected. The vacancies are located within the central atomic chains extending inside the pentagonal anti-prismatic columns. Since there are four such columns per unit cell, (c.f. Fig. 7.6c) each central chain contains only eight instead of ten Zn atoms within the repeat unit leaving in the average

every fifth pentagonal anti-prism empty. Nevertheless, the atoms are nearly equally spaced at a distance of about $\frac{5}{8} \sqrt{2} a_\beta$ ($268.7(1) \text{ pm} \leq d \leq 281.1(1) \text{ pm}$). Consequently, the spacing does not simply match with the sublattice of the columnar framework. This particular mismatch is a salient structural feature of Pt₁₁Zn₃₂. In the γ -phase the ratio of the repeat distance of the two distinct sublattices is $\frac{3}{5}$, for Pt₁₁Zn₃₂ the misfit seems to lock in at $\frac{5}{8}$. At slightly different compositions the ratio may be irrational resulting in an incommensurate structure. Some transition metal silicides and germanides, the so-called Nowotny chimney-Ladder structures, show similar structural characteristics [97, 98]. They are composed of an interior helical substructure - the ladder - built up by atoms of a main group element and a surrounding β -tin-type framework - the chimney - formed by transition metal atoms, both substructures exhibiting their own translational symmetry. In Pt₁₁Zn₃₂, the chimney corresponds to a pentagonal antiprismatic Pt₁₁Zn₂₄ columnar framework. The ladder is formed by the residual Zn atoms arranged into zigzag chains inside the columns. The mismatch of the two sublattices depends upon the vacancy concentration which, by all indications, is affected by the Pt/Zn ratio in the columnar framework. Accounting to the short distances ($265.2(1) \leq d \leq 293.2(1) \text{ pm}$) the atoms of the two substructures interact strongly. Thus, the γ -brass derivative Pt₁₁Zn₃₂ represents a unique type of a composite structure.

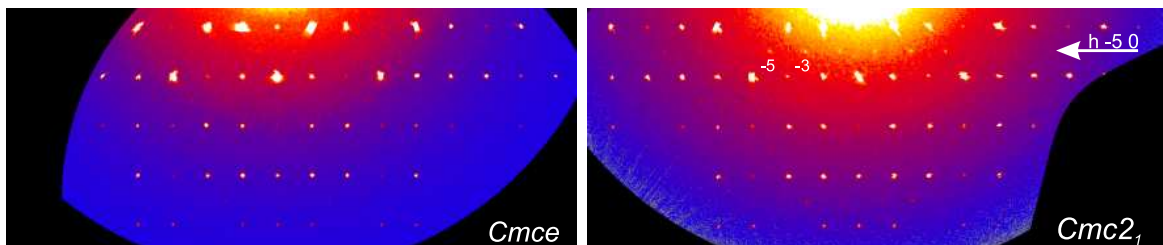


Figure 7.7: A reciprocal space section of $hk0$ for the phase Pt₁₁Zn₃₂. Left: Reciprocal section obtained for the crystal annealed at 970 K (as synthesized). Right: Reciprocal section obtained for the crystal which is annealed at 770 K for 7 days.

In accordance with the high degree of structural differentiation there is little disorder in Pt₁₁Zn₃₂. Only one out of 15 crystallographic sites seems to be statistically occupied by Pt and Zn. The site is found to be occupied by 47(1)% Pt and 53% Zn yielding an overall composition of Pt_{10.8}Zn_{32.2(1)}. Structure analyses of three different crystals produced coincident results indicating a barely detectable homogeneity range for the phase. For sake of simplicity, the phase Pt_{10.8}Zn_{32.2} has been named as Pt₁₁Zn₃₂. Extended annealing of the crystals at 770 K was found to trigger a phase

transition which shows up in additional weak reflections violating the e-glide operations of Cmce, cf. Fig. 7.7. Two structure refinements in space group Cmc2₁ revealed a partial annihilation of the substitutional disorder as a possible driving force for the transition. A significant enrichment of Pt (70%) and Zn (86%) was found on the two symmetrically independent sites of Cmc2₁ into which the single mixed-occupied site of Cmce splits, see Table 7.4.

As seen from the intensity distribution in the *0kl* and *h0l* section of the reciprocal lattice (c.f. Fig. 7.8) many intensities are very weak or absent along *c**. This is a typical feature of modulated structures [72, 99]. For Pt₁₁Zn₃₂ the periodicity along the modulation accounts to 2126.3 pm and is metrically related to the face diagonal of a β -brass type structure.

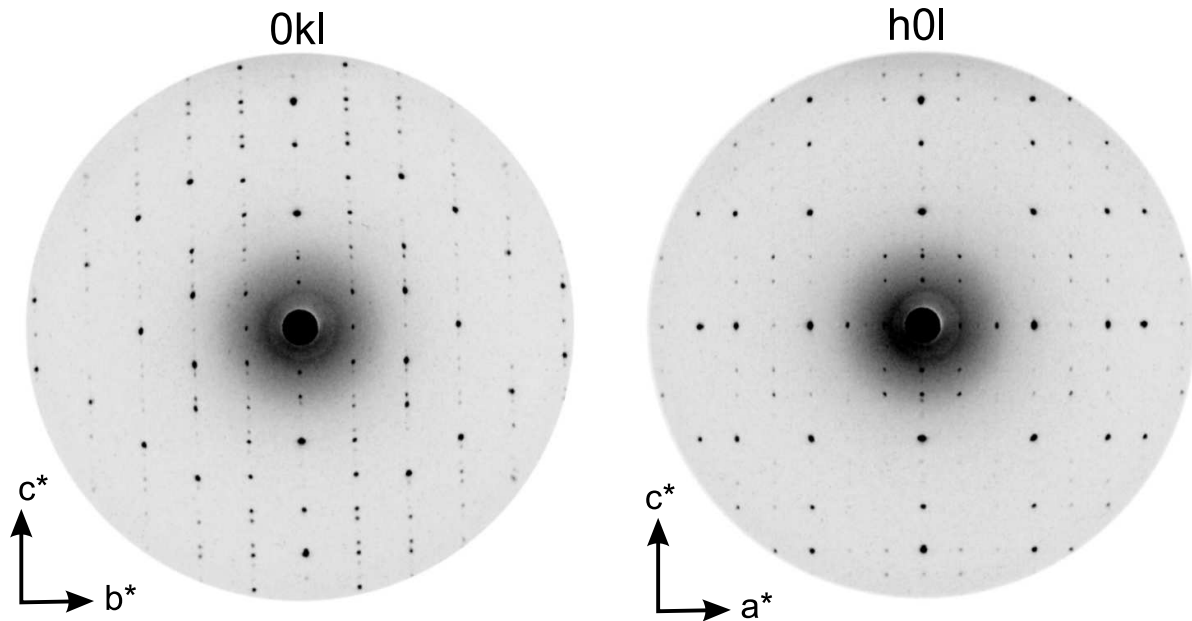


Figure 7.8: Precession diffraction photographs from the *0kl* and *h0l* reciprocal space section plans of Pt₁₁Zn₃₂ (Cmce).

7.6 Summary

- Adjacent to γ -brass type related Pt₅Zn₂₁ [68] the Pt-Zn system accommodates a series of structurally complex phases. They are situated in a narrow phase field extending from $0.24 < x_{\text{Pt}} < 0.265$, very close to the field which previously was believed to host a cubic γ -brass type structure of approximate composition Pt₃Zn₁₀ [13].
- Pt₁₁Zn₃₂ is the first member with the shortest translation period of a series of orthorhombic structures.
- Pt₁₁Zn₃₂ crystallizes in the space group Cmce with 172 atoms in the unit cell. One out of 15 distinct crystallographic sites is found to be statistically occupied by Pt (47%) and Zn (53%).
- Annealing of the phase at 773 K triggers a reduction of the substitutional disorder. The phase transformation is reflected in the appearance of additional reflections which are incompatible with an a-glide operation perpendicular to the c-axis.
- The structure of Pt₁₁Zn₃₂ represents a γ -brass type related, vacancy-ordered derivate of the elemental body centred cubic atomic arrangement. The interrelations are demonstrated quantitatively by means of a group-subgroup analysis. Contrary to other brass-like systems the vacancy concentration increases from $\frac{2}{27}$ for Pt₅Zn₂₁ to $\frac{2}{43}$ for Pt₁₁Zn₃₂ parallel with cumulative valence electron concentration. As a consequence the voids are no more isotropic dispersed in Pt₁₁Zn₃₂ but accumulate in chains of Zn atoms extending along pentagonal anti-prismatic columns. The columnar substructure is connected into a three-dimensional porous framework. An inherent mismatch of the repeat distance of the basic unit of the framework and the inter-atomic mean distance in the chain confers the structure a composite character.

Chapter 8

General characteristics of γ -brass related phases

The lattices of the structures under consideration may be regarded as superlattices of the W-type body centered cubic (bcc) unit cell. Each of the metrical relations can be expressed by a basic transformation of the form:

$$\begin{aligned}\mathbf{a} &\approx 3 \mathbf{a}_{bcc} \\ \mathbf{b} &\approx 3 \sqrt{2} \mathbf{a}_{bcc} \\ \mathbf{c} &\approx n \sqrt{2} \mathbf{a}_{bcc}.\end{aligned}$$

Thus, structures of this type are identified by an integer 'n' commonly the quantity of an increment into which the only variable lattice vector of these structures can be subdivided uniformly. Accordingly, n is the next nearest integer nint of an axial ratio:

$$n = \text{nint}\left[3 \left(\frac{b}{c}\right)\right]$$

Furthermore, the number N_0 of atoms per unit cell for a complete set of bcc arrangement is related to n and is given by

$$N_0 = 36 n$$

The above relation implies 2 atoms per volume increment a_{bcc}^3 . Once, the actual number N of atoms per unit cell for the structure is known, the integral number v of vacancies relative to the bcc arrangement can be calculated:

$$v = 36n - N$$

According to the meaning of n , another integer m can be defined by:

$$m = 2n - \frac{v}{4}$$

Considering the presently known structures of this family, n and v (or m) are bound to some restrictions:

- i) Each value of n is associated with one and only one value of v .
- ii) There are not more than two linearly independent pairs (n_i, v_i) . All other pairs can be obtained by linear combination of two basic pairs:

$$n_i = p n_1 + q n_2$$

$$v_i = p v_1 + q v_2,$$

where $p, q \geq 0$

The chosen numbers are:

$$n_1 = 3 \quad n_2 = 5$$

$$v_1 = 4 \quad v_2 = 8$$

The pair of numbers mark γ -Pt₂Zn₁₁ (oF104) and Pt₁₁Zn₃₂ (oC172). Note, that the cubic lattice of γ -Pt₂Zn₁₁ has been transferred into an adequate orthorhombic setting.

Table 8.1 summaries characteristic quantities of γ -brass type Pt₂Zn₁₁ and those of five identified related phases and of three intermediate possible structural candidates. In addition to the items defined above the normalized volume $\frac{V}{N}$, the mole fraction x_{Pt} , the valence electron concentration vec , and the valence concentration $\frac{v}{N_0}$ have been inserted into the table.

Table 8.1: Summary of crystallographic and chemical data for γ -brass related phases in the Pt-Zn binary system

	cI52	oC172	oC276	oC380 [§]	oF448 [§]	–	–	–	oF656 [§]
n	3	5	8	11	13	14	17	18	19
N	104	172	276	380	448	484	588	620	656
N ₀	108	180	288	396	468	504	612	648	684
v	4	8	12	16	20	20	24	28	28
m	5	8	13	18	21	23	28	29	31
p	1	0	1	2	1	3	4	1	3
q	0	1	1	1	2	1	1	3	2
Space group [†]	F2mm*	Ccme	Ccme	Ccme	F2mm	–	–	–	F2mm
a / pm	908.19(4)	910.3(4)	911.24(7)	910.2(2)	911.02(9)	–	–	–	910.2(1)
b / pm	1284.4(4)	1290.2(4)	1293.04(13)	1291.5(3)	1290.7(1)	–	–	–	1292.6(1)
c / pm	1284.4(4)	2120.3(6)	3408.0(3)	4706.7(9)	5527.8(4)	–	–	–	8095.7(3)
$\frac{V}{N}$ 10 ⁶ pm ³	14.41	14.48	14.5	14.56	14.51	–	–	–	14.52
Formula	Pt ₂ Zn ₁₁	Pt _{43.5} Zn _{128.5(1)}	Pt _{71.7} Zn _{204.3(1)}	Pt _{100.4} Zn _{279.6(2)}	Pt _{108.8} Zn _{339.2(2)}	–	–	–	Pt _{172.3} Zn _{483.7(1)}
x _{Pt} [%]	15.4	25.3	26.0	26.4	24.3	–	–	–	26.3
<i>vec</i>	1.61	1.49	1.48	1.47	1.51	–	–	–	1.47
m/n	1.667	1.60	1.625	1.636	1.615	1.643	1.647	1.611	1.632
$\frac{v}{N_0}$ [%]	3.70	4.44	4.17	4.04	4.27	3.97	3.92	4.32	4.09

* unconventional orthorhombic setting of cubic γ -Pt₂Zn₁₁ phase. The transformation is shown below,

$$\bar{I}43m \xrightarrow{t[3]} \bar{I}42m \xrightarrow[a' = a-b, b' = a+b, c' = b]{t[2]} Fmm2 \xrightarrow[a' = -c, b' = b, c' = a]{} F2mm$$

[†] A standard space group setting for corresponding structure.

[§] Atomic parameters and details on data collections are given in the appendix.

Chapter 9

Pt₁₈Zn₅₁ - A γ -brass related composite structure

9.1 Structure determination

X-ray diffraction studies were carried out with a single crystal (nominal composition of 26 at.% Pt) of $0.14 \times 0.15 \times 0.10 \text{ mm}^3$ size on an IPDS-II diffractometer. The collected reflections were subjected to Lorentz polarization and numerical absorption corrections using the programs X-SHAPE and X-RED [61, 62]. Subsequently, the structure was solved in space group Cmce (No. 64) by applying direct methods using the program SHELX-97 [58] based on $|F|^2$. The final refinement cycles using anisotropic displacement parameters converged at residual value $R1 = 0.0532$ for 1985 with $I_o > 2\sigma(I_o)$ out of 2857 reflections for 175 variables. The details concerning crystallographic data are tabulated in Table 9.1. The positional parameters and anisotropic displacement parameters are gathered in Table 9.2 and 9.3.

The structure was confirmed by a refinement of a data set of the second crystal selected from a sample of nominal composition 26 at.% Pt. (Independent batch). The lattice constants for second crystal are obtained from IPDS-I. The lattice parameters are as following; $a = 1292.9(2)$ pm, $b = 911.4(1)$ pm and $c = 3403.4(7)$ pm.

Table 9.1: Crystallographic and technical data for the single-crystal structure determination

Sum formula	Pt _{17.9} Zn _{51.1(1)}
Space group (No.)	Cmce (64)
Z	4
a / pm	1293.04(13)
b / pm	911.24(7)
c / pm	3408.0(3)
V / 10 ⁶ pm ³	4015.5(6)
Molar mass / g mol ⁻¹	6845.25
ρ_{cal} / g cm ⁻³	11.323
μ / mm ⁻¹	92.17
<i>Data collection</i>	
Crystal size / mm ³	0.14 × 0.15 × 0.10
Diffractometer	IPDS-II (STOE & Cie)
Temperature / K	293(2)
Radiation / monochromator	MoK α / Graphite
Distance crystal-IP / mm	100
ϕ ; $\omega_{min} - \omega_{max}$; $\Delta\omega$	0; 0–180; 1
ϕ ; $\omega_{min} - \omega_{max}$; $\Delta\omega$	165; 60–160; 1
$2\theta_{max}$ / °	60.0
Collected reflections	–17 ≤ h ≤ 17 –12 ≤ k ≤ 12 –47 ≤ l ≤ 46
Total No. of reflections	30538
<i>Data reduction</i>	
Program	IPDS-II-Software [57]/X-RED [61]
Absorption correction	X-SHAPE [62], Numerical
Max. / Min.transmission	0.0547 / 0.0094
Unique reflections	2857
R _{int}	0.1257
<i>Refinement</i>	
Program	SHELXL-97 [58]
Refined on	F _o ²
Reflections I _o > 2σ(I _o)	1985
Variables	175
R ₁ (I _o > 2σ(I _o))	0.0532
R ₁ (all)	0.0715
wR ₂ (all)	0.1208
Goodness of fit	1.181
$\Delta\rho_{max} / \Delta\rho_{min} / 10^{-6}$ e pm ⁻³	3.922 / –3.577
Extinction coefficient	0.000106(6)

$$1/w = [\sigma^2(F_o^2) + (0.0356(\text{Max}(F_o^2, 0) + 2F_c^2)/3)^2 + 519.52(\text{Max}(F_o^2, 0) + 2F_c^2)/3]$$

Table 9.2: Positional and equivalent isotropic displacement parameters $U_{eq}(\text{pm}^2)$ for Pt₁₈Zn₅₁

Atom No.	Wy.	x	y	z	sof	U_{eq}
Zn1	4a	0	0	0	1	181(7)
Zn2	8f	0	0.4596(3)	0.42233(9)	1	175(5)
Zn3	8f	0	0.0519(3)	0.15424(9)	1	159(5)
Zn4	8f	0	0.4462(3)	0.27207(9)	1	205(5)
Zn5	8f	0	0.0082(3)	0.30712(9)	1	205(6)
Zn6	8f	0	0.0248(3)	0.38498(8)	1	161(5)
Zn7	8f	0	0.4435(3)	0.03566(8)	1	151(5)
Zn8	16g	0.1205(2)	0.2020(2)	0.03181(6)	1	169(4)
Zn9	16g	0.1252(1)	0.2377(2)	0.40720(6)	1	164(4)
Zn10	16g	0.1775(1)	0.0916(2)	0.10119(5)	1	103(3)
Zn11	16g	0.1864(1)	0.3694(2)	0.34056(7)	1	191(4)
Zn12	16g	0.1171(1)	0.29286(2)	0.15643(6)	1	167(4)
Zn13	16g	0.1814(2)	0.1058(2)	0.21124(6)	1	225(4)
Zn14	16g	0.1238(2)	0.2139(2)	0.28016(6)	1	187(4)
Zn15	16g	0.1729(2)	0.4022(2)	0.08781(7)	1	229(4)
Zn16	16g	0.1863(1)	0.1191(2)	0.47658(6)	1	134(2)
Pt1	8f	0	0.22031(9)	0.46973(2)	1	120(2)
Pt2	16g	0.18065(2)	0.41469(6)	0.46252(2)	1	111(2)
Pt3	8f	0	0.2449(1)	0.09327(3)	1	111(2)
Pt4	8f	0	0.27483(8)	0.34295(3)	1	123(2)
Pt5	8f	0	0.2285(1)	0.21844(2)	1	136(2)
Pt6	16g	0.18154(4)	0.07695(6)	0.34610(3)	1	132(2)
M7	16g	0.17981(8)	0.4091(1)	0.22543(3)	0.52 ^a	144(4)

^a sof of Zn, sof of (Pt) = 1 – sof of (Zn)

Table 9.3: Anisotropic displacement parameters U (pm²) for Pt₁₈Zn₅₁

Atom No.	U11	U22	U33	U12	U13	U23
Zn1	143(16)	137(15)	260(20)	0	15(14)	0
Zn2	169(11)	132(11)	222(13)	0	29(9)	0
Zn3	205(12)	112(10)	160(11)	0	21(9)	0
Zn4	203(13)	160(12)	251(14)	0	-82(10)	0
Zn5	173(13)	229(13)	213(13)	0	-69(11)	0
Zn6	120(11)	121(11)	241(13)	0	57(9)	0
Zn7	218(12)	110(10)	126(11)	0	-2(8)	0
Zn8	193(8)	173(8)	140(8)	56(7)	11(6)	29(6)
Zn9	172(8)	167(8)	153(8)	2(7)	-26(6)	6(6)
Zn10	87(6)	101(6)	122(7)	25(6)	-4(6)	-7(6)
Zn11	149(7)	146(8)	279(10)	-35(6)	1(7)	12(8)
Zn12	186(8)	178(7)	138(8)	-48(6)	0(7)	7(7)
Zn13	191(8)	270(10)	214(10)	75(8)	21(8)	38(7)
Zn14	176(9)	255(9)	130(8)	22(7)	28(7)	-2(6)
Zn15	219(10)	265(10)	202(9)	-78(8)	-28(8)	51(7)
Zn16	94(6)	144(7)	164(8)	27(6)	-1(6)	0(6)
Pt1	102(4)	111(3)	149(4)	0	-12(3)	0
Pt2	119(3)	117(3)	97(3)	-26(2)	-9(2)	8(2)
Pt3	107(3)	105(3)	122(3)	0	-1(2)	0
Pt4	103(3)	107(3)	159(4)	0	29(3)	0
Pt5	118(4)	160(4)	130(4)	0	-21(3)	0
Pt6	123(3)	124(3)	149(3)	20(2)	4(2)	1(2)
M7	142(5)	137(5)	153(5)	-13(3)	9(3)	9(3)

9.2 Results and discussion

9.2.1 Phase relations

Pt₁₈Zn₅₁ crystallizes in the orthorhombic, centrosymmetric space group Cmce (No. 64). The lattice parameters are $a = 1293.04(13)$, $b = 911.24(7)$ and $c = 3408.0(3)$ pm, $Z = 4$, Pearson symbol oC276. In view of the metrical relation with the β -brass type structure, the structure of Pt₁₈Zn₅₁ can be classified as an ordered $3\sqrt{2} a_\beta \times 3 a_\beta \times 8\sqrt{2} a_\beta$ defect variant of index 144 with 12 vacancies per unit cell.

The structure Pt₁₈Zn₅₁ is isotypic to NiZn₃ [12]. Both Pt₁₈Zn₅₁ and NiZn₃ can be described as a γ - or β -brass related structure with ordered vacancies. The volume of the orthorhombic phase provides space for 288 atoms per unit cell. Comparison with the Pearson symbol reveals 12 vacant positions in the unit cell.

In the γ -brass type structures, the vacancy concentration ($\frac{v}{N_0}$) increases with increasing valence electron concentration (vec). This trend was observed in the Cu-Ga and Cu-Al systems by Hume-Rothery and co-workers [100]. In contrast, the vacancy concentration increases with decreasing valence electron concentration in the γ -brass related phases in the Pt-Zn system. The values of $\frac{v}{N_0}$ and vec for the structure of Pt₁₈Zn₅₁ are $\frac{1}{24}$ and 1.48, respectively. For calculating vec , the valence for Pt is taken to be zero and two for Zn. These assigned values are chosen according to Hume-Rothery's rule.

The single crystal and powder diffraction analyses showed that the homogeneity of the phase seems to be narrow. At the Pt-rich border the phase coexist with Pt₄₃Zn₁₂₁, a γ -brass related structure with 656 atoms in the F-centered orthorhombic cell. On the other hand, at Zn-rich side the phase coexist with Pt₁₁Zn₃₂.

9.2.2 Structural description

The complex γ -brass related phase Pt₁₈Zn₅₁ is composed of 276 atoms distributed over 23 distinct atomic sites. 16 atomic positions are occupied by Zn atoms and 6 by Pt atoms. Only one out of 23 crystallographic sites seems to be statistically occupied by Pt and Zn. Accordingly, the site is found to be occupied by 48(1)% Pt and 52% Zn yielding an overall composition of Pt_{17.9}Zn_{51.1(1)}.

The structure of Pt₁₈Zn₅₁ can be lucidly described in terms of pentagonal anti-prismatic columns parallel to [001]. This approach of describing the structure is opted to establish structural relations with other existing γ -brass related phases. Moreover, this kind of structural features are generally observed in γ -brass [101] and related phases as described in the earlier chapter 7.

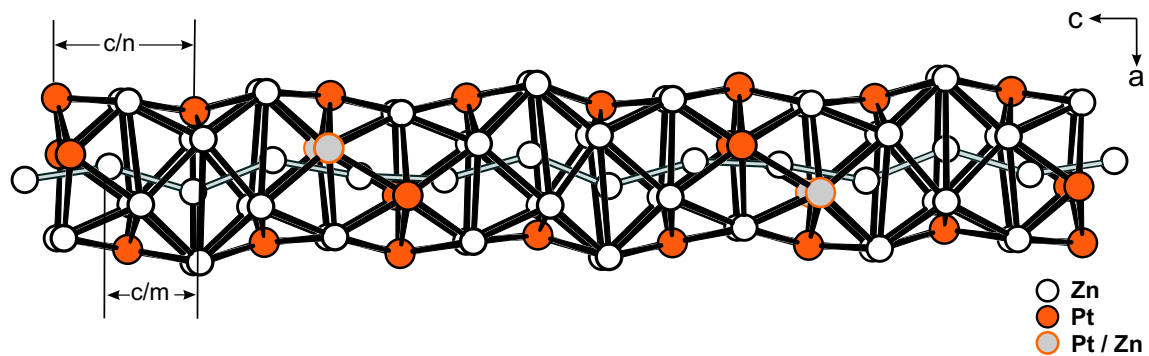


Figure 9.1: A structural motif of the Pt₁₈Zn₅₁ structure. The pentagonal anti-prismatic column with a zig-zag chain of Zn atoms. The labels c/m and c/n refers to the two sublattices which give rise to a mismatch between the chimney and the ladder, where c signifies the long axis of the unit cell.

Fig. 9.1, depicts a single pentagonal anti-prismatic column with a zig-zag chain of Zn atoms extended inside. The presence of ordered vacancies are common features of γ -brass and related phases. In the Pt₁₈Zn₅₁ structure the vacancies are accumulated inside the columns. There are 12 ordered vacancies per unit cell. The vacancies are distributed over four columns, where each column accommodates 3 vacancies per repeating distance. The chain of Zn atoms inside the columns is slightly puckered. For a clear understanding, the structure is sub-divided into two entities with reference to the Nowotny's chimney-ladder phases [97, 98]. The pentagonal anti-prismatic frame forms a so-called "chimney" and the Zn atoms form of a "ladder" inside the chimney. In spite of the vacancies the Zn atoms inside the column are nearly equally spaced at a distance of 264.0 – 280.4 pm. Consequently, the spacing does not match with the sublattice

of the columnar framework thus, causing a mismatch between the pentagonal columnar frame and the chain of unequally spaced central Zn atoms. Similar structural features are observed in Nowotny-Chimney-ladder structures commonly found in some of the transition metal silicides [98] and germanides [97].

In the γ -Pt₂Zn₁₁ phase, the ratio of the repeat distance of two distinct sublattices is $\frac{3}{5}$ (corresponds to the ratio of c/n and c/m as defined in Fig. 9.1). However, for Pt₁₈Zn₅₁ structure, the misfit seems to lock-in at the rational value $\frac{8}{13}$. The letters ‘ c/m ’ and ‘ c/n ’ in Fig. 9.1 refers to the lengths of two distinct sublattices that give rise to mismatch between the chimney and the ladder. For Pt₁₈Zn₅₁ the length c/m corresponds to $\frac{c}{13}$ and c/n to $\frac{c}{8}$, where c signifies the long axis of the unit cell.

Fig. 9.2 depicts structure projected along [010] and four decomposed atomic layers at the heights $z \approx \frac{1}{32}, \frac{3}{32}, \frac{5}{32}$ and $\frac{7}{32}$, respectively. These layers include all crystallographic distinct atoms and mimic the overall composition of the phase. The pentagonal columns in the structure are connected via sharing edges and vertices. The peripheral atoms in the adjacent pentagonal columns form a row of distorted octahedrons and tetrahedrons. They are situated in the intercolumnar regions.

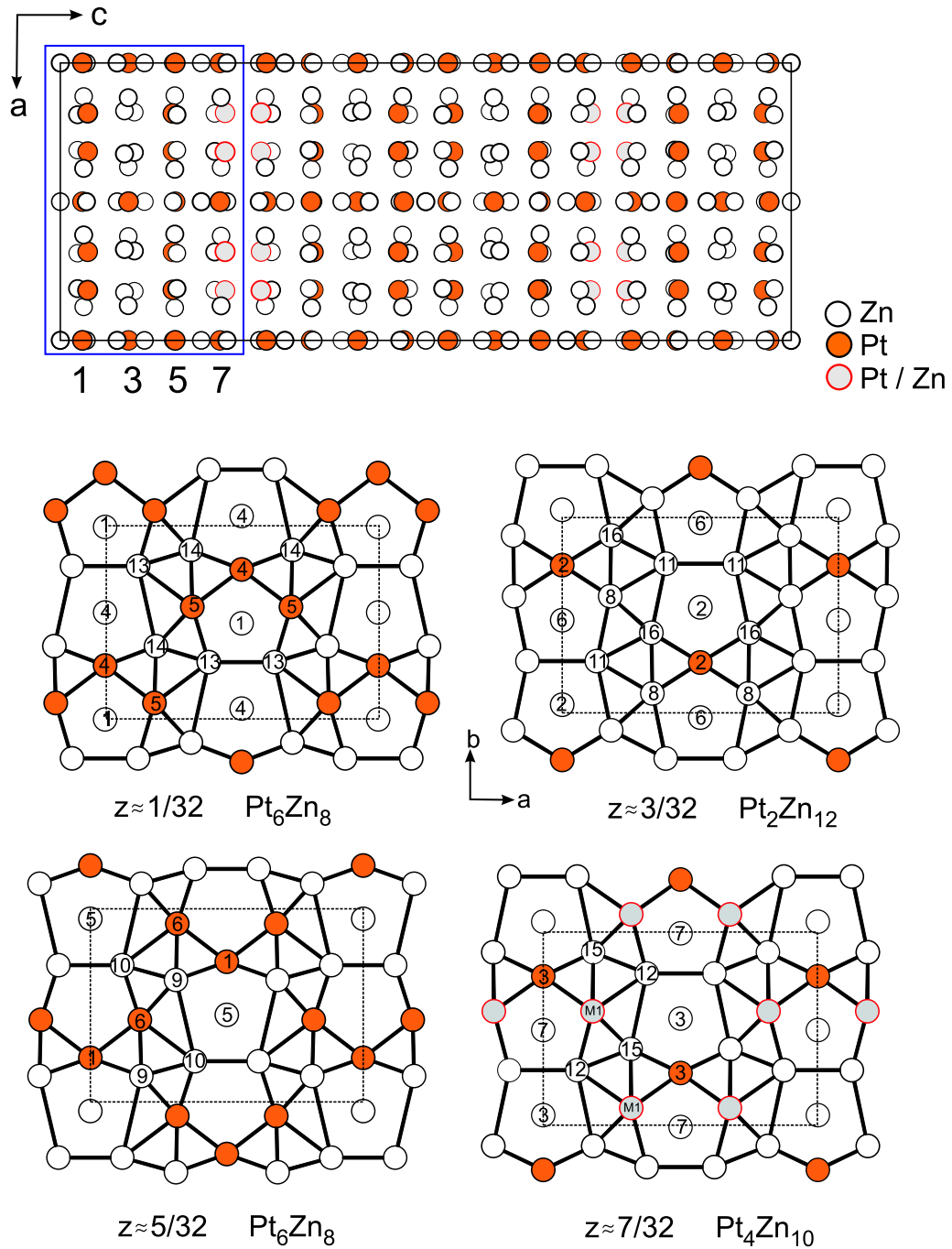


Figure 9.2: The unit cell along [010] and the projection of four decomposed atomic layers of Pt₁₈Zn₅₁ along [001] direction.

9.3 Summary

- Pt₁₈Zn₅₁ is isostructural to Ni₁₈Zn₅₁ and Pd₁₅Zn₅₄ in the congenetic Ni-Zn and Pd-Zn systems.
- The structure comprises 276 atoms in a C-centered orthorhombic cell with 12 ordered vacancies per unit cell. Vacancies are located inside the pentagonal anti-prismatic columns.
- The structure can be viewed as a new type of Nowotny chimney-ladder structure. The chimney corresponds to pentagonal anti-prismatic column and the ladder to a zig-zag chain of Zn atoms running inside the column. For Pt₁₈Zn₅₁ the two sublattices lock in at the rational value $\frac{8}{13}$ conferring the structure a composite type character.

Chapter 10

Pt₂₉Zn₄₉ - A complex defective AlB₂-type derivative structure

10.1 Introduction

A comprehensive report on the relation between phases in the intermediate range $0.3 < x_{\text{Pt}} < 0.45$ of the Pt-Zn phase diagram was first given by Schubert *et al.* [64]. They provide evidence for the existence of four brass-like phases [64] in this intermediate range. According to Schubert's proposal three of the phases form from a high temperature phase termed PtZn_{1.7} (ht3) with hitherto unknown structure in a cascade of eutectoid reactions upon cooling together with a phase which erroneously was considered to be Pt₃Zn₁₀ [13, 68]. The first transition occurs at 1092 K. It leads to PtZn_{1.7} (ht2) for which an AlB₂-type related structure was proposed [40]. Unreasonably short distances ($d(\text{Zn-Zn}) = 119$ pm), however, call for a reassessment of the structure. Below 962 K PtZn_{1.7} (ht2) transforms into Pt₇Zn₁₂ (ht1) adopting a superstructure of the AlB₂-type with ordered defects [42]. Pt₇Zn₁₂ (ht1) transmutes finally into PtZn_{1.7} (rt) below 852 K. Provided that the Pt content of the phases increases steadily upon cooling, a structure determination of the rt phases may deliver insight into the mechanism how these brass-like phases structurally adjust small stepwise changes of the valence electron concentration. The resulting phase formed at the Zn-rich phase was not characterized before. Its structure and properties are subject of the following chapter. An account on Pt₂₉Zn₄₉ has been submitted for the publication [102].

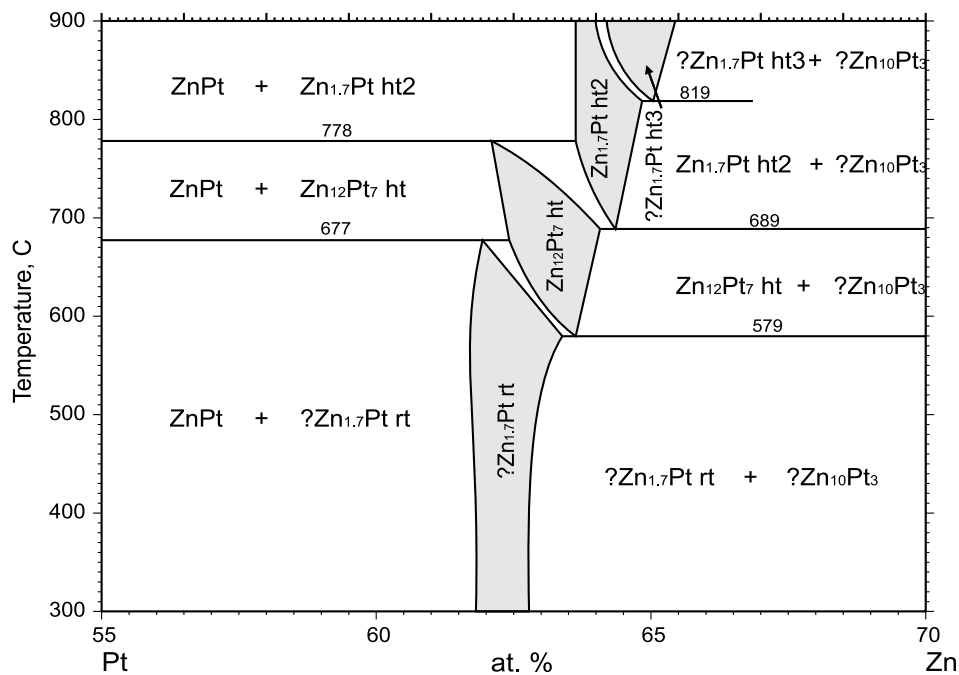


Figure 10.1: Intermediate part of binary phase diagram Pt-Zn after Schubert *et al.* [64] obtained from PaulingFile [103].

10.2 Syntheses and structure determination

10.2.1 Syntheses

Syntheses were carried out from pure elements in evacuated silica ampoules. The molar fraction of Pt was varied between 0.35 to 0.45. The elements were heated continuously at a rate of 60 K h⁻¹ to a temperature of 1420 K at which the ampoules were kept for 0.5 h. Hereafter, the temperature was reduced to 770 K in the course of 96 h. Subsequently, the sample was brought to ambient temperature by turning off the furnace. The products exhibited dichroic silver-golden metallic luster and a pronounced fibrous morphology as shown in Fig. 10.2.

10.2.2 Phase analyses

The samples were characterized by X-ray powder diffraction using CuK_α radiation ($\lambda = 1.54187 \text{ \AA}$). Selected samples were studied by energy dispersive analysis in an electron microscope and by single crystal X-ray structure analyses. After many ineffective attempts to isolate a suitable crystal finally, a twinned crystal of moderate quality was chosen from a Pt-rich sample containing the

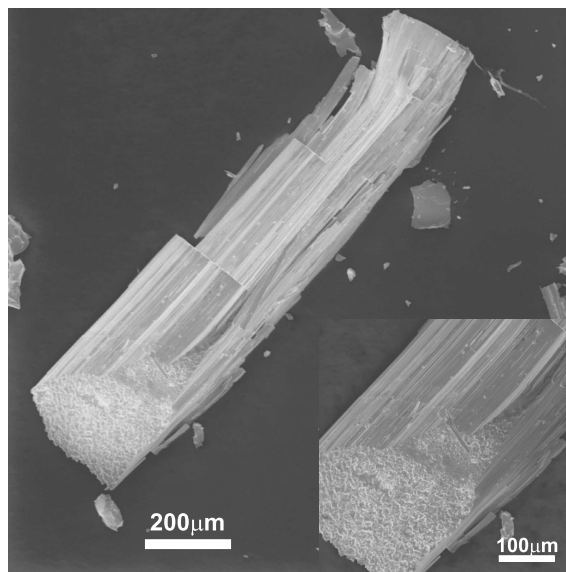


Figure 10.2: SEM micrograph of the phase Pt₂₉Zn₄₉ shows fibrous morphology.

adjacent phase AuCu-type PtZn [40] as major constituent.

The size of the most suitable crystal was $0.04 \times 0.03 \times 0.03 \text{ mm}^3$. Single crystal X-ray diffraction intensities were collected at room temperature using an IPDS-II instrument. The intensities were corrected for Lorentz, polarization and absorption effects based on the numerically optimized shape of the crystal [61, 62]. Application of direct methods (SHELX-97 [58]) produced a crystal-chemically meaningful structure which was refined in space group $Amm2$. The calculations converged at a residual $R1 = 0.1017$ for 373 reflections with $I_o > 2\sigma(I_o)$ out of 1594 reflections for 120 variables including 40 isotropic displacement parameters. The modest quality of the refinement is attributed to the small size of the crystal, the loss of reflections due to twinning, the reduced theta range accessible due to resolution problems associated with the low translational symmetry ($b \approx 120 \text{ \AA}$), and the particular modulation of the structure giving rise to many very weak or absent reflections. In view of the low ratio of symmetrically independent reflections versus variables possible mutual substitution of the two metals on some crystallographic sites was not accounted. Further details concerning crystallographic and technical data are gathered in Tables 10.1 and 10.2.

Table 10.1: Crystallographic and technical data for the single-crystal structure determination

Sum formula	Pt ₂₉ Zn ₄₉
Space group (No.)	Amm2 (38)
Z	2
a / pm	279.0(1)
b / pm	11895.2(4)
c / pm	698.0(1)
V / 10 ⁶ pm ³	2316.5(7)
Molar mass / g mol ⁻¹	8860.5
ρ_{cal} / g cm ⁻³	12.703
μ / mm ⁻¹	111.923
<i>Data collection</i>	
Crystal size / mm ³	0.04 × 0.03 × 0.03
Diffractometer	IPDS-II (STOE & Cie)
Temperature / K	293(2)
Radiation / monochromator	MoK α / Graphite
Distance crystal-IP / mm	180
ϕ ; $\omega_{min} - \omega_{max}$; $\Delta\omega$	0; 0–180; 1
ϕ ; $\omega_{min} - \omega_{max}$; $\Delta\omega$	60; 0–99; 1
$2\theta_{max}$ / °	42.7
Collected reflections	$-2 \leq h \leq 2$ $-120 \leq k \leq 120$ $-7 \leq l \leq 7$
Total No. of reflections	5357
<i>Data reduction</i>	
Programm	IPDS-II-Software [57] / X-RED [61]
Absorption correction	Numerical, X-SHAPE [62]
Max. / Min.transmission	0.0308 / 0.0027
Unique reflections	1594
R_{int}	0.2611
<i>Refinement</i>	
Program	SHELXL-97[58]
Refined on	$ F_o ^2$
Reflections $I_o > 2\sigma(I_o)$	373
Variables	120
R_1 ($I_o > 2\sigma(I_o)$)	0.1017
R_1 (all)	0.2458
w R_2 (all)	0.3141
Goodness of fit	0.902
$\Delta\rho_{max} / \Delta\rho_{min} / 10^{-6}$ e pm ⁻³	3.836 / -3.575
Extinction coefficient	0.000026(12)
$1/w = \sigma^2(F_o^2) + (0.1(\text{Max}(F_o^2, 0) + 2F_c^2)/3)^2$	

Table 10.2: Positional and equivalent isotropic displacement parameters $U_{\text{eq}}(\text{pm}^2)$ for Pt₂₉Zn₄₉ phase

Atom No.	Wy.	x	y	z	U_{eq}
Pt1	2b	$\frac{1}{2}$	0	-0.009(3)	590(60)
Pt2	4e	$\frac{1}{2}$	0.03320(17)	0.029(3)	840(60)
Pt3	4e	$\frac{1}{2}$	0.06991(15)	0.031(2)	790(50)
Pt4	4e	$\frac{1}{2}$	0.10241(15)	-0.038(2)	740(60)
Pt5	4e	$\frac{1}{2}$	0.13729(19)	0.973(3)	810(50)
Pt6	4e	$\frac{1}{2}$	0.17274(18)	0.978(3)	800(60)
Pt7	4e	$\frac{1}{2}$	0.20579(14)	0.911(2)	590(50)
Pt8	4e	$\frac{1}{2}$	0.24272(16)	0.907(3)	730(60)
Pt9	4e	$\frac{1}{2}$	0.22444(18)	0.454(2)	680(60)
Pt10	4e	$\frac{1}{2}$	0.19114(15)	0.414(2)	700(50)
Pt11	4e	$\frac{1}{2}$	0.15399(15)	0.431(2)	680(60)
Pt12	4e	$\frac{1}{2}$	0.12131(16)	0.509(3)	800(50)
Pt13	4e	$\frac{1}{2}$	0.08550(12)	0.503(2)	600(40)
Pt14	4e	$\frac{1}{2}$	0.05097(12)	0.483(2)	640(50)
Pt15	4e	$\frac{1}{2}$	0.01861(16)	0.542(2)	820(60)
Zn1	2a	0	0	0.624(11)	1100(200)
Zn2	4d	0	0.0170(4)	-0.132(7)	830(140)
Zn3	4d	0	0.0122(4)	0.242(6)	640(120)
Zn4	4d	0	0.0385(4)	0.724(6)	660(120)
Zn5	4d	0	0.0337(4)	0.361(8)	890(160)
Zn6	4d	0	0.0505(5)	0.127(9)	1200(200)
Zn7	4d	0	0.0633(4)	-0.261(7)	780(130)
Zn8	4d	0	0.0685(4)	0.367(6)	660(120)
Zn9	4d	0	0.0847(3)	-0.167(6)	590(130)
Zn10	4d	0	0.0889(4)	0.202(7)	900(150)
Zn11	4d	0	0.1032(4)	0.617(6)	760(140)
Zn12	4d	0	0.1134(3)	0.222(6)	580(100)
Zn13	4d	0	0.1205(4)	0.851(7)	720(150)
Zn14	4d	0	0.1401(5)	0.651(7)	930(160)
Zn15	4d	0	0.1360(5)	0.283(8)	1000(190)
Zn16	4d	0	0.1557(4)	0.086(6)	650(130)
Zn17	4d	0	0.1722(3)	0.344(6)	480(120)
Zn18	4d	0	0.1639(4)	0.707(6)	800(140)
Zn19	4d	0	0.1865(5)	0.745(7)	840(150)
Zn20	4d	0	0.1909(4)	0.112(7)	750(150)
Zn21	4d	0	0.2060(5)	0.586(8)	800(200)
Zn22	4d	0	0.2125(3)	0.210(5)	520(100)
Zn23	4d	0	0.2242(4)	0.838(5)	540(120)
Zn24	4d	0	0.2586(4)	0.092(7)	580(140)
Zn25	4d	0	0.2365(5)	0.217(8)	1020(190)

10.3 Results and discussion

The phase Pt₂₉Zn₄₉ crystallizes in the A-centered orthorhombic space group Amm2. The lattice parameters are: $a = 279.0(1)$, $b = 11895.2(4)$ and $c = 698.0(1)$ pm. The number of formula unit Z is 2. The cell accommodates 156 atoms. Thus, the Pearson symbol is oA156. The structure is built up by 40 crystallographic distinct atoms, 15 Pt and 25 Zn atoms. It represents a unique superstructure of an AlB₂-type structure for which the following metrical relations hold: $a_o = c_h$, $b_o = 29 a_h$, $c_o = \sqrt{3} a_h$. The subscript o refers to the orthorhombic A-lattice of Pt₂₉Zn₄₉, the subscript h to the hexagonal lattice of an AlB₂-type structure. Thus the ratio of the two cell volumes is 58, the order of the superstructure. An adjustment of the two formulas reveals that 9 out of every 58 Zn positions are vacant in the AlB₂-type derivative. As seen from the intensity distribution in the $0kl$ section of the reciprocal lattice (c.f. Fig. 10.3) the structural complexity arises from a modulation along a_h with a period of nearly 12 nm length. The modulated structure of Pt₂₉Zn₄₉ in its commensurate approximation is compatible with orthorhombic space group symmetry Amm2.

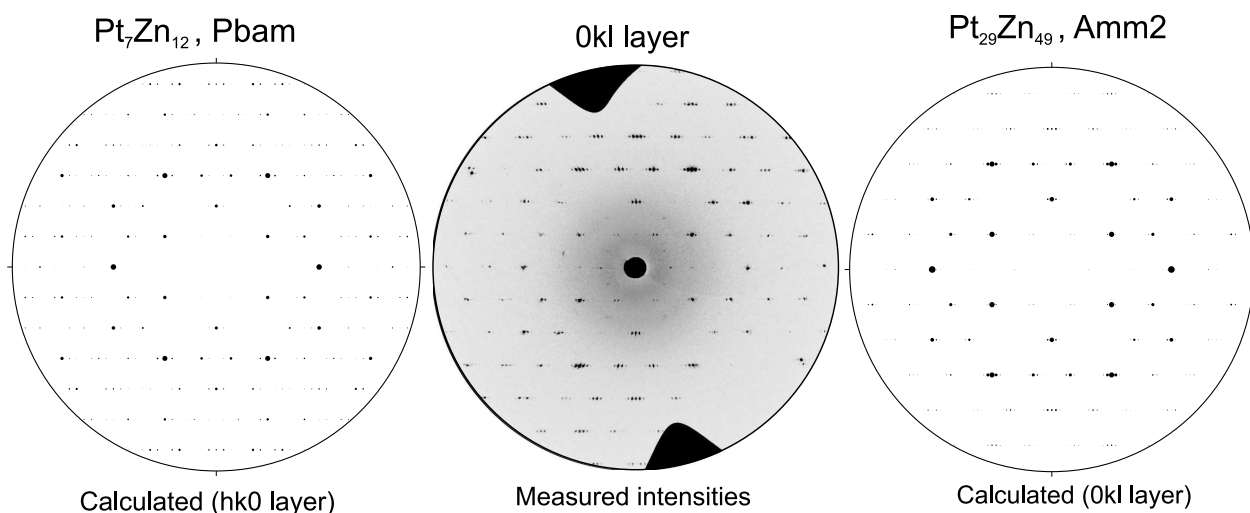


Figure 10.3: Comparison of the calculated intensities (MoK α) for the structures of Pt₇Zn₁₂ ($hk0$ layer [42]) and Pt₂₉Zn₄₉ ($0kl$) with measured intensities of the respective reciprocal section of Pt₂₉Zn₄₉.

In view of the long translation period the structure appears to be rather complex at first glance. However, it can be conveniently analyzed by decomposing it into two distinct atomic layers alternatively stacked along [100]. The layers resembles to those of the well known AlB₂-type structure [78]. The atomic layers of the AlB₂-aristo-type structure can be adequately described

in terms of nets. The vertices of the nets correspond to the position of the atoms in the layers. For AlB₂, the Al atoms are arranged in planar 3⁶ nets and the B atoms in honeycomb-type 6³ nets. In this notation (Schläfli symbol) the number of the basis refers to the polygon of the net and the exponent refers to the vertex configuration *i.e.*, the number of polygons arranged around each vertex. The two distinct nets are stacked alternately along [001].

A projection of the structure of Pt₂₉Zn₄₉ along the short a_o axis is shown in Fig. 10.5. The structure results from an alternating stacking of two sorts of atomic layers at the heights $x = 0$ and $\frac{1}{2}$, respectively, modulo a_o . The Pt atoms are depicted as filled circles in Fig. 10.5 and situated in the layers at $x = \frac{1}{2}$. The Pt atoms define distorted 3⁶ nets, similar to the arrangement of Al atoms in AlB₂. The layers at $x = 0$ consist exclusively of Zn atoms. They are located at the vertices of an irregular net composed of pentagons, triangles, and hexagons. The Zn atoms are represented by open circles in Fig. 10.5. The irregular net results from a concerted distortion of a 6³ honeycomb net (as formed by the B atoms in AlB₂) in which 9 out of 58 vertices are missing. Fig. 10.4 sketches the coherent distortion associated with the defects, the positions which coincide with the centers of the gray triangles in Fig. 10.4. The particular orientation of the triangles along c_o discloses the intrinsic lack of a center of symmetry of the structure.

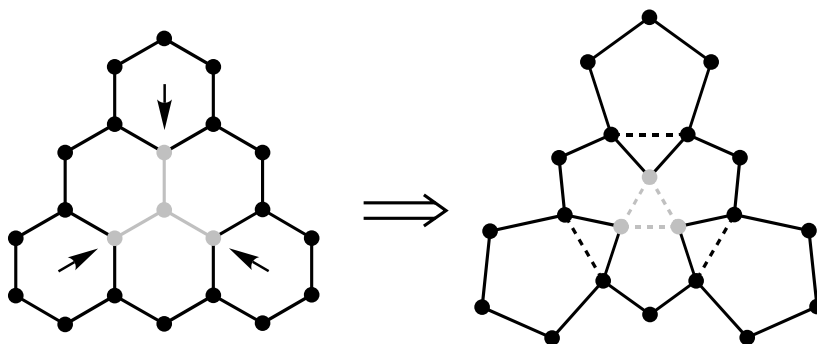


Figure 10.4: Schematic representation of the distortion in the honeycomb net (6³ net) which is due to ordered vacancy. This can be achieved by removing one of the vertex in the 6³ net and allow the net to relax, now composed of triangles, pentagons and hexagons.

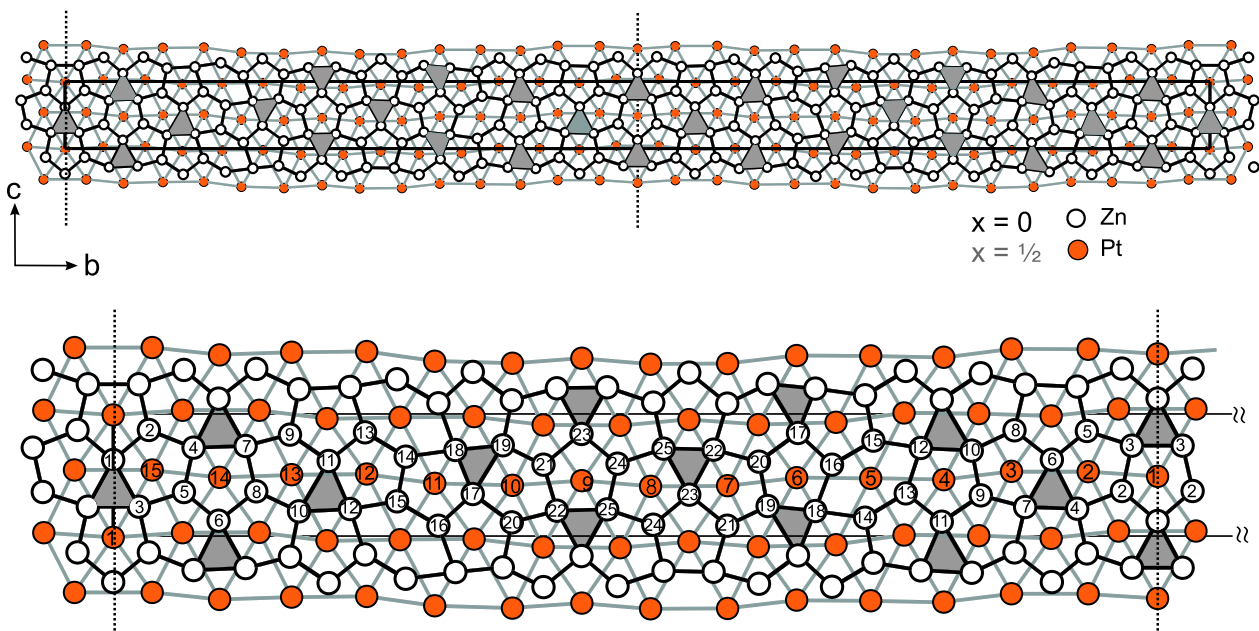


Figure 10.5: View of two adjacent atomic layers along $[100]$ of the crystal structure of $\text{Pt}_{29}\text{Zn}_{49}\square_9$. Note that each shaded triangle in the defective 6^3 atomic layer formed by Zn atoms corresponds to one vacant position. The Pt atoms (shown as orange circles) are arranged at the vertices of 3^6 nets. The figure in the lower part is a magnification of half of the upper figure.

From the given relations of the lattice parameters of $\text{Pt}_{29}\text{Zn}_{49}$ we obtain the following intra- and inter-layer distances for fictitious AlB_2 -type PtZn_2 : $d(\text{Pt}-\text{Pt}, \text{intra}) = 406.5 \text{ pm}$, $d(\text{Zn}-\text{Zn}, \text{intra}) = 234.7 \text{ pm}$, and $d(\text{Pt}-\text{Zn}, \text{inter}) = 273.0 \text{ pm}$. The corresponding distances in the $\text{Pt}_{29}\text{Zn}_{49}$ structure vary between $375.2 - 449.9 \text{ pm}$, $256.4 - 295.3 \text{ pm}$, and $253.6 - 291.5 \text{ pm}$, respectively. The variation provides a measure of the degree of distortion induced by the defects. Furthermore, it reflects the expansion of the otherwise too short Zn-Zn distances in the defective AlB_2 -type derivative structure of $\text{Pt}_{29}\text{Zn}_{49}\square_9$ with \square denoting the vacancies. The interatomic distances are gathered in Table 10.5.

The subsequent part deals with the structural and thermochemical interrelations between various $\text{PtZn}_{1.7}$ [40] phases. In accordance with the proposed phase relations $\text{Pt}_{29}\text{Zn}_{49}$ bears a close structural and compositional resemblance with the intermediate high temperature precursor $\text{Pt}_7\text{Zn}_{12}$ forming a slightly distinct AlB_2 -type derivative structure of the order 14, space group Pbam , $a = 2879 \text{ pm}$, $b = 695 \text{ pm}$ and $c = 276 \text{ pm}$ [42], see Fig. 10.6. There are two ordered vacancies per formula unit $\text{Pt}_7\text{Zn}_{12}\square_2$ and the modulation period ($7a_h$), again, corresponds strictly to the stoichiometric coefficient of Pt in the formula. If the supposed phase width is neglected,

Pt₂₉Zn₄₉ contains about 1% more Pt and about 9% more vacancies than Pt₇Zn₁₂. The vacancy concentration increases from $\frac{2}{14}$ for Pt₇Zn₁₂ to $\frac{9}{58}$ for Pt₂₉Zn₄₉.

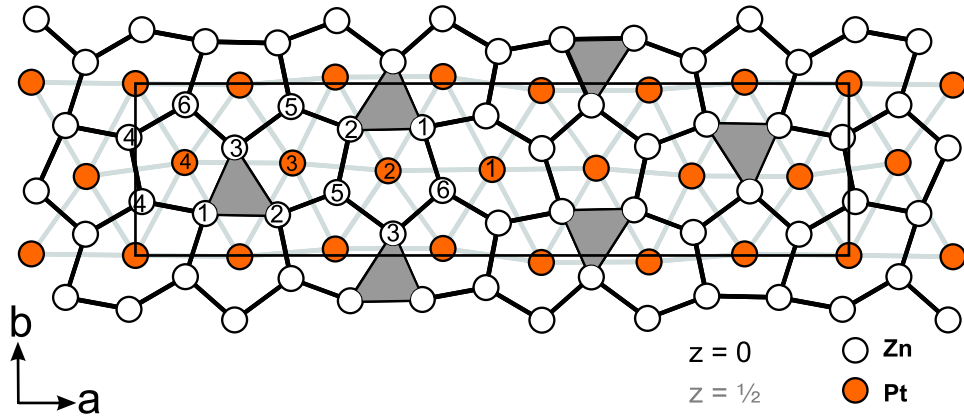


Figure 10.6: A perspective view of AlB₂-type atomic layers along [001] of Pt₇Zn₁₂□₂ structure.

Metrical relationship in terms of AlB₂ and vacancy concentration for the phases Pt₂₉Zn₄₉ and Pt₇Zn₁₂ are given in Table 10.3, and a graphical representation is shown in Fig. 10.7.

Table 10.3: Metrical relationship between Pt₇Zn₁₂ and Pt₂₉Zn₄₉, respectively, and an AlB₂-type structure for which $a_h \approx 4.1 \text{ \AA}$ and $c_h \approx 2.7 \text{ \AA}$ [40]

Phase	Space group	Lattice parameters			AlB ₂ form	Vacancy concentration
		a	b	c		
Pt ₇ Zn ₁₂ [42]	Pbam	c_h	$\sqrt{3} a_h$	$7a_h$	Pt ₁₄ (Zn ₁₂ □ ₂) ₂	$\frac{1}{7}$
Pt ₂₉ Zn ₄₉	Amm2	c_h	$\sqrt{3} a_h$	$29a_h$	Pt ₅₈ (Zn ₄₉ □ ₉) ₂	$\frac{9}{58}$

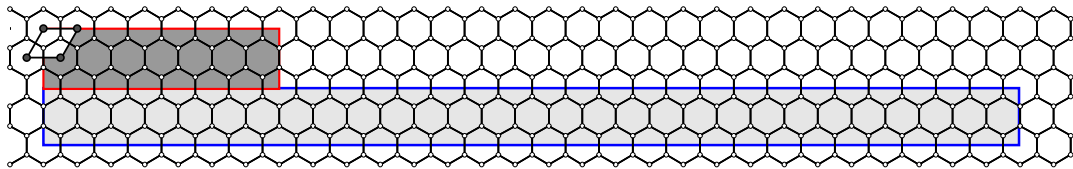


Figure 10.7: Metrical relationship between Pt₇Zn₁₂ and Pt₂₉Zn₄₉. The red box refers to the cell of Pt₇Zn₁₂ and blue to that of Pt₂₉Zn₄₉. The cell of an AlB₂ structure is shown in the upper left corner.

In view of the subtle structural distinctions the X-ray powder diffractograms of the two phases differ barely. The main differences show up in few additional reflections in the pattern of Pt₂₉Zn₄₉ in the low 2θ range, see Fig. 10.8. The extra reflections are also seen in the pattern calculated from the structural parameters of Pt₂₉Zn₄₉ and are missing in the accordant pattern of Pt₇Zn₁₂, as seen from Fig. 10.9. Moreover, it has been shown that the phases mutually transform into each other. Pt₂₉Zn₄₉ was obtained from an appropriately heat-treated sample (37 at.% Pt) which was finally annealed at 773 K. Pt₇Zn₁₂ was obtained from the same sample after quenching in cold water from 1123 K. All attempts, however, to obtain the high temperature precursor of Pt₇Zn₁₂ at ambient temperature by quenching failed. Consequently, the transformation PtZn_{1.7} (ht2) \rightarrow Pt₇Zn₁₂ takes place without any discernable repression.

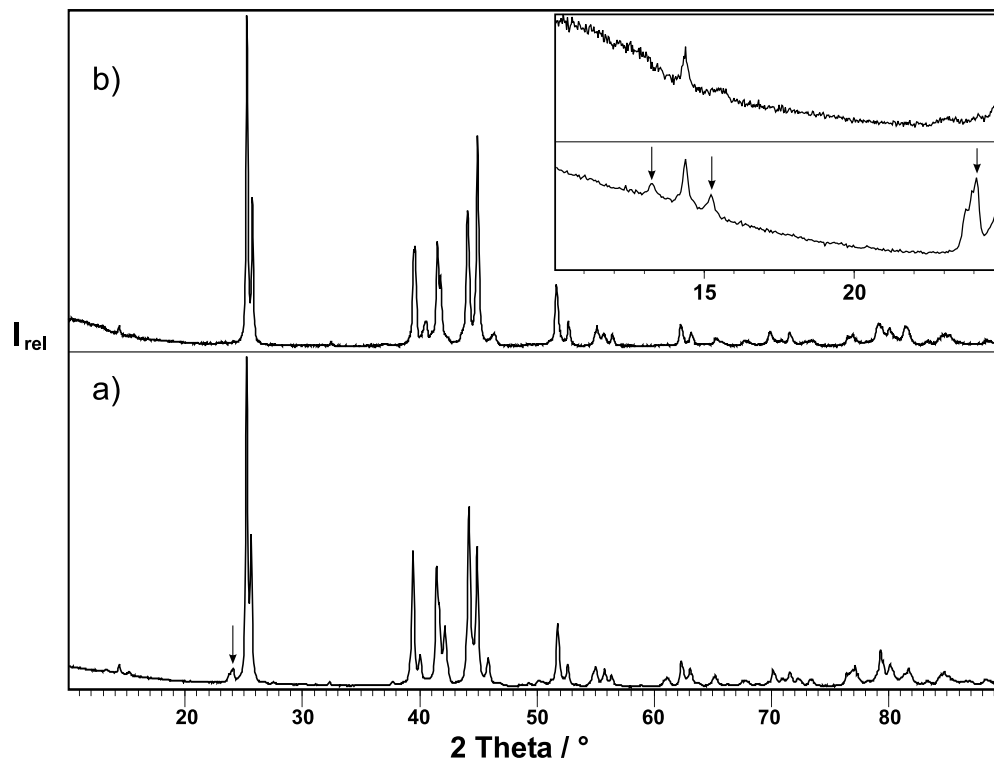


Figure 10.8: a) X-ray powder diffractograms of PtZn_{1.7} (nominal composition of 37 at.% Pt) annealed at two different temperatures: (a) The sample annealed at 773 K is Pt₂₉Zn₄₉. (b) The pattern of the sample annealed at 1123 K resembles that of Pt₇Zn₁₂. The insert shows a magnification of the intensities at low diffraction angles. The arrows highlight major differences between the two patterns.

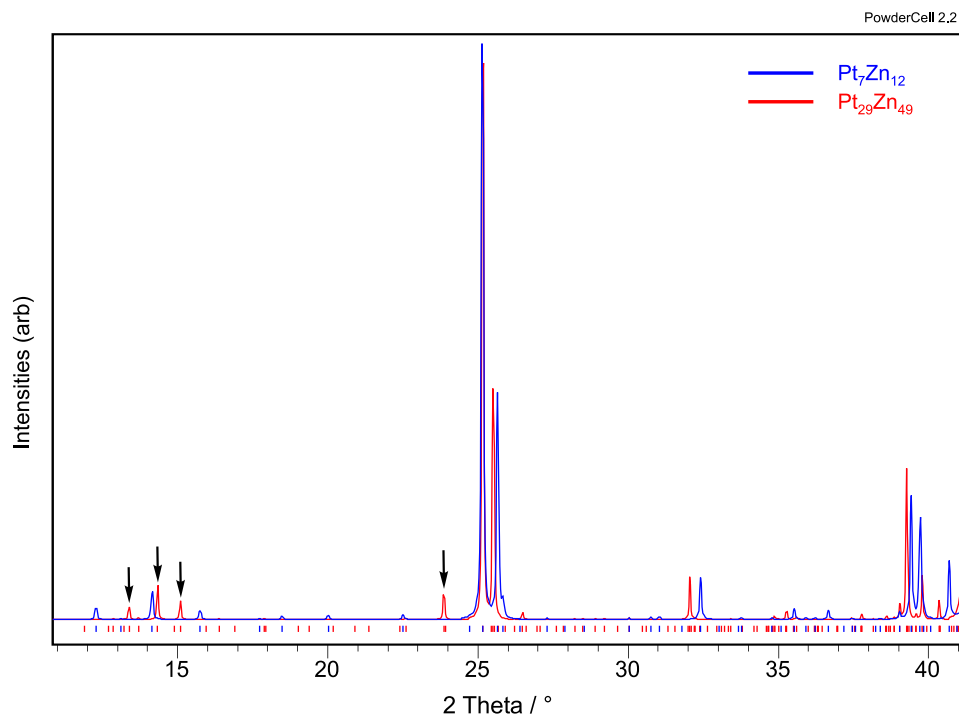


Figure 10.9: Comparison of calculated X-ray intensities ($\text{CuK}\alpha$) of the structures $\text{Pt}_7\text{Zn}_{12}$ (blue) and $\text{Pt}_{29}\text{Zn}_{49}$ (red). The arrows indicate the major differences between patterns of the two phases.

DTA analyses provided additional pieces of information about the expected transformations. Fig. 10.10 shows two typical thermograms of a Zn-rich (37% Pt) and a Pt-rich (40%) sample. The effect at 1020 - 1028 K is less sensitive to compositional changes than the weaker effects at lower temperatures. The transformation temperatures of three representative DTA analyses are listed in Table 10.4. It is noteworthy to mention that the observed temperatures differ significantly from those attributed to the eutectoid/peritectoid reactions marked in the phase diagram [103], see Fig 10.1. In particular, the thermal event at 1020 K seems not to descend from the transformation $\text{PtZn}_{1.7}$ (ht2) \rightarrow $\text{Pt}_7\text{Zn}_{12}$ (ht1). Firstly, the pronounced thermal hysteresis (ΔT ca. 30 K) of the event suggests - opposed to our findings - that $\text{PtZn}_{1.7}$ (ht2) should be quenchable. Secondly, samples quenched from temperatures above 1020 K produce the diffraction pattern of $\text{Pt}_7\text{Zn}_{12}$ whereas patterns obtained from samples quenched below 1020 K showed extra peaks similar to $\text{Pt}_{29}\text{Zn}_{49}$. Hence, the thermal effect at 1020 K is associated with the decomposition of $\text{Pt}_7\text{Zn}_{12}$. This has been confirmed by DTA and powder X-ray diffraction analysis. The origin of the thermal events below 1000 K needs further clarification.

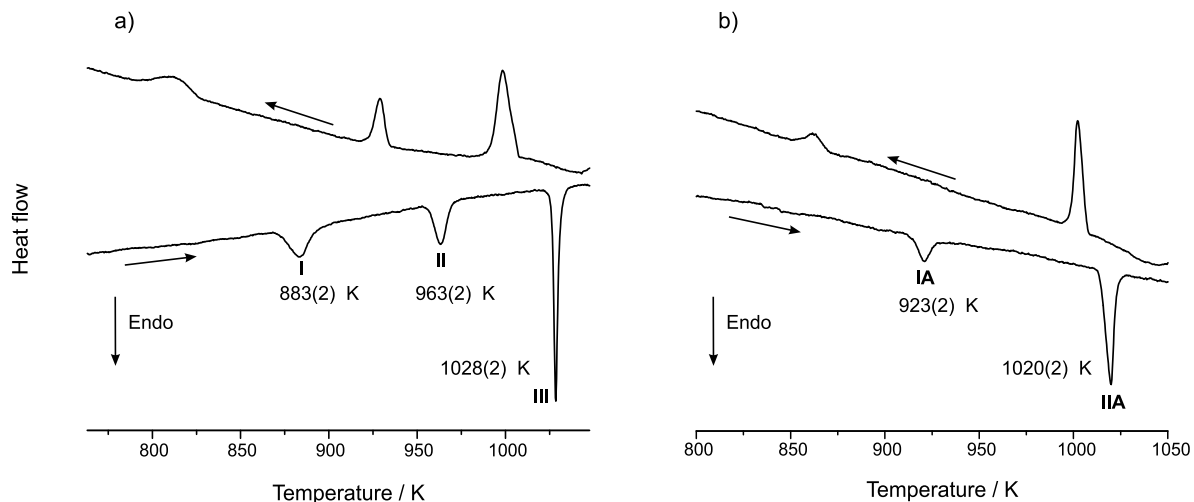


Figure 10.10: Thermochemical analysis of two different samples of nominal composition of 37 (a) and 40 at.% of Pt (b).

Table 10.4: DTA analysis - Recorded temperatures for three different samples

Nominal composition	P.T I	P.T II / IA	P.T III / IIA
	Temp. K	Temp. K	Temp. K
Pt ₃₅ Zn ₆₅	865	961	–
Pt ₃₇ Zn ₆₃	884	963	1028
Pt ₄₀ Zn ₆₀	–	921	1022

The structure analysis of PtZn_{1.7} (rt) reveals that the composition of the phase is reasonably approximated by the formula Pt₂₉Zn₄₉ which complies with the results of the EDX analyses of the same crystal ($x_{\text{Pt}} = 0.37(1)$) and other samples.

Magnetic susceptibility as a function of temperature of the single phase sample shows diamagnetic behavior. The Pauli paramagnetism of the metallic phase seems to be slightly overcompensated by the core diamagnetism of its constituent. The temperature independent molar susceptibility was calculated from the slope of a linear plot $\chi_{\text{mol}}T$ versus T . The value for Pt₂₉Zn₄₉ is $-1.3 \times 10^{-10} \text{ m}^3 \text{ mol}^{-1}$ refers to an average atom of the compound, *i.e.*, although slightly less negative, compares well with the molar susceptibilities measured for Pt₁₁Zn₃₂. Fig. 10.11 shows the magnetic susceptibility of a single phase sample of Pt₂₉Zn₄₉ as a function of temperature.

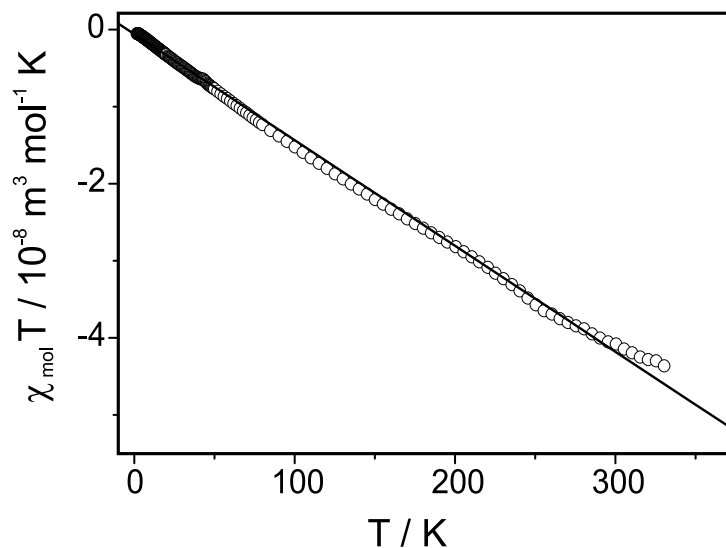


Figure 10.11: Magnetic susceptibility multiplied with temperature of single phase Pt₂₉Zn₄₉ as a function of temperature.

10.4 Summary

The sparsely characterized high temperature phase PtZn_{1.7} undergoes a series of eutectoid reactions upon cooling which finally end up with the formation of the apparently Pt-richest phase in the field $0.32 \leq x_{\text{Pt}} \leq 0.40$. A X-ray structure analysis revealed the composition Pt₂₉Zn₄₉. The phase is structurally and compositionally closely related with its intermediate high temperature precursor Pt₇Zn₁₂ exhibiting a slightly reduced vacancy concentration of $\frac{2}{14}$. Pt₂₉Zn₄₉ forms a complex superstructure of an AlB₂-type structure in which 9 out of every 58 Zn positions in a graphite-like atomic arrangement remain vacant. The ordering of the vacancies entails a coherent distortion within the layers resulting in a modulated structure with a translation period of nearly 12 nm. Additional thermal events in DTA analyses and subtle distinctions in X-ray powder patterns of some quenched samples suggest the existence of further defective AlB₂-type derivatives in this phase field.

Chapter 11

A general introduction to the binary system Ni-Zn

The phase diagram and experimental studies on the Ni-Zn system was first reported by Hansen *et al.* [104]. The thermodynamic optimization of the phase diagram based on available experimental data was performed by Vassilev [105, 106]. So far in the Ni-Zn system four binary phases have been identified which are NiZn [107, 108], γ -Ni₅Zn₂₁ [11], NiZn₃ [12], and δ -NiZn₈ [109]. Morton studied the γ -brass region of Ni-Zn system by means of transmission electron microscopy (TEM) and electron diffraction (ED) methods. As indicated by ED and TEM the structural complexity is associated with a modulation along the [110] direction of the parent γ -phase [32, 34]. The structural differentiation is reflected in striations appearing in suitably oriented TEM images. The image contrast is suggested to arise from inversion anti-phase domains whose size sensitively depends on composition. The translational ordering of domains ranges from 33 Å up to 107 Å at Ni-rich and Zn-rich phase boundary, respectively, see Fig. 11.2. The reported phase diagram for the Ni-Zn binary system is shown in Fig. 11.1, and the crystallographic data for known structures are summarized in Table 11.1.

Table 11.1: A survey of crystallographic data for the known phases in the Ni-Zn phase diagram

Phase	Pearson symbol	Space group	Structure type
$\text{Ni}_{1-x}\text{Zn}_x$	cF4	$\text{Fm}\bar{3}\text{m}$	Cu [108]
NiZn	tP2	$\text{P4}/\text{mmm}$	AuCu [107, 108]
$\gamma\text{-Ni}_5\text{Zn}_{21}$	cI52	$\bar{\text{I}}43\text{m}$	Cu_5Zn_8 [11]
NiZn_3	oA276	$\text{Abm}2$	NiZn_3 [12]
$\delta\text{-NiZn}_8$	mC50	$\text{C}2/\text{m}$	NiZn_8 [109]
Zn	hP2	$\text{P}6_3/\text{mmc}$	Mg

Assessed Ni-Zn phase diagram.

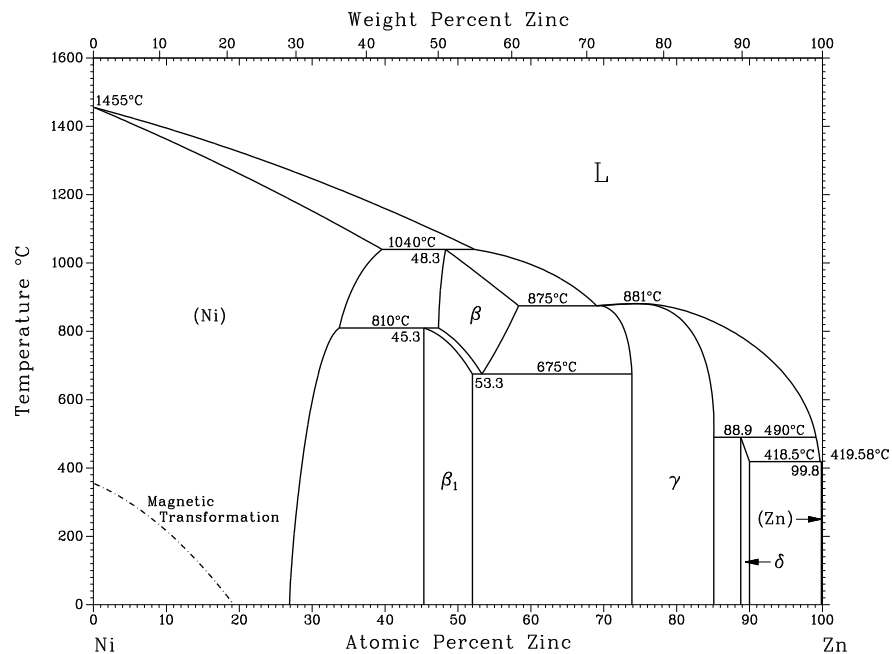


Figure 11.1: Phase diagram of the Ni-Zn system from ASM [65].

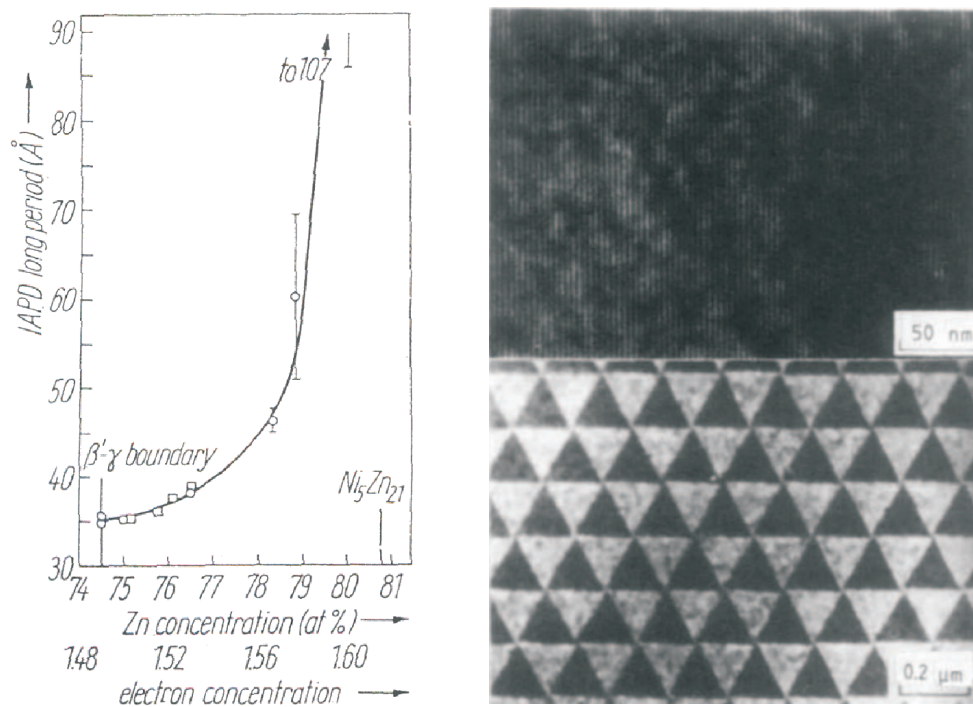


Figure 11.2: **Left:** A graph showing the variation of the planar IAPD with composition and with valence electron concentration. **Right top:** bright-field image of the planar anti-phase domain structure. **Right bottom:** dark field image of the triangular IADP structure along the beam direction [111] (taken from Morton [32, 34])

Chapter 12

Ni₇Zn_{57- δ} ($\delta = 0.54(6)$) - A reappraisal of a zinc-rich monoclinic phase

12.1 Introduction

The zinc-rich phase NiZn₈ was first reported by Critchley *et al.* [109]. According to their findings, the NiZn₈ phase crystallizes in the C2/m space and the unit cell comprises 50 atoms. The structure was poorly determined with reported R(F) of about 12 %. The X-ray diffraction intensities were collected from visual analyses of Weissenberg photographs. Moreover, there is no structural discussion on the NiZn₈ phase. From these points, the structure of NiZn₈ calls for redetermination.

12.2 Syntheses

Single crystals of NiZn₈ were synthesized from the pure elements (Ni:Zn \approx 1:15) sealed in evacuated silica ampoules. The reactant mixtures were heated continuously at a rate of 60 K h⁻¹ to 870 K at which the ampoules were kept for 12 h. Subsequently, the ampoules were cooled down to 720 K over a period of 72 h, before they were quenched in water. The product was embedded in a matrix of Zn which was removed by using dilute hydrochloric acid. The crystals thus obtained had a regular polyhedral shape with metallic luster, see Fig. 12.1. In addition, the syntheses were also carried out using the melt centrifugation technique, as described earlier (cf. Introduction).

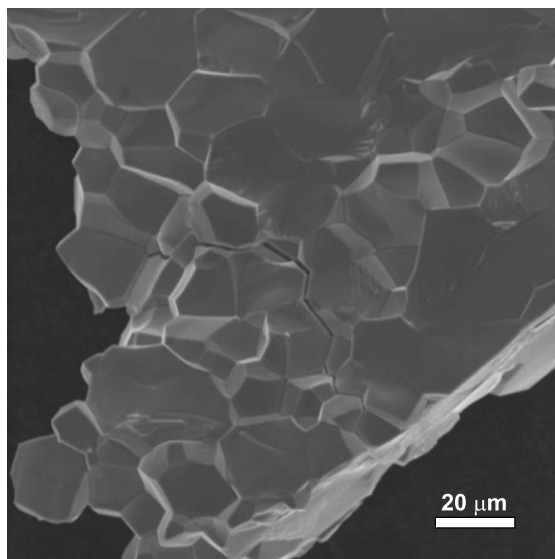


Figure 12.1: SEM studies showed that the crystals exhibit polyhedral forms with crystal sizes ranging between 20 to 80 μm .

12.3 Structure determination

The single phase and two phase mixtures were routinely characterized by means of X-ray powder diffraction using $\text{CuK}\alpha$ ($\lambda = 1.54060 \text{ \AA}$) radiation, operating in Bragg-Brentano geometry equipped with a secondary monochromator.

Single crystal X-ray diffraction studies were carried out with a single crystal $0.12 \times 0.04 \times 0.06 \text{ mm}^3$ in size, on an IPDS-I X-ray diffractometer using $\text{MoK}\alpha$ radiation ($\lambda = 0.71073 \text{ \AA}$). The diffraction intensities were collected at room temperature in the range of $3.8 \leq 2\theta \leq 65.8$. The measured reflections were subjected to Lorentz, polarization and numerical absorption correction by optimizing the crystal shape with a numerical method based on the face indexation of the crystal under consideration [61, 62]. Among 13826 collected reflections, 3575 reflections were unique of which 1039 reflections were $I_o > 2\sigma(I_o)$.

For structural refinement the starting atomic parameters of the structure of PtZn_7 were opted. By all indications the structure of NiZn_8 is isostructural to PtZn_7 . However, the weak X-ray scattering contrast of Ni and Zn hampered an unambiguous assignment of the two constituents in the structure. Thus, the atomic positions of Pt were replaced by Ni and the mixed-occupied positions were assigned to either Pt or Zn sites depending on the site occupancies. The atoms

whose site occupancies close to unity were assigned to either Ni or Zn. However, one of the atomic position in the PtZn_7 structure whose site occupancy was about 50% of Zn and Pt appeared to be fully occupied by Zn in the NiZn_8 structure. This position was assigned to a fully occupied Zn site. Furthermore, two of the atomic positions were refined as partial occupied sites. The final cycles of the refinement were performed with anisotropic displacement parameters. The residual R_1 value smoothly converged to 0.0401, $wR_2 = 0.1616$ for 1039 reflections with $I_o > 2\sigma(I_o)$ for 179 variables. Noteworthy, the wR_2 value is quite large because some of the measured intensities for the structure are very weak, see Fig. 12.3. However, for few atoms the displacement parameters are noticeably high possibly due to incommensurate structure modulation. Details concerning the structure determination and data collection are tabulated in Table 12.1. The atomic coordinates with isotropic displacement parameters and anisotropic displacement parameters are listed in Table 12.2 and 12.3, respectively.

Table 12.1: Crystallographic and technical data for the single-crystal structure determination

Sum formula	Ni ₇ Zn _{57-δ}
Space group (No.)	C2/m (12)
Z	2
a / pm	1337.0(3)
b / pm	748.3(1)
c / pm	1848.5(3)
β / °	97.82(3)
V / 10 ⁶ pm ³	1835.0(7)
Molar mass / g mol ⁻¹	516.3
ρ_{cal} / g cm ⁻³	7.435
μ / mm ⁻¹	39.61
<i>Data collection</i>	
Crystal size / mm ³	0.12 × 0.04 × 0.06
Diffractometer	IPDS-I (STOE & Cie)
Temperature / K	293(2)
Radiation / monochromator	MoK α / Graphite
Distance crystal-IP / mm	40
$\phi_{min} - \phi_{max}; \Delta\phi$	0 – 210; 1
$2\theta_{max}$ / °	65.8
Collected reflections	-20 ≤ h ≤ 20 -11 ≤ k ≤ 11 -28 ≤ l ≤ 28
Total No. of reflections	13826
<i>Data reduction</i>	
Program	IPDS-Software [57] / X-RED [61]
Absorption correction	Numerical, X-SHAPE [62]
Max. / min. transmission	0.2827 / 0.0903
Unique reflections	3575
R _{int}	0.1045
<i>Refinement</i>	
Program	SHELXL-97[58]
Refined on	F _o ²
Reflections I _o > 2 σ (I _o)	1039
Variables	179
R ₁ (I _o > 2 σ (I _o))	0.0401
R ₁ (all)	0.1646
wR ₂ (all)	0.1616
Goodness of fit	0.618
$\Delta\rho_{max} / \Delta\rho_{min} / 10^{-6}$ e pm ⁻³	2.561 / -2.09
$1/w = \sigma^2(F_o^2) + (0.1(\text{Max}(F_o^2, 0) + 2F_c^2)/3)^2$	

The composition of the phase Ni₇Zn_{57- δ} is very close to NiZn₈. Further on, the phase Ni₇Zn_{57- δ} is termed as NiZn₈ for the sake of simplicity.

Table 12.2: Positional and equivalent isotropic displacement parameters U_{eq} (pm²) for NiZn₈

Atom No.	Wy.	x	y	z	sof	U_{eq}
Ni1	2a	0	0	0	1	59(8)
Ni2	4i	0.1344(2)	0	0.6092(1)	1	65(6)
Ni3	4i	0.2692(2)	0	0.2169(2)	1	56(6)
Ni4	4i	0.4014(2)	0	0.8257(2)	1	58(5)
Zn1	2c	0	0	$\frac{1}{2}$	1	172(9)
Zn2	4i	0.0664(2)	0	0.7349(1)	1	112(6)
Zn3	4i	0.0651(2)	0	0.8728(1)	1	115(6)
Zn4	4i	0.1962(2)	0	0.4812(1)	1	128(6)
Zn5	4i	0.1972(2)	0	0.3429(1)	1	117(6)
Zn6	4i	0.3217(2)	0	0.0889(1)	1	127(6)
Zn7	4i	0.1318(1)	0	0.1110(1)	1	168(7)
Zn8	4i	0.4529(2)	0	0.6976(1)	1	157(6)
Zn9	4i	0.3320(2)	0	0.9525(1)	1	90(6)
Zn10	4i	0.4690(2)	0	0.5648(2)	1	138(6)
Zn11	4i	0.2643(2)	0	0.7212(1)	0.91(1)	223(11)
Zn12	8j	0.0279(1)	0.1806(3)	0.37747(9)	1	126(4)
Zn13	8j	0.1115(1)	0.1896(3)	0.23350(9)	1	143(4)
Zn14	8j	0.1622(1)	0.1793(3)	0.9859(1)	1	112(4)
Zn15	8j	0.2972(1)	0.1775(3)	0.59529(9)	1	125(4)
Zn16	8j	0.2538(1)	0.3089(3)	0.1555(1)	1	152(4)
Zn17	8j	0.3798(1)	0.1956(3)	0.4627(1)	1	184(5)
Zn18	8j	0.4331(1)	0.1762(2)	0.1958(1)	1	104(3)
Zn19	8j	0.4834(1)	0.1968(3)	0.92639(9)	1	145(4)
Zn20	8j	0.3495(1)	0.1960(3)	0.31683(9)	0.91(1)	194(7)

Table 12.3: Anisotropic displacement parameters U (pm²) for NiZn₈

Atom No.	U11	U22	U33	U12	U13	U23
Ni1	30(13)	80(30)	66(17)	0	0	-9(11)
Ni2	55(11)	64(19)	70(13)	0	0	-11(8)
Ni3	47(9)	61(17)	61(11)	0	0	5(7)
Ni4	53(9)	70(16)	47(10)	0	0	-9(7)
Zn1	95(14)	300(30)	111(16)	0	0	-23(11)
Zn2	141(10)	96(17)	105(11)	0	0	36(8)
Zn3	145(10)	143(18)	60(11)	0	0	20(8)
Zn4	141(10)	153(18)	88(11)	0	0	14(8)
Zn5	138(10)	116(18)	102(12)	0	0	34(8)
Zn6	120(10)	184(19)	78(11)	0	0	16(8)
Zn7	83(10)	320(20)	87(11)	0	0	-43(8)
Zn8	190(12)	190(16)	90(9)	0	0	14(9)
Zn9	110(10)	90(17)	76(11)	0	0	27(8)
Zn10	161(11)	128(18)	127(12)	0	0	28(9)
Zn11	58(11)	530(30)	69(12)	0	0	-41(8)
Zn12	97(6)	116(12)	164(8)	-35(6)	-10(8)	15(5)
Zn13	123(7)	130(12)	180(9)	56(7)	52(8)	35(6)
Zn14	68(6)	87(12)	181(8)	-19(6)	-15(8)	13(5)
Zn15	93(6)	115(12)	161(8)	-30(6)	-18(7)	-7(5)
Zn16	124(7)	118(12)	220(9)	56(7)	62(8)	47(6)
Zn17	181(7)	183(13)	189(9)	53(8)	96(9)	28(6)
Zn18	68(4)	104(8)	139(5)	-19(7)	-10(9)	15(4)
Zn19	154(7)	150(12)	135(8)	-67(7)	-48(8)	32(5)
Zn20	216(9)	253(15)	132(9)	-170(8)	-127(8)	94(6)

12.4 Physical properties of NiZn₈

12.4.1 Thermochemical analyses

The zinc-rich monoclinic phase NiZn₈ undergoes peritectic decomposition at 790(3) K upon heating into the cubic γ -brass type phase Ni₅Zn₂₁ and Zn. The successive endothermic peak at 1100(3) K corresponds to the incongruent melting of the γ -Ni₅Zn₂₁ phase. During the cooling process, three exothermic events were observed. As proven by X-ray powder diffraction of a quenched sample, the first exothermic peak at 1090(2) K corresponds to the re-formation of γ -Ni₅Zn₂₁. The next one at 753(2) K refers to the partial conversion of the NiZn₈ phase followed by a peak at 692(1) K corresponding to the solidification of residual Zn. Noteworthy, the zinc-rich phase re-forms almost complete upon cooling with an applied cooling rate of 10 K min⁻¹, if the sample is thermally treated not higher than 900 K (cf. Inset Fig. 12.2). However, when the sample was heated above the melting point of the Ni₅Zn₂₁ phase, the Zn-rich phase resists to transform completely into the monoclinic phase, only partial conversion into the Zn-rich phase is observed. This could be due to partial evaporation of Zn from the sample or due to the sluggish peritectic formation of NiZn₈ from γ -Ni₅Zn₂₁ and liquid Zn. A typical thermogram of NiZn₈ is shown in Fig. 12.2.

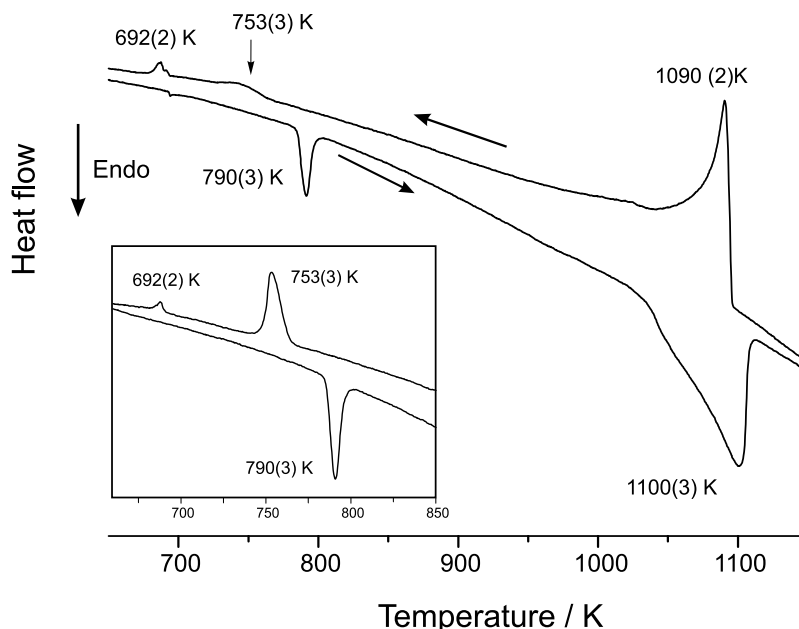


Figure 12.2: A typical thermogram of the phase NiZn₈. The inset shows that the formation of the zinc-rich phase almost completely upon cooling.

12.5 Results and discussion

The redetermination of the structure of NiZn_8 phase reveals that the lattice parameters differ quite significantly from the reported ones by Critchley *et al.* [109]. The obtained lattice parameters are as follows; $a = 1337.0(3)$, $b = 748.3(1)$, $c = 1848.5(3)$ pm and $\beta = 97.82(3)^\circ$ in a C-centered monoclinic system, $C2/m$ space group (Pearson symbol, mC128). The reported structure is a spatially averaged structure, since the superstructure reflections along c^* are not perfectly commensurate. The structural refinement of the average structure yielded large correlations between different atoms. Significant residual charge densities are shown in the difference Fourier map. This indicates that the structure is presumably incommensurately modulated. Hence, the structure was treated as an incommensurately modulated structure. The modulation is quite strong and well pronounced in the case of the PtZn_7 structure. However, in the case of NiZn_8 the superstructure reflections are very close to a commensurate approach, see Fig. 12.3.

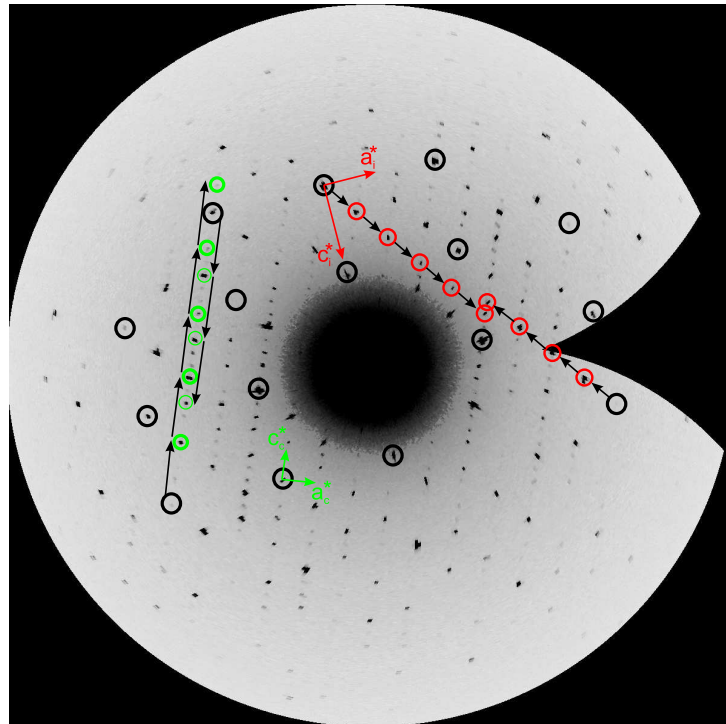


Figure 12.3: The $h0l$ section of NiZn_8 reciprocal space, reconstructed from area detector data. Main reflections are marked in black circles. Green circles indicate the q -vector $\frac{5}{23}[\bar{3} 0 2]^*$ that is compatible with the commensurate super cell. Red circles indicate a different indexing that adheres to the incommensurate PtZn_7 model.

The NiZn₈ structure can be adequately described in the (3+1)-dimensional superspace. A set of strong reflections could be indexed with a basic C-centered monoclinic cell. The lattice parameters are: $a = 423.14$ pm, $b = 763.35$ pm, $c = 258.77$ pm and $\beta = 92.05^\circ$. The subset of weak reflections, so-called satellites, can be indexed with a modulation vector $\mathbf{q} \approx \frac{1}{9} [3\ 0\ 4]^*$. Finally, the structure was refined in the (3+1)-dimensional superspace group $C2/m(\alpha 0 \gamma)00$ using the program JANA2000 [59]. Fig. 12.3 shows two indexing schemes of reflections based on the cells of the commensurate and incommensurate structures, respectively.

12.5.1 Metrical relation between commensurate and incommensurate structural models

The single crystal X-ray diffraction pattern of the compound NiZn₈ displays a subset of strong reflections that leads to a fairly straight-forward indexing on the basis of a C-centred monoclinic unit cell with the following parameters,

$$\begin{aligned} a &= 4.2314 \text{ \AA} \\ b &= 7.6335 \text{ \AA} \quad \beta = 92.05^\circ \\ c &= 2.5877 \text{ \AA} \end{aligned}$$

Note however that several strong reflections remain un-indexed in Fig. 12.3. The subset of weaker reflections may be indexed using an additional vector, $\mathbf{q} \approx \frac{1}{9} [3\ 0\ 4]^*$. This choice enables one to index all reflections and gives a clear, hierarchical, intensity distribution. The q-vector refines to (0.3478, 0, 0.435). Note that the corresponding Ni compound, δ -NiZn₈ reported by Critchley *et al.* [109], has been reported in a cell that corresponds well to $\mathbf{q} = \frac{1}{9} [3\ 0\ 4]^*$. The commensurate q vector indicated implies a transformation matrix of the form

$$M_1 = \begin{pmatrix} -3 & 0 & 2 \\ 0 & -1 & 0 \\ 0 & 0 & 3 \end{pmatrix}$$

yielding the unit cell

$$\begin{aligned} a &= 7.7631 \text{ \AA} \\ b &= 7.6335 \text{ \AA}, \quad \beta = 110.41^\circ \\ c &= 13.5361 \text{ \AA}. \end{aligned}$$

differing (apart from the setting) only slightly from the reported δ -NiZn₈ [109] cell of

$$\begin{aligned}a &= 13.37 \text{ \AA} \\b &= 7.47 \text{ \AA}, \quad \beta = 111.3^\circ \\c &= 7.65 \text{ \AA}.\end{aligned}$$

Interestingly, a re-determination of δ -NiZn₈ shows the q-vector actually differing significantly from this value, and that a far superior description is given by the cell

$$\begin{aligned}a &= 13.371 \text{ \AA} \\b &= 7.482 \text{ \AA}, \quad \beta = 97.40^\circ \\c &= 18.512 \text{ \AA}.\end{aligned}$$

This implies a transformation (again ignoring the setting)

$$M_2 = \begin{pmatrix} -7 & 0 & 2 \\ 0 & -1 & 0 \\ 1 & 0 & 3 \end{pmatrix}$$

or, for the reciprocal cell

$$M_2^{-1} = \begin{pmatrix} \frac{-3}{23} & 0 & \frac{2}{23} \\ 0 & -1 & 0 \\ \frac{1}{23} & 0 & \frac{7}{23} \end{pmatrix}$$

implying the q-vector $\mathbf{q} = \frac{n}{23}[\bar{3} 0 2]^*$ which is quite apparent in Fig. 12.3 (n chosen as 5). This value appears to be an approximation as indicated by slight misalignments and irregular intensity distribution along $[\bar{3} 0 2]^*$, while on the other hand, the $\sim[3 0 4]^*$ direction again yields perfectly aligned reflections with a very regular intensity decline with increasing satellite order.

In spite of these observations, the NiZn₈ phase is treated as a commensurate structure for the benefit of a clear description of the structure. The structural features of NiZn₈ are not described herein. By all indications the structure of NiZn₈ is isotypic to the PtZn₇ structure. The structural description for PtZn₇ is given in Chapter 4.

An approximate composition of the phase was established from EDX analyses on selected crystals. According to EDX analyses the composition was found to be 11 ± 1 at.% of Ni. This value agrees fairly with the composition obtained from the single crystal structural refinement with the proposed structural model. Single crystal X-ray diffraction analyses of a second crystal from another batch revealed that the homogeneity range of the phase is narrow.

As seen from Fig. 12.4, the commensurately approximated modulated structure of NiZn_8 produces calculated intensities which are in much better agreement with the observed intensities than those calculated with structural model proposed by Critchley *et al.* [109]. In addition, the assigned composition of the phase is also in good agreement with the one obtained from EDX analyses.

The interatomic distances of Ni-Zn cover the range from 247.6 – 265.3 pm. The shorter distances compare well with the sum of covalent radii of Ni ($r_{\text{Ni}}^c = 121$ pm) and Zn ($r_{\text{Zn}}^c = 131$ pm) while longer distances compare fairly well with the sum of atomic radii $r_{\text{Ni}}^a = 124$ pm and $r_{\text{Zn}}^a = 133.5$ pm. The interatomic distances for NiZn_8 are listed in Table 12.4.

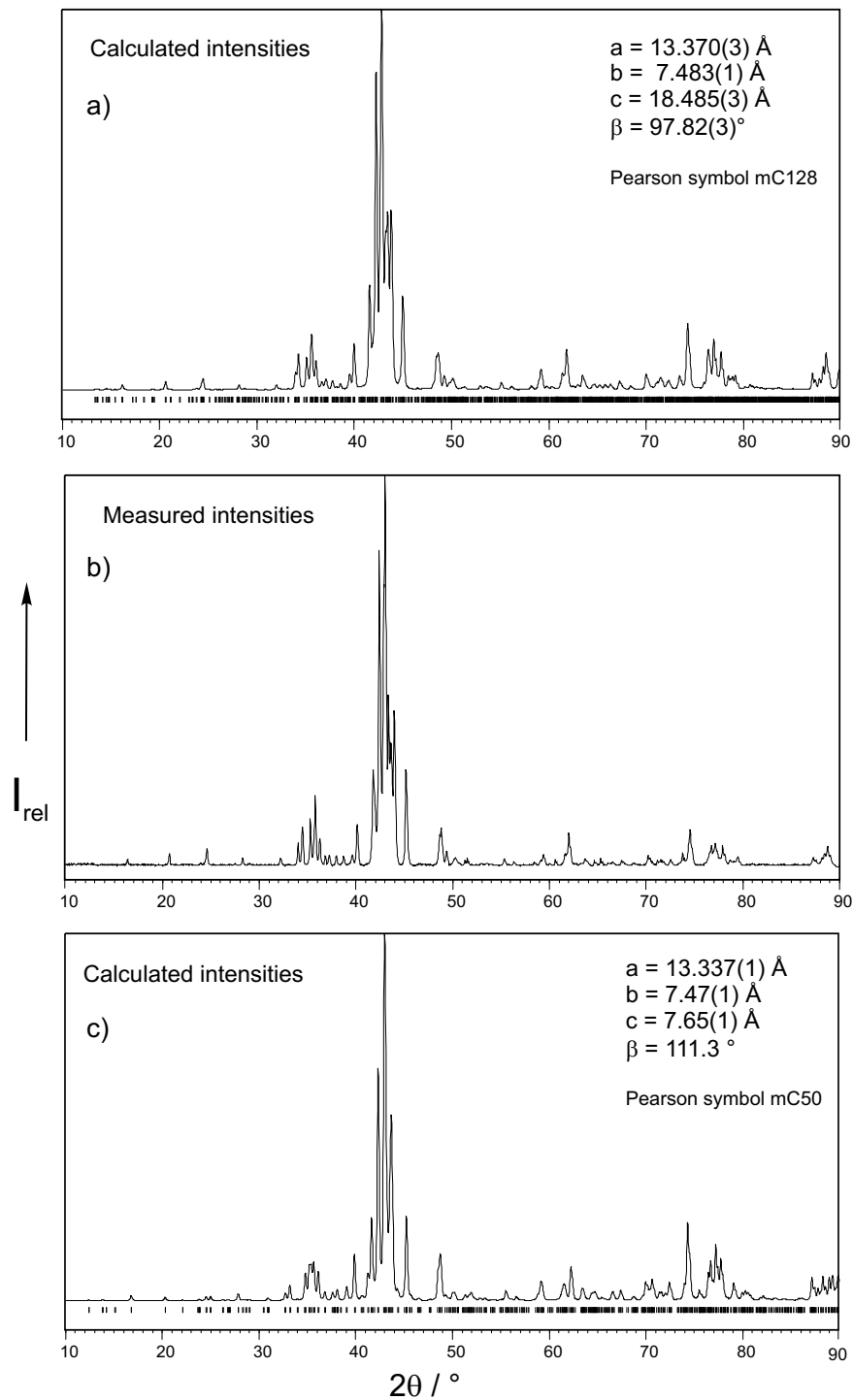


Figure 12.4: Calculated and measured X-ray intensities for NiZn₈. a) Calculated intensities from the present work. b) Measured intensities from the single phase sample. c) Calculated intensities from Critchley *et al.* [109].

Table 12.4: Interatomic distances for NiZn₈ (< 320 pm)

Ni1	Zn7	251.9(5)	2×	Zn5	Zn4	256.3(4)	1×	Zn12	Zn15	255.5(3)	1×	Zn16	Ni3	257.2(3)	1×																									
	Zn14	259.4(2)	4×		Zn13	260.6(4)	2×		Ni2	259.7(3)	1×		Ni4	258.1(3)	1×																									
	Zn3	262.0(3)	2×		Zn20	260.7(3)	2×		Zn10	261.6(2)	1×		Zn9	259.4(4)	1×																									
	Zn19	264.0(2)	4×		Ni3	264.1(5)	1×		Zn2	265.2(4)	1×		Zn18	260.8(3)	1×																									
Ni2	Zn1	251.6(5)	1×	Zn6	Zn15	266.8(2)	2×	Zn12	Zn20	266.0(4)	1×	Zn11	Zn13	269.1(4)	1×																									
	Zn11	251.7(5)	1×		Zn12	278.5(3)	2×		Zn12	270.3(3)	1×		Zn11	273.1(3)	1×																									
	Zn15	259.2(3)	2×		Zn9	254.9(4)	1×		Zn1	271.0(2)	1×		Zn6	282.7(3)	1×																									
	Zn12	259.7(3)	2×		Ni3	256.2(4)	1×		Zn5	278.5(3)	1×		Zn16	286.0(3)	1×																									
	Zn2	261.2(4)	1×		Zn7	262.5(3)	1×		Zn8	279.4(3)	1×		Zn7	288.3(3)	1×																									
	Zn4	261.3(4)	1×		Zn18	265.9(4)	2×		Zn17	284.9(4)	1×		Zn3	292.1(3)	1×																									
	Zn17	263.2(3)	2×		Zn14	279.3(3)	2×		Zn13	302.8(4)	1×		Zn14	298.7(4)	1×																									
	Zn20	264.9(3)	2×		Zn16	282.7(3)	2×		Zn4	306.6(5)	1×		Zn20	319.8(4)	1×																									
Ni3	Zn20	248.6(4)	2×	Zn7	Zn14	297.9(5)	2×	Zn13	Zn17	318.5(4)	1×	Zn17	Zn10	255.4(4)	1×																									
	Zn7	249.8(5)	1×		Zn19	304.1(3)	2×		Ni4	256.4(2)	1×		Zn10	260.2(3)	1×																									
	Zn6	256.2(4)	1×		Ni3	249.8(5)	1×		Ni3	259.4(3)	1×		Ni2	263.2(3)	1×																									
	Zn16	257.2(3)	2×		Ni1	251.9(5)	1×		Zn18	259.6(3)	1×		Zn15	263.9(4)	1×																									
	Zn13	259.4(3)	2×		Zn6	262.5(3)	1×		Zn5	260.6(4)	1×		Zn20	267.5(3)	1×																									
	Zn18	263.1(3)	2×		Zn3	269.0(3)	1×		Zn16	269.1(4)	1×		Zn4	275.4(3)	1×																									
	Zn5	264.1(5)	1×		Zn13	272.0(3)	2×		Zn7	272.0(3)	1×		Zn1	281.9(2)	1×																									
	Ni4	Zn11	247.6(5)		1×	Zn8	Zn13		272.0(3)	2×	Zn12		Zn13	283.7(3)	1×	Zn15	Zn15	282.9(4)	1×																					
Zn19		250.8(4)	2×	Zn14	275.5(3)		2×	Zn8	283.9(3)	1×		Zn12	284.9(4)	1×																										
Zn8		255.7(4)	1×	Zn19	277.6(3)		2×	Zn2	289.7(3)	1×		Zn4	291.9(3)	1×																										
Zn13		256.4(2)	2×	Zn16	288.3(3)		2×	Zn11	291.1(3)	1×		Zn17	292.7(3)	1×																										
Zn16		258.1(3)	2×	Zn10	249.8(4)		1×	Zn12	302.8(4)	1×		Zn12	318.5(4)	1×																										
Zn9		263.9(5)	1×	Ni4	255.7(4)		1×	Zn19	317.4(4)	1×		Zn18	Zn13	259.6(3)	1×																									
Zn18		265.3(3)	2×	Zn11	261.7(3)		1×	Zn3	319.3(5)	1×			Zn16	260.8(3)	1×																									
Zn1		Ni2	251.6(5)	2×	Zn12		Zn18	267.2(4)	2×	Zn14			Zn14	256.3(3)	1×		Zn18	Ni3	263.1(3)	1×																				
	Zn4		269.2(3)	2×		Zn12	279.4(3)	2×	Ni1		259.4(2)		1×	Zn18	263.7(2)	1×																								
	Zn12		271.0(2)	4×		Zn13	283.9(3)	2×	Zn9		265.4(2)		1×	Zn20	264.1(4)	1×																								
	Zn17		281.9(2)	4×		Zn15	293.5(5)	2×	Zn19		266.0(4)		1×	Ni4	265.3(3)	1×																								
	Zn2		Zn3	255.5(4)		1×	Zn9	Zn20	306.6(3)		2×		Zn7	Zn3	267.0(4)	1×		Zn19	Zn6	265.9(4)	1×																			
				Ni2		261.2(4)		1×	Zn6		254.9(4)			1×	Zn14	268.3(3)			1×	Zn19	266.0(4)	1×																		
				Zn12		265.2(4)		2×	Zn16		259.4(4)	2×		Zn7	275.5(3)	1×			Zn8	267.2(4)	1×																			
				Zn11		269.2(3)		1×	Zn19		260.1(3)	2×		Zn9	277.7(3)	1×			Zn3	273.7(2)	1×																			
Zn18		274.1(2)		2×	Ni4	263.9(5)		1×	Zn6	279.3(3)	1×	Zn2		274.1(2)	1×																									
Zn20		276.6(3)		2×	Zn14	265.4(2)		2×	Zn19	285.4(4)	1×	Zn19		Ni4	250.8(4)	1×																								
Zn13		289.7(3)		2×	Zn14	277.7(3)		1×	Zn6	297.9(5)	1×			Zn9	260.1(3)	1×																								
Zn3		Zn2		255.5(4)	1×	Zn10		Zn14	277.7(3)	1×	Zn15			Zn16	298.7(4)	1×	Ni1		264.0(2)	1×																				
	Ni1		262.0(3)	1×	Zn8		249.8(4)	1×	Zn12	255.5(3)			1×	Zn14	266.0(4)	1×																								
	Zn14		267.0(4)	2×	Zn17		255.4(4)	2×	Ni2	259.2(3)			1×	Zn18	266.0(4)	1×																								
	Zn7		269.0(3)	1×	Zn17		260.2(3)	2×	Zn17	263.9(4)			1×	Zn19	270.1(3)	1×																								
	Zn18		273.7(2)	2×	Zn12		261.6(2)	2×	Zn15	265.6(3)			1×	Zn3	276.1(3)	1×																								
	Zn19		276.1(3)	2×	Zn10		264.3(5)	1×	Zn5	266.8(2)			1×	Zn7	277.6(3)	1×																								
	Zn16		292.1(3)	2×	Zn15		277.7(3)	2×	Zn4	269.7(4)		1×	Zn14	285.4(4)	1×																									
	Zn13		319.3(5)	2×	Zn11		Ni4	247.6(5)	1×	Zn11		277.0(3)	1×	Zn19	294.5(3)	1×																								
Zn4	Zn5	256.3(4)	1×	Zn11		Ni2	251.7(5)	1×	Zn10	277.7(3)	1×	Zn6	304.1(3)	1×																										
		Ni2	261.3(4)			1×	Zn8	261.7(3)	1×	Zn4	280.6(2)	1×	Zn13	317.4(4)	1×																									
		Zn1	269.2(3)			1×	Zn2	269.2(3)	1×	Zn17	282.9(4)	1×	Zn20	Ni3	248.6(4)	1×																								
		Zn15	269.7(4)			2×	Zn16	273.1(3)	2×	Zn20	287.3(4)	1×		Zn5	260.7(3)	1×																								
		Zn17	275.4(3)			2×	Zn15	277.0(3)	2×	Zn8	293.5(5)	1×		Zn18	264.1(4)	1×																								
		Zn15	280.6(2)			2×	Zn20	277.4(3)	2×	Zn15	Zn8	293.5(5)		1×	Ni2	264.9(3)	1×																							
		Zn17	291.9(3)			2×	Zn13	291.1(3)	2×						Zn12	266.0(4)	1×	Zn12	266.0(4)	1×																				
		Zn12	306.6(5)		2×	Zn11	Zn11	291.1(3)	2×						Zn17	267.5(3)	1×	Zn17	267.5(3)	1×																				
Zn4	Zn5	256.3(4)	1×	Zn11	Zn11										291.1(3)	2×	Zn2	276.6(3)	1×	Zn2	276.6(3)	1×																		
		Ni2	261.3(4)														1×	Zn11	Zn11	291.1(3)	2×	Zn11	277.4(3)	1×	Zn11	277.4(3)	1×													
		Zn1	269.2(3)										1×				Zn11					Zn11	291.1(3)	2×	Zn15	287.3(4)	1×	Zn15	287.3(4)	1×										
		Zn15	269.7(4)										2×												Zn11	Zn11	291.1(3)	2×	Zn20	293.3(3)	1×	Zn20	293.3(3)	1×						
		Zn17	275.4(3)										2×																Zn11	Zn11	291.1(3)	2×	Zn8	306.6(3)	1×	Zn8	306.6(3)	1×		
		Zn15	280.6(2)							2×	Zn11	Zn11	291.1(3)	2×																			Zn16	319.8(4)	1×	Zn16	319.8(4)	1×		
		Zn17	291.9(3)							2×																							Zn11	Zn11	291.1(3)	2×				
		Zn12	306.6(5)			2×	Zn11	Zn11	291.1(3)	2×																														

12.6 Summary

- Single crystals of NiZn₈ were prepared with the use of the melt centrifugation technique and by a conventional solid state method. The most Zn-rich phase undergoes peritectic decomposition at 790 K into γ -Ni₅Zn₂₁ and Zn.
- Re-determination of the structure revealed that the reported cell parameters are quite far off from the obtained cell parameters. The structure is approximated as a commensurate superstructure of a defective AlB₂-structure with the following lattice parameters; a = 1337.0(3) pm, b = 748.3(1) pm, c = 1848.5(3) pm, $\beta = 97.82(3)^\circ$ in space group C2/m. The structure can more precisely be described as an incommensurate modulated structure with a modulation vector $\mathbf{q} \approx \frac{1}{9}[3\ 0\ 4]^*$, C2/m($\alpha 0 \gamma$)00, a = 423.14 pm, b = 763.35 pm, c = 258.77 pm and $\beta = 92.05^\circ$.
- By all indications the NiZn₈ structure is isostructural to that of PtZn₇.

Chapter 13

Ni₁₈Zn₅₁ – A γ -brass related composite structure

13.1 Introduction

The structure of NiZn₃ was reported by Schubert *et al.* [12]. This phase is known to be one of the complex phases which is related to γ -brass type structure with orthorhombic symmetry. According to authors, the γ -brass related phase NiZn₃ crystallizes in the acentric space group Abm2. The unit cell comprised of 276 atoms, and the Pearson symbol is oA276. In addition, similar kind of structures were uncovered in the congeneric Pd-Zn and Pt-Zn system. These structures are adequately described in Cmce space group. This chapter focuses on the syntheses and characterization of the γ -brass related phase, to which Schubert *et al.* [12] assigned the composition NiZn₃ [12].

13.2 Syntheses

The syntheses were carried out in previously out-gassed, evacuated silica ampoules using pure Ni and Zn as a starting materials. The mole fraction x_{Ni} was systematically varied between 0.24 and 0.35. The ampoules were heated continuously at a rate of 120 K h⁻¹ to a temperature of 1325 K at which the reactants mixtures were kept for 12 h. Subsequently, the ampoules were cooled to 970 K in the course of 72 h and then quenched or brought to room temperature in less than 12 h.

13.3 Structure determination

X-ray diffraction studies were carried out with a single crystal of $0.18 \times 0.14 \times 0.15 \text{ mm}^3$ in size on an IPDS-II diffractometer. The collected reflections were subjected for Lorentz polarization and numerical absorption correction using the programs X-SHAPE and X-RED [61, 62]. The structure was first refined in the space group Abm2 from the known structural model NiZn₃ [12] using the program SHELX-97 [58]. Final cycles of refinement with isotropic displacement parameters converged to the R1 value of 5.8% for 160 parameters. However, the results of the refinement showed large correlations between the atomic positions of Zn and Ni. This was taken as an indication of possible missing symmetry elements. For this purpose, the data was evaluated using the program PLATON [60] to find correct symmetry. It suggested the presence of a-glide plane and an inversion center leading to the space group Cmce (No. 64). Moreover, a similar type structure Pt₁₈Zn₅₁ has been found in the Pt-Zn system, which is described in Cmce space group with ordered atomic distribution of Pt and Zn. The starting parameters for the structural refinement were taken from Pt₁₈Zn₅₁ assuming that both the structures are isotypic. Subsequently, the atomic positions of Pt atoms were replaced to Ni and one of the mixed position was set to Zn. However, the weak X-ray scattering contrast of Ni and Zn hampered an unambiguous assignment of the two constituents in the structure. The final refinement cycles using anisotropic thermal displacement parameters converged to R1 value of 3.5% for 173 parameters. The details concerning crystallographic data, refinement and atomic parameters are tabulated in Table 13.1 and 13.2, respectively.

Table 13.1: Crystallographic and technical data for the single-crystal structure determination

Sum formula	Ni ₁₈ Zn ₅₁
Space group (No.)	Cmce (64)
Z	4
a / pm	1250.6(3)
b / pm	885.3(2)
c / pm	3325.0(7)
V / 10 ⁶ pm ³	3681.3(13)
Molar mass / g mol ⁻¹	4390.65
ρ_{cal} / g cm ⁻³	7.946
μ / mm ⁻¹	41.69
<i>Data collection</i>	
Crystal size / mm ³	0.18 × 0.14 × 0.15
Diffractometer	IPDS-II (STOE & Cie)
Temperature / K	293(2)
Radiation / Monochromator	MoK α / Graphite
Distance crystal-IP / mm	120
ϕ ; $\omega_{min} - \omega_{max}$; $\Delta\omega$	0; 0–180; 1
ϕ ; $\omega_{min} - \omega_{max}$; $\Delta\omega$	80; 0–180; 1
$2\theta_{max}$ / °	54.0
Collected reflections	–15 ≤ h ≤ 15 –11 ≤ k ≤ 11 –41 ≤ l ≤ 42
Total No. of reflections	25578
<i>Data reduction</i>	
Program	IPDS-II-Software [57] / X-RED [61]
Absorption correction	Numerical, X-SHAPE [62]
Max. / Min. transmission	0.0547 / 0.0094
Unique reflections	2090
R _{int}	0.1093
<i>Refinement</i>	
Program	SHELXL-97 [58]
Refined on	F _o ²
Reflections I _o > 2σ(I _o)	1024
Variables	168
R ₁ (I _o > 2σ(I _o))	0.0358
R ₁ (all)	0.0684
wR ₂ (all)	0.1453
Goodness of fit	0.85
$\Delta\rho_{max} / \Delta\rho_{min} / 10^{-6}$ e pm ⁻³	1.095 / –1.617

$$1/w = \sigma^2(F_o^2) + (0.1(\text{Max}(F_o^2, 0) + 2F_c^2)/3)^2$$

Table 13.2: Atomic coordinates and equivalent isotropic displacement parameters $U_{\text{eq}}(\text{pm}^2)$ for $\text{Ni}_{18}\text{Zn}_{51}$

Atom No.	Wy.	x	y	z	sof	U_{eq}
Zn1	4a	0	0	0	1	234(5)
Zn2	8f	0	0.4666(2)	0.42293(5)	1	233(4)
Zn3	8f	0	0.0481(1)	0.15442(6)	1	218(3)
Zn4	8f	0	0.4555(2)	0.27092(6)	1	267(4)
Zn5	8f	0	0.01009(16)	0.30743(5)	1	237(4)
Zn6	8f	0	0.02495(18)	0.38560(5)	1	241(4)
Zn7	8f	0	0.44999(18)	0.03612(5)	1	236(4)
Zn8	16g	0.1172(1)	0.20309(12)	0.03225(4)	1	221(3)
Zn9	16g	0.1262(1)	0.24042(14)	0.40721(4)	1	247(3)
Zn10	16g	0.1776(1)	0.09676(12)	0.10251(4)	1	221(3)
Zn11	16g	0.18653(8)	0.37372(11)	0.34093(5)	1	269(3)
Zn12	16g	0.11273(8)	0.29920(10)	0.15579(4)	1	231(3)
Zn13	16g	0.1809(1)	0.10716(14)	0.20997(4)	1	262(3)
Zn14	16g	0.1228(1)	0.21822(14)	0.27958(4)	1	273(3)
Zn15	16g	0.1778(1)	0.40519(12)	0.08646(4)	1	236(3)
Zn16	16g	0.1858(1)	0.11979(13)	0.47609(4)	1	235(3)
Zn17	16g	0.1772(1)	0.40889(13)	0.22365(4)	1	229(3)
Ni1	8f	0	0.2338(2)	0.46895(6)	1	206(4)
Ni2	8f	0	0.2464(2)	0.09337(6)	1	194(4)
Ni3	8f	0	0.2649(2)	0.34362(7)	1	202(4)
Ni4	8f	0	0.2386(2)	0.21878(5)	1	193(4)
Ni5	16g	0.1756(1)	0.41444(14)	0.46557(4)	1	215(3)
Ni6	16g	0.17560(8)	0.08257(11)	0.34510(5)	1	196(3)

Table 13.3: Anisotropic displacement parameters U (pm^2) for $\text{Ni}_{18}\text{Zn}_{51}$

Atom No.	U11	U22	U33	U12	U13	U23
Zn1	251(12)	215(10)	235(11)	0	56(8)	0
Zn2	254(9)	238(7)	207(8)	0	39(6)	0
Zn3	257(7)	194(6)	205(7)	0	-4(7)	0
Zn4	295(9)	210(7)	295(9)	0	-52(6)	0
Zn5	213(9)	249(8)	249(8)	0	-37(6)	0
Zn6	253(9)	217(7)	253(8)	0	65(6)	0
Zn7	274(9)	215(7)	218(8)	0	26(6)	0
Zn8	261(7)	228(5)	175(6)	27(4)	-4(4)	14(4)
Zn9	265(5)	275(5)	202(5)	7(5)	-45(4)	0(5)
Zn10	217(6)	241(5)	205(6)	40(5)	9(4)	-13(5)
Zn11	242(5)	234(5)	332(7)	-38(3)	-34(5)	-1(6)
Zn12	267(5)	243(5)	183(5)	-26(3)	-16(5)	2(6)
Zn13	242(7)	287(6)	257(7)	50(5)	7(5)	11(5)
Zn14	281(7)	345(6)	192(6)	39(5)	32(4)	-8(5)
Zn15	245(6)	240(6)	224(6)	-30(4)	2(4)	20(4)
Zn16	228(6)	236(5)	241(6)	31(4)	-9(4)	-24(5)
Ni1	232(10)	179(8)	207(9)	0	-10(7)	0
Ni2	217(8)	183(7)	181(7)	0	-6(5)	0
Ni3	193(7)	196(7)	216(8)	0	12(9)	0
Ni4	184(10)	213(9)	181(9)	0	4(7)	0
Ni5	249(7)	218(6)	179(7)	-35(4)	-7(5)	14(5)
Ni6	218(5)	180(5)	190(6)	8(3)	3(5)	2(6)

13.4 Results and discussion

NiZn₃ is known to be the first γ -brass related complex phase reported by Schubert *et al.* [12]. According to them, the structure crystallizes in the acentric orthorhombic space group Abm2. So far, this is the only structural evidence for the existence of structurally complex phase next to the γ -brass region of Ni-Zn system as reported by Morton [32, 34]. However, redetermination of the phase revealed that the structure can appropriately be described in the centrosymmetric Cmce space group. The lattice parameters are nearly the same as reported by Schubert *et al.* [12]. The average composition determined by EDX analyses was 26 ± 1 at.% of Ni. This value agrees well with the assigned composition Ni₁₈Zn₅₁ ($x_{\text{Ni}} = 0.261$).

Ni₁₈Zn₅₁ crystallizes in a C-centered orthorhombic cell in space group Cmce ($a = 1250.6(3)$, $b = 885.3(2)$ and $c = 3325.0(7)$ pm). The unit cell accommodates 276 atoms, and the Pearson symbol is oC276. The lattice parameters of the orthorhombic structure are related to that of γ -brass type Ni₅Zn₂₁ [11] according to $a_o \approx \sqrt{2} a_\gamma$, $b_o \approx a_\gamma$ and $c_o \approx 8 \sqrt{2} \frac{a_\gamma}{3}$ ($a_\gamma = 892.06(2)$ pm). The structure of Ni₁₈Zn₅₁ is isotypic to that of Pt₁₈Zn₅₁ (See chapter 9).

Several attempts were made to synthesize NiZn₃ at the nominal composition of 25 at.% of Ni. They all were unsuccessful. Interestingly, at this starting composition another new phase Ni₂₃Zn₇₂ was found. The lattice parameters for this phase are: $a = 1251.6(3)$, $b = 885.1(2)$ and $c = 4571.2(9)$ pm, $Z = 4$, Pearson symbol oC380. The structure was refined in the space group Cmce (No. 64); it is composed of 380 atoms per unit cell. The structure of Ni₂₃Zn₇₂ is isotypic to Pt₅Zn₁₄ in the congeneric Pt-Zn system. It can also be classified as a derivative structure of the elemental bcc atomic arrangement of order 198 ($3\sqrt{2} \times 11\sqrt{2} \times 3 a_{bcc}^3$) with 16 ordered vacancies per unit cell. The crystallographic informations for Ni₂₃Zn₇₂ are given in the appendix.

13.4.1 Structural description and phase relation

The volume of the orthorhombic cell Ni₁₈Zn₅₁ offers space for 288 atoms, consequently, 12 positions are unoccupied. The vacancy concentration of the phase Ni₁₈Zn₅₁ is increased to $\frac{3}{72}$ compared to $\frac{1}{27}$ for that of the ordinary γ -phase (Ni₅Zn₂₁) [11]. Noteworthy, for all γ -brass related phases in the Pt-Zn system the vacancy concentration increases with decreasing valence electron concentration (*vec*), compared to ordinary γ -Pt₂Zn₁₁. This is contrary to the observation made

by Hume-Rothery and co-workers for the γ -brass type structures in the Cu-Al and Cu-Ga systems [100]. They found that the vacancy concentration increases with increasing valence electron concentration (*vec*).

Similar structures were found in the congeneric Pt-Zn ($\text{Pt}_{18}\text{Zn}_{51}$) and Pd-Zn ($\text{Pd}_{15}\text{Zn}_{54}$) systems [39]. In the case of the Pd-Zn system, the phase occurs at the Zn-rich side compared to the Ni-Zn and Pt-Zn system. Moreover, $\text{Pd}_{15}\text{Zn}_{54}$ [39] exhibit more structural disorder compared to the $\text{Pt}_{18}\text{Zn}_{51}$ phase. In the case of Pd-Zn, four atomic positions are statistically occupied whereas in the Pt-Zn system only one is mixed-occupied. The lattice parameters of the respective phases in congeneric M-Zn systems (M = Ni, Pd and Pt) are given in Table 13.4.

Table 13.4: Lattice parameters of the three isostructural phases phases in congeneric M-Zn systems (M = Ni, Pd and Pt)

Phase	$\text{Ni}_{18}\text{Zn}_{51}$	$\text{Pd}_{15}\text{Zn}_{54}$ [39]	$\text{Pt}_{18}\text{Zn}_{51}$
Space group (No.)		Cmce (64)	
Pearson symbol		oC276	
No. of vacancies		12	
a / pm	1250.6(3)	1290.95(5)	1293.04(13)
b / pm	885.3(2)	910.96(4)	911.24(7)
c / pm	3325.0(7)	3404.7(1)	3408.0(3)
V / 10^6 pm^3	3681.3	4003.9	4015.5

The structure of $\text{Ni}_{18}\text{Zn}_{51}$ can lucidly be described in terms of pentagonal anti-prismatic columns parallel to [001]. This approach of rationalizing the structure is opted to establish structural relations with other existing γ -brass related phases in Pt-Zn system. The structural features of $\text{Ni}_{18}\text{Zn}_{51}$ are similar to those of $\text{Pt}_{18}\text{Zn}_{51}$. In addition, this kind of structural features are generally observed for γ -brass [101] and related phases as described in chapter 7 & 9.

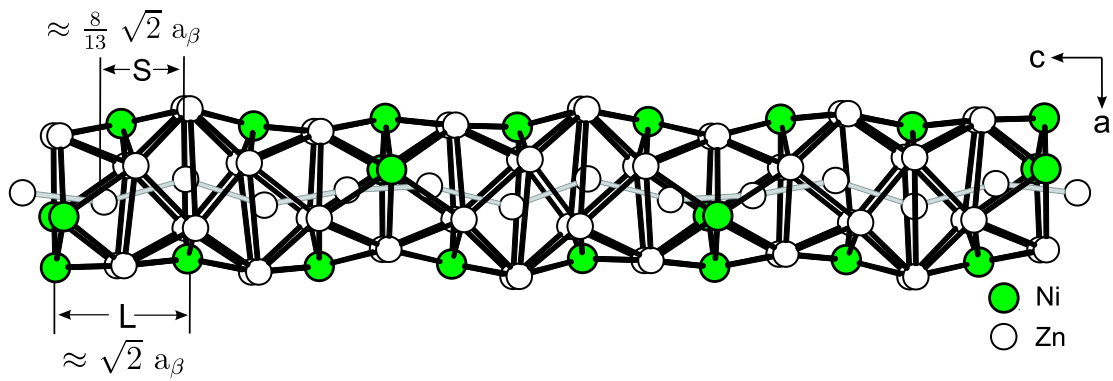


Figure 13.1: The pentagonal anti-prismatic column of the $\text{Ni}_{18}\text{Zn}_{51}$ structure. The letter S and L refers to the two sublattices which give rise to a mismatch between the chimney and the ladder.

Fig. 13.1, illustrates a single pentagonal anti-prismatic column filled with a zig-zag chain of Zn atoms. The presence of ordered vacancies is common features of γ -brass and related phases. In the $\text{Ni}_{18}\text{Zn}_{51}$ structure the vacancies are accumulated inside the columns. There are 12 ordered vacancies per unit cell. The vacancies are distributed over four columns, where each column accommodates 3 vacancies per repeating unit. The chain of Zn atoms inside the columns is slightly puckered. For a clear understanding, the structure is sub-divided into two entities. The pentagonal anti-prismatic frame forms a so-called chimney and the Zn atoms inside the column form of a ladder inside the columns. In spite of the vacancies the Zn atoms inside the column are nearly equally spaced at a distance of 258.0 – 268.7 pm (about $\frac{8}{13} \sqrt{2} a_{\beta}$). Consequently, the spacing does not match with the sublattice of the columnar framework thus, causing mismatch between the pentagonal columnar frame and the unequally spaced central Zn atoms. Similar structural features are observed in Nowotny-Chimney-ladder structures commonly found in some of the transition metal silicides [98] and germanides [97].

For the γ - $\text{Ni}_5\text{Zn}_{21}$ structures, the ratio of the repeat distance of two distinct sublattices is $\frac{3}{5}$ (corresponds to the ratio of L and S as described in Fig. 13.1). However, for the $\text{Pt}_{18}\text{Zn}_{51}$ structure, the misfit seems to lock-in at $\frac{8}{13}$. The letters ‘S’ and ‘L’ in Fig. 13.1 corresponds to the lengths of two sublattices that give rise to mismatch between the chimney and the ladder. The length S corresponds to $\approx \frac{8}{13} \sqrt{2} a_{\beta}$ and L to $\approx \sqrt{2} a_{\beta}$, where, a_{β} is the lattice parameter of a basic body centred cubic cell.

The X-ray powder diffraction analyses of the sample from which crystals were selected for X-ray diffraction studies showed few additional peaks. The additional peaks can be assigned to the tetragonal NiZn phase (AuCu type). This observation is in accordance with Morton's report [32, 34]. The diffractogram of the sample from which the crystals was selected for X-ray diffraction studies is shown in Fig 13.2.

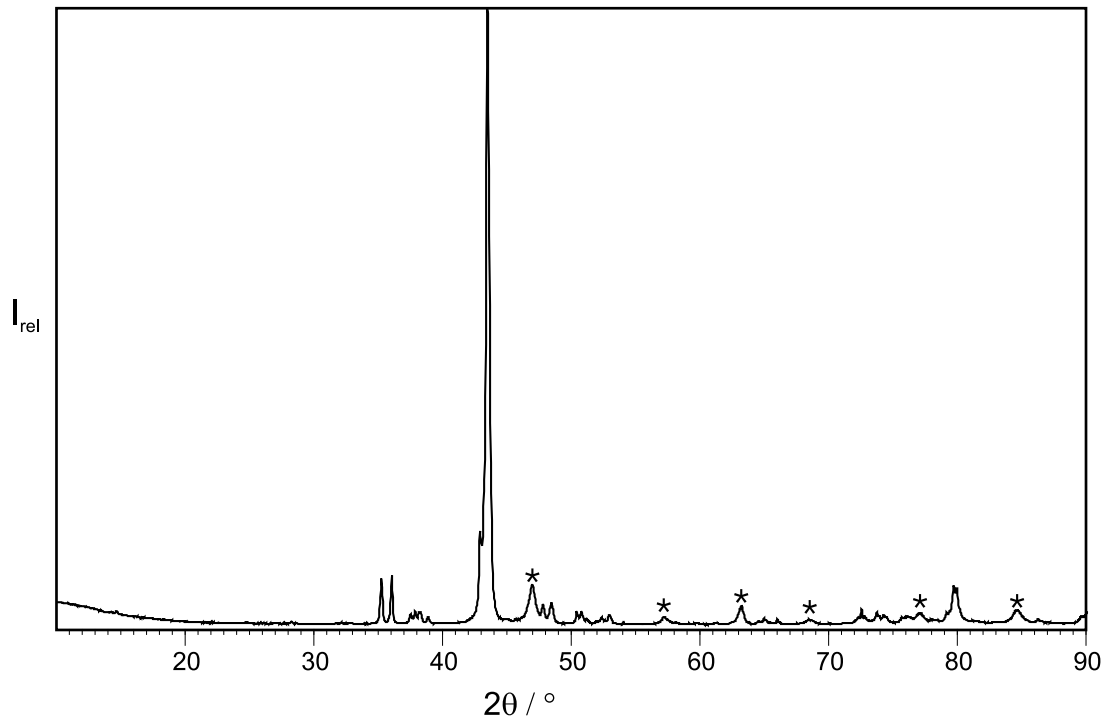


Figure 13.2: X-ray powder diffractogram ($\text{CuK}\alpha$) of the sample containing 34 at.% of Ni. Main peaks refer to $\text{Ni}_{18}\text{Zn}_{51}$, reflections indicated with asterisk are due to Ni-rich phase.

13.5 Summary

- Redetermination of the structure of $\text{Ni}_{18}\text{Zn}_{51}$, previously named as NiZn_3 , showed that the structure can be appropriately described in the orthorhombic, centrosymmetric space group Cmce (No. 64).
- The structure can be viewed as a γ -brass derivative structure. The metrical relations with respect to γ - $\text{Ni}_5\text{Zn}_{21}$ are: $a_o \approx \sqrt{2} a_\gamma$, $b_o \approx a_\gamma$ and $c_o \approx 8 \sqrt{2} \frac{a_\gamma}{3}$ ($a_\gamma = 892.06(2)$ pm).
- The structural features are related to those found for the well known Nowotny chimney-ladder composite structures. The chimney is made up of pentagonal anti-prismatic column and the ladder by Zn atoms arranged to zig-zag chains inside the chimney.
- It is shown that $\text{Ni}_{18}\text{Zn}_{51}$ coexist with NiZn (AuCu type).

Chapter 14

Phase analyses

14.1 X-ray powder diffraction

X-ray powder diffraction is used as a preliminary characterization method to identify γ -brass related phases. These phases exist next to the γ -Pt₅Zn₂₁ phase field region. Most of the X-ray powder patterns were collected with CuK $_{\alpha}$ radiation. Only selected samples have been subjected to high energy synchrotron radiation. The diffractograms obtained from X-ray synchrotron radiation show a better peak resolution compared to ones acquired with ordinary X-ray radiation (compare Fig. 14.1 and Fig. 14.2). The careful study of relative shifts in the peak positions gave a clear picture of the evolution of different phases with changing composition. Noteworthy, it is known from the congeneric Ni-Zn and Pd-Zn systems that the γ -region in these systems accommodate not only one structure, instead they accommodate a series of structures which are related to the γ -brass type structure. At first glance, the powder diffractograms of the samples between 23 – 28 at.% Pt appear to be rather similar. However, a closer look at some particular range (between $30^{\circ} < 2\theta < 40^{\circ}$ for CuK $_{\alpha}$ radiation) revealed some relative shifts in the peak positions with change in composition. Fig. 14.1 shows three diffractograms corresponding to the phase Pt₁₁Zn₃₂, Pt₁₈Zn₅₁ and Pt₅Zn₁₄. The magnified area is shown in the Fig. 14.1b.

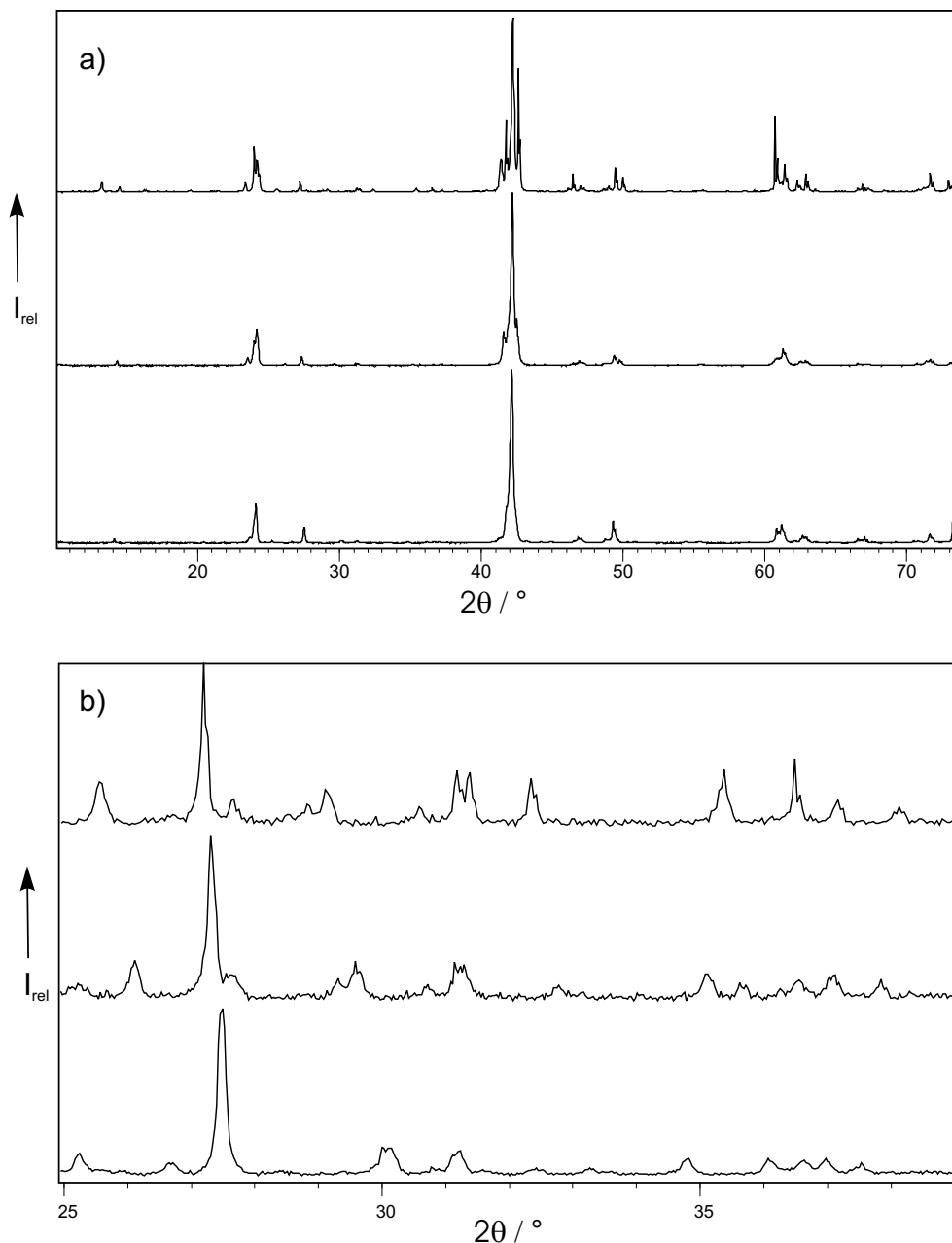


Figure 14.1: X-ray powder patterns collected for three different phases with $\text{CuK}\alpha$ radiation.

The high resolution X-ray diffractograms are obtained by synchrotron radiation from beamline X3B1 at the National Synchrotron Light Source, Brookhaven National Laboratory, New York, USA of wavelength $\lambda = 1.150626 \text{ \AA}$. The powder data were collected between $15^\circ < 2\theta < 40^\circ$. Fig. 14.2 is an example where one could see the major differences in the evolution of peak positions. Three phases were chosen for the evaluation of powder patterns, *i.e.* $\text{Pt}_{11}\text{Zn}_{32}$, $\text{Pt}_{18}\text{Zn}_{51}$ and $\text{Pt}_5\text{Zn}_{14}$ for which m/n values are $5/8$, $8/13$ and $18/11$, respectively.

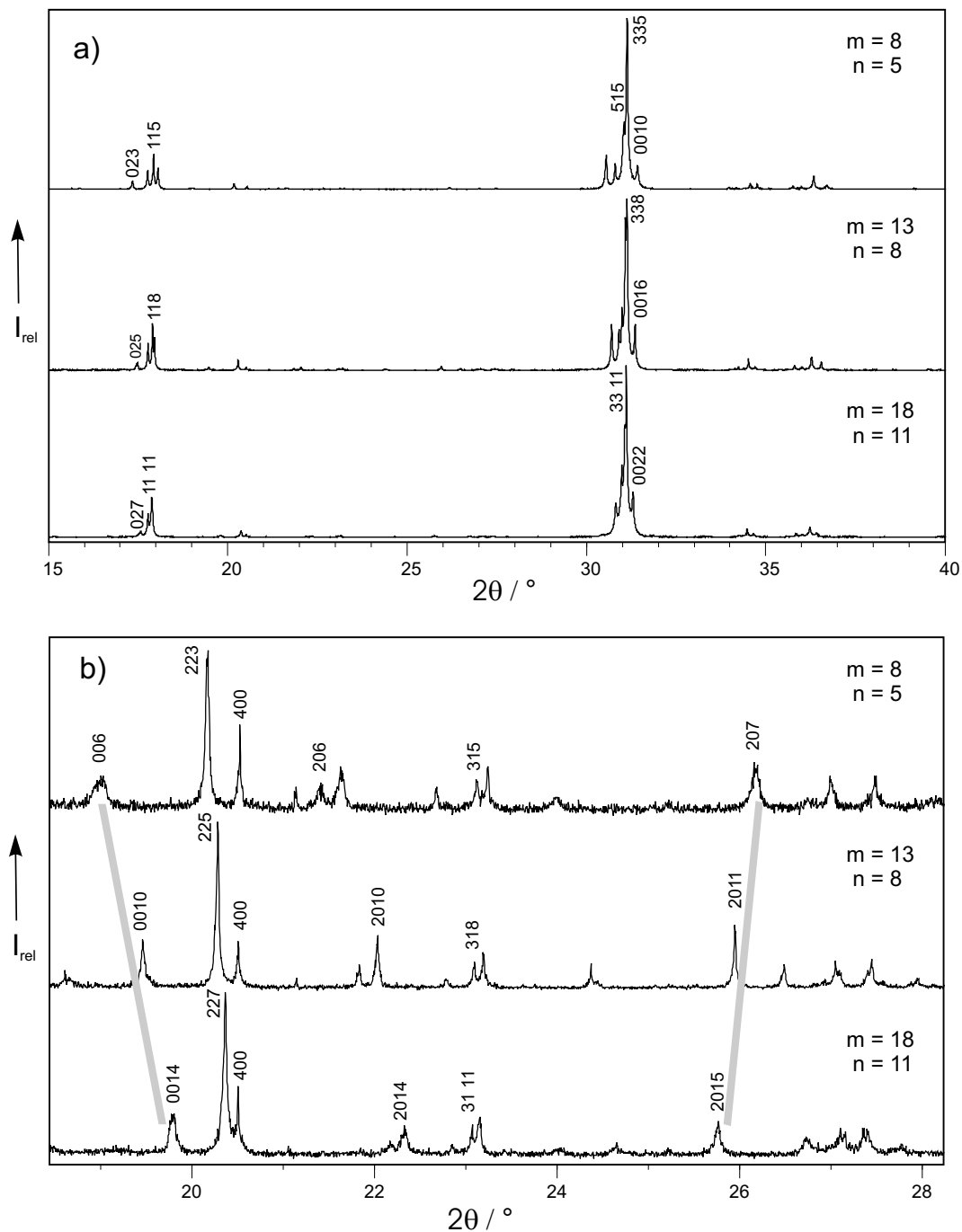


Figure 14.2: a) X-ray diffraction patterns are acquired from synchrotron radiation of wavelength $\lambda = 1.150626 \text{ \AA}$. The three phases correspond to $\text{Pt}_{11}\text{Zn}_{32}$, $\text{Pt}_{18}\text{Zn}_{51}$ and $\text{Pt}_5\text{Zn}_{14}$ (top to bottom). b) A magnified region of the diffractograms range between 19° and 28° in 2θ .

Fig. 14.2b shows that the $00l$ and $22l$ reflections are relatively shifted with respect to the 400 peak for the various phases. Such shifts are found not just in the region shown in Fig. 14.2b but are seen in other regions, too. In order to find the structural evolution from the relative shifts in the peak positions, a certain group of reflections are considered for the peak indexation procedure. The reflections which are relatively strong and clearly separated are taken into consideration. In

addition, reflections are chosen in such a way that the indices of h and k remain same for different γ -brass related phases but l changes according to m or n or $(m-n)$. The integers m and n are fixed for each γ -brass related phases. These values are tabulated in Table 8.1 for corresponding phases.

As seen in Fig. 14.2b, $00l$ and $22l$ reflections are noticeably shifted towards to higher 2θ as the c axis increases. For these reflections the indices l can be written in terms of m and n as $002(m-n)$ and $22(m-n)$. In contrary, $20l$ reflections (peak around 26° in 2θ) are shifted towards lower 2θ as the c axis increases. This group of $20l$ reflections can be expressed in terms of m and n as $203n-m$. These kinds of peak shifts are observed for other group of reflections, see Fig. 14.2b. Further studies are required to understand more about the structural evolution from these peak shifts.

14.2 Isopiestic measurements

The isopiestic vapor pressure method is an advantageous technique for the understanding of phase formation, stability and width (homogeneity range) from one single experiment. Fig. 14.3 displays the sequence of phase formation in the Zn-rich region of the Pt-Zn system. The phase region between 63 and 85 at.% Zn can be subdivided into four region. X-ray powder diffraction studies showed that the two regions at the Zn-rich side belong to the γ and γ_1 phases ($\text{Pt}_2\text{Zn}_{11-\delta}$ and $\text{Pt}_5\text{Zn}_{21}$). The region next to this accommodates a series of phases with orthorhombic symmetry, which are related to the γ -brass structure type. However, this region appears to be a single phase region. Indeed, single crystal structural analyses showed evidence for the existence of at least five new phases with very narrow homogeneity range. The Zn-poor region (63 at.% of Zn) accommodates two phases, which are related by a defective super-structure of the AlB_2 -type structure ($\text{Pt}_7\text{Zn}_{12}(\text{ht})$ and $\text{Pt}_{29}\text{Zn}_{49}(\text{rt})$). The compositions of these two phases are very close. The phase richest in Zn, PtZn_7 is not observed during these measurements. This is attributed to the low decomposition temperature of this phase compared to others. PtZn_7 decomposes into $\text{Pt}_2\text{Zn}_{11-\delta}$ and Zn at 752 K.

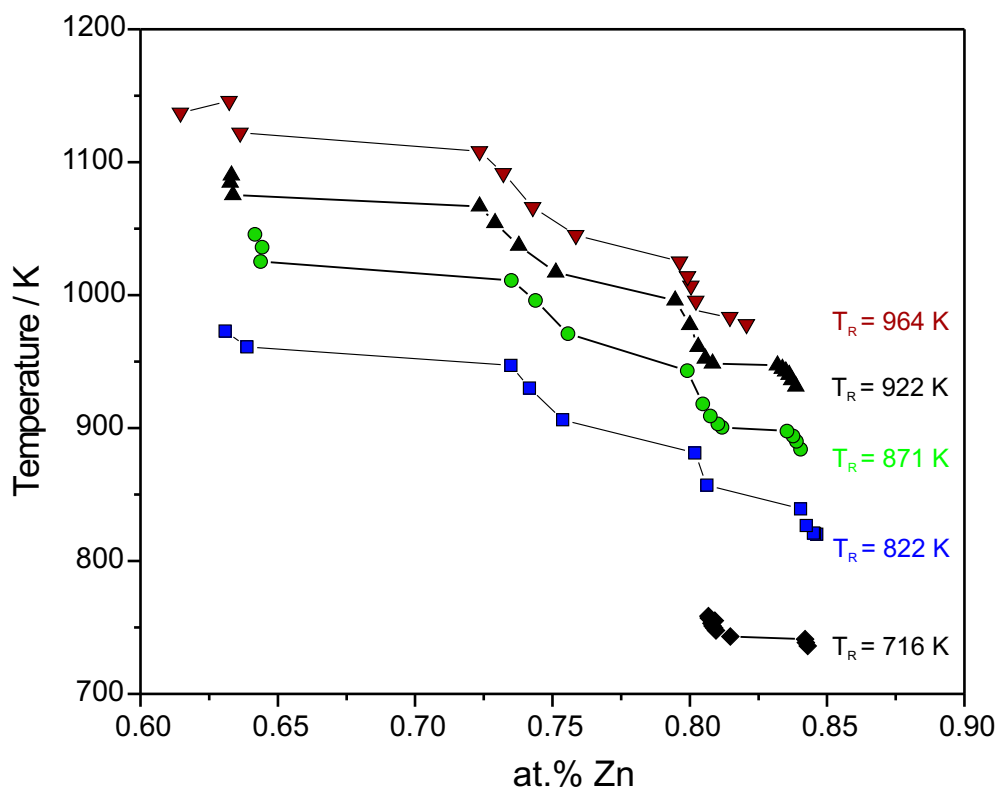


Figure 14.3: Sample temperature (T_S) vs. sample composition (isopiestic equilibrium curves) in the Pt-Zn system for the composition range between 60 and 85 at.% Zn.

Five successful isopiestic experiments were carried out with reservoir temperatures (T_R) varying between 716 and 964 K. Fig. 14.3 shows the results from five measurements with different reservoir temperature. The isopiestic equilibrium curves, i.e. sample temperature vs. sample composition, are shown in Fig. 14.3 for the composition range 63 to 85 at.% Zn. It is estimated that the uncertainty of the composition is less than 0.25 at.% and that the temperatures are accurate within ± 1 to 2 K.

14.3 Thermochemical analyses

Thermochemical analyses have been carried out on the samples containing up to 40 at.% of Pt. The thermal events from the different phases are summarized in Table 14.1. DTA curves are shown in Fig. 14.4. No clear trend was observed for the sample containing 23 to 27 at.% of Pt. The melting temperatures of these compositions scatter between 1275 and 1284 K. This region has to be studied with greater care.

Table 14.1: Results of DTA experiments

Phase	Approx. composition range (at.% of Pt)	Thermal effect / K	Result
PtZn ₇	12.5	752	decomposes into Pt ₂ Zn ₁₁ + Zn
γ -Pt ₂ Zn ₁₁	15.3	1133	melting
γ_1 & γ'_1 -Pt ₅ Zn ₂₁	17.2 – 20.0	1238 – 1251	melting
γ -brass related phases	23 to 27	1275 – 1284	melting
Pt ₂₉ Zn ₄₉	37.1	1020	phase transforms into Pt ₇ Zn ₁₂

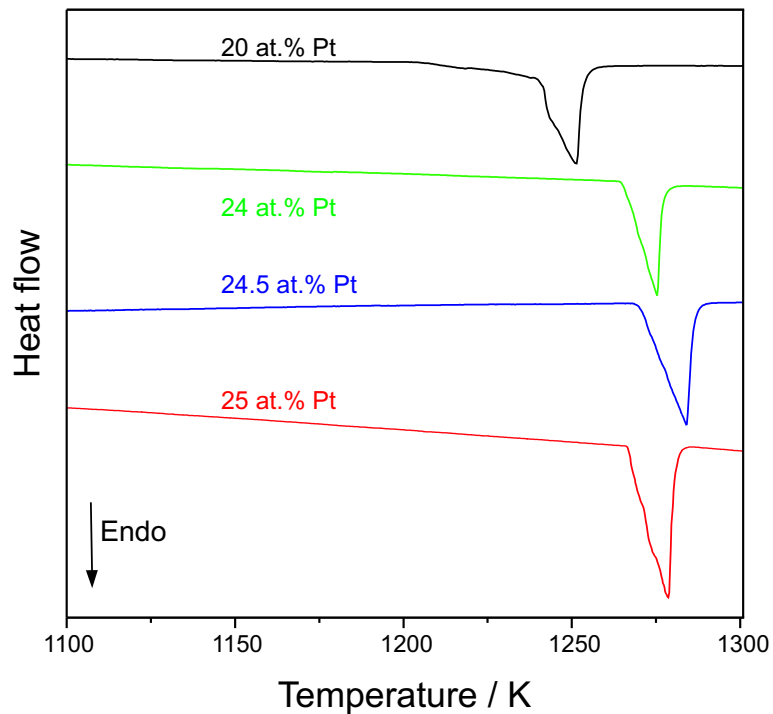


Figure 14.4: Thermograms for the sample containing 20 to 25 at.% of Pt.

Chapter 15

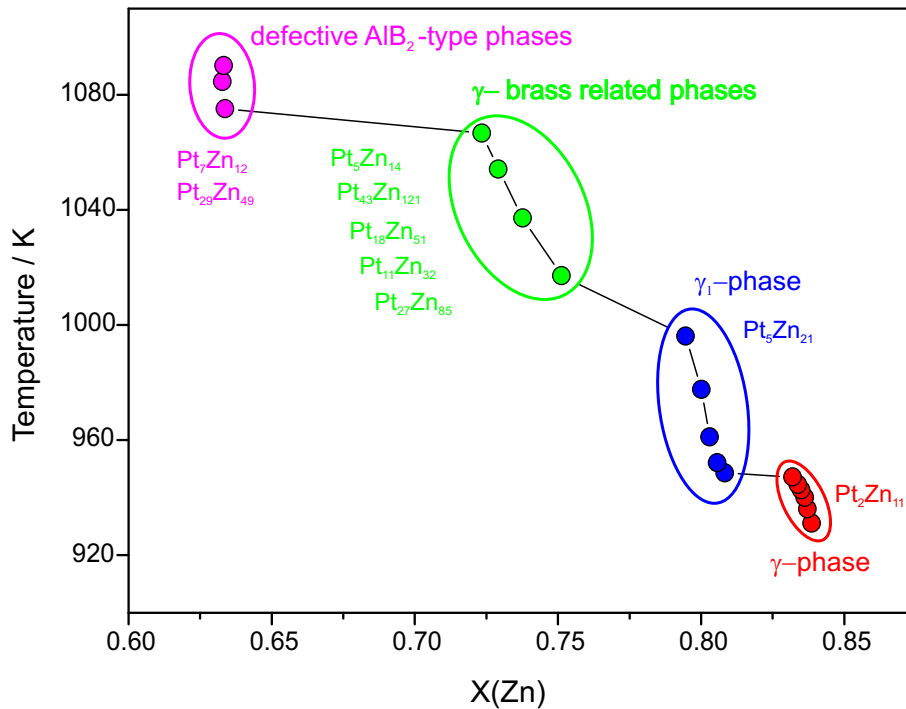
Summary

A systematic reinvestigation of the zinc-rich portions of the binary systems platinum-zinc and nickel-zinc was motivated by the prospect to uncover and identify new structurally complex intermetallic phases in the proximity of the γ -phase regions of brass-like systems. Detailed analyses of such phases are expected to provide new insight into mechanisms and causes of structural complexity in elementary binary systems. The work of Morton provided hope for a success in this endeavour. He provided the existence of first representatives of structurally differentiated γ -brass related phases by means of electron microscopy. The present work essentially confirms Morton's findings, resolves several structures with atomic resolution by single crystal X-ray diffraction means and extends this chemistry into the related Pt-Zn system. The Pt-Zn system was selected due to the optimal scattering contrast between the components which enabled for the first time a precise determination of the evolution of such structures with composition.

Syntheses were carried out using three different methods; isopiestic method, melt centrifugation technique (the self-flux method) and conventional solid state syntheses. The mole fraction x_{Zn} was systematically varied between 0.50 and 0.95. The structures were characterized by using X-ray single crystal and powder diffraction methods. High resolution X-ray powder patterns were acquired from synchrotron radiation for selected samples.

Measurements of physical properties such as density, thermal behaviour, magnetic susceptibility, and electrical conductivity were also performed on selected samples.

The melt centrifugation technique was successfully employed for the synthesis of Zn-rich phases and particularly the growth of crystals of PtZn_7 , $\text{Pt}_2\text{Zn}_{11}$ and NiZn_8 . Isopiestic measurements performed in a continuous temperature gradient at five different vapour pressures of Zn revealed the sequence of the phases in the Pt-Zn system in the range $0.15 \leq x_{\text{Pt}} \leq 0.37$. This region can be divided into four different phase regions. γ - $\text{Pt}_2\text{Zn}_{11}$ and γ_1 - $\text{Pt}_5\text{Zn}_{21}$ phases form at the Zn-rich side. A narrow phase field $0.24 \leq x_{\text{Pt}} \leq 0.27$ adjacent to the brass-type phases accommodates a series of structurally and compositionally intimately related phases with distinctly modulated γ -brass-type related structures. Defective AlB_2 -type structures, $\text{Pt}_{29}\text{Zn}_{49}$ and $\text{Pt}_7\text{Zn}_{12}$ were observed at ≈ 37 at.% of Pt. PtZn_7 was not observed. This is attributed to the low decomposition temperature of this phase compared to others. PtZn_7 decomposes at 752 K into $\text{Pt}_2\text{Zn}_{11}$ and liquid Zn (58 K above its lower temperature of formation).

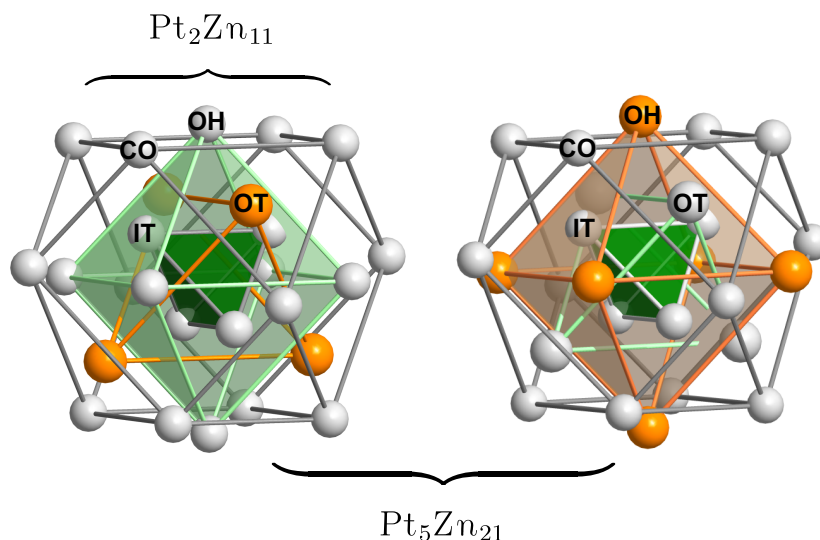


The Zn-richest phase PtZn_7 forms at an approximate composition of 12 at.% Pt. The structure was solved from single crystal X-ray intensities. The structure can precisely be described as an incommensurately modulated structure with a modulation vector $q \approx \frac{1}{9}[304]^*$ in the (3+1)-dimensional superspace group $\text{A}2/\text{m}(\alpha 0\gamma)00$. However, the structure of PtZn_7 can reasonably be approximated as a commensurate super-structure of a defective AlB_2 type structure in space group $\text{C}2/\text{m}$. The commensurate super-structure solution was used for structural description.

The structure can be viewed as consisting of four different, partly condensed polyhedral units. On the other hand, suitable decomposition of the structure into layers reveals a defective AlB₂-type derivative structure of the order 46 as reflected by the formula (Pt₁₅Zn₃₁)Zn₈₂□₁₀ with □ denoting vacancies.

Three distinct γ -brass type phases were identified between 15 and 21 at.% of Pt. All these phases exhibit cubic symmetry. γ -Pt₂Zn_{11- δ} ($0.2 < \delta < 0.3$) ($\bar{I}43m$, cI52) adopts a $3a \times 3a \times 3a$ superstructure of the β -brass type (bcc W-type) structure. The structure exhibits ordered vacancies distributed at the special positions 0,0,0 and $\frac{1}{2}, \frac{1}{2}, \frac{1}{2}$. Following Bradley's concept the structure is described in terms of 26 atoms clusters arranged like W atoms in bcc tungsten. Vacancies on the inner tetrahedral Zn positions (14%) reduce *vec* from $\frac{22}{13}$ towards $\approx \frac{21}{13}$ e/a. This value is the optimum for the formation of a γ -brass phase. The Pt₂Zn_{11- δ} phase melts nearly congruently at 1135 K.

The phases γ_1 -Pt₅Zn₂₁ and γ'_1 -Pt₅Zn₂₁ ($F\bar{4}3m$, cF393-410) adopt $6a \times 6a \times 6a$ superstructures of the β -brass type with ordered vacancies. In the γ -brass type structures four atomic positions per unit cell are vacant with respect to the β -phase. The structures are comprised of four symmetrically independent and three compositionally inequivalent 26 atom clusters. The clusters are pair-wise arranged according to the motif of two interpenetrating diamond-like nets, one with constant composition (Pt₄Zn₂₂) and perfectly ordered, the second one richer in Pt and variable in composition (Pt_{6 \pm δ} Zn_{20 \pm δ'}).

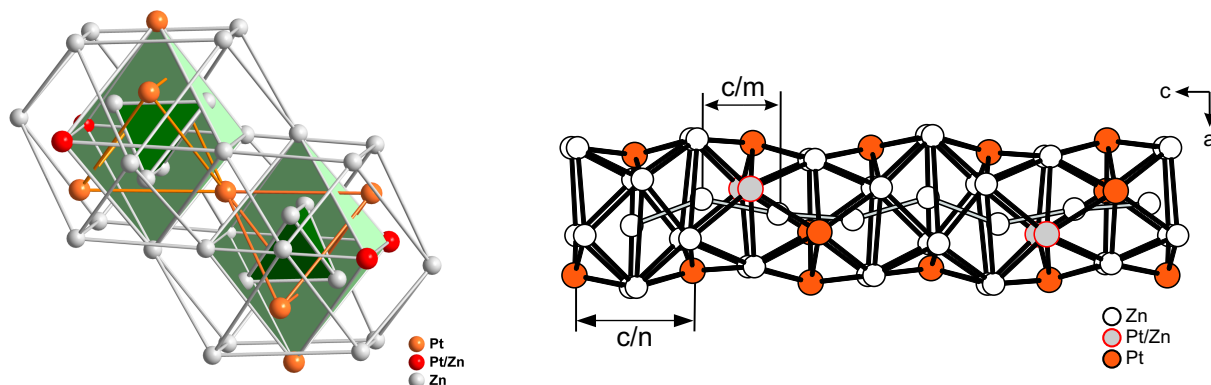


Five new γ -brass related phases were uncovered between 23–27 at.% of Pt, adjacent to $\text{Pt}_5\text{Zn}_{21}$. The structures of $\text{Pt}_{11}\text{Zn}_{32}$, $\text{Pt}_{18}\text{Zn}_{51}$, $\text{Pt}_5\text{Zn}_{14}$, $\text{Pt}_{27}\text{Zn}_{85}$ and $\text{Pt}_{43}\text{Zn}_{121}$ were solved from single crystal X-ray diffraction intensities. They all exhibit orthorhombic symmetry. The structures can be described as derivatives of the β or γ -brass type structure with progressive increase in the longest crystallographic axis. The lattice parameters of all these structures can be expressed by a basic transformation of the form with respect to β -brass type structure with lattice parameter a_{bcc} :

$$\begin{aligned}\mathbf{a} &\approx 3 \mathbf{a}_{bcc} \\ \mathbf{b} &\approx 3 \sqrt{2} \mathbf{a}_{bcc} \\ \mathbf{c} &\approx n \sqrt{2} \mathbf{a}_{bcc}.\end{aligned}$$

Six members of the series with $n = 3, 5, 8, 11$ and 19 were identified in the course of this project. The $n = 3$ member corresponds to $\gamma\text{-Pt}_2\text{Zn}_{11-\delta}$ in a pseudo-orthorhombic setting. All other phases have truly orthorhombic symmetry: $\text{Pt}_{11}\text{Zn}_{32}$ ($n = 5$, oC172), $\text{Pt}_{18}\text{Zn}_{51}$ ($n = 8$, oC276), $\text{Pt}_5\text{Zn}_{14}$ ($n = 11$, oC380), $\text{Pt}_{27}\text{Zn}_{85}$ ($n = 13$, oF448) and $\text{Pt}_{43}\text{Zn}_{121}$ ($n = 19$, oF656). In all cases, the lattice parameters of \mathbf{a} and \mathbf{b} are nearly constant (apart from setting) and the \mathbf{c} axis increases according to ‘ n ’. The presence of vacancies is a prominent feature of the γ -brass related phases. For five new γ -brass related phases $\text{Pt}_{11}\text{Zn}_{32}$, $\text{Pt}_{18}\text{Zn}_{51}$, $\text{Pt}_5\text{Zn}_{14}$, $\text{Pt}_{27}\text{Zn}_{85}$ and $\text{Pt}_{43}\text{Zn}_{121}$, the number of vacancies found to be 8, 12, 16, 20 and 28, respectively, per unit cell.

$\text{Pt}_{11}\text{Zn}_{32}$ crystallizes in space group Cmce with 172 atoms in the unit cell ($Z = 4$). There are 8 ordered vacancies per unit cell. The structure can be described as being composed of pairwise interpenetrating γ -brass-type clusters, each comprising 45 atoms. From a different point of view, the structure can be related to Nowotny chimney-ladder type structure. The major part of the atoms including all the Pt atoms form a network of partly condensed and connected pentagonal antiprismatic columns which offer space for the remaining Zn atoms arranged in zig-zag chains. The columns correspond to the chimney and the chains to the ladder. As in Nowotny chimney-ladder structures both substructure have their own translational symmetry conferring the structure a composite type character. The two distinct translational symmetries can give rise to mismatch. For $\text{Pt}_{11}\text{Zn}_{32}$ the ratio of the two lengths locks in at $\frac{5}{8}$.



$\text{Pt}_{29}\text{Zn}_{49}$ forms a complex superstructure of a defective AlB_2 -type structure ($\text{Amm}2$, $Z=2$). In the structure 9 out of 58 possible Zn positions in a graphite-like (6^3 nets) atomic arrangement are vacant ($\text{Pt}_{29}\text{Zn}_{49}\square_9$). $\text{Pt}_{29}\text{Zn}_{49}$ is stable at ambient temperature. At 1020 K it transforms into $\text{Pt}_7\text{Zn}_{12}$ (Pbam , $Z=2$), which is another defective AlB_2 -type structure. The transformation from $\text{Pt}_{29}\text{Zn}_{49}$ to $\text{Pt}_7\text{Zn}_{12}$ was confirmed by X-ray powder diffraction and DTA analyses.

The structure of NiZn_8 , the binary phase richest in Zn, was redetermined. Opposed to earlier reports, NiZn_8 adopts an incommensurately modulated structure which can be described in the $(3+1)$ -dimensional superspace group $\text{C}2/m(\alpha 0 \gamma)00$ with a modulation vector $q \approx \frac{1}{9}[304]^*$. Advantageously for discussion, the structure is very well rationally approximated including anisotropic displacement parameters in the space group $\text{C}2/m$ with $Z=16$. The structure is isoconfigurational to that of PtZn_7 . NiZn_8 undergoes peritectic decomposition at 790 K into $\gamma\text{-Ni}_5\text{Zn}_{21}$ and Zn.

The structure of $\text{Ni}_{18}\text{Zn}_{51}$ (Cmce , $Z=4$) is isoconfigurational to those of $\text{Pt}_{18}\text{Zn}_{51}$ and $\text{Pd}_{15}\text{Zn}_{54}$ in the congenetic Pt-Zn and Pd-Zn systems. Redetermination of the structure revealed that the structure can more precisely be described in the centrosymmetric space group $\text{Cmce}(64)$. This structure was earlier known as NiZn_3 and described in the non-centrosymmetric space group $\text{Abm}2$. It has been shown that the structure coexists with NiZn . This result is in accordance with Morton's report.

Chapter 16

Zusammenfassung

Synthese, Charakterisierung und Phasenbeziehungen zinkreicher Phasen in den Zweistoffsystemen Platin-Zink und Nickel-Zink

Eine nochmalige, systematische Untersuchung der zinkreichen Zustandsgebiete der Zweistoffsysteme Platin-Zink und Nickel-Zink wurde durch die Aussicht auf die Aufklärung neuer, strukturell komplexer intermetallischer Phasen motiviert, wie man sie häufig in der Nachbarschaft zur γ -Phase in messingartigen Systemen antrifft. Detaillierte Analysen solcher Phasen sollten neue Einsichten in die Ursachen und Mechanismen struktureller Komplexität in diesen stofflich eher einfachen Systemen liefern. Frühere elektronenmikroskopische Arbeiten von Morton zu strukturell differenzierten, γ -artigen Ni-Zn Phasen gaben hierzu die ersten Anhaltspunkte und bestärkten die Hoffnung auf einen dahingehenden Erfolg. Daran anknüpfend kann die vorliegende Arbeit Mortons Entdeckungen im wesentlichen bestätigen und erhärtet sie im weiteren durch die Anwendung der Röntgeneinkristallstrukturanalyse zur Aufklärung der Strukturen mehrerer, vormals unbekannter Phasen mit atomarer Auflösung. Dadurch erweitert sich der konzeptuelle Anwendungsbereich von Mortons grundlegenden Arbeiten auf das Platin-Zink System, welches aufgrund des deutlichen Streukontrastes für die verwendete Röntgenstrahlung ausgewählt wurde. Auf dieser Grundlage ist es nun erstmals möglich, die Evolution derartiger Strukturen in Abhängigkeit von ihrer Zusammensetzung zu untersuchen.

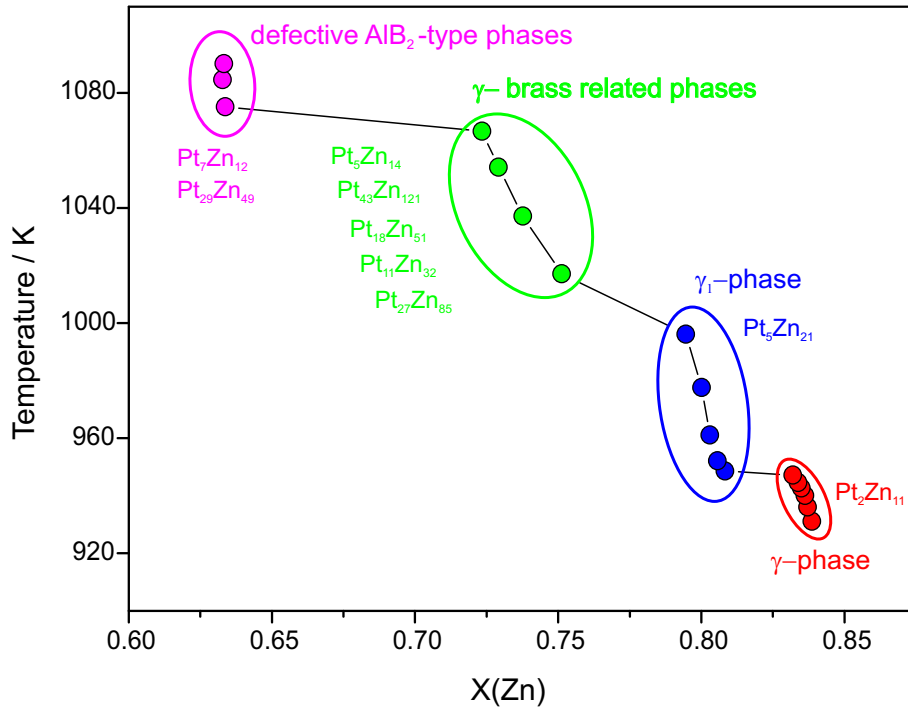
Zur Darstellung der Phasen wurde der Zink-Stoffmengenanteil x_{Zn} systematisch im Bereich von 0,50 bis 0,95 variiert und neben konventionellen Hochtemperatursynthesen auch die sogenannte *Isopiestic Methode* und die Technik der *Schmelz-Zentrifugation* angewendet. Die strukturelle

Charakterisierung erfolgte durch Röntgenbeugung an Pulvern und Einkristallen. Hochoaufgelöste Pulverdiffraktogramme wurden für ausgewählte Proben durch Beugungsexperimente mit Synchrotronstrahlung erhalten.

An ausgewählten Proben wurden weiterhin die physikalischen Eigenschaften bestimmt; darunter ihre Dichte, ihr thermisches Verhalten und ihre magnetischen und elektrischen Eigenschaften, ausgedrückt durch die magnetische Suszeptibilität und den spezifischen Widerstand.

Die Schmelz-Zentrifugationstechnik konnte im allgemeinen erfolgreich zur Synthese zinkreicher Phasen eingesetzt werden, insbesondere aber zur Kristallzucht an den Phasen PtZn_7 , $\text{Pt}_2\text{Zn}_{11}$ und NiZn_8 . Nach der isopiestic Methode in einem kontinuierlichen Temperaturgradienten bei fünf verschiedenen Zink Dampfdrücken durchgeführte Experimente eröffneten die Abfolge der Phasen im Platin-Zink System im Bereich von $0,15 \leq x_{\text{Pt}} \leq 0,37$. Danach kann diese Region des Zustandsdiagramms in vier verschiedene Phasenbereiche unterteilt werden: $\gamma\text{-Pt}_2\text{Zn}_{11}$ und $\gamma_1\text{-Pt}_5\text{Zn}_{21}$ repräsentieren die zinkreiche Seite. Im engen Bereich von $0,24 \leq x_{\text{Pt}} \leq 0,27$, in unmittelbarer Nachbarschaft zu den erwähnten messingartigen Legierungen vom γ -Typ, findet sich eine Serie strukturell und hinsichtlich ihrer Zusammensetzung aufs engste verwandter Phasen, die allesamt als in unterschiedlicher Weise modulierte Abkömmlinge des γ -Messings verstanden werden können. Schließlich lassen sich mit $\text{Pt}_{29}\text{Zn}_{49}$ und $\text{Pt}_7\text{Zn}_{12}$ bei etwa 37 at.% Platin Phasen darstellen, deren Strukturen als spezielle Defektvarianten zum AlB_2 Strukturtyp beschrieben werden.

Berichte zur Existenz einer Phase der Zusammensetzung PtZn_7 unter den vormals angegebenen Bedingungen konnten allerdings nicht bestätigt werden, was auf die gefundene niedrige Zersetzungstemperatur dieser Phase im Vergleich zu anderen zurückgeführt wurde. PtZn_7 zersetzt sich bei 752 K, und damit nur 58 K oberhalb der entsprechenden unteren Bildungstemperatur, peritektisch zu $\text{Pt}_2\text{Zn}_{11}$ und flüssigem Zink. Die Struktur konnte aus am Einkristall gewonnenen Intensitäten gelöst werden. Die Strukturbeschreibung erfolgt auf Basis einer inkommensurablen Modulation, mit einem Modulationsvektor $q \approx \frac{1}{9}[304]^*$ in der (3+1) dimensionalen Raumgruppe $A2/m(\alpha 0 \gamma)00$. Daneben ist aber auch eine annähernde Strukturbeschreibung über eine kkommensurable Überstruktur in der Raumgruppe $C2/m$ möglich. Die kkommensurable Näherung wurde aufgrund ihrer Anschaulichkeit zur Strukturbeschreibung verwendet, sie erhellt die Ableitung der Struktur als Defektvariante der Ordnung 46 zum AlB_2 Typ. Dies lässt sich gemäß der For-

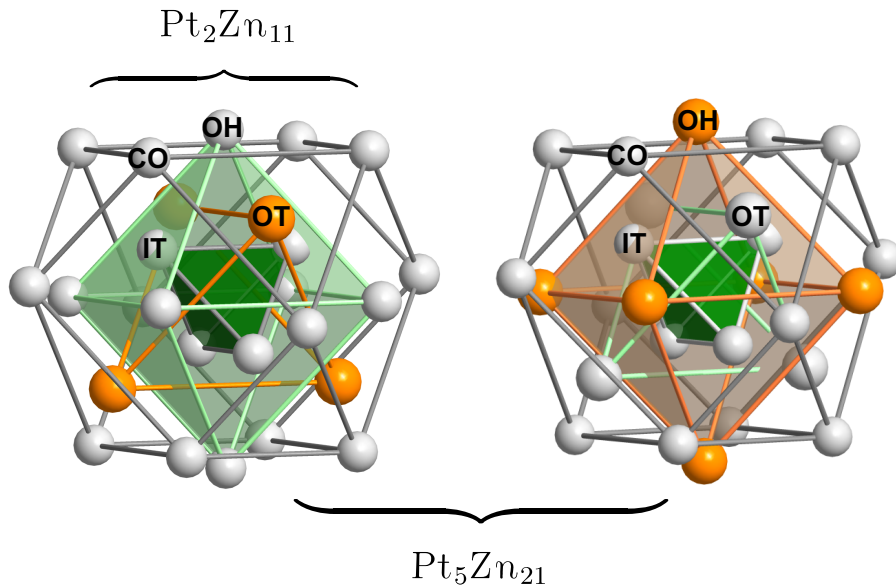


mulierung als $(\text{Pt}_{15}\text{Zn}_{31})\text{Zn}_{82}\square_{10}$ ausdrücken, worin das Symbol \square zur Kennzeichnung formaler Leerstellen verwendet wird. Neben der Zerlegung in AlB₂-artige Schichten lässt sich die Struktur auch als aus vier verschiedenen, teilweise kondensierten, polyedrischen Baueinheiten aufgebaut denken.

Drei unterschiedliche messingartige Phasen konnten zwischen 15 und 21 at.% Platin identifiziert werden. Allen gemeinsam ist die kubische Symmetrie. γ -Pt₂Zn₁₁ ($0,2 < \delta < 0,3$) ($I\bar{4}3m$, $cI52$) bildet eine $3a \times 3a \times 3a$ Überstruktur zum β -Messing (kubisch innenzentrierter W-Typ). Die formalen Lücken sind auf der speziellen Lage 0,0,0 entsprechend der Innenzentrierung geordnet. Nach Bradley kann die Struktur mittels eines 26-atomigen Clusters beschrieben werden, welcher nach dem Motiv der Atome des W-Typs angeordnet ist. Eine 86%ige Teilbesetzung der sogenannten inneren Tetraederlagen durch Zn reduziert die sogenannte Valenzelektronenkonzentration VEK vom ursprünglichen Wert $\frac{22}{13}$ auf annähernd $\frac{21}{13}$ Elektronen pro Atom, was dem für die Stabilisierung der γ -Phasen als optimal angesehenen Wert entspricht. Pt₂Zn₁₁ schmilzt nahezu kongruent bei 1135 K.

Die Phasen γ_1 -Pt₅Zn₂₁ und γ_1' -Pt₅Zn₂₁ ($F\bar{4}3m$, cF 393-410) bilden eine $6a \times 6a \times 6a$ Überstruktur zum β -Messing mit ebenfalls geordneten formalen Leerstellen. Bezüglich der β -Phase bleiben

vier Positionen pro Überstrukturzelle unbesetzt. Der Aufbau der Struktur erfolgt erneut durch diesmal vier symmetrisch unabhängige 26 Atome zählende Cluster. Die Anordnung der paarweise in ihrer Zusammensetzung übereinstimmenden Cluster folgt dem Motiv sich durchdringender Diamantnetze. Das eine hiervon ist bei perfekter Ordnung in seiner Zusammensetzung konstant ($\text{Pt}_4\text{Zn}_{22}$), während das platinreichere andere eine deutliche Variabilität aufweist ($\text{Pt}_{6\pm\delta}\text{Zn}_{20\pm\delta'}$), welche die beobachtete Phasenbreite bedingt.



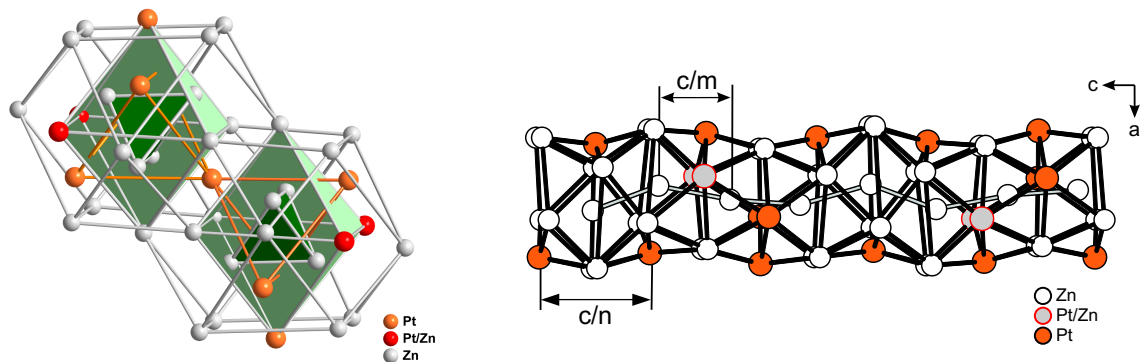
Fünf neue messingartige Phasen wurden im Bereich zwischen 23–27 at.% Platin gefunden. Die Strukturen von $\text{Pt}_{11}\text{Zn}_{32}$, $\text{Pt}_{18}\text{Zn}_{51}$, $\text{Pt}_5\text{Zn}_{14}$, $\text{Pt}_{27}\text{Zn}_{85}$ und $\text{Pt}_{43}\text{Zn}_{121}$ wurden aus Einkristalldaten gelöst und besitzen alle eine orthorhombische Symmetrie. Als Abkömmlinge der β - oder γ -Phase unterscheiden sie sich durch eine zunehmende Verlängerung in der längsten orthorhombischen Achse. Die Gitterparameter lassen sich durch eine Basistransformation aus denen der β -Phase (a_{bcc}) berechnen:

$$\begin{aligned}
 \mathbf{a} &\approx 3 \mathbf{a}_{bcc} \\
 \mathbf{a} &\approx 3\sqrt{2} \mathbf{a}_{bcc} \\
 \mathbf{a} &\approx n\sqrt{2} \mathbf{a}_{bcc}
 \end{aligned}$$

Sechs Vertreter dieser Serie mit $n = 3, 5, 8, 11$ und 19 wurden im Verlauf dieses Projektes identifiziert. Der Repräsentant mit $n = 3$ entspricht der γ -Messing Struktur in einer pseudo-orthorhombischen Aufstellung, wohingegen alle weiteren Phasen über eine echte orthorhombische Symmetrie verfügen: $\text{Pt}_{11}\text{Zn}_{32}$ ($n = 5$, $oC172$), $\text{Pt}_{18}\text{Zn}_{51}$ ($n = 8$, $oC276$), $\text{Pt}_5\text{Zn}_{14}$ ($n = 11$, $oC380$),

$\text{Pt}_{27}\text{Zn}_{85}$ ($n = 13, oF448$) und $\text{Pt}_{43}\text{Zn}_{121}$ ($n = 19, oF656$). In allen Fällen stimmen die a und b Gitterparameter, abgesehen von eventuell unterschiedlicher Aufstellung der Zelle, jeweils sehr gut überein. Die c Achse nimmt entsprechend der erwähnten Basistransformation mit n zu. Das Vorhandensein formaler Lücken wird als ein wichtiges Prinzip bei γ -artigen Phasen angesehen; die Anzahl für $\text{Pt}_{11}\text{Zn}_{32}$, $\text{Pt}_{18}\text{Zn}_{51}$, $\text{Pt}_5\text{Zn}_{14}$, $\text{Pt}_{27}\text{Zn}_{85}$ und $\text{Pt}_{43}\text{Zn}_{121}$ ist dann 8, 12, 16, 20 und 28, jeweils bezüglich einer Elementarzelle.

$\text{Pt}_{11}\text{Zn}_{32}$ kristallisiert im Raumgruppentyp $Cmce$ mit 172 Atomen in der Elementarzelle ($Z = 4$). Es gibt 8 formale Leerstellen pro Zelle in der Struktur. Eine Strukturbeschreibung über sich paarweise durchdringende γ -artige Cluster, mit dann 45 Atomen pro Baueinheit, ist ebenso möglich, wie eine Beschreibung in Anlehnung an das Konzept der Nowotnyschen, sogenannten *chimney-ladder*-Phasen. In dieser Beschreibung bildet die Mehrzahl aller Atome, darunter alle Edelmetallatome, ein Netzwerk aus antiprismatisch aufeinanderfolgenden pentagonalen Einheiten. Im Innern derartiger Kolumnen sind ausschließlich Zinkatome in Zick-Zack Ketten aufgereiht. Wie in Nowotny chimney-ladder Phasen üblich besitzen die peripheren Atome des Schornsteins (*chimney*) und die zentralen der Leiter (*ladder*) jeweils unterschiedliche Periodizitäten, wodurch die Struktur zunächst als Kompositstruktur bezeichnet werden kann. Die unterschiedlichen Translationssymmetrien können aber auch inkommensurabel zueinander sein, wodurch die Strukturen als inkommensurabel modulierte Phasen behandelt werden müssen, oder zumindest als rationale Approximanten dazu. Für $\text{Pt}_{11}\text{Zn}_{32}$ ergibt sich dann das relative Längenverhältnis zu $\frac{\sqrt{5}}{8}$. Die weiteren Vertreter dieser Serie von Strukturen folgen dem eben beschriebenen Konzept, bis auf entsprechende Änderungen der numerischen Parameter.



$\text{Pt}_{29}\text{Zn}_{49}$ bildet eine komplexe Überstruktur zum AlB_2 Typ ($Amm2, Z = 2$). Neun von 58 möglichen Zinkpositionen in einer graphitartigen Schicht von Atomen (6^3 -Netz) sind geordnet

nicht besetzt, entsprechend der Formel $\text{Pt}_{29}\text{Zn}_{49}\square_9$. Die Phase ist unter Umgebungsbedingungen stabil. Bei 1020 K erfolgt Umwandlung zu $\text{Pt}_7\text{Zn}_{12}$ (*Pbam*, $Z = 2$), eine AlB_2 -artige Defektvariante mit veränderter Struktur. Die Umwandlung wurde thermoanalytisch verfolgt und röntgenographisch an Pulverproben bestätigt.

Die Struktur von NiZn_8 , die zinkreichste binäre Phase, wurde nochmals bestimmt. Im Gegensatz zu früheren Berichten handelt es sich bei NiZn_8 ebenfalls um eine inkommensurabel modulierte Phase, die in der (3+1)-dimensionalen Raumgruppe $C2/m(\alpha0\gamma)00$ mit einem Modulationsvektor $q \approx \frac{1}{9}[304]^*$ beschrieben wurde. Vorteilhafterweise lässt sich die modulierte Struktur in einer Überstrukturnäherung ($Z = 16$) beschreiben; im Raumgruppentyp $C2/m$ sind alle Atomlagen anisotrop verfeinerbar. Die Struktur ist isokonfigurationell zu PtZn_7 . Ähnlich diesem zersetzt sich NiZn_8 oberhalb 790 K peritektisch zu $\gamma\text{-Ni}_5\text{Zn}_{21}$ und Zink.

Die Struktur von $\text{Ni}_{18}\text{Zn}_{51}$ (*Cmce*, $Z = 4$), früher unter der Zusammensetzung NiZn_3 berichtet, ist isokonfigurationell zu denen von $\text{Pt}_{18}\text{Zn}_{51}$ und $\text{Pd}_{15}\text{Zn}_{54}$ der analogen Systeme Pt-Zn und Pd-Zn. Die erneute Bestimmung der Struktur ergab, daß eine bessere Beschreibung in der zentrosymmetrischen Raumgruppe *Cmce* möglich ist, als in der vormals angegebenen azentrischen *Abm2*. Es wurde gezeigt, daß $\text{Ni}_{18}\text{Zn}_{51}$ im nickelreicheren Zustandsgebiet mit NiZn koexistiert, in Übereinstimmung mit Mortons früheren Arbeiten.

APPENDIX

All the relevant data are deposited to Prof. Dr. B. Harbrecht, Fachbereich Chemie der Philipps-Universität Marburg, in the electronic form.

A 1: Indexation, 2θ values, calculated and observed X-ray intensities for $\text{Pt}_2\text{Zn}_{10.73(2)}$ ($\text{CuK}\alpha$), $a = 908.89(2)$ pm, $\frac{I_{\text{obs}}}{I_{\text{max}}} \geq 0.01$)

h	k	l	$2\theta / ^\circ$	I_{calc}	I_{obs}
1	1	0	13.767	20	18
2	0	0	19.517	34	32
2	1	1	23.962	156	148
2	2	0	27.738	7	7
3	1	0	31.090	20	18
3	3	0	42.145	410	} 688
4	1	1	42.145	270	
3	3	2	46.844	32	33
4	2	2	49.060	50	56
5	2	1	55.314	8	8
5	3	0	59.246	21	24
6	0	0	61.125	39	} 91
4	2	2	61.125	50	
5	3	2	62.989	15	16
6	2	0	64.821	6	5
5	4	1	66.627	18	16
6	3	1	70.168	10	11
4	4	4	71.909	36	32
5	5	0	73.632	17	18
5	5	2	77.036	4	} 152
6	3	3	77.036	74	
7	2	1	77.036	72	
8	0	0	85.371	4	4
7	4	1	87.021	81	} 80
5	5	4	87.021	4	
8	2	0	88.668	11	} 15
6	4	4	88.668	4	

A 2: Indexation, 2θ values (measured, CuK_α), calculated and observed X-ray intensities for $\text{Pt}_5\text{Zn}_{21}$ ($x_{\text{Pt}} = 0.193$, $a = 1811.9(1)$ pm), $I_o > 0.005 I_{\text{max}}$

h	k	l	$2\theta / ^\circ$	I_{calc}	I_{obs}
1	1	3	16.202	10	9
1	3	3	21.358	56	57
2	2	4	24.033	170	162
1	1	5	25.515	117	} 165
3	3	3	25.515	45	
0	4	4	27.822	8	8
1	3	5	29.125	10	10
4	4	4	34.251	7	6
1	1	7	35.339	7	7
2	4	6	37.092	11	8
1	3	7	38.110	14	15
3	3	7	40.719	62	68
0	6	6	42.281	954	} 1473
2	2	8	42.281	451	
5	5	5	43.197	48	54
4	6	6	46.998	23	26
1	3	9	47.842	26	29
4	4	8	49.224	65	68
1	7	7	50.039	5	} 37
3	3	9	50.039	13	
5	5	7	50.039	13	
1	5	9	52.168	6	7
3	7	9	60.152	19	19
0	0	12	61.339	106	} 197
4	8	8	61.339	88	
1	5	11	62.045	75	69
2	2	12	63.221	12	13
4	6	10	66.876	33	} 55
2	8	10	66.876	18	
1	7	11	67.540	15	} 24
3	9	9	67.540	11	

Redetermination of PtZn structure – AuCu-type structure

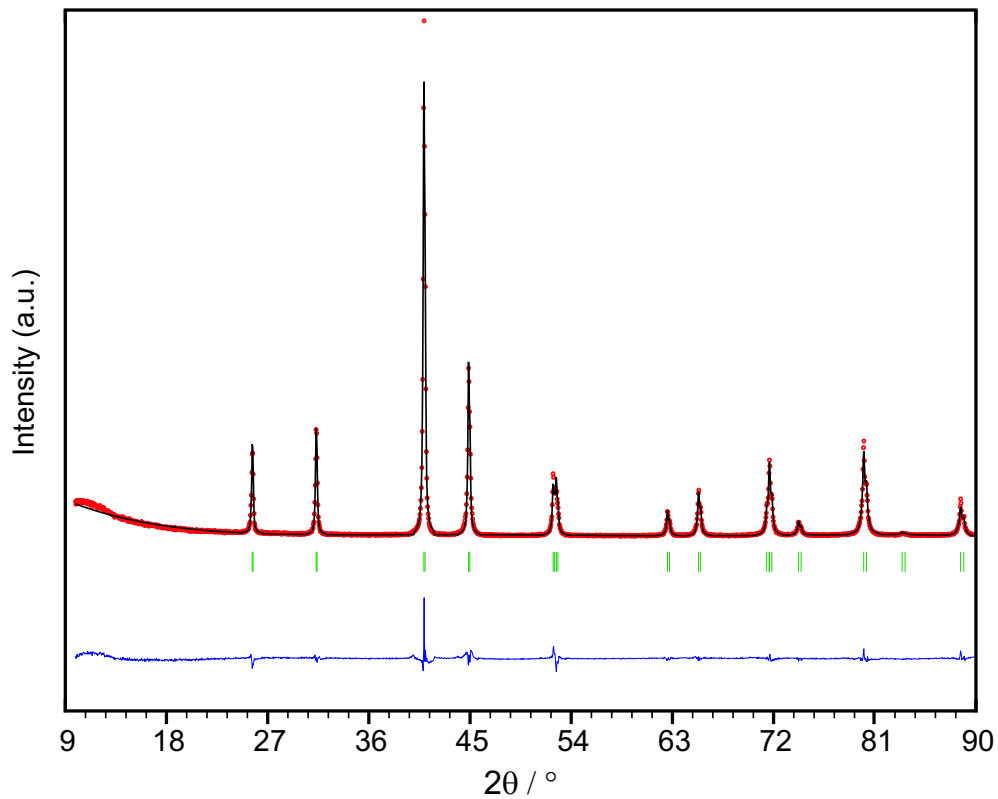


Figure 1: X-ray diffractogram (red) of PtZn together with the profile fit (black), the difference spectrum (blue) and the Bragg positions (bars, green); $\text{CuK}\alpha$, $a = 285.45(1)$ pm, $c = 347.25(2)$ pm, $R_B = 3.31$. The Rietveld refinement was carried out using the program FULLPROF [56].

A 3: Positional and displacement parameters $B_{\text{iso}}(\text{pm}^2)$ for PtZn: Space group, $P4/mmm$

Atom	Wy.	x	y	z	B_{iso}
Pt	1a	0	0	0	103(10)
Zn	1d	$\frac{1}{2}$	$\frac{1}{2}$	$\frac{1}{2}$	125(9)

A 4: Indexation, 2θ values, calculated and observed X-ray intensities (CuK_α) for PtZn

h	k	l	$2\theta / ^\circ$	I_{calc}	I_{obs}
0	0	1	25.632	408	400
1	0	0	31.310	508	519
1	0	1	40.891	2396	2411
1	1	0	44.869	932	992
1	1	1	52.387	278	315
0	0	2	52.672	300	282
1	0	2	62.565	178	182
2	0	0	65.326	332	348
2	0	1	71.395	132	140
1	1	2	71.633	523	525
2	1	0	74.227	121	125
2	1	1	80.014	808	805
2	0	2	88.634	331	361

The phase $\text{Pt}_5\text{Zn}_{14}$:

The synthesis were carried out as described in the experimental part. The structure of $\text{Pt}_5\text{Zn}_{14}$ crystallizes in space group Cmca , oC380 , $a = 1291.5(3)$ pm, $b = 910.2(2)$ pm, $c = 4706.7(9)$ pm. The crystals were selected from a sample of a nominal composition of 29 at.% of Pt. X-ray powder diffraction studies showed that the $\text{Pt}_5\text{Zn}_{14}$ phase coexists on the Pt-rich side with $\text{Pt}_{29}\text{Zn}_{49}$. The structure of $\text{Pt}_5\text{Zn}_{14}$ was solved from 2828 unique reflections, 240 variables to R1 value of 0.0714 with anisotropic displacement parameters. The details on data collection, atomic parameters and thermal displacement parameters are tabulated in Table 5, 6 and 7, respectively.

The structure of $\text{Pt}_5\text{Zn}_{14}$ was independently reconfirmed by selecting crystals from a second batch of a nominal composition of 30 at.% of Pt, containing $\text{Pt}_{29}\text{Zn}_{49}$ as a second phase. This was confirmed from X-ray powder diffraction analyses. The lattice parameters for the second crystal obtained from IPDS-I are: $a = 1294.0(3)$ pm, $b = 910.8(2)$ pm, $c = 4689.8(9)$ pm.

In view of the metrical relation with the β -brass type structure, the structure of $\text{Pt}_5\text{Zn}_{14}$ can be classified as an ordered $3\sqrt{2} a_\beta \times 3 a_\beta \times 11\sqrt{2} a_\beta$ defect variant of a β -brass type structure of index 198 with 16 vacancies per unit cell. The complex γ -brass related phase $\text{Pt}_5\text{Zn}_{14}$ is composed of 380 atoms distributed over 32 distinct atomic sites in which, 22 atomic positions are occupied by Zn atoms and 9 by Pt atoms. Only one out of 32 crystallographic sites seems to be statistically occupied by Pt and Zn. This site is occupied by 48(1)% Zn and 52% Pt, yielding an overall composition of $\text{Pt}_5\text{Zn}_{14.0(2)}$. Compared to all γ -brass related phases, $\text{Pt}_5\text{Zn}_{14}$ is the most Pt-rich phase.

A 5: Crystallographic and technical data for the single-crystal structure determination

Sum formula	Pt ₅ Zn _{14.0(1)}
Space group (No.)	Cmce (64)
Z	20
a / pm	1291.5(3)
b / pm	910.2(1)
c / pm	4707.0(1)
V / 10 ⁶ pm ³	5533.1(2)
Molar mass / g mol ⁻¹	1890.63
ρ_{cal} / g cm ⁻³	11.360
μ / mm ⁻¹	92.71
<i>Data collection</i>	
Crystal size / mm ³	0.12 × 0.16 × 0.15
Diffractometer	IPDS-II (STOE & Cie)
Temperature / K	293(2)
Radiation / monochromator	MoK α / Graphite
Distance crystal-IP / mm	140
ϕ ; $\omega_{min} - \omega_{max}$; $\Delta\omega$	0; 0–158; 1
$2\theta_{max}$ / °	50.0
Collected reflections	-14 ≤ h ≤ 15 -10 ≤ k ≤ 9 -55 ≤ l ≤ 55
Total reflections	12682
<i>Data reduction</i>	
Program	IPDS-II-Software [57]/X-RED [61]
Absorption correction	Numerical, X-SHAPE [62]
max. / min. Transmission	0.0547 / 0.0094
Unique reflections	2828
R_{int}	0.1910
<i>Refinement</i>	
Program	SHELXL-97[58]
Refined on	F _o ²
Reflections I _o > 2σ(I _o)	797
Variables	240
R ₁ (I _o > 2σ(I _o))	0.0714
R ₁ (all)	0.1376
wR ₂ (all)	0.2144
Goodness of fit	0.771
$\Delta\rho_{max} / \Delta\rho_{min} / 10^{-6}$ e pm ⁻³	5.469 / -4.606
Extinction coefficient	0.000027(3)
$1/w = \sigma^2(F_o^2) + (0.1(\text{Max}(F_o^2, 0) + 2F_c^2)/3)^2$	

A 6: Positional and equivalent isotropic displacement parameters $U_{\text{eq}}(\text{pm}^2)$ for $\text{Pt}_5\text{Zn}_{14.0(1)}$

Atom No.	Wy.	x	y	z	sof	U_{eq}
Pt1	4a	0	0	0	1	277(11)
Pt2	8f	0	0.4894(4)	0.13648(6)	1	281(8)
Pt3	8f	0	0.0210(3)	0.18245(8)	1	265(6)
Pt4	8f	0	0.4673(3)	0.40932(7)	1	257(7)
Pt5	8f	0	0.0257(4)	0.45404(6)	1	259(8)
Pt6	8f	0	0.4723(4)	0.22734(7)	1	297(8)
Pt7	16g	0.1814(1)	0.3224(2)	0.32002(5)	1	278(4)
Pt8	16g	0.1813(2)	0.3308(2)	0.04167(4)	1	288(6)
Pt9	16g	0.1807(2)	0.1613(2)	0.09544(4)	1	263(5)
M1	16g	0.1796(3)	0.1535(4)	0.26759(5)	0.48(1) ^a	290(11)
Zn1	8d	0.1264(7)	0	$\frac{1}{2}$	1	320(20)
Zn2	8f	0	0.2962(7)	0.1806(2)	1	283(15)
Zn3	8f	0	0.190(1)	0.23428(18)	1	290(20)
Zn4	8f	0	0.1899(10)	0.40589(19)	1	360(20)
Zn5	8f	0	0.3035(10)	0.45738(18)	1	300(20)
Zn6	8f	0	0.2070(1)	0.12532(19)	1	340(20)
Zn7	8f	0	0.2859(9)	0.01326(18)	1	310(20)
Zn8	8f	0	0.2699(9)	0.34843(18)	1	310(20)
Zn9	8f	0	0.2456(11)	0.0691(2)	1	306(15)
Zn10	8f	0	0.2544(10)	0.29199(19)	1	350(20)
Zn11	16g	0.1746(5)	0.1490(7)	0.3679(1)	1	304(14)
Zn12	16g	0.1768(5)	0.3443(6)	0.4948(1)	1	242(13)
Zn13	16g	0.1861(5)	0.3661(6)	0.4142(1)	1	306(13)
Zn14	16g	0.1204(5)	0.4515(7)	0.0917(1)	1	308(15)
Zn15	16g	0.1812(5)	0.3499(7)	0.2213(1)	1	288(13)
Zn16	16g	0.1863(5)	0.1252(7)	0.4493(1)	1	303(13)
Zn17	16g	0.1233(5)	0.4592(8)	0.2717(1)	1	344(16)
Zn18	16g	0.1194(5)	0.0446(8)	0.0452(1)	1	309(16)
Zn19	16g	0.1756(5)	0.3386(7)	0.1418(1)	1	339(14)
Zn20	16g	0.1170(4)	0.0371(5)	0.31804(16)	1	286(11)
Zn21	16g	0.1262(6)	0.4834(7)	0.3638(1)	1	340(17)
Zn22	16g	0.1864(4)	0.1161(6)	0.1843(1)	1	349(13)

^a sof of Zn, sof of (Pt) = 1 – sof of (Zn)

A 7: Anisotropic displacement parameters U (pm²) for Pt₅Zn_{14.0(1)}

Atom No.	U11	U22	U33	U12	U13	U23
Pt1	310(20)	230(30)	300(20)	0	-17(18)	0
Pt2	350(20)	215(19)	277(16)	0	4(13)	0
Pt3	324(13)	120(13)	349(14)	0	-9(15)	0
Pt4	309(17)	137(17)	325(17)	0	8(13)	0
Pt5	331(18)	182(19)	263(17)	0	20(12)	0
Pt6	370(20)	246(19)	278(15)	0	-4(12)	0
Pt7	331(8)	166(9)	337(9)	12(7)	16(9)	8(12)
Pt8	336(11)	225(12)	303(10)	23(11)	-3(8)	-3(10)
Pt9	338(11)	182(11)	269(10)	-24(10)	-11(8)	-24(9)
M10	356(19)	201(19)	313(17)	11(16)	8(11)	-20(14)
N10	356(19)	201(19)	313(17)	11(16)	8(11)	-20(14)
Zn11	390(50)	210(50)	340(50)	0	-50(40)	0
Zn12	400(40)	160(40)	290(30)	0	40(40)	0
Zn13	420(50)	90(50)	370(50)	0	60(30)	0
Zn14	460(60)	210(50)	400(50)	0	70(40)	0
Zn15	330(50)	230(60)	320(50)	0	50(40)	0
Zn16	300(50)	330(60)	390(50)	0	-80(40)	0
Zn17	410(50)	170(50)	340(50)	0	-60(40)	0
Zn18	350(50)	190(50)	380(50)	0	100(40)	0
Zn19	370(30)	180(40)	360(30)	0	40(30)	0
Zn20	440(50)	200(50)	410(50)	0	-60(40)	0
Zn21	410(30)	200(30)	300(30)	-60(30)	30(20)	-10(30)
Zn22	380(30)	130(30)	210(30)	70(30)	30(20)	10(30)
Zn23	380(30)	150(30)	380(30)	0(30)	30(20)	-80(30)
Zn24	420(40)	220(40)	290(30)	-20(30)	10(30)	30(30)
Zn25	360(30)	200(30)	310(30)	50(30)	40(20)	-60(30)
Zn26	310(30)	240(30)	350(30)	-20(30)	-40(20)	-30(30)
Zn27	370(40)	290(40)	370(30)	30(30)	-10(30)	-30(30)
Zn28	400(40)	210(40)	310(30)	-70(30)	0(30)	-50(30)
Zn29	420(30)	230(40)	360(30)	0(30)	-10(30)	-20(30)
Zn30	360(30)	190(30)	310(30)	-48(19)	20(30)	-20(30)
Zn31	460(40)	310(40)	250(30)	-30(30)	30(30)	-30(20)
Zn32	380(20)	180(30)	480(30)	-50(20)	30(20)	0(40)

The phase $\text{Pt}_{27}\text{Zn}_{85}$:

Structurally most disordered compared to other γ -brass related phases is $\text{Pt}_{27}\text{Zn}_{85}$. It crystallizes in space group Fmm2, $a = 1293.1(3)$ pm, $b = 5535.10(11)$ pm, $c = 913.40(18)$ pm. The structure contains 448 atoms in the unit cell, Pearson symbol is oF448. Single crystals were selected from the sample of nominal composition of 25 at.%. Application of direct methods via SHELX-97 [58] revealed all the atom positions. The final anisotropic least-squares refinements converged at $R1 = 0.0514$, $wR2 = 0.1781$ with 291 parameters and 2221 independent reflections with $I_o > 2\sigma(I_o)$. The displacement parameters of four atoms (M1, M2, M3 and M4) were relatively high compared to rest of the atoms suggesting that these positions could be mixed occupied. The final refinement cycles showed that the occupancy factors of M1, M2, M3 and M4 positions are 71%, 74%, 35%, and 10% of Zn, resulting in the composition $\text{Pt}_{27.2}\text{Zn}_{84.8(2)}$. In addition, the structure was refined as racemic twin. The batch scale factor (BASF) for the unequal twin components was 0.46(2).

An attempt was made to minimize the structural disorder. For that purpose, a sample from a second batch was annealed at 770 K for a week. The crystals from the annealed sample were subjected to X-ray diffraction studies. The lattice parameters from a second crystal were some what shorter than the lattice parameters from the first crystal (annealed at 970 K). No additional structural ordering was observed. The lattice parameters for second crystal (annealed at 770 K) are: $a = 1290.4(3)$ pm, $b = 5529.8(11)$ pm and $c = 911.5(2)$ pm.

The structure of $\text{Pt}_{27}\text{Zn}_{85}$ can be described as an ordered $3 \sqrt{2} a_\beta \times 3 a_\beta \times 13 \sqrt{2} a_\beta$ defect variant of a β -brass type structure of index 234 with 20 vacancies per unit cell. The structure is composed of 448 atoms distributed over 39 distinct atomic sites in which 26 atomic positions are occupied by Zn atoms, 9 by Pt atoms and 4 positions are mixed occupied. This phase is the most Zn-rich and disordered phase in the phase field $0.24 < x_{\text{Pt}} < 0.27$ of γ -brass related phases.

A 8: Crystallographic and technical data for the single-crystal structure determination

Sum formula	Pt _{27.2} Zn _{84.8} (2)
Space group (No.)	Fmm2(42)
Z	4
a / pm	1293.1(3)
b / pm	5535.1(11)
c / pm	913.40(18)
V / 10 ⁶ pm ³	6538(2)
Molar mass / g mol ⁻¹	10849.83
ρ_{cal} / g cm ⁻³	11.023
μ / mm ⁻¹	88.32
<i>Data collection</i>	
Crystal size / mm ³	0.13 × 0.12 × 0.13
Diffractometer	IPDS-II (STOE & Cie)
Temperature / K	293(2)
Radiation / monochromator	MoK α / Graphite
Distance crystal-IP / mm	100
ϕ ; ω_{min} – ω_{max} ; $\Delta\omega$	0; 0–130; 0.5
$2\theta_{max}$ / °	53.7
Collected reflections	–16 ≤ h ≤ 13 –62 ≤ k ≤ 70 –11 ≤ l ≤ 11
Total reflections	7150
<i>Data reduction</i>	
Program	IPDS-II [57] / X-RED [61]
Absorption correction	Numerical, X-SHAPE [62]
max. / min. Transmission	0.0586 / 0.0076
Unique reflections	3531
R_{int}	0.0798
<i>Refinement</i>	
Program	SHELXL-97 [58]
Refined on	$ F_o ^2$
Reflections $I_o > 2\sigma(I_o)$	2221
Variables	291
R_1 ($I_o > 2\sigma(I_o)$)	0.0514
R_1 (all)	0.0720
w R_2 (all)	0.1781
Goodness of fit	1.064
$\Delta\rho_{max}$ / $\Delta\rho_{min}$ / 10 ⁻⁶ e pm ⁻³	4.735 / –6.725
Extinction coefficient	0.000021(3)
Absolute structure factor	0.46(2)

$$1/w = \sigma^2(F_o^2) + (0.1053(\text{Max}(F_o^2, 0) + 2F_c^2)/3)^2$$

A 9: Positional and equivalent isotropic displacement parameters U_{eq} (pm²) for Pt₂₇Zn₈₅

Atom No.	Wy	x	y	z	sof	U_{eq}
Zn1	4a	0	0	0.3151(8)	1	147(17)
Zn2	8c	0	0.04603(11)	0.2154(7)	1	207(12)
Zn3	8c	0	0.09497(12)	0.2601(8)	1	217(8)
Zn4	8c	0	0.14356(11)	0.2950(7)	1	232(13)
Zn5	8c	0	0.19107(8)	0.2079(7)	1	133(12)
Zn6	8c	0	0.23691(11)	0.3097(6)	1	200(13)
Zn7	8c	0	0.21449(11)	0.7458(7)	1	221(11)
Zn8	8c	0	0.16565(10)	0.7297(6)	1	158(10)
Zn9	8c	0	0.11774(10)	0.8186(6)	1	155(13)
Zn10	8c	0	0.07371(10)	0.7117(6)	1	136(11)
Zn11	8c	0	0.02343(10)	0.7768(7)	1	211(11)
Zn12	8d	0.1155(4)	0	0.5574(7)	1	194(11)
Zn13	8d	0.1860(4)	0	0.1320(7)	1	225(14)
Zn14	16e	0.1804(3)	0.03390(8)	0.3554(5)	1	173(9)
Zn15	16e	0.1247(3)	0.03909(7)	0.9892(5)	1	178(8)
Zn16	16e	0.1210(3)	0.07611(7)	0.4668(5)	1	188(9)
Zn17	16e	0.1192(3)	0.11576(7)	0.0564(5)	1	219(9)
Zn18	16e	0.1270(2)	0.15348(8)	0.5177(6)	1	216(7)
Zn19	16e	0.1747(3)	0.15842(8)	0.1624(5)	1	167(9)
Zn20	16e	0.1859(3)	0.19409(8)	0.3861(5)	1	194(10)
Zn21	16e	0.1179(3)	0.19197(6)	0.9644(5)	1	177(9)
Zn22	16e	0.1236(3)	0.23164(6)	0.5426(6)	1	222(9)
Zn23	16e	0.1800(3)	0.22586(8)	0.1487(5)	1	181(10)
Zn24	16e	0.1772(3)	0.14971(8)	0.8496(6)	1	200(9)
Zn25	16e	0.1844(3)	0.11141(8)	0.6390(5)	1	185(10)
Zn26	16e	0.1852(3)	0.08164(9)	0.8732(5)	1	223(11)
Pt1	4a	0	0	0.0353(3)	1	173(6)
Pt2	8c	0	0.03850(3)	0.5004(2)	1	137(4)
Pt3	8c	0	0.07745(4)	0.9851(2)	1	199(5)
Pt4	16e	0.18024(11)	0.11804(3)	0.34166(14)	1	181(4)
Pt5	8c	0	0.15367(4)	0.0118(3)	1	130(3)
Pt6	8c	0	0.19258(4)	0.4802(2)	1	180(6)
Pt7	8c	0	0.23059(3)	0.0239(2)	1	149(4)
Pt8	16e	0.18051(11)	0.19082(2)	0.67747(16)	1	168(4)
Pt9	8d	0.18175(14)	0	0.8365(2)	1	127(4)
M1	16e	0.17908(12)	0.07310(3)	0.17185(17)	0.71(1) ^a	139(5)
M2	8c	0	0.11498(4)	0.5349(2)	0.74(1) ^a	104(7)
M3	16e	0.17997(18)	0.23470(5)	0.8468(3)	0.35(1) ^a	185(9)
M4	16e	0.1747(3)	0.04216(6)	0.6638(5)	0.098(11) ^a	169(12)

^a sof of Zn, sof of (Pt) = 1 – sof of (Zn)

A 10: Anisotropic displacement parameters $U(\text{pm}^2)$ for $\text{Pt}_{27}\text{Zn}_{85}$

Atom No.	U11	U22	U33	U12	U13	U23
Zn1	300(40)	110(40)	40(30)	0	0	0
Zn2	210(30)	210(30)	210(30)	0	-10(20)	0
Zn3	240(19)	191(18)	219(18)	0	-38(14)	0
Zn4	200(30)	310(30)	180(30)	0	140(20)	0
Zn5	130(20)	100(30)	170(30)	0	-40(17)	0
Zn6	290(30)	250(30)	60(20)	0	-100(20)	0
Zn7	130(20)	330(30)	200(20)	0	-110(20)	0
Zn8	130(20)	180(30)	160(20)	0	30(20)	0
Zn9	270(30)	120(30)	80(20)	0	10(20)	0
Zn10	170(20)	70(20)	170(30)	0	0(20)	0
Zn11	240(30)	180(20)	220(30)	0	40(20)	0
Zn12	200(20)	160(20)	230(30)	0	0	0(20)
Zn13	210(30)	220(30)	240(30)	0	0	-110(20)
Zn14	164(18)	163(19)	190(20)	-19(14)	17(17)	-41(14)
Zn15	161(16)	166(19)	208(18)	-85(12)	-23(14)	19(14)
Zn16	256(18)	191(19)	116(18)	-49(14)	-4(15)	58(15)
Zn17	234(18)	81(16)	340(20)	-53(14)	36(17)	-13(15)
Zn18	287(14)	100(13)	261(15)	-83(17)	-62(11)	22(19)
Zn19	176(17)	110(17)	220(20)	-51(13)	61(18)	-100(15)
Zn20	143(19)	290(20)	150(20)	65(13)	-22(13)	-8(13)
Zn21	270(20)	95(17)	170(20)	-39(12)	-31(13)	105(16)
Zn22	258(19)	39(15)	370(20)	39(13)	49(17)	-51(17)
Zn23	179(19)	147(17)	220(20)	54(13)	2(16)	-66(13)
Zn24	190(18)	188(19)	220(20)	-7(15)	-20(19)	-4(16)
Zn25	195(18)	160(17)	200(20)	73(13)	17(14)	-54(13)
Zn26	210(20)	210(19)	250(30)	59(14)	-64(18)	37(14)
Pt1	193(13)	126(13)	200(15)	0	0	0
Pt2	131(8)	112(9)	170(9)	0	-7(7)	0
Pt3	220(10)	175(11)	204(12)	0	26(7)	0
Pt4	203(7)	144(7)	194(7)	-22(4)	21(7)	34(6)
Pt5	159(6)	84(6)	147(6)	0	-8(5)	0
Pt6	169(10)	213(12)	157(11)	0	13(7)	0
Pt7	189(9)	83(9)	175(9)	0	1(7)	0
Pt8	187(7)	150(8)	168(7)	-5(4)	2(5)	26(6)
Pt9	154(8)	77(9)	148(9)	0	0	51(7)
M1	190(8)	76(7)	152(8)	-26(5)	-29(8)	9(6)
M2	112(11)	72(11)	127(12)	0	-10(8)	0
M3	168(13)	194(13)	192(14)	-18(8)	33(11)	26(9)
M4	224(19)	98(16)	186(19)	15(11)	45(15)	-17(13)

The phase $\text{Pt}_{43}\text{Zn}_{121}$:

Structurally most complex compared with other γ -brass related phase is $\text{Pt}_{43}\text{Zn}_{121}$. It crystallizes in the non-centrosymmetric space group $Fm\bar{m}2$. The lattice parameters were found to be $a = 1291.8(1)$ pm, $b = 8096.8(6)$ pm, $c = 909.1(1)$ pm, $Z = 4$, Pearson symbol oF656. The single crystal was obtained from the sample of nominal composition 27.5 at.% of Pt. Application of direct methods via SHELX-97 [58] revealed all the atom positions. The calculations converged at a residual $R1 = 0.0614$ for 3759 reflections with $I_o > 2\sigma(I_o)$ out of 5422 reflection for 416 variables including anisotropic displacement parameters. The displacement parameters of the atom Zn17 (U_{11}) is very small compared to other two principal axis. The final cycles of list-squares refinement suggest the possible racemic twinning. The BASF for the unequal components in a twin refinement was 0.49(1). The maximal residual electron density of $6.15 \cdot 10^{-6} \text{e pm}^{-3}$ was found close to the Pt4 atom. Noteworthy, one out of 56 crystallographic site seems to be statistically occupied by Pt and Zn (47(1)% Zn and 53% Pt). The composition is found to be $\text{Pt}_{43.1}\text{Zn}_{120.9(1)}$.

A 11: Crystallographic and technical data for the single-crystal structure determination

Sum formula	Pt _{43.1} Zn _{120.9(1)}
Space group (No.)	Fmm2(42)
Z	4
a / pm	1291.8(1)
b / pm	8096.8(6)
c / pm	909.1(1)
V / 10 ⁶ pm ³	9509(1)
Molar mass / g mol ⁻¹	16309.34
ρ_{cal} / g cm ⁻³	11.393
μ / mm ⁻¹	92.877
<i>Data collection</i>	
Crystal size / mm ³	0.13 × 0.18 × 0.15
Diffractometer	IPDS-II (STOE & Cie)
Temperature / K	293
Radiation / monochromator	MoK α / Graphite
Distance Crystal-IP / mm	120
$\omega_{min} - \omega_{max}; \Delta\omega$	0-165; 0.5
$2\theta_{max}$ / °	54.2
Collected reflections	-16 ≤ h ≤ 16 -102 ≤ k ≤ 102 -11 ≤ l ≤ 11
Total reflections	25124
<i>Data reduction</i>	
Program	IPDS-II-Software [57]/X-RED [61]
Absorption correction	X-SHAPE [62], Numerical
max. / min. Transmission	0.1075 / 0.0068
Unique reflections	5422
R_{int}	0.1074
<i>Refinement</i>	
Program	SHELXL-97 [58]
Refined on	F _o ²
Reflections I _o > 2σ(I _o)	3759
Variables	416
R ₁ (I _o > 2σ(I _o))	0.0614
R ₁ (all)	0.0867
wR ₂ (all)	0.1689
Goodness of fit	0.913
$\Delta\rho_{max} / \Delta\rho_{min} / 10^{-6} \text{e pm}^{-3}$	6.149 / -5.198
Absolute structure factor	0.49(1)
$1/w = \sigma^2(F_o^2) + (0.1(\text{Max}(F_o^2, 0) + 2F_c^2)/3)^2$	

A 12: Positional and equivalent isotropic displacement parameters U_{eq} (pm²) for Pt₄₃Zn₁₂₁

Atom No.	Wy.	x	y	z	sof	U_{eq}
Pt1	4a	0	0	0.0035(4)	1	164(7)
Pt2	8c	0	0.21090(3)	0.0481(2)	1	136(5)
Pt3	8c	0	0.13199(3)	0.5543(2)	1	148(5)
Pt4	8c	0	0.07851(3)	0.5019(2)	1	144(5)
Pt5	8c	0	0.05304(3)	0.0592(2)	1	152(6)
Pt6	8c	0	0.02627(3)	0.5414(2)	1	162(5)
Pt7	8c	0	0.10489(3)	0.0281(3)	1	136(3)
Pt8	8c	0	0.18396(3)	0.5171(2)	1	134(4)
Pt9	8c	0	0.23695(3)	0.5013(2)	1	158(5)
Pt10	8c	0	0.15786(3)	0.9951(2)	1	133(5)
Pt11	8d	0.1816(2)	0	0.2049(2)	1	149(4)
Pt12	16e	0.1801(1)	0.08089(2)	0.6984(1)	1	141(3)
Pt13	16e	0.1809(1)	0.16040(2)	0.1902(1)	1	131(3)
Pt14	16e	0.1823(1)	0.20939(2)	0.8523(1)	1	149(4)
Pt15	16e	0.1813(1)	0.12918(2)	0.3602(2)	1	151(3)
Pt16	16e	0.1811(1)	0.04959(2)	0.8683(2)	1	178(4)
M1	16e	0.1781(2)	0.23958(3)	0.6832(2)	0.47(1) ^a	173(7)
Zn1	4a	0	0	0.7261(10)	1	220(20)
Zn2	8c	0	0.0802(1)	0.2291(8)	1	259(19)
Zn3	8c	0	0.01610(8)	0.2654(6)	1	163(11)
Zn4	8c	0	0.17716(8)	0.2387(6)	1	174(13)
Zn5	8c	0	0.09669(8)	0.7525(7)	1	152(12)
Zn6	8c	0	0.2414(1)	0.2270(8)	1	289(17)
Zn7	8c	0	0.15988(9)	0.7169(8)	1	223(16)
Zn8	8c	0	0.06488(7)	0.7813(6)	1	181(12)
Zn9	8c	0	0.2097(1)	0.3273(7)	1	110(13)
Zn10	8c	0	0.1298(1)	0.8338(6)	1	120(13)
Zn11	8c	0	0.1454(1)	0.2782(9)	1	213(9)
Zn12	8c	0	0.0502(1)	0.3392(6)	1	126(12)
Zn13	8c	0	0.0313(1)	0.8336(7)	1	174(12)
Zn14	8c	0	0.2262(1)	0.7863(7)	1	224(13)
Zn15	8c	0	0.1927(1)	0.8047(7)	1	222(13)
Zn16	8c	0	0.1122(1)	0.3187(7)	1	181(12)
Zn17	8d	0.1899(5)	0	0.9128(8)	1	203(14)
Zn18	8d	0.1142(6)	0	0.4894(8)	1	221(14)
Zn19	16e	0.1733(3)	0.18224(6)	0.6794(6)	1	163(10)
Zn20	16e	0.1775(3)	0.02914(5)	0.3770(5)	1	99(9)
Zn21	16e	0.1721(3)	0.10255(6)	0.1857(6)	1	172(10)
Zn22	16e	0.1833(4)	0.23331(6)	0.3795(6)	1	227(11)
Zn23	16e	0.1880(3)	0.15475(6)	0.8953(5)	1	180(10)
Zn24	16e	0.1182(4)	0.21053(5)	0.5676(5)	1	156(9)
Zn25	16e	0.1206(4)	0.13138(6)	0.0715(5)	1	202(10)
Zn26	16e	0.1774(3)	0.02334(6)	0.6870(6)	1	187(10)
Zn27	16e	0.1781(4)	0.18758(5)	0.3688(6)	1	186(10)
Zn28	16e	0.1884(3)	0.07600(6)	0.4055(5)	1	166(9)
Zn29	16e	0.1232(4)	0.05230(5)	0.5755(5)	1	181(10)
Zn30	16e	0.1242(4)	0.02666(5)	0.0542(5)	1	182(10)
Zn31	16e	0.1266(4)	0.18388(5)	0.0159(6)	1	195(10)
Zn32	16e	0.1824(4)	0.05583(6)	0.1669(5)	1	172(10)
Zn33	16e	0.1236(4)	0.23740(5)	0.9878(6)	1	249(11)
Zn34	16e	0.1195(4)	0.15821(5)	0.4785(5)	1	173(9)
Zn35	16e	0.1161(4)	0.07875(6)	0.9802(6)	1	204(10)
Zn36	16e	0.1259(3)	0.10514(7)	0.5328(7)	1	186(7)
Zn37	16e	0.1842(4)	0.13445(6)	0.6543(5)	1	196(10)
Zn38	16e	0.1764(4)	0.10856(6)	0.8723(7)	1	204(10)
Zn39	16e	0.1834(4)	0.21188(6)	0.1456(6)	1	248(12)

^a sof of Zn, sof of (Pt) = 1 – sof of (Zn)

A 13: Anisotropic displacement parameters U (pm^2) for $\text{Pt}_{43}\text{Zn}_{121}$

Atom No.	U11	U22	U33	U12	U13	U23
Pt1	87(14)	251(16)	152(15)	0	0	0
Pt2	115(10)	182(11)	109(11)	0	-18(8)	0
Pt3	123(10)	175(9)	145(11)	0	-23(8)	0
Pt4	144(9)	222(10)	81(9)	0	0	-6(8)
Pt5	149(11)	166(11)	140(13)	0	-40(8)	0
Pt6	163(11)	177(11)	146(10)	0	2(8)	0
Pt7	125(7)	173(7)	110(6)	0	3(5)	0
Pt8	113(10)	127(9)	162(10)	0	-14(8)	0
Pt9	93(10)	173(11)	208(12)	0	7(8)	0
Pt10	73(10)	191(10)	134(12)	0	28(8)	0
Pt11	98(10)	187(10)	145(11)	0	-6(8)	0
Pt12	151(7)	165(7)	106(7)	3(5)	3(6)	-3(6)
Pt13	135(7)	140(6)	119(7)	6(5)	17(6)	-1(6)
Pt14	71(6)	164(6)	210(9)	8(5)	-7(6)	23(6)
Pt15	87(6)	163(7)	204(8)	12(5)	0(7)	31(6)
Pt16	140(7)	200(6)	195(8)	14(5)	7(7)	39(7)
M1	168(12)	170(11)	181(13)	15(8)	24(10)	9(9)
Zn1	300(60)	260(50)	100(40)	0	0	0
Zn2	170(40)	400(40)	210(40)	0	-20(30)	0
Zn3	110(30)	290(30)	100(20)	0	-20(20)	0
Zn4	190(30)	230(30)	100(20)	0	-50(20)	0
Zn5	110(30)	250(30)	90(20)	0	-40(20)	0
Zn6	250(40)	370(40)	250(40)	0	110(30)	0
Zn7	240(40)	170(30)	260(40)	0	0(30)	0
Zn8	120(30)	290(30)	130(30)	0	40(20)	0
Zn9	40(20)	100(30)	180(30)	0	15(19)	0
Zn10	130(30)	160(30)	70(30)	0	40(20)	0
Zn11	180(20)	260(20)	210(20)	0	26(17)	0
Zn12	120(30)	200(30)	60(20)	0	-40(20)	0
Zn13	80(20)	270(30)	170(30)	0	-10(20)	0
Zn14	180(30)	200(30)	300(30)	0	50(20)	0
Zn15	220(30)	220(30)	230(30)	0	-50(20)	0
Zn16	140(30)	200(30)	210(30)	0	0(20)	0
Zn17	0(20)	300(30)	310(30)	0	0	-10(20)
Zn18	190(30)	160(30)	320(40)	0	0	70(30)
Zn19	80(20)	170(19)	240(20)	21(14)	-22(19)	49(17)
Zn20	131(18)	112(17)	55(18)	11(14)	-7(16)	55(16)
Zn21	90(20)	250(20)	180(20)	33(15)	-86(19)	43(17)
Zn22	210(20)	250(20)	220(20)	43(17)	0(20)	70(20)
Zn23	140(20)	240(20)	150(20)	8(15)	-24(18)	32(17)
Zn24	160(20)	200(20)	110(20)	-13(14)	-3(14)	-42(17)
Zn25	230(30)	270(20)	100(20)	-11(19)	0(16)	-38(18)
Zn26	90(20)	210(20)	260(20)	17(15)	-87(19)	39(17)
Zn27	200(20)	146(19)	210(20)	-2(16)	71(18)	83(19)
Zn28	79(18)	190(20)	230(20)	38(14)	8(16)	14(16)
Zn29	220(20)	170(20)	150(20)	-14(15)	-9(15)	-60(18)
Zn30	160(20)	230(20)	160(20)	-10(15)	11(16)	0(16)
Zn31	130(20)	200(20)	250(20)	-29(15)	45(18)	32(17)
Zn32	120(20)	167(18)	230(20)	-16(16)	36(19)	-35(17)
Zn33	170(20)	170(20)	410(30)	12(15)	-14(19)	40(20)
Zn34	115(19)	135(18)	270(30)	27(16)	49(16)	44(18)
Zn35	180(20)	165(19)	270(30)	-16(17)	13(16)	50(19)
Zn36	175(17)	170(15)	214(16)	0(20)	50(12)	0(20)
Zn37	140(20)	280(20)	170(20)	-15(17)	-11(18)	-26(18)
Zn38	250(20)	174(19)	190(20)	-66(17)	-10(19)	90(20)
Zn39	280(30)	380(30)	90(20)	15(19)	38(15)	-49(18)

The Phase Ni₂₃Zn₇₂

A 14: Crystallographic and technical data for the single-crystal structure determination

Sum formula	Ni ₂₃ Zn ₇₂
Space group (No.)	Cmce (64)
Z	4
a / pm	1251.6(3)
b / pm	885.1(2)
c / pm	4571.2(9)
V / 10 ⁶ pm ³	5063.9(2)
Molar mass / g mol ⁻¹	6111.97
ρ_{cal} / g cm ⁻³	7.945
μ / mm ⁻¹	41.63
<i>Data collection</i>	
Crystal size / mm ³	0.13 × 0.12 × 0.15
Diffractometer	IPDS-I (STOE & Cie)
Temperature / K	293
Radiation / monochromator	MoK α / Graphite
Distance crystal-IP / mm	100
$\phi_{min} - \phi_{max}; \Delta\phi$	0 – 145; 1
$2\theta_{max}$ / °	42.0
Collected reflections	-12 ≤ h ≤ 12 -8 ≤ k ≤ 8 -41 ≤ l ≤ 43
Total No. reflections	6410
<i>Data reduction</i>	
Program	IPDS-I-Software [57] / X-RED [61]
Absorption correction	Numerical, X-SHAPE [62]
max. / min. Transmission	0.0547 / 0.0094
Unique reflection	1373
R _{int}	0.0936
<i>Refinement</i>	
Program	SHELXL-97 [58]
Refined on	F _o ²
Reflections I _o > 2σ(I _o)	1373
Variables	111
R ₁ (I _o > 2σ(I _o))	0.0367
R ₁ (all)	0.1580
wR ₂ (all)	0.1415
Goodness of fit	0.505
Extinction coefficient	0.000031(4)
$\Delta\rho_{max} / \Delta\rho_{min} / 10^{-6}$ e pm ⁻³	1.192 / -1.873
$1/w = \sigma^2(F_o^2) + (0.1(\text{Max}(F_o^2, 0) + 2F_c^2)/3)^2$	

A 15: Positional and equivalent isotropic displacement parameters $U_{\text{iso}}(\text{pm}^2)$ for $\text{Ni}_{23}\text{Zn}_{72}$

Atom No.	Wy	x	y	z	sof	U_{iso}
Ni1	4a	0	0	0	1	160(50)
Ni2	8f	0	0.4948(12)	0.1361(3)	1	30(30)
Ni3	8f	0	0.0161(10)	0.1812(4)	1	110(30)
Ni4	8f	0	0.4835(13)	0.4090(3)	1	90(30)
Ni5	8f	0	0.0171(13)	0.4544(3)	1	60(40)
Ni6	8f	0	0.4912(13)	0.2270(3)	1	120(40)
Ni7	16g	0.1753(7)	0.3340(7)	0.3188(3)	1	118(17)
Ni8	16g	0.1753(10)	0.3327(10)	0.0436(2)	1	60(20)
Ni9	16g	0.1755(9)	0.1638(9)	0.0936(2)	1	70(20)
Zn11	8d	0.1273(14)	0	$\frac{1}{2}$	1	160(30)
Zn12	8f	0	0.2994(9)	0.1807(3)	1	110(20)
Zn13	8f	0	0.2076(12)	0.2355(3)	1	170(30)
Zn14	8f	0	0.1993(11)	0.4047(3)	1	120(30)
Zn15	8f	0	0.2986(13)	0.4572(3)	1	110(30)
Zn16	8f	0	0.2154(12)	0.1258(3)	1	140(30)
Zn17	8f	0	0.2807(11)	0.0134(3)	1	130(30)
Zn18	8f	0	0.2707(11)	0.3476(3)	1	100(30)
Zn19	8f	0	0.2494(13)	0.0688(3)	1	120(20)
Zn20	8f	0	0.2648(11)	0.2911(3)	1	160(30)
Zn21	16g	0.1781(9)	0.1567(8)	0.3686(2)	1	150(20)
Zn22	16g	0.1773(9)	0.3450(8)	0.49418(19)	1	70(20)
Zn23	16g	0.1836(9)	0.3652(8)	0.4152(2)	1	130(20)
Zn24	16g	0.1183(10)	0.4586(7)	0.0918(2)	1	140(20)
Zn25	16g	0.1819(10)	0.3601(8)	0.2209(2)	1	170(20)
Zn26	16g	0.1863(9)	0.1275(8)	0.4500(2)	1	160(20)
Zn27	16g	0.1226(9)	0.4659(8)	0.2711(2)	1	160(20)
Zn28	16g	0.1141(10)	0.0491(8)	0.04456(18)	1	90(20)
Zn29	16g	0.1778(9)	0.3492(8)	0.14310(18)	1	120(20)
Zn30	16g	0.1127(7)	0.0508(6)	0.3183(3)	1	133(17)
Zn31	16g	0.1262(9)	0.4888(8)	0.3640(2)	1	150(20)
Zn32	16g	0.1875(6)	0.1228(5)	0.1828(3)	1	140(16)
Zn33	16g	0.1779(10)	0.1594(9)	0.2691(2)	1	150(20)

References

- [1] P. Villars, *Pearson's Handbook, Desk Ed.* (ASM, Materials Park, OH, 1997).
- [2] J. Nagamatsu, N. Nakagawa, T. Muranaka, Y. Zenitani, J. Akimitsu, *Nature* **410**, 63 (2001).
- [3] C. Pfleiderer, M. Uhlarz, S. M. Hayden, R. Vollmer, H. v. Löhneysen, N. R. Bernhoeft, G. G. Lonzarich, *Nature* **412**, 58 (2001).
- [4] G. J. Snyder, M. Christensen, E. Nishibori, T. Caillat, B. B. Iversen, *Nature Mater.* **3**, 458 (2004).
- [5] J. Nylén, M. Andersson, S. Lidin, U. Häussermann, *J. Am. Chem. Soc.* **126**, 16306 (2004).
- [6] F. J. DiSalvo, *Science* **285**, 703 (1999).
- [7] X. Huang, G. J. Ackland, K. M. Rabe, *Nature Mater.* **2**, 307 (2003).
- [8] S. M. Kauzlarich, ed., *Chemistry, Structure and Bonding of Zintl Phases* (VCH Publishes, New York, 1996).
- [9] R. Nesper, *Angew. Chem. Int. Ed. Engl.* **30**, 789 (1991).
- [10] C. H. E. Belin, R. C. H. Belin, *J. Solid State Chem.* **151**, 85 (2000).
- [11] A. Johansson, H. Ljung, S. Westman, *Acta Chem. Scand.* **22**, 2743 (1968).
- [12] G. Nover, K. Schubert, *J. Alloys Comp.* **75**, 51 (1980).
- [13] A. Johansson, S. Westman, *Acta Chem. Scand.* **24**, 3471 (1970).
- [14] W. Hume-Rothery, *J. Inst. Metals* **35**, 295 (1926).
- [15] W. Hume-Rothery, G. V. Raynor, *The Structure of Metals and Alloys* (Institute of Metals, London, 1954).
- [16] L. Pauling, J. Ewing, *Reviews of Modern Physics* **20**, 112 (1948).
- [17] G. D. Preston, *Phil. Mag.* **5**, 1207 (1928).
- [18] K. H. J. Buschow, P. van Engen, R. Jongebreur, *J. Mag. Mag. Mater.* **38**, 1 (1983).
- [19] A. Westgren, G. Phragmen, *Phil. Mag.* **5**, 280 (1928).
- [20] A. J. Bradley, J. Thewlis, *Proc. Roy. Soc. London* **112A**, 678 (1926).
- [21] A. Westgren, G. Phragmen, *Z. Metallkde* **18**, 279 (1926).
- [22] A. Westgren, G. Phragmen, *Trans. Faraday Soc.* **25**, 379 (1929).
- [23] U. Mizutani, T. Takeuchi, H. Sato, *Prog. Mat. Sci.* **49**, 227 (2004).
- [24] R. Asahi, H. Sato, T. Takeuchi, U. Mizutani, *Phys. Rev.* **B72**, 125102 (2005).
- [25] H. Jones, *Proc. Phys. Soc.* **49**, 250 (1937).
- [26] N. F. Mott, H. Jones, *The Theory of the Properties of Metals and Alloys* (Dover, New York,

- 1958).
- [27] T. Takeuchi, H. Sato, U. Mizutani, *J. Alloys Comp.* **342**, 355 (2002).
- [28] H. Sato, R. S. Toth, *Phys. Rev. Letters* **8**, 239 (1962).
- [29] R. Asahi, H. Sato, T. Takeuchi, U. Mizutani, *Phys. Rev.* **B71**, 165103 (2005).
- [30] A. T. Paxton, M. Methfessel, D. G. Pettifor, *Proc. Roy. Soc. Lond.* **A453**, 1493 (1997).
- [31] G. T. de Laissardière, D. N. Manh, L. Magaud, J. P. Julien, F. Cyrot-Lackmann, D. Mayou, *Phy. Rev.* **B52**, 7920 (1995).
- [32] A. J. Morton, *Phys. Status Solidi (a)* **44**, 205 (1977).
- [33] A. J. Morton, *Phys. Status Solidi (a)* **33**, 395 (1976).
- [34] A. J. Morton, *Acta Metallurgica* **27**, 863 (1979).
- [35] Y. Koyama, J. Yoshida, H. Hoshiya, Y. Nakamura, *Phy. Rev.* **B40**, 5378 (1989).
- [36] Y. Koyama, M. Hatano, M. Tanimura, *Phy. Rev.* **B53**, 11462 (1996).
- [37] B. Grushko, E. Kowalska-Strzęciwilk, B. Przepiórzyński, M. Surowiec, *J. Alloys Comp.* **402**, 98 (2005).
- [38] V. Demange, J. Ghanbaja, F. Machizaud, J. M. Dubois, *Phil. Mag.* **85**, 1261 (2005).
- [39] M. Armbrüster, B. Harbrecht, S. Lee, *ECSSC OSLO* (2001). Book of Abstracts.
- [40] H. Nowotny, E. Bauer, A. Stempfl, H. Bittner, *Monatsh. Chem.* **83**, 221 (1952).
- [41] W. Ekman, *Z. Physik. Chem. B* **12**, 57 (1931).
- [42] W. Carl, K. Schubert, *J. Less-Common Met.* **19**, 279 (1969).
- [43] H. Nowotny, E. Bauer, A. Stempfl, *Monatsh. Chem.* **81**, 1164 (1950).
- [44] M. Boström, S. Hovmöller, *J. Alloys Comp.* **314**, 154 (2001).
- [45] M. A. Zhuravleva, X. Wang, A. J. Schultz, T. Bakas, M. G. Kanatzidis, *Inorg. Chem.* **41**, 6056 (2002).
- [46] R. Belin, M. Tillard, L. Monconduit, *Acta Crystallogr.* **C56**, 267 (2000).
- [47] P. C. Canfield, Z. Fisk, *Phil. Mag.* **B65**, 1125 (1992).
- [48] M. G. Kanatzidis, R. Pöttgen, W. Jeitschko, *Angew. Chem. Int. Ed. Engl.* **44**, 6996 (2005).
- [49] M. Boström, S. Hovmöller, *J. Solid State Chem.* **153**, 398 (2000).
- [50] M. Boström, Crystal structures and phase equilibria in the Mn-Ga system, Ph.D. thesis, Stockholm University (2002).
- [51] H. Ipser, R. Krachler, K. L. Komarek, *Thermochemistry of Alloys* (Kluwer Academic, Dordrecht, 1989).
- [52] K. W. Richter, S. Besana, G. Borzone, H. Ipser, *J. Alloys Comp.* **365**, 181 (2004).

- [53] H. Ipsen, *Ber. Bunsenges. Phys. Chem.* **102**, 1217 (1998).
- [54] L. Voisin, M. Hino, K. Itagaki, *Mater. Trans.* **44**, 2654 (2003).
- [55] Philips Analytical, X'Pert Plus (1.0) (1999). Almelo.
- [56] J. Rodriguez-Carvajal, FULLPROF—A Program Package for Rietveld and Refinement and Pattern Matching Analysis, Version 2000, Acta Crystallogr. (1981).
- [57] Program Package for X-ray Diffraction. Version 2.75, Stoe & Cie., Darmstadt (Germany) (1996).
- [58] G. M. Sheldrick, SHELX-97—A Program Package for the Solution and Refinement of Crystal Structures, Universität Göttingen (Germany) (1997).
- [59] V. Petricek, M. Dusek, L. Palatinus, JANA2000. The Crystallographic Computing System, Institute of Physics, Praha, Czech Republic (2000).
- [60] A. L. Spek, PLATON—A Multipurpose Crystallographic Tool, Utrecht University (The Netherlands) (2000).
- [61] X-RED (1.02)—Data Reduction Program, Stoe & Cie., Darmstadt (Germany) (2001).
- [62] X-SHAPE (2.01)—Crystal Optimization for Numerical Absorption Correction, Stoe & Cie., Darmstadt (Germany) (2001).
- [63] W. Massa, *Crystal Structure Determination* (Springer-Verlag, Germany, 2004), second edn.
- [64] Y. Khan, B. V. R. Murty, K. Schubert, *J. Less-Common Met.* **21**, 293 (1970).
- [65] T. Massalski, *CD-ROM, Binary Phase Diagrams* (ASM International, Materials Park, OH, 1996), second edn.
- [66] T. Nash, W. Jeitschko, *J. Solid State Chem.* **143**, 95 (1999).
- [67] M. Boström, S. Lidin, *J. Solid State Chem.* **166**, 53 (2002).
- [68] S. Thimmaiah, K. W. Richter, S. Lee, B. Harbrecht, *Solid State Sciences* **5**, 1309 (2003).
- [69] X. Chen, W. Jeitschko, M. E. Danebrock, C. B. H. Evers, K. Wagner, *J. Solid State Chem.* **118**, 219 (1995).
- [70] W. Hornfeck, S. Thimmaiah, S. Lee, B. Harbrecht, *Chem. Eur. J.* **10**, 4616 (2004).
- [71] Q. Lin, J. D. Corbett, *Inorg. Chem.* **43**, 1912 (2004).
- [72] H. Lind, M. Boström, V. Petricek, S. Lidin, *Acta Crystallogr* **B59**, 720 (2003).
- [73] P. J. Brown, *Acta Crystallogr.* **15**, 608 (1962).
- [74] N. Gross, G. Kotzyba, B. Künnen, W. Jeitschko, *Z. Anorg. Allg. Chem.* **627**, 155 (2001).
- [75] B. Harbrecht, S. Thimmaiah, M. Armbrüster, C. Pietzonka, S. Lee, *Z. Anorg. Allg. Chem.* **628**, 2744 (2002).

- [76] D. Gratias, F. Puyraimond, M. Qusiquandon, A. Katz, *Phy. Rev.* **B63**, 024202 (2001).
- [77] E. Abe, A. P. Tsai, *Phy. Rev. Lett.* **83**, 753 (1999).
- [78] R.-D. Hoffmann, R. Pöttgen, *Z. Kristallogr.* **216**, 127 (2001).
- [79] N. Gross, G. Kotzyba, B. Künnen, W. Jeitschko, *Z. Anorg. Allg. Chem.* **627**, 155 (2001).
- [80] L. Arnberg, S. Westman, *Acta Chem. Scand.* **26**, 513 (1972).
- [81] V. Edström, S. Westman, *Acta Chem. Scand.* **23**, 279 (1969).
- [82] H. Bärnighausen, *Commun. Math. Chem.* **9**, 139 (1980).
- [83] U. Müller, *Inorganic Structural Chemistry* (Wiley, Chichester, 1993).
- [84] A. J. Bradley, P. Jones, *J. Inst. Metals* **51**, 131 (1933).
- [85] S. Mahne, B. Harbrecht, *J. Alloys Comp.* **203**, 271 (1994).
- [86] F. Bonhomme, K. Yvon, *J. Alloys Comp.* **227**, L1 (1995).
- [87] R. Nesper, H.-G. von Schnering, *J. Solid State Chem.* **70**, 48 (1987).
- [88] A. J. Bradley, J. Thewlis, *Proc. Roy. Soc. London* **115A**, 456 (1927).
- [89] L. Arnberg, *Acta Crystallogr* **B36**, 527 (1980).
- [90] S. Samson, *Acta Crystallogr.* **B28**, 936 (1972).
- [91] J. P. A. Makongo, Y. Prots, U. Burkhardt, R. Niewa, C. Kudla, G. Kreiner, *Phil. Mag. Let.* (In press).
- [92] S. Samson, D. A. Hansen, *Acta Crystallogr.* **B28**, 930 (1972).
- [93] L. Arnberg, A. Jonsson, S. Westman, *Acta Chem. Scand.* **30**, 187 (1976).
- [94] C. Lupu, J. Mao, J. W. Rabalais, A. M. Guloy, J. J. W. Richardson, *Inorg. Chem.* **42**, 3765 (2003).
- [95] M. L. Fornasini, B. Chabot, E. Parthé, *Acta Crystallogr.* **B34**, 2093 (1978).
- [96] S. Thimmaiah, M. Conrad, S. Lee, B. Harbrecht, *Z. Anorg. Allg. Chem.* **630**, 1762 (2004).
- [97] W. Jeitschko, E. Parthé, *Acta Crystallogr* **22**, 417 (1967).
- [98] A. Wittmann, H. Nowotny, *J. Less-Common Met.* **9**, 303 (1965).
- [99] S. v. Smaalen, *Z. Kristallogr.* **219**, 681 (2004).
- [100] W. Hume-Rothery, J. O. Betterton, J. Reynolds, *J. Inst. Metals* **52**, 609 (1951).
- [101] C. Dong, *Phil. Mag.* **A73**, 1519 (1996).
- [102] S. Thimmaiah, B. Harbrecht, *J. Alloys Comp.* (In press).
- [103] NIMS, Paulingfile. <http://crystdb.nims.go.jp/>.
- [104] M. Hansen, K. Anderko, *Constitution of Binary Alloys* (McGraw-Hill, New York, 1958), second edn.

REFERENCES

- [105] G. P. Vassilev, *J. Alloys Comp.* **190**, 107 (1992).
- [106] G. P. Vassilev, T. Gomez-Acebo, J. Tedenac, *J. Phase Equi.* **21**, 287 (2000).
- [107] J. Schramm, *Z. Metallkd* **30**, 122 (1938).
- [108] R. P. Anantatmula, D. B. Masson, *Metall. Trans.* **5**, 605 (1974).
- [109] J. K. Critchley, S. Denton, *J. Inst. Metals* **99**, 26 (1971).

Acknowledgments

I would like to express my heartfelt gratitude to Prof. Dr. B. Harbrecht for giving me the opportunity to join his group, for his essential scientific and personal support, and for his participation in the preparation of this thesis.

I would also thank Prof. Dr. W. Massa for taking on the task of co-examiner.

My sincere thanks go to Dr. M. Conrad for introducing me into broad field of crystallography and essential support and suggestions he gave me whenever I encountered problems in this domain.

I am very much thankful to Prof. S. Lee, Cornell University, Ithaca, USA, for the scientific collaboration and for providing X-ray synchrotron data.

I am grateful to Prof. S. Lidin, University of Stockholm, Sweden, for the solutions of incommensurately modulated structures.

I would also thank Dr. M. Boström, European Synchrotron Radiation Facility, France, for the collaboration and introducing me to the melt centrifugation technique.

Thanks to Dr. K. W. Richter, University of Vienna, Austria, for conducting the isopiestic measurements on my behalf.

I would like to thank Prof. H. Keller, University of Dortmund, for arranging the density measurements.

I am highly indebted to Prof. R. Seshadri, University of California Santa Barbara, USA, for introducing me into broad field of solid state of chemistry in the early stage of my research carrier.

My best thanks go to Ch. Wannek, M. Janetzky, C. Allio and A. Kitta for being very friendly co-workers during this project. Special thanks to W. Hornfeck for reading my manuscript and giving me helpful comments.

A lot of thanks to C. Pietzonka for magnetic susceptibility, conductivity measurements and EDX analysis.

My thanks to S. Freistein, U. Kesper, R. Penzel and M. Lohmer for sample preparation, DTA measurements and technical assistance.

Last but not the least, I thank undergraduate students, specially S. Enck, T. Still and A. Holzmeister for partial experimental support for this project.

“DFG for my financial support”.

Declaration

I declare that I myself wrote this study and carried out the experimental work described in it, without using any other sources and aids than those that are stated.

Marburg, November 2005

Curriculum Vitae

SRINIVASA THIMMAIAH

Fachbereich Chemie

Philipps-Universität

Hans-Meerwein-Straße

D-35032 Marburg

Personal: Single, born 27th March 1976, Jagalur, India

Education:

July 2001–September 2005 Pursuing Ph.D in the Department of Chemistry, Philipps University, Marburg, Germany.

1997–1999 M. Sc., Industrial Chemistry, Kuvempu University, Shimoga, India.

1994–1997 B. Sc., Physics, Chemistry and Mathematics, Kuvempu University, Chitradurga, India.

Research Experience:

July 2001–September 2005 Graduate student under supervision of **Prof. B. Harbrecht** in the Department of Chemistry, Philipps University, Marburg, Germany.

Thesis: Synthesis, characterization and phase relations of zinc-rich phases in the binary systems platinum-zinc and nickel-zinc.

Jan.2000–May 2001 Project Assistant with Prof. R. Seshadri in the Department of Solid State and Structural Chemistry Unit, Indian Institute of Science, Bangalore, India (At present, University of California Santa Barbara).

Project1: Synthesis of nano particles via solvothermal decomposition of metal cupferron complexes.

Project2: Synthesis of macro porous solids.

June 1999–Dec.1999 Project Assistant with Prof. M. S. Hegde in the Department Solid State and Structural Chemistry Unit, Indian Institute of Science, Bangalore, India.

Project: Synthesis of rare earth manganates using NaCl / KCl flux.

Publications:

- i) **S. Thimmaiah**, M. Conrad, S. Lee and B. Harbrecht, Pt₁₁Zn₃₂, a γ -brass type related composite structure, (Manuscript under preparation).
- ii) **S. Thimmaiah** and B. Harbrecht, Pt₂₉Zn₄₉, a complex defective AlB₂-type derivative structure, *J. Alloys Compd.*, (In press).
- iii) **S. Thimmaiah**, M. Conrad, S. Lee and B. Harbrecht, The commensurate misfit structure of γ -brass-related Pt₁₁Zn₃₂, *Z. Anorg. Allg. Chem.*, **630**(2004)1762 (Conference abstract).
- iv) W. Hornfeck, **S. Thimmaiah**, S. Lee and B. Harbrecht, Structure-composition relation for the partly disordered Hume-Rothery Phase Ir_{7+7 δ} Zn_{97-11 δ} ($0.31 < \delta < 0.58$), *Chem. Eur. J.*, **10**(2004)4616.
- v) **S. Thimmaiah**, K. W. Richter, S. Lee and B. Harbrecht, γ_1 -Pt₅Zn₂₁ – a reappraisal of a γ -brass type complex alloy phase, *Solid State Sci.*, **5**(2003)1309.
- vi) B. Harbrecht, **S. Thimmaiah**, M. Armbrüster, C. Pietzonka and S. Lee, Structure and properties of γ -brass-type Pt₂Zn_{11- δ} ($0.2 < \delta < 0.3$), *Z. Anorg. Allg. Chem.*, **628**(2002)2744.
- vii) B. Harbrecht, **S. Thimmaiah**, M. Armbrüster, C. Pietzonka and S. Lee, Resolving structural differentiation in the Hume-Rothery phases Pt₂Zn_{11- δ} and Pt_{5 \pm δ} Zn_{21- δ'} , *Z. Anorg. Allg. Chem.*, **628**(2002)2150 (Conference abstract).
- viii) **S. Thimmaiah**, M. Rajamathi, N. Singh, P. Bera, F. Meldrum, N. Chandrasekhar and R. Seshadri, A solvothermal route to capped nanoparticles of γ -Fe₂O₃ and CoFe₂O₄, *J. Mater. Chem.*, **11**(2001)3215
- ix) C. Shiva Kumara, M. S. Hegde, **T. Srinivasa**, N. Y. Vasanthacharya, G. N. Subbanna and N. P. Lalla, Synthesis, structure and magnetic properties of Ln_{1-x}A_xMnO₃ (Ln = Pr, Nd; A = Na, K) from NaCl or KCl flux, *J. Mater. Chem.*, **11**(2001)2572
- x) M. Rajamathi, **S. Thimmaiah**, P. E. D. Morgen and R. Seshadri, Macroporous materials from crystalline single-source precursors through decomposition followed by selective leaching, *J. Mater. Chem.*, **11**(2001)2489

Conferences:

- i) C. Allio, **S. Thimmaiah**, W. Hornfeck and B. Harbrecht, Zinc-rich rhodium compounds - phase and structure relations, GD für Kristallographie, February 28 to March 4, 2005, Köln, Germany.
- ii) **S. Thimmaiah**, M. Conrad, S. Lee and B. Harbrecht, The commensurate misfit structure of γ -brass-related $\text{Pt}_{11}\text{Zn}_{32}$, 12th Conference of GDCh Division for Solid State Chemistry and Material Research "Structure-properties -relation", September 13th–15, 2004, Marburg, Germany.
- iii) **S. Thimmaiah**, W. Hornfeck, M. Conrad and B. Harbrecht, $\text{IrZn}_{10\pm\delta}$ and $\text{Pt}_{5\pm\delta}\text{Zn}_{21-\delta'}$, a comparative study of γ -related Hume-Rothery phases, 9th European Conference on Solid State Chemistry, September 3rd–6th, 2003, Stuttgart, Germany.
- iv) B. Harbrecht, **S. Thimmaiah**, M. Armbrüster, C. Pietzonka and S. Lee, Resolving Structural Differentiation in the Hume-Rothery Phases $\text{Pt}_2\text{Zn}_{11-\delta}$ and $\text{Pt}_{5\pm\delta}\text{Zn}_{21-\delta'}$, 11th GDCh Conference on Structure, properties and relation of Solids, September 24th–26th, 2002, Dresden, Germany.